Side View and End View Mixing measurements of a Sonic Transverse Jet in a Supersonic Crossflow

By

Adam R. Pizzaia

A thesis submitted to the

Graduate School-New Brunswick

Rutgers, The State University of New Jersey

In partial fulfillment of the requirements

For the degree of

Master of Science

Graduate Program in Mechanical and Aerospace Engineering

Written under the direction of

Professor Doyle Knight

And approved by

_____

_____

_____

New Brunswick, New Jersey

May, 2014

ABSTRACT OF THE THESIS

Side View and End View Mixing measurements of a Sonic Transverse Jet in a Supersonic Crossflow

By ADAM R. PIZZAIA

Thesis Director:
Professor Doyle Knight

The primary investigation was to determine if mixing of a sonic transverse jet in the side-view plane was correlated to or equal to the mixing in the end-view plane. The analysis was conducted by imaging a sonic jet in a supersonic crossflow at jet momentum ratios of 1.2, 2.7, and 5.2. Because of the difficulty of placing a camera streamwise to a supersonic crossflow to obtain end view images, off axis imaging was carried out. Overall, the jets appear to be more symmetric when injected into the thin boundary layer than in the thick boundary layer. Centerline probability density functions in the end view plane were compared with probability density functions in the side view plane. The probability of finding unmixed fluid at the windward side of the jet was higher than finding unmixed fluid toward the center or near the orifice plane. Different paths other than those that fall on the mid planes were analyzed and compared in the end-view plane. The effect of the boundary layer thickness on the penetration and mixing of the sonic jet in supersonic flow was investigated.

Acknowledgments

I would like to thank Dr. Doyle Knight and Dr. Tobias Rossmann for their time in advising me on this research. I would like to thank them for the opportunity they provided me with for conducting this research and looking out for my best interest. I would like to thank Ximing Gao, Marc Triebwasser, Esther Lee, Dina Polack, Yasin Abul-Huda, Sarid Shinwari, Mohammad Khan, Jonathan Grova, Charlie Kawczynski, Greg Mastroianni, and Anthony Ho for their technical advice, encouragement, and help with wind tunnel runs. I would like to thank John Petrowski for his time and expertise on trouble shooting problems. I would like to thank all my friends and family for their love, spiritual encouragement, and support.

Table of Contents

List of Tables

List of Figures

Nomenclature

C=concentration

C_0=initial concentration

C_{avg}=maximum concentration in the time average data set

C_{cl}=local maximum centerline concentration value in the z/d=0 plane

C_{max}=maximum concentration value in instantaneous image

d= jet diameter

H=solenoid valve

I=intensity after the filter

I_0= incident intensity

J= jet momentum flux ratio

M_c = convective Mach number

M_j=Mach number of jet

P=probability of mixed fluid

P_{cf}= static pressure of crossflow

P_{0j}=stagnation pressure of jet

P_j=static pressure of jet

$r=U_j/U_{cf}$

R=universal gas constant

U_{cf}=velocity of crossflow

U_j=injection velocity of jet

x/d= stream wise distance normalized by jet diameter

$\delta_{5\%}$= distance from orifice plane to 5 % concentration line at windward side of jet at z/d=0

ϵ=width of bin in histograms

δ=boundary layer thickness

λ_B= Batchelor scale

ρ_j=density of jet

Acronyms

ANV=actuated needle valve

BV=ball valve

CCD= charge coupled device

Cf=crossflow

CL=centerline

CP=critical point

CVP=counter rotating vortex pair

EV=end view

MM=mixed mean

ND=neutral density

OD=optical density

PDF = probability density function

PLIF = planar laser induced fluorescence

PLMS=planar laser mie scattering

PRV=pressure reducing regulator

STP= standard temperature and pressure

SV=side view

TM=true mean

TMF=true mixed fraction

TMFC=total mixed fluid concentration

Chapter 1 Introduction

1.1 Background and motivation

NASA's X-43 was the first aircraft to reach hypersonic speeds using an air-breathing engine. Unlike a rocket that draws oxygen from an oxidizer tank, air-breathing engines intake oxygen from the atmosphere. Without the presence of a heavy oxidizer tank on board, an aircraft can be designed to fly faster and farther. The type of engine that the X-43 used was a supersonic combustion ramjet (scramjet) engine. Ramjet engines have few moving parts and use the contour of the engine inlet to compress the incoming air. The air inside the combustor remains at subsonic speeds while mixing with the fuel. The main difference from a ramjet engine is that the scramjet engine does not decelerate the air to subsonic speeds due to the adverse effects associated of slowing down air from hypersonic to subsonic speeds. An adverse effect of decelerating the flow subsonicaly would be the decrease in total pressure from the additional shocks in the air intake system. The worst offender in total pressure recovery of a supersonic inlet that decelerates the flow to subsonic speeds is the terminal normal shock in the inlet (Farokhi, 2009). There is also an increase in drag due to the turning of the flow through additional oblique shock waves. Now, for a scramjet engine, the incoming flow of air into the combustor remains at supersonic speeds. Scramjet engine lengths are designed to be short for light weight autonomous aircraft. Typical residence time that the incoming compressed air spends in the combustor is on the order of milliseconds. With these issues in mind, researchers try to design and develop efficient scramjet engines based on the mission for which they will be used. Often, the design objective in the propulsion system is to have the fuel and incoming air to mix effectively in the shortest distance possible

before combustion. There are many different injection schemes that have been researched and designed in order to enhance the mixing process.

Researchers have experimented with injecting the jet at different angles into the crossflow (Costa *et al*., 2006) and giving the jet swirl before entering the crossflow (Terzis *et al*., 2012) in hope of accelerating the mixing process. Research has also been conducted with changing the physical geometry of the flow field in order to enhance mixing. Fuller *et al*., (1996) added a physical ramp to the flow field before the injection point which launched shock waves that interacted with the large scale structures in the jet. However there were significant stagnation pressure losses that occurred with the added obstruction of the physical object. Research has shown that the primary vortical structure of mixing in oblique and transverse jets in crossflow is the counter-rotating vortex pair (CVP) (Su and Mungal 2005). The breakdown of the counter-rotating vortex pair into finer turbulent eddies will certainly lead to better solution of mixing and more efficient scramjet engines. Figure 1.1 shows an image of a jet in a supersonic crossflow and depicts the vortical structures that could appear in the flow field of a scramjet engine. In addition to the 3D vortical structures of the jet shown in Fig. 1.1, a coordinate system is shown. The *x* direction is the streamwise direction, the *y* direction is the transverse direction, and the *z* direction is the spanwise direction.

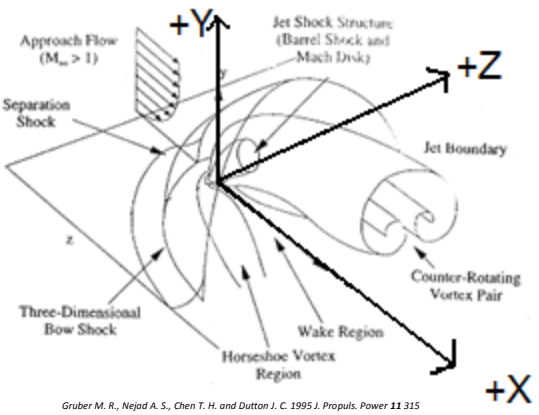

Gruber M. R., Nejad A. S., Chen T. H. and Dutton J. C. 1995 J. Propuls. Power ***11*** *315*

Figure 1.1

The large scale structures like the CVP dominate most of the mixing between the jet fluid and crossflow fluid in the near field. However it is the smaller turbulent eddies in the far field that mix the jet fluid on a molecular level needed for combustion. An appropriate analogy to indicate the degree of mixing that is desired is that of two kinds of paint being mixed together in the same container. If one side of the container has red paint and the other white and they are stirred, one can make out the two distinct kinds of paint in the swirl. However if the container is vigorously shaken, the colors will be truly mixed at the smallest scale. In the case of the scramjet engine, the breakdown of the large scale vortical fuel structures into smaller eddies that molecularly diffuse into the crossflow of air is essential for combustion. Many researchers have recorded the breakdown of the CVP through the use of imaging systems and monitored the jet in crossflow as it developed downstream. Among various injector designs, the transverse injection of fuel through a wall orifice into the supersonic environment is one of the simplest yet most effective configurations (Zhang and Yang 2012). Mixing

measurements of the jet in crossflow are commonly conducted from side-view and end-view planes of the jet as it develops downstream.

The flow field of the jet in cross flow depends primarily upon the ratio of the jet momentum flux to the crossflow momentum flux (Kawai and Lele, 2007). This ratio is known as the jet momentum flux ratio (*J*) and is shown in Eq. (1.1).

$$J = \frac{\rho_j * V_j^2}{\rho_{cf} * V_{cf}^2} \qquad (1.1)$$

In equation 1.1, ρ and *V* refer to density and velocity, respectively. The subscript "*j*" is assigned to the jet conditions at the jet exit and the subscript "*cf*" is assigned to the conditions outside of the boundary layer in the crossflow. Equation 1.1 can be further reduced. If the jet and crossflow behave as an ideal gas, then one can obtain equation 1.2. If the flow in the wind tunnel and jet injector is considered adiabatic and isentropic, then the compressible flow theory in equations 1.3a and 1.3b can be applied.

$$J = \frac{(\frac{P_j}{T_j R_j}) * (M_j \sqrt{\gamma_j R_j T_j})^2}{(\frac{P_{cf}}{T_{cf} R_{cf}}) * (M_{cf} \sqrt{\gamma_{cf} R_{cf} T_{cf}})^2} \qquad (1.2)$$

$$\frac{P_{0j}}{P_j} = \left[1 + \frac{\gamma - 1}{2} M_j^2\right]^{\frac{\gamma}{\gamma - 1}} \qquad (1.3a)$$

$$\frac{P_{0cf}}{P_{cf}} = \left[1 + \frac{\gamma - 1}{2} M_{cf}^2\right]^{\frac{\gamma}{\gamma - 1}} \qquad (1.3b)$$

In Equation 1.2, the variables P_j, T_j, R_j, M_j, γ_j, P_{cf}, T_{cf}, R_{cf}, M_{cf}, γ_{cf} are the static pressure of the jet, static temperature of the jet, the gas constant of the jet, the Mach number of the jet, the ratio of specific heat of the jet, the static pressure of the crossflow, the static temperature of the crossflow, the gas constant of the crossflow, the Mach number of the crossflow, and the ratio of specific heat of the crossflow, respectively. In equation 1.3, the variables P_{0j} , P_j , M_j , P_{0cf} , P_{cf}, and M_{cf} are the stagnation pressure of the jet, the static pressure of the jet, the Mach number of the jet, the stagnation pressure of the crossflow, the static pressure of the crossflow, and the Mach number of the crossflow, respectively (Osthuizen and Carscallen, 1997). The ratio of specific heat of the jet and crossflow are assumed to be nearly equal and so are labeled γ in equation 1.3. Sonic velocity occurs at the exit of a converging nozzle when the ratio of the external ambient air pressure to the upstream stagnation air pressure is less than 0.528 (Sujith, 2010). At this pressure ratio and smaller, the flow becomes choked and the Mach number of the jet becomes fixed at unity. In the experiments analyzed in this report, the choked condition in the jet injector was satisfied and was verified by the test conditions tabulated in Table 2.1. The test conditions in Table 2.1 will be later discussed in Chapter 2. Further, with the given information thus far, equation 1.2 can be simplified into a final equation.

$$J = \frac{P_j}{P_{cf} M_{cf}^2} \qquad (1.4)$$

In equation 1.4 for choked conditions, P_j can be changed by varying the stagnation pressure of the jet which can be seen with the help of equation 1.3a. If one is using a wind tunnel that has fixed Mach number for a given stagnation pressure, the denominator

of equation 1.4 can be calculated. The previous statement can be seen with the help of equation 1.3b.

Further, another calculation important to compressible flow is the calculations of the static and crossflow temperatures. Calculations of these thermodynamic properties can help one determine other parameter such as density, viscosity and Reynolds number of the jet and cross flow.

$$\frac{T_{0j}}{T_j} = 1 + \frac{\gamma-1}{2} M_j{}^2 \qquad (1.5a)$$

$$\frac{T_{0cf}}{T_{cf}} = 1 + \frac{\gamma-1}{2} M_{cf}{}^2 \qquad (1.5b)$$

In equation 1.5a and 1.5b, T_{0j} is the stagnation temperature of the jet and T_{0cf} is the stagnation temperature of the crossflow.

1.2 Literature Review

1.2.1Side view imaging

There are many techniques to obtain information about the flow field of a jet in crossflow. An anemometer could be used to measure the speed at which vortical structures convect downstream and a pressure transducer can be used to obtain pressure fluctuations across shock structures. A common technique in the area of mixing is to obtain the data from instantaneous or averaged images of the jet. A high quality CCD

array camera is often used to capture the jet in cross flow. Planar imaging eliminates the need for sampling at multiple points in the flow. The jet in crossflow is usually visualized by seeding the jet with a chemical that will illuminate when a laser light is shined on the atomized particles. The side-view plane of the jet offers much detail about the trajectory of the jet and the many interactions the jet encounters with the cross flow. Common large scale structures that have been observed in side-view imaging planes are Kelvin-Helmholtz instabilities (Sau *et al.,* 2005), double helix structures (Kawai and Lele 2007), and finger-like wake structures (Gamba *et al*., 2012). The types of the vortical structures that appear in the flow often depend on the speed regime of the flow field. For example, an under expanded sonic jet will expand through a Prandtl-Meyer fan at the lip of the jet orifice before the jet flow is compressed by a barrel shock and Mach disk (Kawai and Lele 2007). The presence of shock structures often impact the mixing of a jet in crossflow because of the characteristic density and pressure changes across the shock. When shock structures are not present in the flow, mixing depends heavily on other vortical structure enhancement techniques to encourage mixing. A review of the current research carried out for side-view imaging of a jet in subsonic crossflow will soon be carried out below.

1.2.2 End view Imaging

End view imaging allows the jet to be viewed from a whole different perspective. Instantaneous and average end-view images provide a great deal of information of the jet in crossflow. The end-view plane can reveal transverse and lateral penetrations of the jet. Instantaneous images can provide details about the vortical structures in the end-view plane. The CVP is best viewed from instantaneous images in the end view plane. Often

the average images of the CVP in the end-view plane look kidney shaped (Gruber and Nejad, 1995). One can record the formation of the CVP by placing the laser sheet at different stream wise stations downstream of the injection point. Mixing measurements can be obtained from both the instantaneous and average images. The common line between the side-view and end-view plane is important to keep in mind when comparing images from different orthogonal views (Smith 1996). There is a lack of qualitative data from end-view imaging because of the difficulty of placing a camera parallel to the flow. Fuller *et al.* (1996) avoided using an imaging system entirely and obtained concentration measurements at discrete points in the flow through isokinetic sampling. The images formed were not of great quality in the analysis and the contour color scales were not consistent between plots. Often, when end view images are taken in a supersonic crossflow flow field, the camera is placed at an angle to the flow. Supersonic wind tunnels are often associated with bulky structures with few glass planes because of the high dynamic pressure inside. When the camera is placed at an angle, the images are then corrected and de-warped in a computer program. End view images of jets in subsonic flows can be recorded parallel to a flow if a water tank is being used or if it is a small scale wind tunnel.

1.2.3 Jets in Subsonic Crossflows

The jet in subsonic crossflow is quite common in many physical applications. They can appear in the form of exhaust fumes from locomotives or in the scenario of a smoke stack from factories exhausting smoke on a windy day. Mixing measurements of

jets in subsonic crossflow are easier to record because of the flexibility of studying the flow field in small scale wind tunnel or water tunnel. Many researchers have obtained velocity and pressure measurements of the flow field without attempting to calculate the mixedness. Fric and Roshko (1994) obtained high quality side-view images of a jet in crossflow. They showed that the boundary layer on the wall from which the jet issued from was the main source of vorticity. The qualitative images solely addressed the formation of the wake structures in the complex 3D flow field and the results did not conclude the effect that the vortical structures had on mixing in the flow field. Recker *et al*. (2010) provided high quality pixel mean average images of the jet in crossflow. They also used their averaged images as qualitative in nature only. Their side-view images qualitatively complemented their z-vorticity image maps. The majority of research in side-view imaging at subsonic speeds is trying to understand the mixing mechanisms that develop in the jet. In lower Reynolds number flow, it is easier to observe and conclude about the large scale vortical structures that develop than to conclude about mixing. Of the jets that are quantified by mixing, it is usually parallel injection. Quantitative mixing measurements were conducted at subsonic speeds in the experiments conducted by Island (1997). Island conducted mixing of two shear layers flowing parallel to each other and he measured the fraction of mixed fluid (mixing efficiency) through the layer using cold chemistry Planar Laser Induced Fluorescence (PLIF). Island denoted the mixing efficiency as the fraction of fluid in the layer which is molecularly mixed and is defined as the integral of the probability of mixed fluid profile. In this thesis, the probability of mixed fluid profile has the form of equation 4.7, latter to be discussed in section 4.3. The mixing efficiency was measured as 0.5, 0.54, 0.60, and 0.62 at M_c =0.25, 0.39, 0.63, and

0.76, respectively. In Island's work, M_c was the convective Mach number. He characterized the compressibility of the mixing layer as $M_c=(U_1-U_2)/(a_1-a_2)$. (U_1-U_2) and (a_1-a_2) are the velocity difference and speed of sound difference between the two mixing layers, respectively. He attributed the increase of mixing efficiency with compressibility.

Experiments have been carried out to investigate the jet in crossflow in the end-view plane. Instantaneous end-view images of the jet in subsonic crossflow revealed extensive motion of the CVP by Smith and Mungal (1998). Although their experimental setup was symmetric, their averaged images showed that the jet concentration was not symmetric about the streamwise midplane. They noted that asymmetries were also seen in the work of Eiff (1996), McCann &Bowersox (1996) and Liscinsky, True & Holdeman (1996). In Smith and Mungal concentration profiles and probability density functions (PDF's) were created at different stream wise stations for side-view images, but they failed to provide extensive mixing information on the end-view plane. Concentration profiles are common plots to extract from instantaneous and average images. Smith (1996) made conclusions on jet asymmetry and complex behavior in his experiments. He showed that the CVP may be symmetric or asymmetric, but the asymmetry occurs in different forms. The left or right lobe of the CVP may contain more jet fluid than the other and the CVP may tilt left or right closer to the wall independent of which lobe has more jet fluid contain in it. The two lobes in the CVP may appear to be widely spaced from each or squeezed close together. Smith (1996) noted jet fluid to be present in between the CVP in some images and absent in others. Quantifying the end-view plane by constructing probability density functions and mean plots may provide numerical trends not easily seen from qualitative observation.

1.2.4 Jets in Supersonic Crossflow

There are trends that suggest mixing becomes more efficient as the crossflow Mach number increases. As the Mach number of the crossflow increases, the flow field becomes more turbulent. Turbulence is a fundamental ingredient for the enhancement of mixing. Freund *et al.* (2000) performed turbulent annular mixing simulations. They noted that increasing the crossflow Mach number, the mixing efficiency went from 0.5 at M_c=0.1 to 0.67 at M_c=1.5. They showed that mixing efficiency increased with Mach number. Their subsonic results on mixedness in the side-view plane correlate well with the results by Island (1997). The research carried out by Island (1997) and Freund *et al.* (2000) did not involve transverse jets in crossflow which is the flow field that will most likely be found in a scramjet engine. In addition, the maximum convective Mach numbers Island (1997) and Freund *et al.* (2000) experimented with were Mach 0.76 and 1.8, respectively. Presently, it appears technically feasible to develop air-breathing engines capable of operating at Mach numbers as high as M=8-12 (Ferri 1973). Ferri's idea should encourage experimental research to be conducted at higher supersonic Mach numbers. Sun *et al.* (2013) experimented with injecting transverse jet in a Mach 2.7 crossflow. They focused on revealing the detailed structures at the jet crossflow interface. One of their claims was that the near field determines the scale of eddies in the far field and affects the whole mixing process. However they did not provide quantitative mixing results to back up their claim. The body of experimental evidence concluding mixing at supersonic Mach numbers in different imaging planes is not too large.

The variety of calculations and analyses of the jet in supersonic crossflow on the end-view plane is limited in scope. Most often the images are not high quality and more

conclusions are drawn on the contours of the plume. Gruber (*et al* 1995) attempted to analyze the end-view plane of the jet in supersonic crossflow by placing the camera at an angle to the crossflow. The average images were poor of quality. Only plume contours and spatial penetration plots of the jet were the highlighted in the report. They evaluated only one *J*-momentum ratio which was 2.9. No attempt on mixing calculations were mentioned or shown. The end-view average images of the jet showed asymmetry in the supersonic crossflow, but was not discussed. Shao *et al.* (2011) recorded side-view and end-view images of two angled jets arranged in a series. The jets were injected into a supersonic crossflow where the Mach number of the crossflow ranged from 4-5. They concluded that the mixing characteristics of the tandem jets were dominated by the entraining and counter-rotating vortices generated beside the jets. Although they did provide instantaneous images of their results for both side-view and end-view imaging, they did not provide quantified data of their analysis. Their conclusions were based on qualitative observations. There is more information on end-view planes by simulations rather than experimentation. Higgins and Schmidt (2007) simulated a sonic jet injection into a Mach 1.6 supersonic crossflow. The contours of Reynolds stresses and turbulent kinetic energy from their simulations were compared with experimental measurements made by Santiago (1995). Reasonable qualitative comparisons were observed, but the simulations tended to under predict the peak values from the experiments. Higgins and Schmidt (2007) showed velocity profiles, but did not show any numerical results on mixing. Because of the lack of information on end-view planes and their correlation to side-view planes, a thorough analysis should be conducted experimentally.

1.3 Research Objective

The body of research devoted to mixing of the jet in crossflow is small (Su and Mungal 2005). The mixing measurements at supersonic Mach numbers, with a transverse injection are even smaller. The primary investigation is to determine if the mixedness of the side-view plane is correlated or equal to the mixedness in the end-view plane. The analysis will be conducted by imaging a sonic jet in a supersonic crossflow at different jet momentum ratios. Because of the difficulty of placing a camera streamwise to a supersonic crossflow to obtain end-view images, off-axis imaging will be carried out. Other goals for the research include investigating how centerline probability density functions in the end view plane compared with probability density functions in the side view plane. Paths other than the streamwise midplane will also be analyzed and compared in the end-view plane. The effect that boundary layer thickness has on the penetration and mixing of the sonic jet in supersonic flow will be investigated.

Chapter 2 Experimental Facility and Techniques

2.1 The Supersonic Wind Tunnel

The experiments were conducted in the supersonic wind tunnel located in the gas dynamics and diagnostics lab at Rutgers. The blow down wind tunnel has a test section Mach number of 3.45 and a typical run time for a single test is about 15 seconds. The dimensions of the test section are 15.24 cm by 15.24 cm. Wind tunnel test conditions are shown in Table 2.1

The air is compressed by a Mako four stage air compressor. After the air is compressed, the water vapor is removed from the air by a Zander dryer. The dry and compressed air are then directed into four storage tanks that have total storage capacity of $8m^3$. The minimum pressure held in the tanks was 900 psig in order to prevent condensation forming in the tanks and to keep a steady stagnation pressure during tests. The maximum pressure the tanks can be filled to is 1900psig. Any pressure greater than 1900psig will cause an emergency shutoff to be triggered.

As shown in Fig. 2.1, valves and systems have been labeled to help explain the process that the compressed air follows through the sequence of the experiment. First air from the storage tanks is brought into the lab by opening ball valve #1. In path 1, there are two valves in series that keep the air in the storage tanks from entering the converging-diverging nozzle. Ball valve #2 regulates the high 900+ psi air from the storage tanks down to 200psig, which is the operating stagnation pressure for the wind tunnel. An emergency actuated needle valve, labeled ANV in Fig. 2.1, is placed in between ball valve #2 and the stagnation chamber to prevent air from flowing into the test section just in case ball valve #2 were to ever fail while ball valve #1 was opened.

The needle valve is left open during a wind tunnel run. As air passes through the ANV, the air settles in a stagnation chamber before going through three honeycomb panels. After the honey comb aligns the flow to become straighter and laminar, the air moves through the converging diverging nozzle. At the exit of the nozzle the air is at Mach 3.45. The air maintains this speed through the constant cross sectional area test section. After the supersonic air exits the test section, it expands and slows down through the diffuser. The air makes a 90 degree turn upwards and exhausts outside on top of the roof.

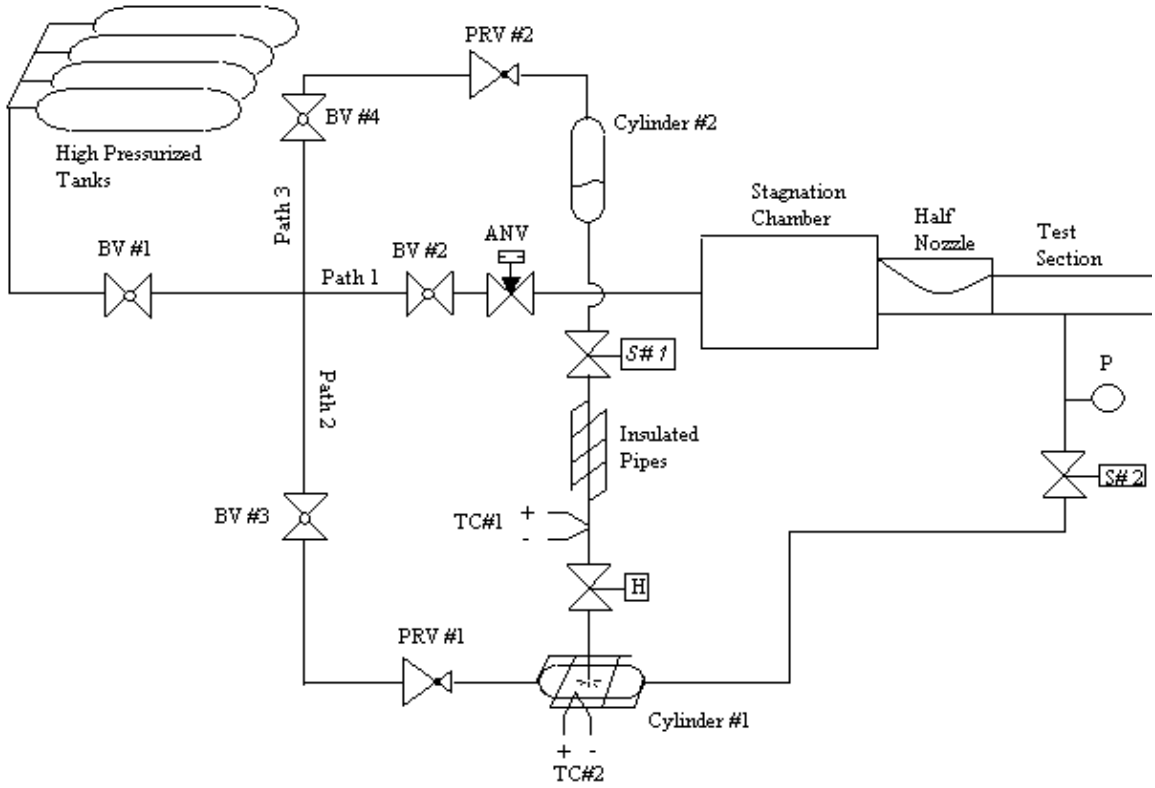

Figure 2.1 Schematic diagram of Wind tunnel

2.1.1 Wind Tunnel Test Conditions

The wind tunnel test conditions are shown in Table 2.1. The first row in Table 2.1 shows the three jet momentum flux ratios that were used in the experiments. The jet momentum flux ratios were calculated from equation 1.4. The Mach number and static

pressure of the crossflow in the denominator of equation 1.4 was kept fixed for all three jet momentum flux ratios. Therefore only the static pressure term in the numerator of equation 1.4 was changed when moving to a different jet momentum flux ratio. The static pressure of the jet (P_j) was measured from the stagnation pressure right before injection. The stagnation pressure was measured by a pressure gage that was placed right after a solenoid valve. The flow of air through the jet system will be discussed in section 2.2. The jet stagnation pressure was set at the beginning of the wind tunnel run. The jet pressure was not exactly constant during the experiments due to the decrease in stagnation pressure as the wind tunnel run progressed. The errors and uncertainties in day to day operation of the wind tunnel will be discussed in section 4.5. After the static pressure is calculated from the stagnation pressure, the density of the jet (ρ_j) can be calculated from the ideal gas law. The ideal gas law is shown in the first set of parenthesis in the numerator of equation 1.2. Likewise the density of the crossflow (ρ_{cf}) can be calculated from the ideal gas law. The velocity of the jet (U_j) was calculated from the product of the speed of sound and Mach number of the jet. The velocity of the crossflow (U_{cf}) was calculated from the product of the speed of sound and Mach number of the crossflow. The dynamic viscosities (μ) for air were calculated from the Sutherland charts in Fox *et al*. (2009).

2.2 Jet and Ethanol System

As shown in Fig. 2.1, the jet system and ethanol system are separated into two different paths that eventually join together in a heated cylinder. The pipes that the air flows through in paths 2 and 3 are 1.27cm in diameter. Path 2 controls the J value of the jet while path 3 controls the ethanol quality that is used to seed the jet. The processes that

the air and ethanol go through before entering the cylinder are important for proper visualization of the jet.

A directional handle ball valve, ball valve #3, when opened allows air to flow down path 2. The compressed air flows to a pressure reducing valve which is labeled PRV # 1 in Fig. 2.1. The self-venting regulator drops the high back pressure to a lower pressure that is desired for the jet. In addition, the pressure of the jet is controlled by PRV # 1. After the air is dropped down to a lower pressure, the compressed air continues to flow through 1.27 cm diameter stainless steel pipes to a 67.8 cm long heated cylinder. The cylinder is labeled cylinder #1 in Fig. 2.1 and has a diameter of 10.16cm and a storage capacity of 3785 cm^3.

The heating and preparation of the ethanol before its entrance into the jet is important for proper seeding. A directional handle ball valve, ball valve #4, when opened allows air to flow down path 3. The compressed air flows to a pressure reducing valve which is labeled PRV #2 in Fig. 2.1. The self-venting regulator drops the high back pressure to a lower pressure that is 100psi greater than the pressure of the jet set by PRV #1. The pressure of the ethanol contained in cylinder #2 and pipes in path 3 are always set greater than the pressure of the jet in path 2 so that the ethanol can make its way into heated cylinder 1. The best pressure differential that was found for optimum atomization of ethanol droplets was 100psi. Ethanol was stored in cylinder 2. Cylinders 1 and 2 have identical physical dimensions.

The ethanol is pressurized to a point set on the vapor dome diagram in Fig. 2.2. The blue saturation curve is generated by the Antoine equation shown below in equation 2.1.

$$\log P = A - \frac{B}{T+C} \qquad (2.1)$$

The Antoine equation is a simple three variable fit to experimental vapor pressures over a limited temperature range. The variables *A*, *B*, *C* are Antoine coefficients and they vary from compound to compound. For ethanol, *A* is equal to 7.61117, *B* is equal to 1332.04, and *C* is equal to 199.2 (Teoh, 2012). In equation 2.1, *P* is equal to pressure in the units of Torr and *T* is equal to temperature in the units of Celsius.

As shown in Fig. 2.1, there is a 25.4cm long section of insulated pipe between Solenoid (S#1) and a pneumatic valve (H). Ethanol is heated under pressure in the 1.905cm diameter pipe. The pneumatic and solenoid valves are wired to a controller box and can be opened or closed by a flip of two switches by the operator. The pipes are heated by an Omega CN9000A Series controller. One K-type thermocouple is placed on the pipe near the pneumatic valve (H) and is used to transmit instrumentation signals to the controller. The sheath material is 304 stainless steel. High temperature insulation is secured to the pipes with heating tape in this section. When the ethanol is heated to a sufficient temperature governed by the heating curve, the pneumatic valve (H) is opened. Solenoid #1 valve is also opened to keep a constant pressure in the insulated pipes. When the pneumatic valve is opened, the heated liquid ethanol flows to the Bete-PJ40 fogging nozzle located in cylinder #1. The ethanol sprays into a much hotter cylinder than the pipes causing the ethanol to go into a vapor state. The temperature of the cylinder is governed by the saturation curve in Fig. 2.2. The temperature of the heated pipes and cylinder depended on the *J* value of the jet. For example, if one looks at the *J*=2.7 case, the ethanol was pressurized in the pipes in path 3 to 300psi therefore the pipes were heated to a temperature close to the heating curve which was 150 degrees Celsius. The

pressure of the jet in path 2 was 200 psi and this was the pressure contained in cylinder #1. So if one would want the ethanol to vaporize upon entering the 200psi cylinder one could make the temperature of cylinder #1 to be 190 degrees Celsius. Cylinder #1 was heated by a second Omega CN9000A Series controller. The cylinder was wrapped in insulating material and had a 304 stainless steel sheath k-type thermocouple on it to sense the temperature.

The seeded air in cylinder #1 then flowed to solenoid valve #2. A pressure gage, labeled P, was placed right after the solenoid valve. There were pressure losses in the pipe system leading up from PRV#1 to the solenoid valve #2, so a pressure gage was placed after solenoid #2 to read the final jet stagnation pressure. Once solenoid valve #2 was switched open, the ethanol and air mixture flowed through the jet injector. The jet injector for the wall injection had an inner diameter of 0.1 inches and was 200 jet diameters in length. The jet injector for the wedge injection had an inner diameter of 0.123 inches and was 163 jet diameters in length. The ethanol vapor condensed upon entering the very cold supersonic crossflow. A laser reflected the fine ethanol droplets and caused the jet to illuminate.

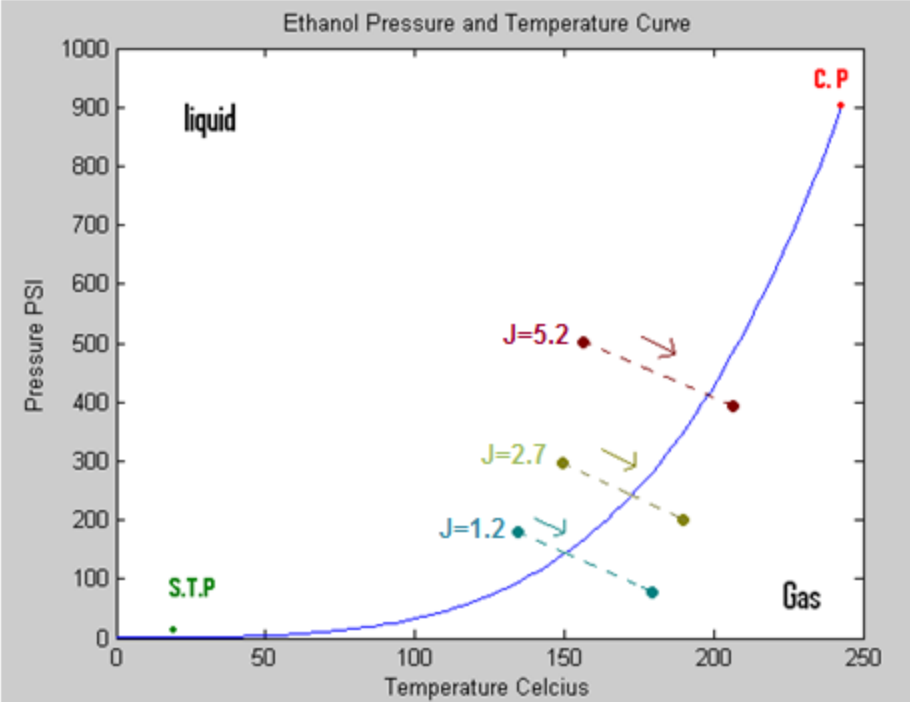

Figure 2.2 Ethanol Saturation curve

2.3 Planar Laser Mie Scattering

A Planar Laser Mie Scattering technique was used to visualize the flow. The laser used was a New Wave Solo 2 Nd-YAG laser. Two laser cavities were used in the experiment. The lasers' *q* switches were triggered at maximum population inversion to illuminate as many ethanol particles as possible. The two cavities were synchronized as close as possible before each run using a Molectron Power Max5200 meter. The laser was placed on a vibration isolation optical table. The mounting holes on the table secured the laser and diagnostic equipment during the wind tunnel runs. The laser was aimed at a 532 nm rounded mirror that was set at about 45degrees to cause the laser beam to make a 90 degree deflection to the test section. As shown in Fig. 2.3 the laser beam would then travel though a series of three cylindrical lenses. From bottom to top the lens measured were 100mm, 11.2 mm and 25mm. The lenses were stacked on a supporting fixture. The

lens caused the laser to expand into a laser sheet that would illuminate a section of the flow. For side-view imaging, the laser sheet was aligned with the geometric centerline of the jet.

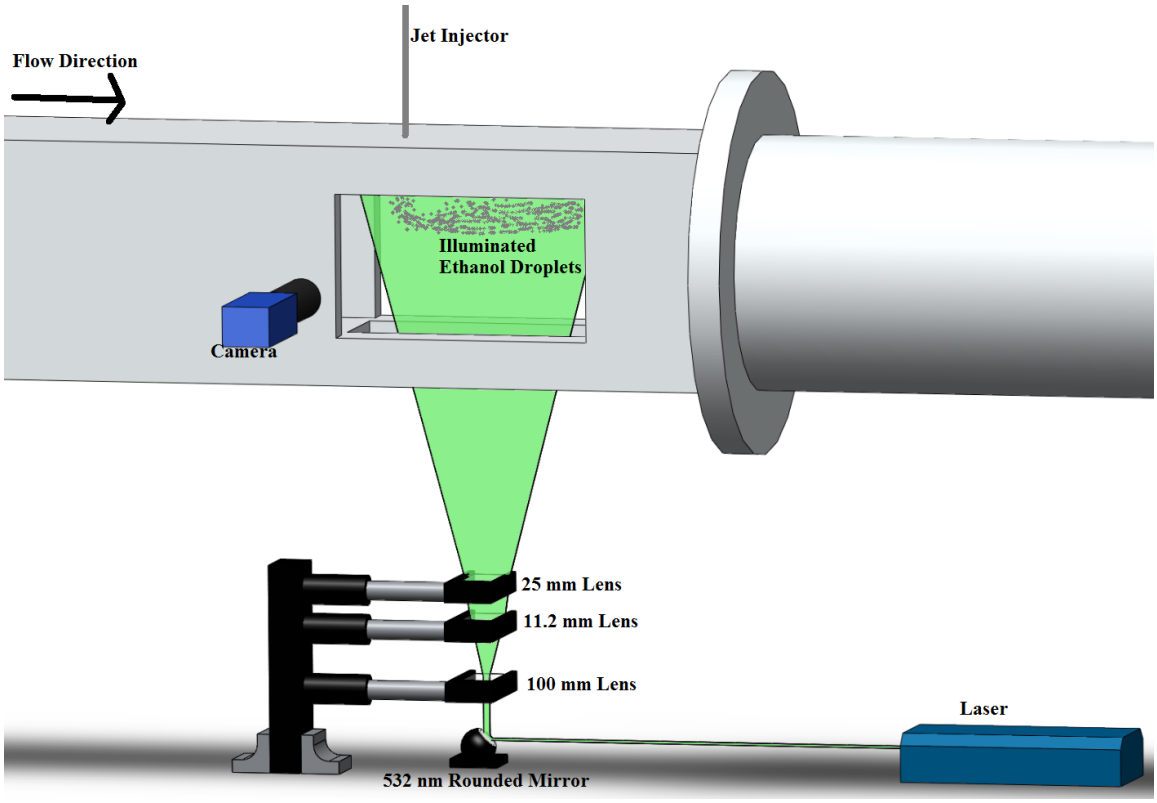

Figure 2.3 Side viewing imaging setup

The camera used in the experiment was a LA vision Imager Pro High speed CCD array camera. A zoom of 1+ was placed on the camera for side-view imaging. The images were 1200X1600 pixels. The camera had a maximum intensity intake of 16383 counts. Any pixels of intensity value greater than that value would over saturate the camera. Since the laser was set on its highest power in order to illuminate as many ethanol droplets as possible, the high signal intensity would often over saturate the pixels on the camera. So a neutral density filter was placed in between the flow and camera to decrease the amount of light transmitted to the camera. The neutral density filter was

placed directly in front of the camera. Based on experimentation it was found that an optical density (od) filter of 1.3 provided the best results. The amount of light blocked by an od filter is mathematically calculated from equation 2.2.

$$od = -\log_{10}\frac{I}{I_0} \qquad (2.2)$$

In equation 2.2, I_0 is the incident intensity while the variable I refers to the intensity after the filter. The variable *od* is the optical density of the filter. So an *od* filter of 1.3 transmits 5% of the incident light to camera. For the experiments, the intensity I after the filter was the largest that could cause the camera to have the greatest dynamic range without over saturating the pixels. The camera was connected to a data acquisition system and the computer software that allowed user interface with the camera was Davis. During the experiments, the camera and laser were controlled externally by a timer program called Trigger.

The camera and laser were connected to an 8 channel Labsmith LC880 pulse delay generator. The channels connections are shown in Fig. 2.4. The diagram below shows the sequence of when the commands were executed. The sequence operated on a 10 hertz clock. The camera had the capability of capturing two frames per cycle. The window of opportunity to get the laser into the first frame was much smaller than for the second frame. It was found that the first frame and second frame of the camera were open for 5.25 microseconds and 32 milliseconds, respectively. There was a 200 nanosecond delay from when the first frame of the camera closed and the second frame opened. The first laser was signaled to fall into the first frame of the camera while the second laser pulse fell into the second frame. The q switches were triggered at maximum population inversion. The time delay of max population inversion differed between the two laser

cavities. The flash lamps were triggered so that maximum population would occur in the small window of time when the camera frames were opened.

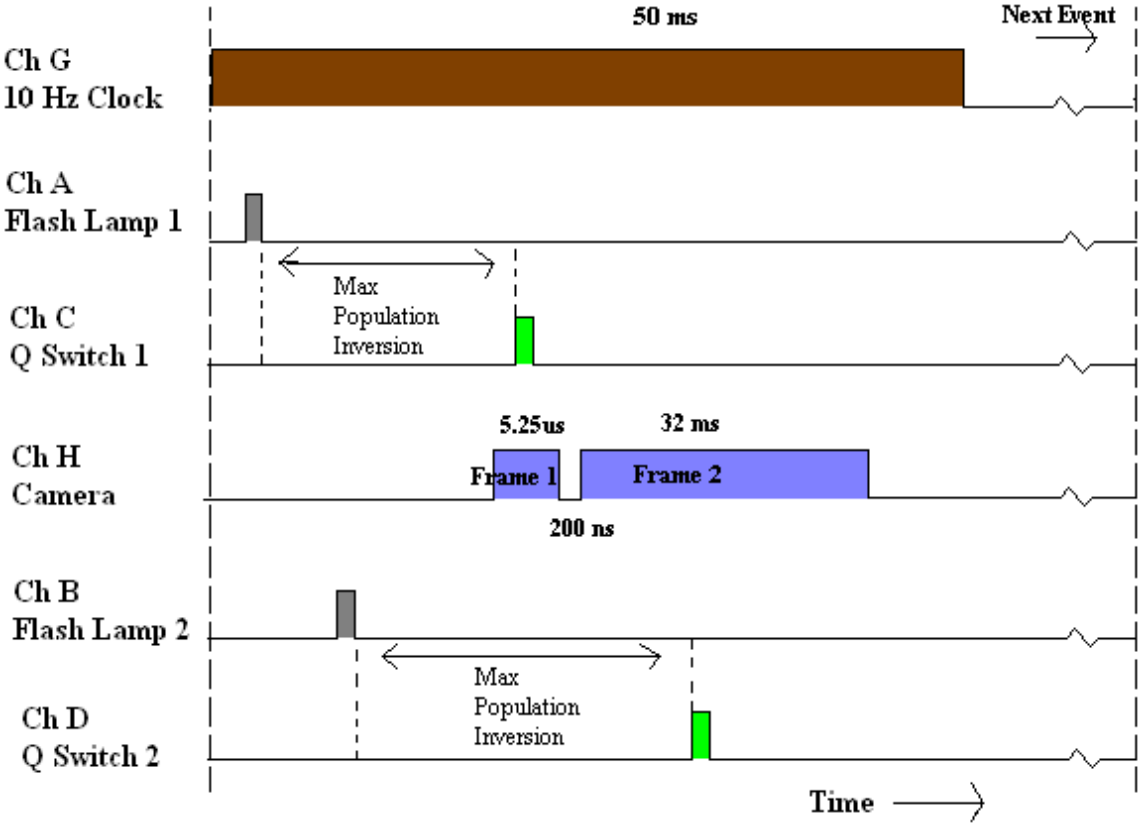

Figure 2.4 Laser Timing Schedule

2.4 Boundary Layer Measurement

2.4.1 Wall Boundary layer

The PLMS images form the basis of the report due to the objective of seeking concentration profiles of the jet and examining mixedness. Schlieren imaging was used to measure the thickness of the wall boundary layer thickness where the jet was injected. The wall boundary layer thickness was measured to be 7.5 jet diameters and in SI units the thickness was 1.9 centimeters. The schlieren images also provided detail about the shock structures developed in the sonic jet in supersonic crossflow. The science of

schlieren imaging involves visualizing the distortion of light rays when they pass through regions of different densities. This distortion can be amplified through a schlieren setup of concave mirrors, lenses, and a knife edge.

The schlieren setup used in the experiments was a Z-type arrangement as shown in Fig. 2.5. The strobe light was a 1531-AB series Strobotac Electronic Stroboscope. The pulse of the light matched the frequency of the camera. The frequency of the strobe light was internally set on the device at 30 Hz. The light from the strobe light reflected off a rectangular mirror to a concave mirror. The light rays became parallel as they reflected off the first concave mirror. The two concave mirrors used had a focal ratio of *f*/8. After the rays passed through the test section, the distorted rays were reflected off a second concave mirror. A knife edge was placed at the focus of the light to sense the density gradients. The orientation of the knife edge was important. A vertical knife edge is used to visualize horizontal density gradients while a horizontal knife edge is used to visualize vertical gradients. After the light passed the through a knife edge, two lenses were used to focus the light on the camera. The camera used for schlieren imaging was the same camera used for PLMS. The camera had a zoom1+ lens attached. Davis was used to control and record the data in one frame of the camera.

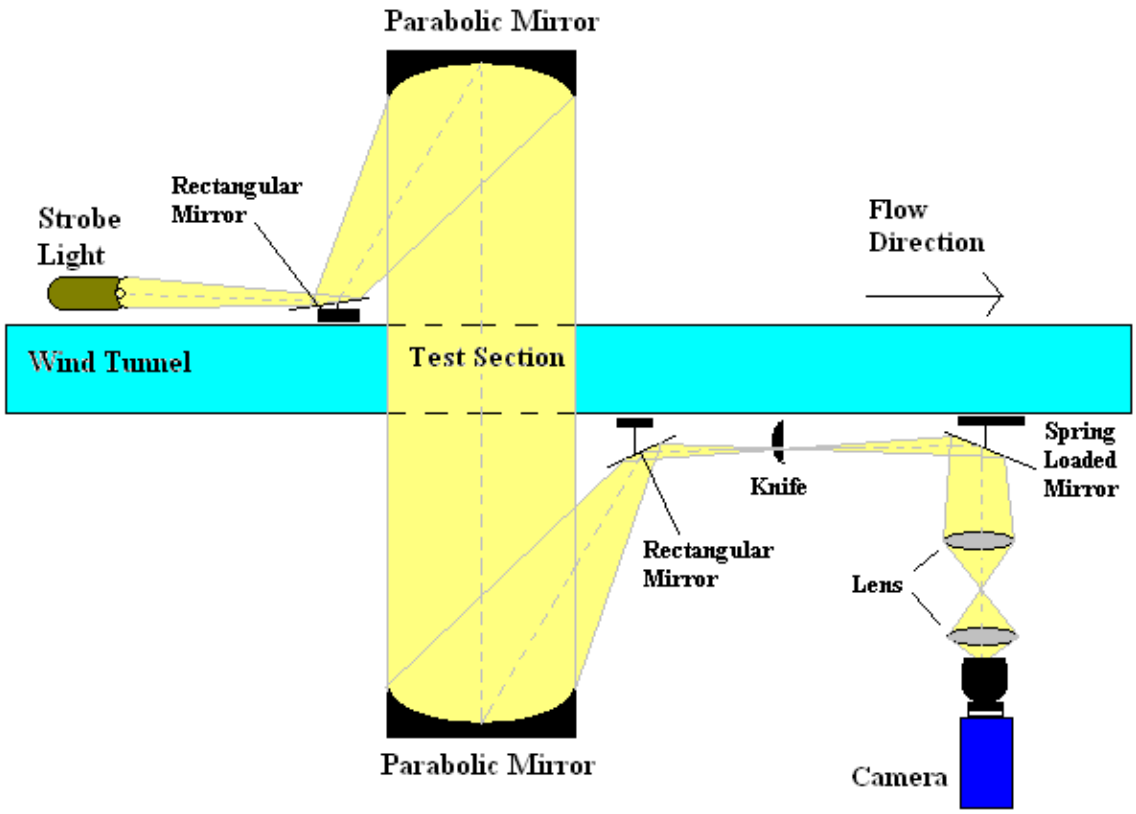

Figure 2.5 Schlieren setup

2.4.2 Wedge Boundary layer

Schlieren imaging was not conducted for the wedge injection experiments. In order to determine the boundary layer thickness, an incompressible turbulent boundary layer formula was used from Fox, Pritchard, and McDonald (2009).

$$\frac{\delta \text{wedge}}{x} \sim \frac{0.382}{Re_x^{.2}} \qquad (2.3)$$

In equation 2.3, δ_{wedge} is the boundary layer thickness on the wedge at the injection point, the variable x is the distance from the leading edge of the flat plate to the injection point, and Re_x is the local Reynolds number right before the injection point on the flat plate. The boundary layer thickness for the wedge was calculated to be about 0.7 jet diameters which in SI units are 0.22 centimeters.

The wall has a boundary layer that is much thicker than the boundary layer that is formed on the wedge. In the following report the jet that is injected into the wall boundary layer (δ/d=7.5) will be referred to as the "thick" boundary layer. The jet that is injected into the wedge boundary layer (δ/d~0.7) will be referred to as the "thin" boundary layer.

2.5 Image Processing

The raw images recorded went through image processing in Matlab. Each data set had anywhere from 80 to 200 images. Eight bit integer images were converted into double float type images in Matlab. Background light was subtracted out from the instantaneous images. The background represents the dark noise and scattering light from the three test section windows. The instantaneous images were divided by a laser sheet profile. The laser sheet profile image was taken immediately before or after an experiment. The laser sheet profile was obtained by aiming the laser sheet on a uniform white background. The laser sheet profile for the entire image is constructed from the row where the intensity profile is known. Since the laser sheet profile is different for both cavities, the two cavities had to be normalized. The laser cavities for the side-view images were then normalized by dividing all the instantaneous images by the same constant value that normalized the average image from values 0 to 1. The normalized images were then written into a folder for further analysis.

2.6 Off Axis Imaging

In order to record images of the end view plane of the jet, the CCD array camera was placed at an angle to the supersonic cross flow. This angle from the streamwise

direction ranged between 15 and 25 degrees. The angle depended on what spanwise plane was being captured. The camera had to be reset and re-zoomed at every span wise plane. For x/d =5 and 10, a zoom 2+ camera lens was placed on the camera. At x/d=20, a zoom 1+ camera lens was used. For end view imaging, the optical setup containing the series of lenses on the isolation table was rotated 90 degrees laterally as shown in Fig. 2.6. This caused the laser sheet to illuminate the cross section of the jet.

Most of the image processing for the end-view was the same as the side-view. However it is necessary to point out the differences. When a camera takes an image at an off-axis angle, the image becomes distorted geometrically. What normally are squares in an image become parallelograms when that image is taken from an angled shot. To overcome this distortion phenomenon, a grid containing squares was placed in the wind tunnel as shown in Fig.2.7. The camera took a picture of the grid at each of the span wise sections that were imaged during the wind tunnel experiments. A code in Matlab de-warped the grid back to squares using a projective transformation. The projective transformation did not preserve the radiance of the image in the x direction. For example, when a parallelogram on the right of the image became transformed into a square, the intensity value decreased. This decrease in intensity occurred linearly across the image. So a simple linear radiance correction was applied to correct the intensity value. An example of the grid at x/d =5 is shown in Fig. 2.7. In addition, the angled imaging presented a problem of creating ghost images to the very right of the image. Because of the location of the ghost image to the right, it did not pose a problem in calculating the mixedness on the geometric centerline. The ghost image was subtracted from the images.

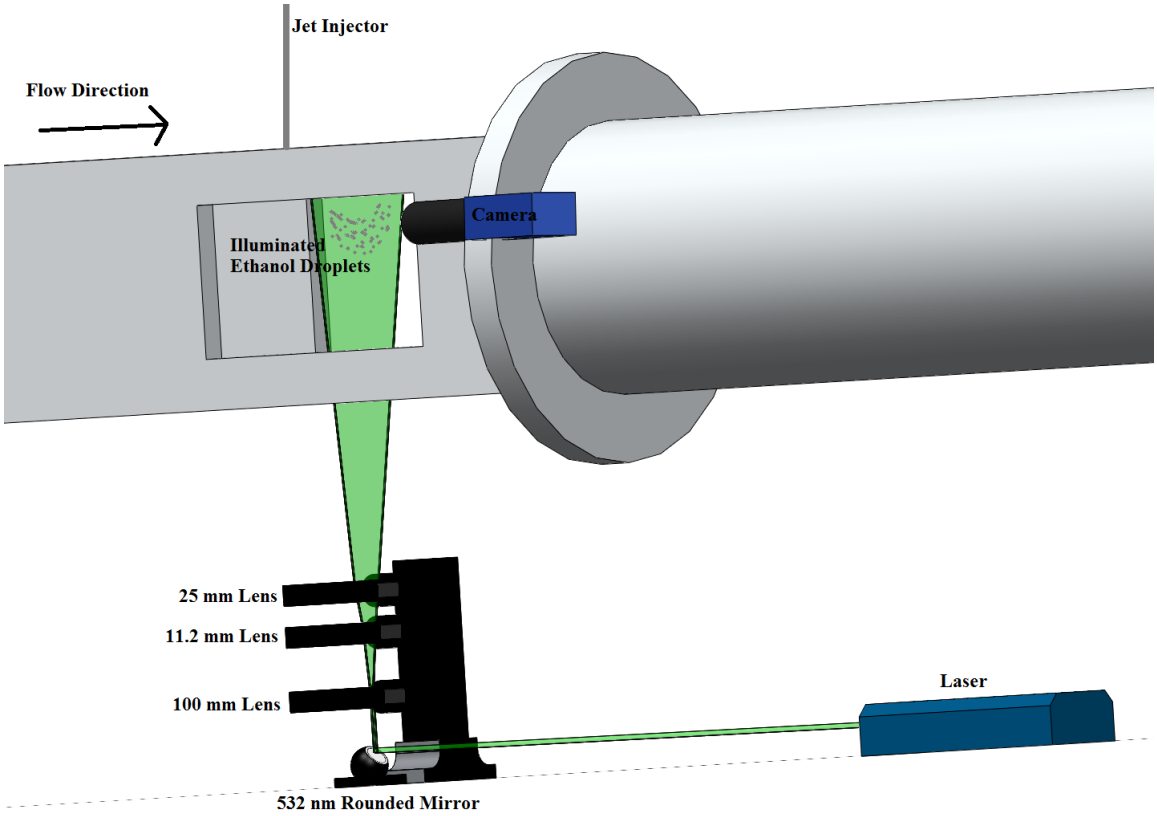

Figure 2.6 End view imaging setup

ORIGINAL DEWARPED

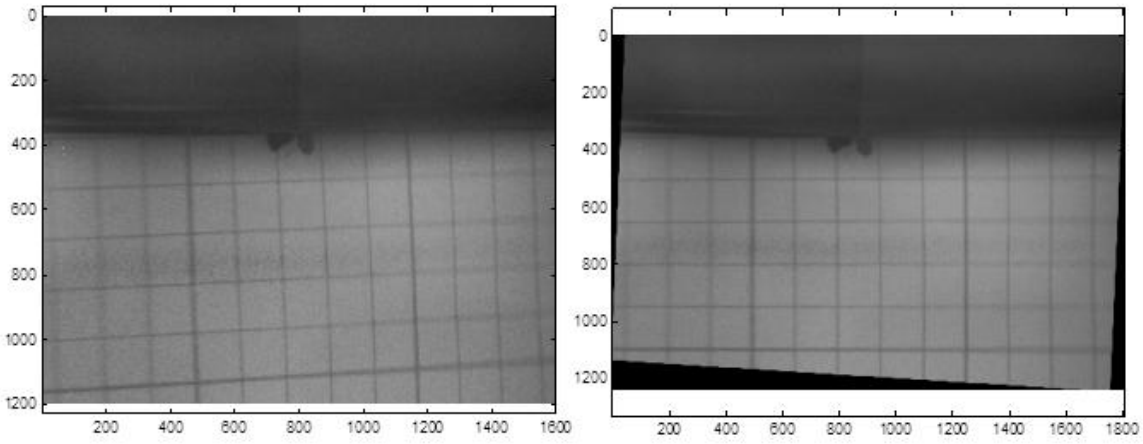

Figure 2.7 Projection Transformation

Table 2.1 Test conditions

Crossflow parameters		**Jet parameters**	**J=1.2**	**J=2.7**	**J=5.2**
T_0	288K	T_0	288K		
T_{cf}	85.19K	T_j	240K		
P_0	1.47MPa	P_0	563 kPa	1252 kPa	2410 kPa
P_{cf}	20.8kPa	P_j	298 kPa	662 kPa	1273 kPa
M_{cf}	3.45	M_j	1		
U_{cf}	638m/s	U_j	310.5m/s		
ρ_{cf}	0.85 kg/m^3	ρ_j	4.3 kg/m^3	9.6 kg/m^3	18.5 kg/m^3
$Re_{wall}=(\rho_{cf}u_{cf}\delta_{wall})/\mu_{cf}$	5.8X10^5	$Re_j=(\rho_j u_J d_{wall})/\mu_J$	2.2X10^5	4.8X10^5	9.4X10^5
$Re_{wedge}=(\rho_{cf}u_{cf}\delta_{wedge})/\mu_{cf}$	6.7X10^4	$Re_j=(\rho_j u_J d_{wedge})/\mu_J$	2.7 X10^5	6 X10^5	1.2 X10^6

Chapter 3 Structural Results

3.1 PLMS Results

3.1.1 Side View Results

PLMS images provide both quantitative and qualitative results. As mentioned in the introduction, PLMS images can provide insight into mixing mechanisms by solely observing the qualitative images. It is worth the investigation to interpret the images which could provide explanations to the numerical mixing results. Discussion of the images also provides a thorough analysis of the work. The side-view imaging results are provided in Figures 3.1-3.12. Average images of the jet are natural logged in order to illuminate smaller signals for appearance purposes. The instantaneous images are normalized and displayed by the pixel intensity values at the jet exit. Matlab has a color map named 'jet' that maps the numerical values in the image from blue to red. A color coded bar on the right of each image indicates the pixel value of the double integer type image. The average image is normalized by the pixel intensity values at the jet exit. Therefore jet fluid issuing from the jet orifice will have values close to 1 while unmixed cross flow fluid will have values closer to 0.

Noticeable in the side-view images, as the *J* value of the jet is increased, the jet penetrates farther into the crossflow in the transverse direction before bending downstream. The side-view average images of the jets issuing into the wall boundary layer appear to be blunter looking than for the wedge cases. A comparison between the wall and wedge boundary layer experiments show that the jets are able to penetrate farther out into the crossflow for the wall boundary layer than for the wedge boundary

layer. The thicker boundary layer has a velocity profile that is still developing in the transverse direction after the first *y/d* jet diameter. After 1 jet diameter in the transverse direction, the velocity profile of the thin boundary layer is already developed and by that point is at the free stream velocity. So the jet in the thicker boundary layer is interacting with a smaller *x* momentum flow than in the thin boundary layer case and so is able to extend further out into the flow before bending downstream.

As the *J* value of the jet increases, a region of unmixed fluid begins to grow on the leeward side of the jet after the injection point. This region is termed the recirculation zone and has many flame holding characteristics. The recirculation zone is clearly visible in both the average and instantaneous images for the thin boundary layer. For the wall boundary layer injections, it is more difficult to distinguish the recirculation region in the average images. In the near field the jet in crossflow has both a *y* component of momentum and an *x* component of momentum, the *x* component coming from the entrainment of the crossflow. However in the far field the *x* momentum dominates and the jet convects in the *x* direction. For each jet, the delay of where the jet exhibits near field and far field behavior depends on the boundary layer thickness and *J* value of the jet. This delay will be quantified in chapter 4 and further clarified. Qualitatively the images show that after the recirculation region, the jet fluid touches the wall. Mixed fluid can be seen near the jet orifice plane after the recirculation region for both side and end view averages. The instantaneous images show concentrations of mixed fluid connecting from the leeward side of the jet to the orifice plane. This phenomenon was also seen in jets in subsonic crossflow (Fric and Roshko 1994).

The side view images show that for wall injections, the J=1.2 (Fig. 3.3) and J=2.7 (Fig. 3.2) jet mix entirely in the boundary layer. The windward side of the J=5.2 (Fig. 3.1) jet partially makes it through the boundary layer into the supersonic crossflow. In any case the wall jets are interacting with a turbulent boundary layer which may contribute to their being excessive amount of mixed fluid in the recirculation regions as compared to the thin boundary cases. For the wedge injection cases, all the jets have sufficient amount of transverse momentum to penetrate through the thin boundary layer in the near field and fully interact with the crossflow. The J=1.2 (Fig. 3.6) and J=2.7 (Fig. 3.5) jets injected into the wedge boundary layers are interacting with a higher x momentum flow than the wall injected J=1.2 (Fig. 3.3) and J=2.7 (Fig. 3.2) jets. Kelvin-Helmholtz instabilities can be seen in the instantaneous side-view images. Figure 3.8 shows a J=2.7 jet that contains peak pixel intensity values contained in the instabilities after three jet diameters downstream. These intensity values are similar to the values immediately at the jet exit. As jet fluid accelerates in the x direction downstream, it becomes difficult to make out the large scale vortical structures because they become broken down and finely mixed.

The ethanol seeding is sensitive to density. When the jet is injected into the cross flow, one can make out a parabolic contour of the jet fluid. The density of the air increases across a shock wave. The high quality PLMS images show an increase of density in ethanol due to the compression of the barrel shock. The Mach disk can also be seen in the jet. In addition, each instantaneous image contains a noticeable high area of signal located on the windward side of the jet in the near field. This illuminated area can sometimes be larger than the signal value immediately at the jet exit. A close up will

reveal that a double helix-like vortical structure containing jet fluid rolls up onto itself to reflect a high signal. This rollup causes an increase in density of the ethanol particle which increases its signal value.

3.1.2 End View Results

Average and instantaneous end view images are provided in Figures 3.13-3.48. The average images are displayed in the report that will allow for best picture quality and clearness. The images are normalized by the maximum pixel value recorded in the average image (C_{avg}) for each data set. The instantaneous images are normalized for display by the maximum value in the instantaneous image (C_{max}). Therefore the dynamic range is numerically from 0 to 1 with a color map that ranges from blue to red.

The average end view results for the thick boundary layer at a first glance shows asymmetry in the sonic jet in the supersonic crossflow. For a symmetric jet, the maximum concentration is located close to the centerline trajectory of the jet as viewed in the side view plane. The *J*=2.7 (Figures 3.16-3.18) jet in the thick boundary layer starts off with a symmetric kidney shape intensity profile. However as it moves downstream the jet becomes asymmetric with peak intensity values dominating in the right lobe. This is the opposite trend of the *J*=5.2 jet in the thick boundary layer, it starts off with asymmetry in the first two stations of *x/d*=5 (Fig. 3.19) and *x/d*=10 (Fig. 3.20) but becomes symmetric at *x/d*=20 (Fig. 3.21). With the exception of the *J*=2.7 jet at *x/d*=5 (Fig. 3.25) and *J*=5.2 jet at *x/d* =20 (Fig. 3.21), all the other jets at the various *x/d* stations in the thick boundary layer have their maximum intensity values located in the right lobe with varying degree of asymmetry. The lower *J* value jets in the thick boundary layer show that the intensity values tend to shift toward the wall as stream wise distance

increases, with exception of the *J*=5.2 jet (Figures 3.19-3.21). A suggestion of why the *J*=5.2 jet does not have strong signal levels at the wall as it develops downstream may be due to it having more transverse momentum in the near field than the other lower *J* values. The *J*=5.2 jet can penetrate farther away from the wall than the other *J* values and keep its maximum concentrations farther away from the wall.

For the thick boundary layer, one can notice that when the jet is asymmetric, maximums intensity values are dominant in the right lobe. However when the jet shows asymmetric behavior in the wedge boundary layer, maximum intensity values are found in the left lobe. The *J*=2.7 jet (Fig. 3.25) and *J*=5.2 jet (Fig. 3.28) at *x/d* =5 show indications of asymmetry with a bias towards the left lobe. As the stream wise distance increases the *J*=2.7 and *J*=5.2 jet even out from an asymmetric status to a more even symmetric state about the *z/d*=0 plane. Overall, the jets appear to be more symmetric when injected into the thin boundary layer rather than the thick boundary layer. With the exception of the *J*=2.7 jet (Fig. 3.25), *J*=5.2 (Fig. 3.28) at *x/d* =5, and *J*=1.2 jet at *x/d* =20 (Fig. 3.24), the averaged end view images of the jet in the thin boundary layer are quite symmetric.

In most of the end-view instantaneous images (Figures 3.31-3.48), the counter rotating vortex pair can be identified. Each vortex can be identified by its center which contains mixed fluid at a very low pixel values with highly mixed fluid edges. The *J*=1.2 jet in a thick boundary layer at *x/d* =20 (Fig. 3.33) is an example that the center of each vortex does not necessarily have the same amount of concentrated jet fluid in it. The right lobe has higher pixel values in it which can often lead to the average image being asymmetric and biased to the right lobe. The instantaneous image of the *J*=2.7 jet injected

into a thin boundary layer at *x/d*=20 (Fig. 3.45) show vortices with almost equal peak pixel values in each center and the centers are equal distant from the wind tunnel wall. However in the *J*=1.2 jet at the *x/d*=5 station (Fig. 3.40) in the thin boundary layer one can see that one lobe can be located geometrically higher than the other in the flow and still have equal concentrations of mixed fluid in each of the centers. Regardless of the boundary layer, the jet can move randomly around with it lobes shifting around geometrically from one another. The instantaneous view of the *J*=5.2 jet at *x/d*=20 (Fig. 3.39) in the thick boundary layer shows the turbulent and the wild nature of the CVP. The left lobe is one jet diameter higher than the right lobe. The streamwise vortices of the wind tunnel wall seem to torque the jet off its center.

3.2 Schlieren

The Z type schlieren setup only allows for side-view imaging of the sonic jet in crossflow. Schlieren imaging allowed for the boundary layer thickness to be measured for the wall injection. In addition, schlieren imaging also showed two shock phenomena occurring in the jet in Fig. 4.49 and Fig. 4.50. A bow shock can be seen right in front of the injector. A bow shock is caused by the blockage of the jet. This bow shock causes the flow to separate from the wall. The separation event causes a shock of its own labeled as a separation shock. As the *J* value of the jet is increased the bow shock becomes blunter looking from the side-view perspective. In other words the angle of the bow shock with respect to the orifice plane is increased as the *J* value increases. Due to the limited resolution of the schlieren setup, other known shock features like the barrel shock and Mach disk cannot be viewed.

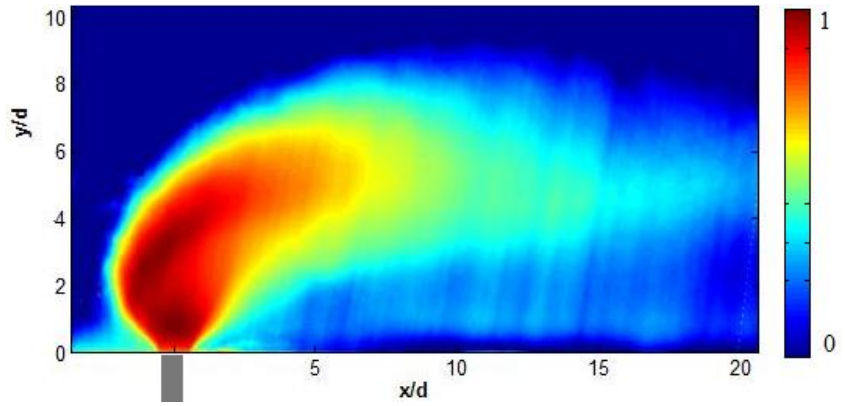

Figure 3.1. Time average Ln(C/C_0) PLMS side view image. δ/d =7.5 and J=5.2. Gray line is the injection point.

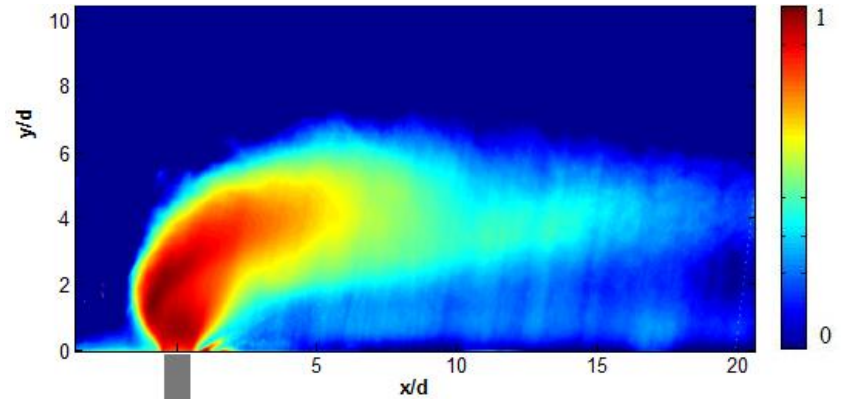

Figure 3.2. Time average Ln(C/C_0) PLMS side view image. δ/d =7.5 and J=2.7. Gray line is the injection point.

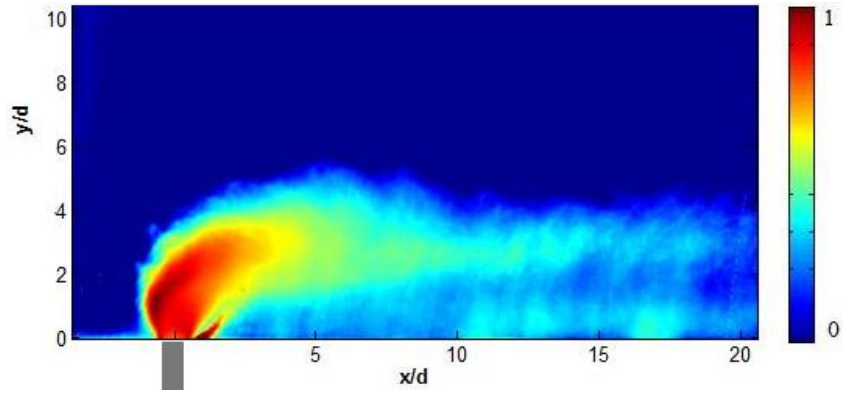

Figure 3.3. Time average Ln(C/C_0) PLMS side view image. δ/d =7.5 and J=1.2. Gray line is the injection point.

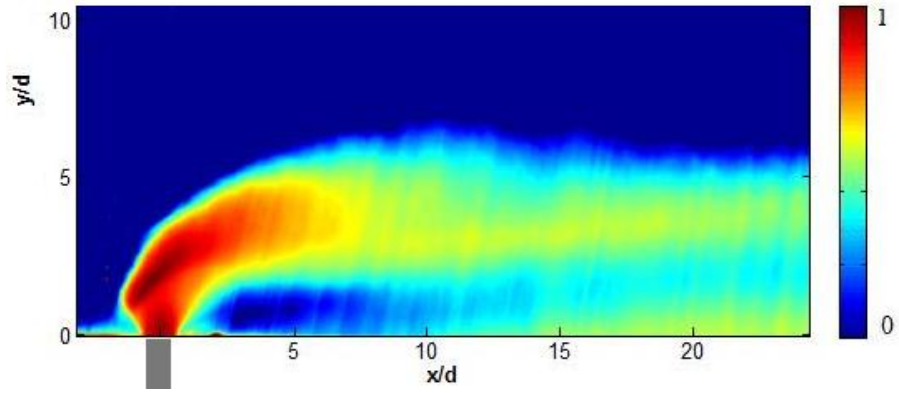

Figure 3.4. Time average $Ln(C/C_0)$ PLMS side view image. δ/d~0.7 and J=5.2. Gray line is the injection point.

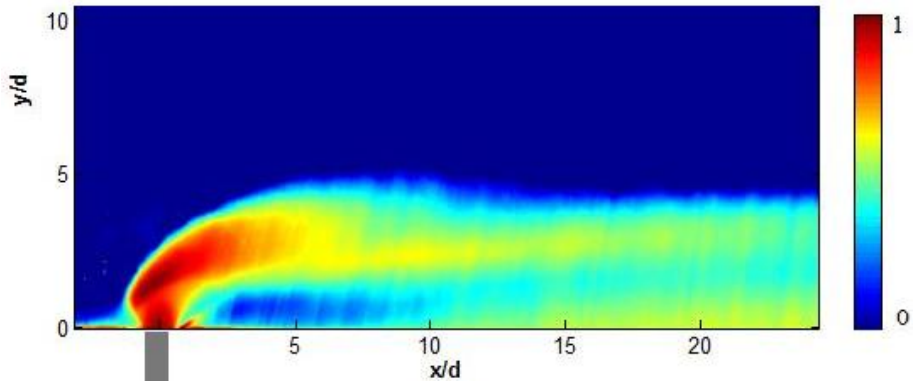

Figure 3.5. Time average $Ln(C/C_0)$ PLMS side view image. δ/d~0.7 and J=2.7. Gray line is the injection point.

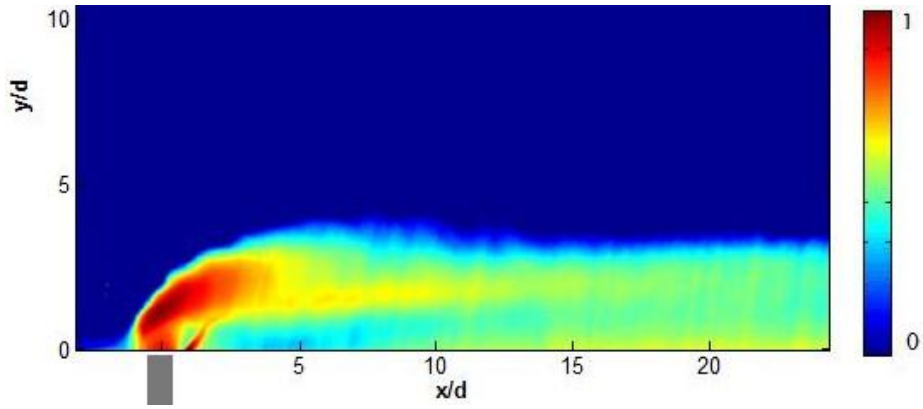

Figure 3.6. Time average $Ln(C/C_0)$ PLMS side view image. δ/d ~0.7 and J=1.2. Gray line is the injection point.

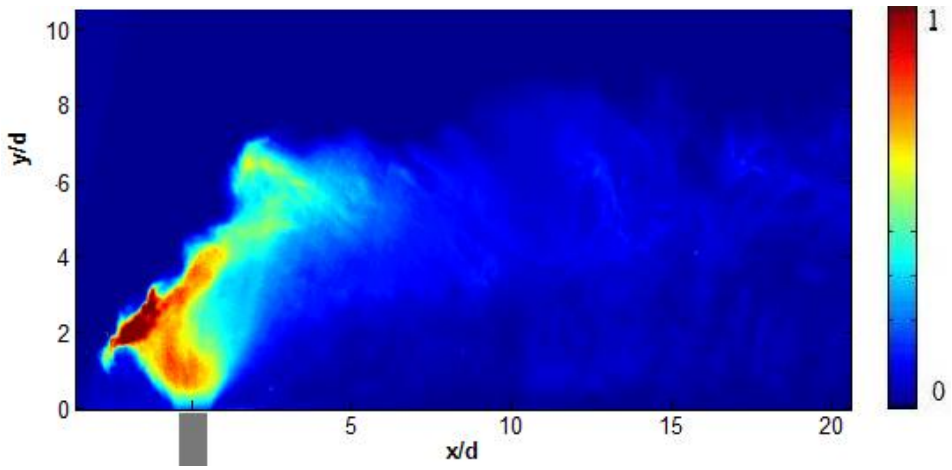

Figure 3.7. Instantaneous (C/C_0) PLMS side view image. δ/d =7.5 and J=5.2. Gray line is the injection point.

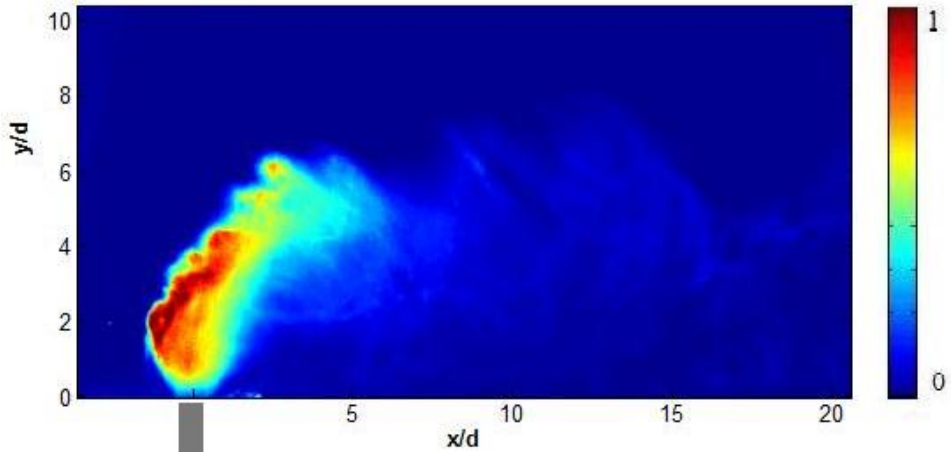

Figure 3.8. Instantaneous (C/C_0) PLMS side view image. δ/d =7.5 and J=2.7. Gray line is the injection point.

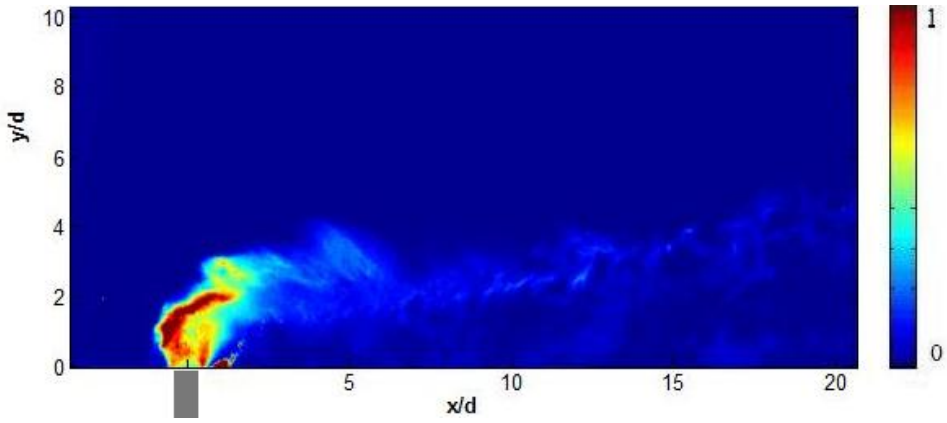

Figure 3.9. Instantaneous (C/C_0) PLMS side view image. δ/d =7.5 and J=1.2. Gray line is the injection point.

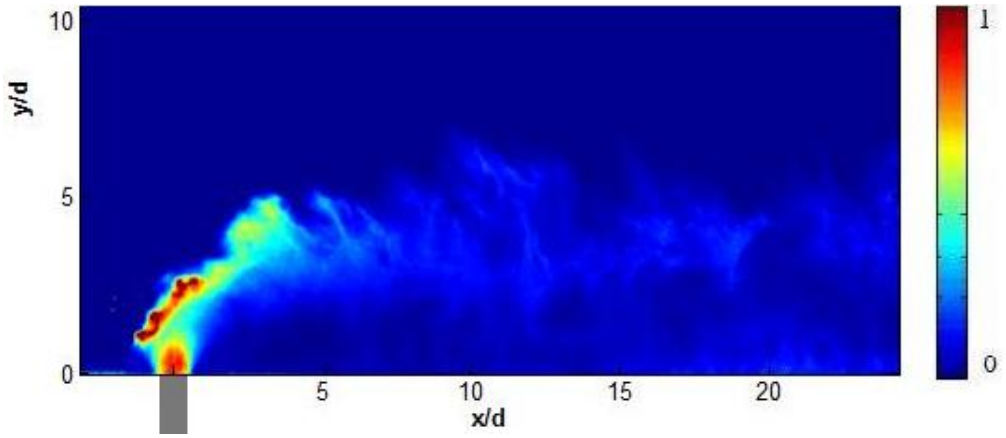

Figure 3.10. Instantaneous (C/C_0) PLMS side view image. δ/d ~0.7 and J=5.2. Gray line is the injection point.

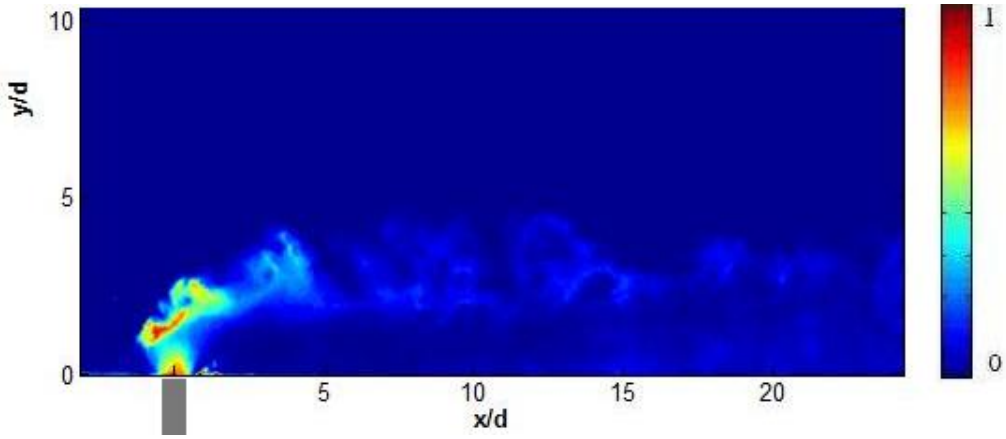

Figure 3.11. Instantaneous (C/C_0) PLMS side view image. δ/d ~0.7 and J=2.7. Gray line is the injection point.

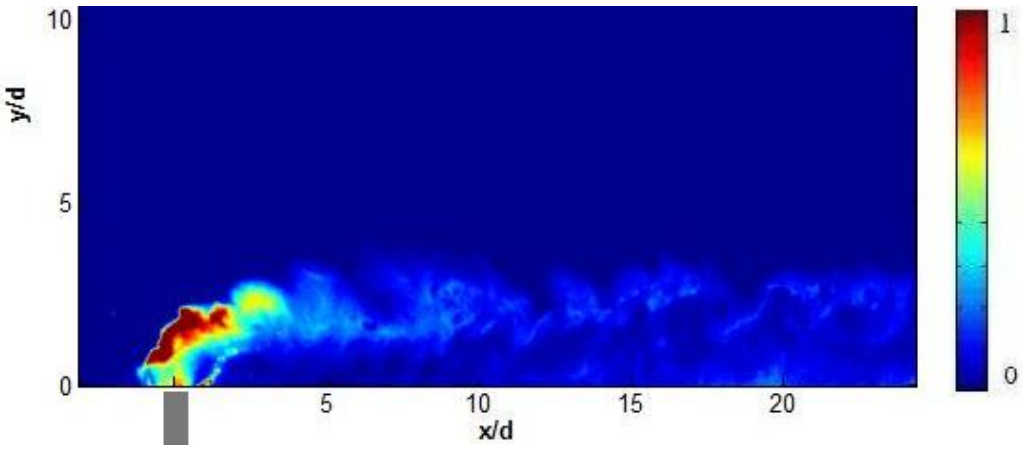

Figure 3.12. Instantaneous (C/C_0) PLMS side view image. δ/d ~0.7 and J=1.2. Gray line is the injection point.

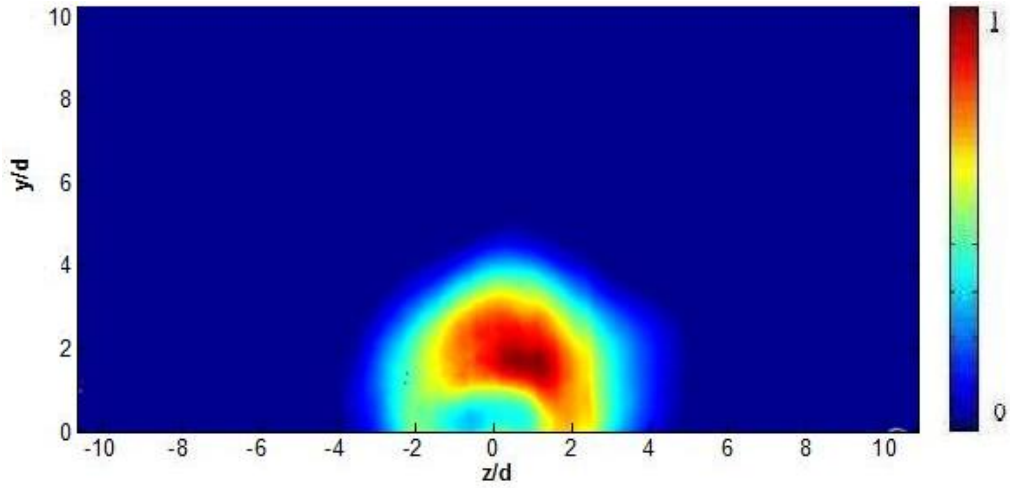

Figure 3.13. Time average (C/C_{avg}) PLMS end view image. δ/d =7.5, J=1.2 and x/d=5.

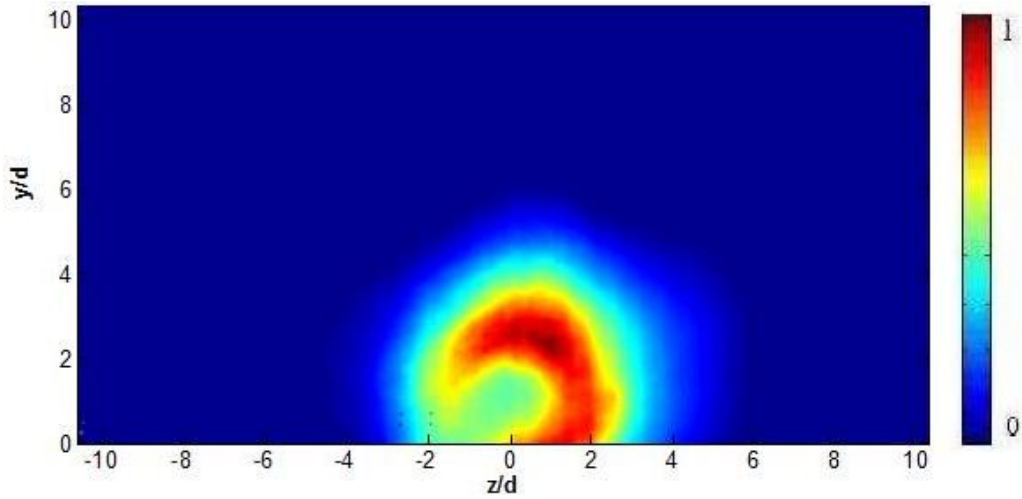

Figure 3.14. Time average (C/C_{avg}) PLMS end view image. δ/d =7.5, J=1.2 and x/d=10.

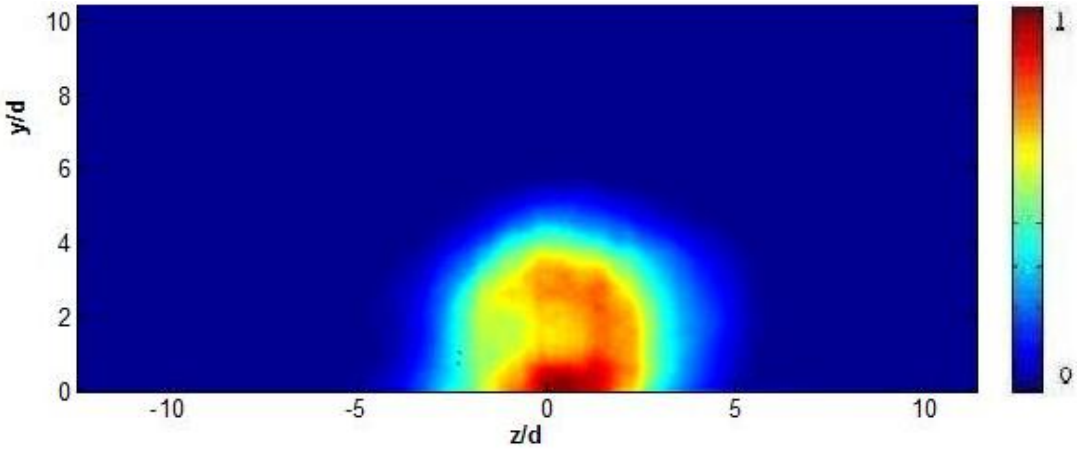

Figure 3.15. Time average (C/C_{avg}) PLMS end view image. δ/d =7.5, J=1.2 and x/d=20.

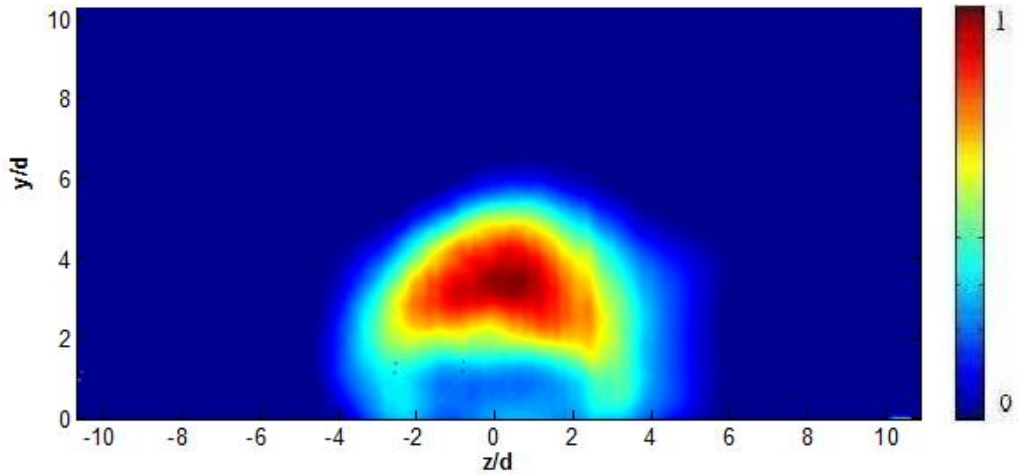

Figure 3.16. Time average (C/C_{avg}) PLMS end view image. δ/d =7.5, J=2.7 and x/d=5.

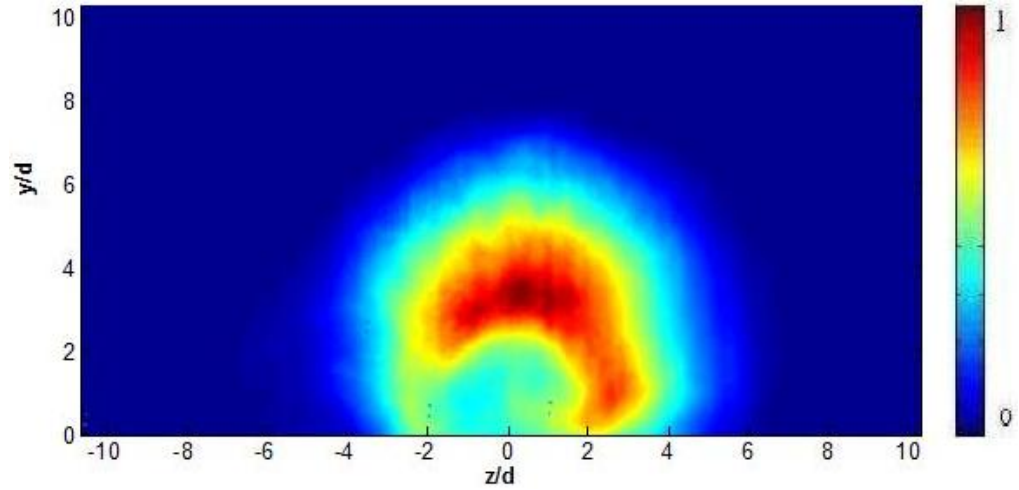

Figure 3.17. Time average (C/C_{avg}) PLMS end view image. δ/d =7.5, J=2.7 and x/d=10.

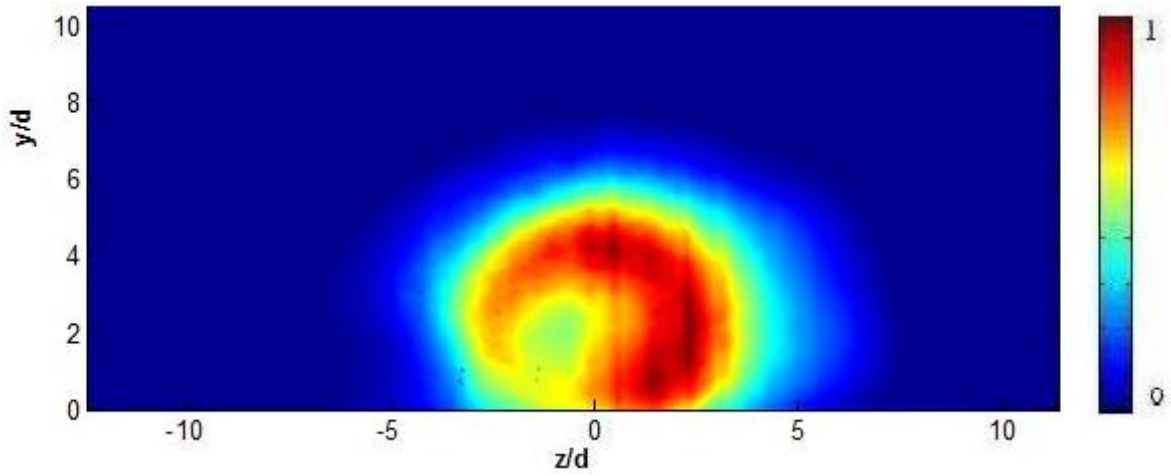

Figure 3.18. Time average (C/C_{avg}) PLMS end view image. δ/d =7.5, J=2.7 and x/d=20.

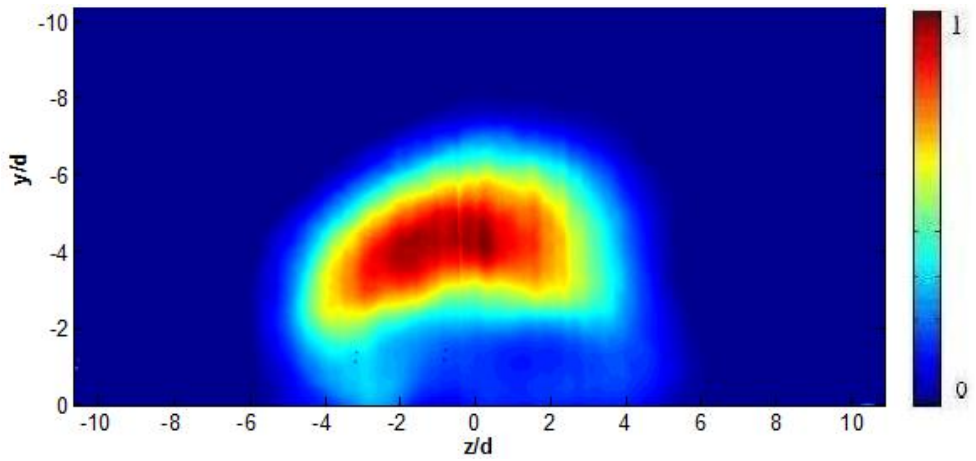

Figure 3.19. Time average (C/C_{avg}) PLMS end view image. δ/d =7.5, J=5.2 and x/d=5.

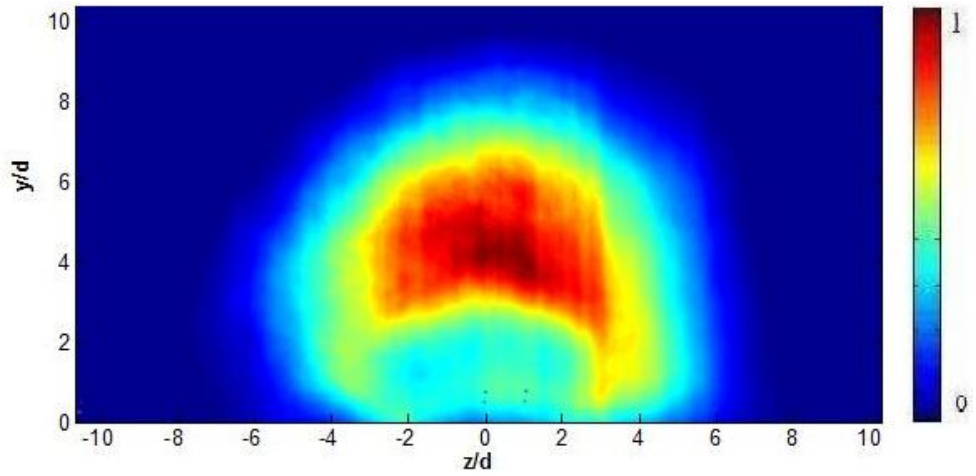

Figure 3.20. Time average (C/C_{avg}) PLMS end view image. δ/d =7.5, J=5.2 and x/d=10.

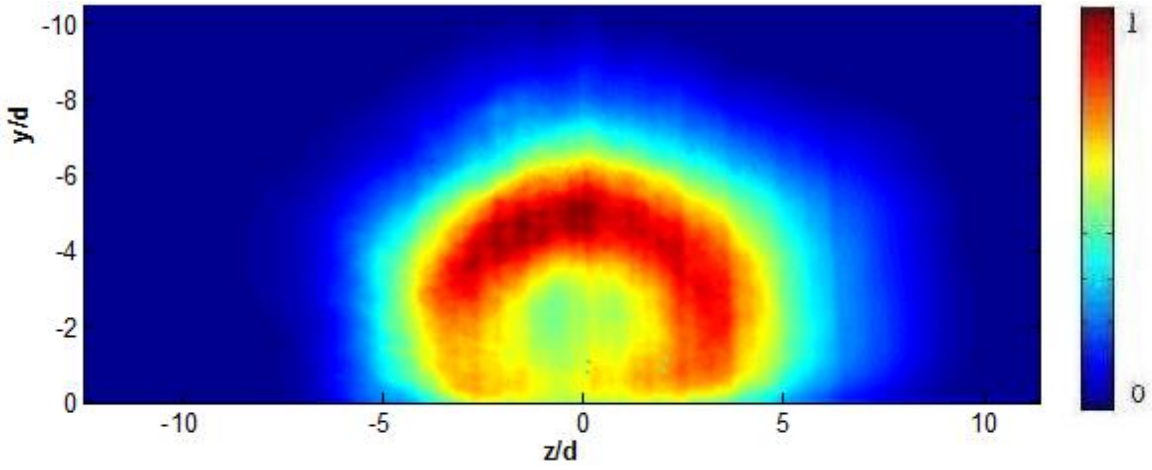

Figure 3.21. Time average (C/C_{avg}) PLMS end view image. δ/d =7.5, J=5.2 and x/d=20.

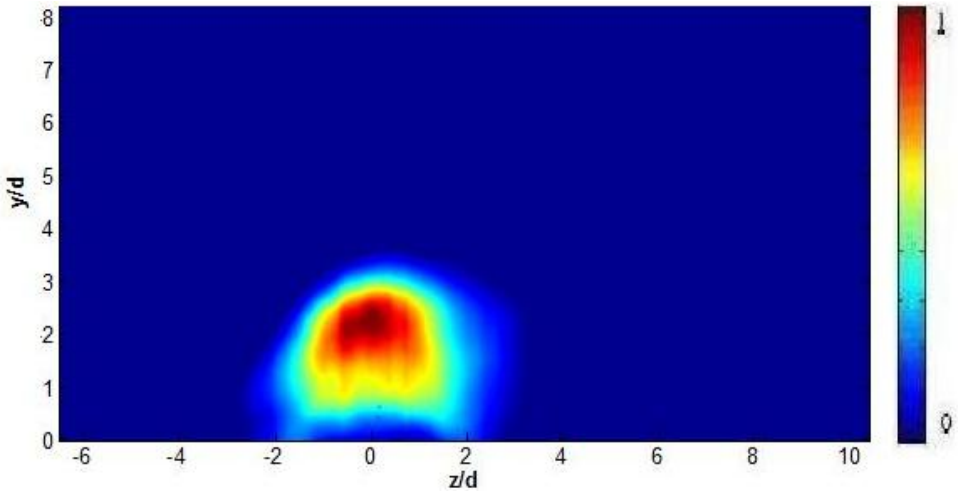

Figure 3.22. Time average (C/C_{avg}) PLMS end view image. δ/d ~0.7, J=1.2 and x/d=5.

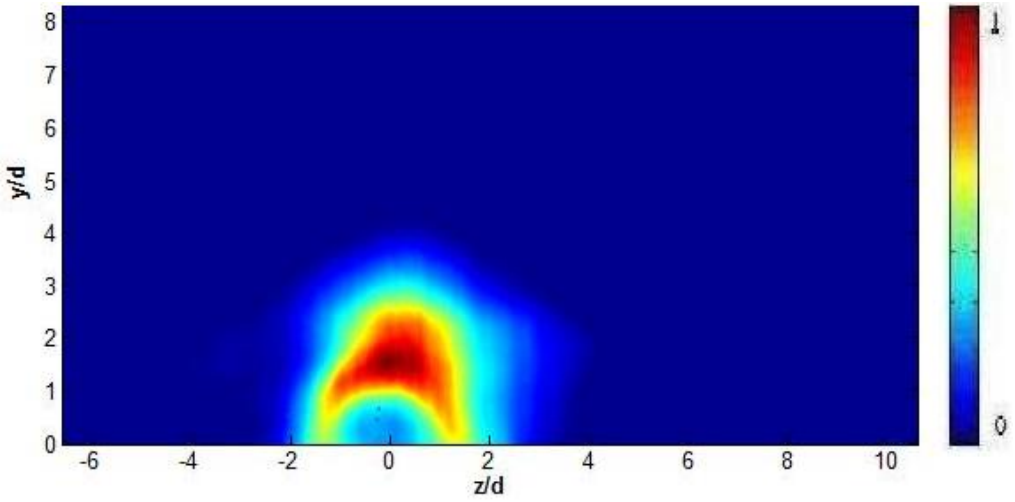

Figure 3.23. Time average (C/C_{avg}) PLMS end view image. δ/d ~0.7, J=1.2 and x/d=10.

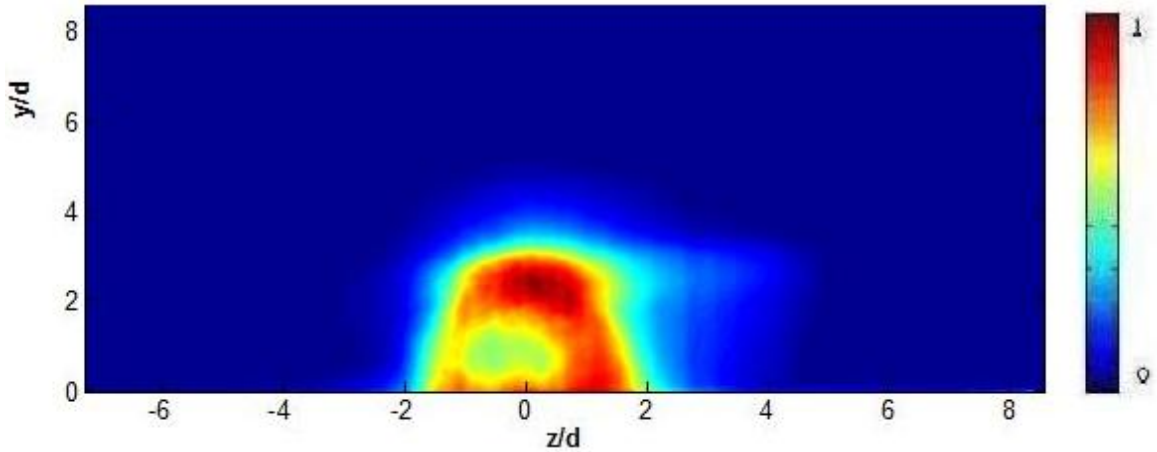

Figure 3.24. Time average (C/C_{avg}) PLMS end view image. δ/d ~0.7, J=1.2, and x/d=20.

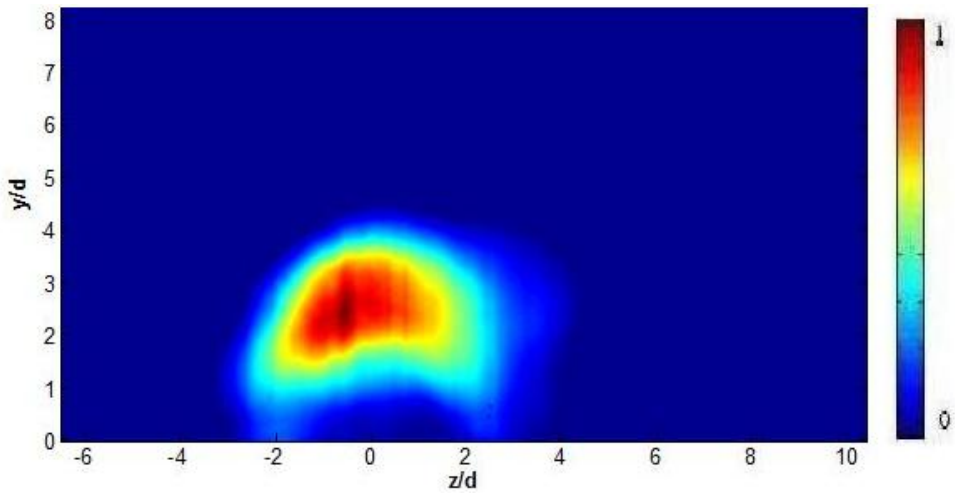

Figure 3.25. Time average (C/C_{avg}) PLMS end view image. δ/d ~0.7, J=2.7 and x/d=5.

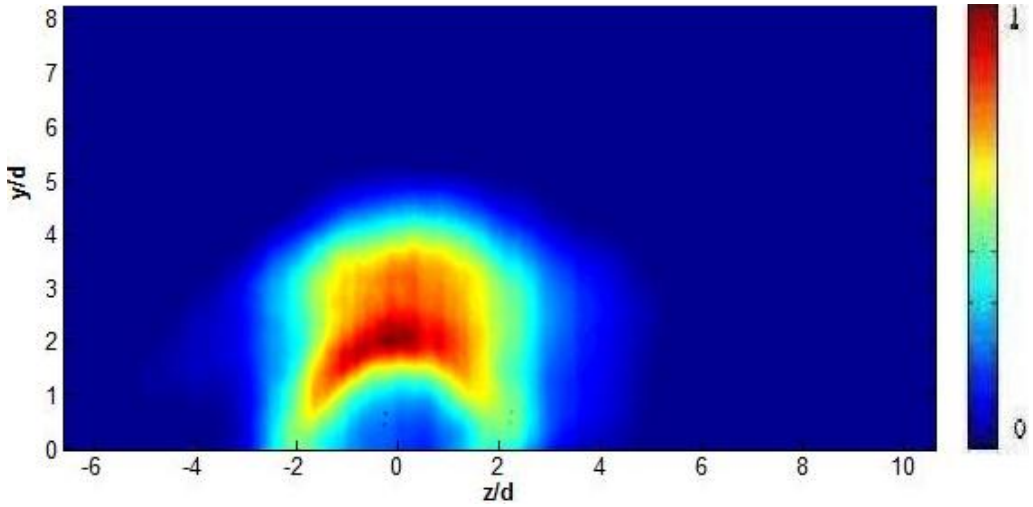

Figure 3.26. Time average (C/C_{avg}) PLMS end view image. δ/d ~0.7, J=2.7 and x/d=10.

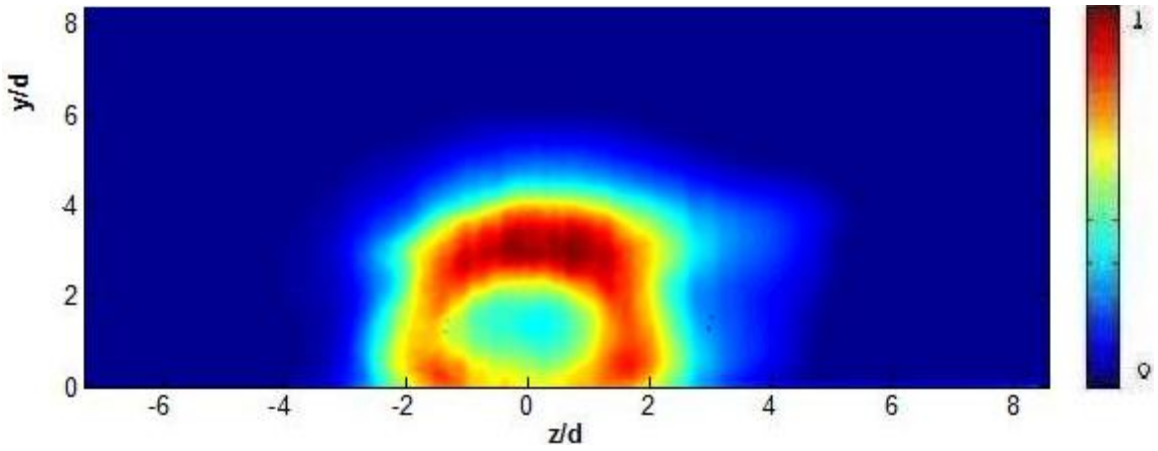

Figure 3.27. Time average (C/C_{avg}) PLMS end view image. δ/d ~0.7, J=2.7, and x/d=20.

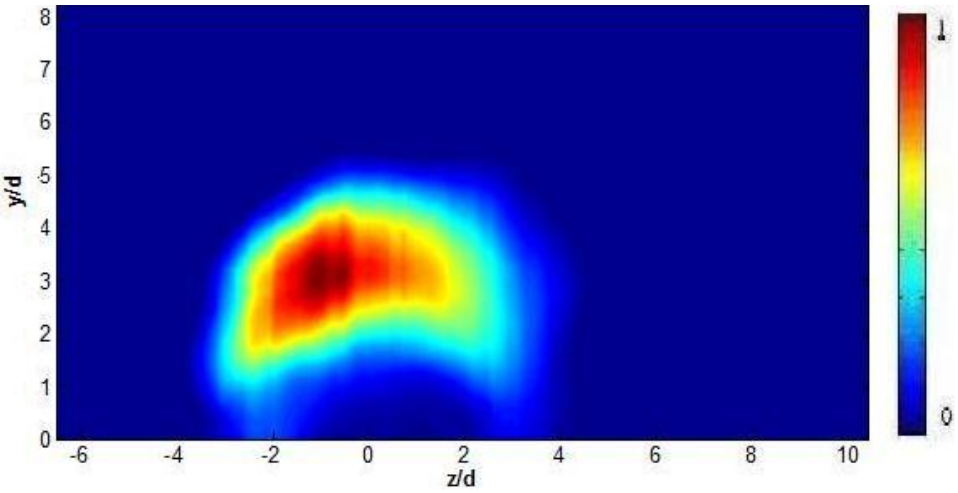

Figure 3.28. Time average (C/C_{avg}) PLMS end view image. δ/d ~0.7, J=5.2 and x/d=5.

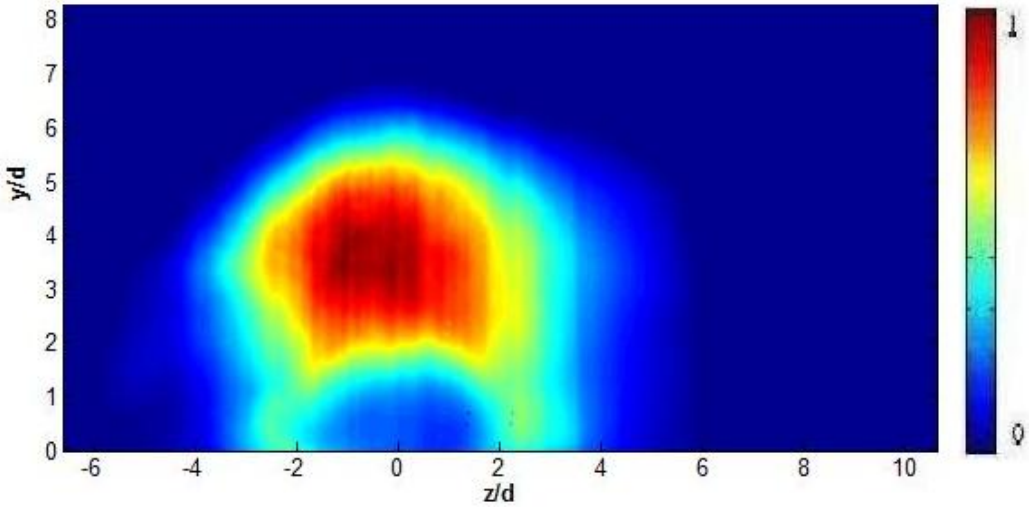

Figure 3.29. Time average (C/C_{avg}) PLMS end view image. δ/d ~0.7, J=5.2 and x/d=10.

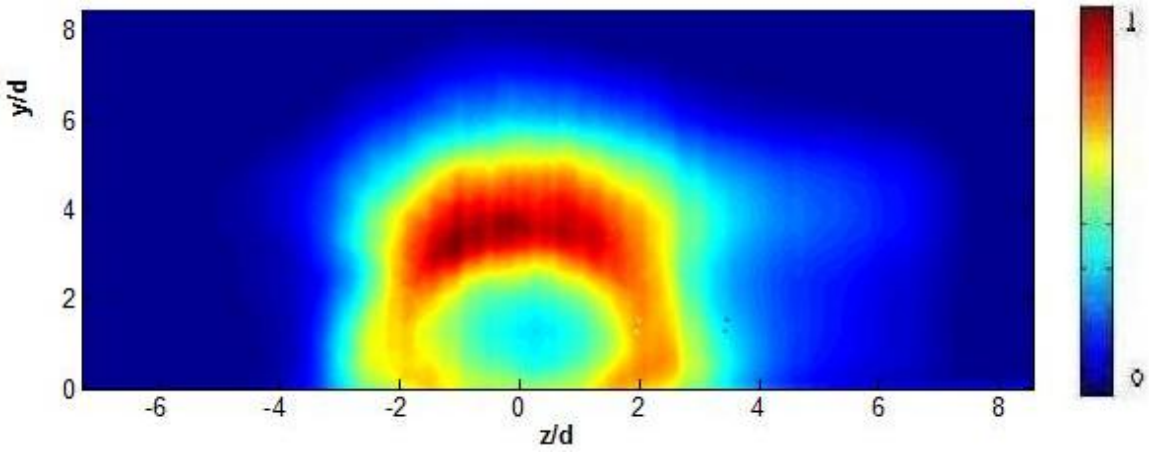

Figure 3.30. Time average (C/C_{avg}) PLMS end view image. δ/d ~0.7, J=5.2 and x/d=20.

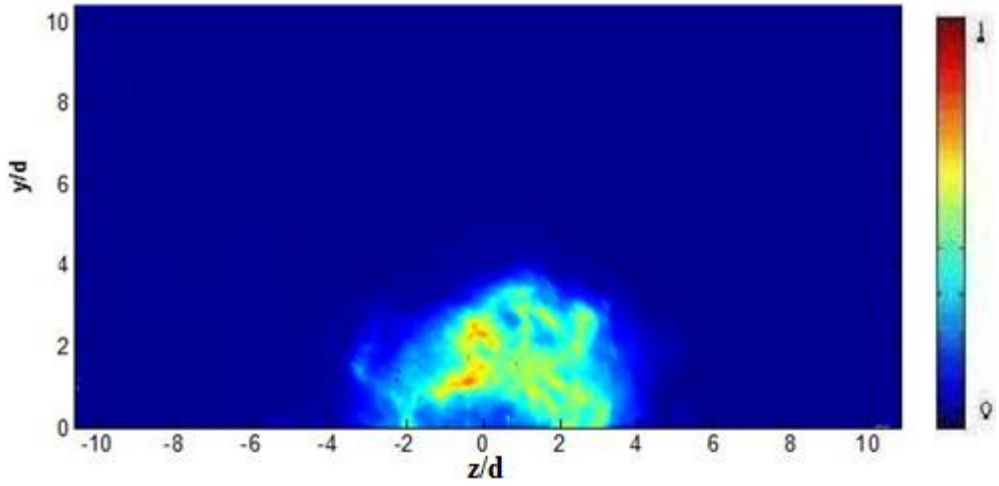

Figure 3.31. Instantaneous (C/C_{max})PLMS end view image. δ/d =7.5, J=1.2, and x/d=5.

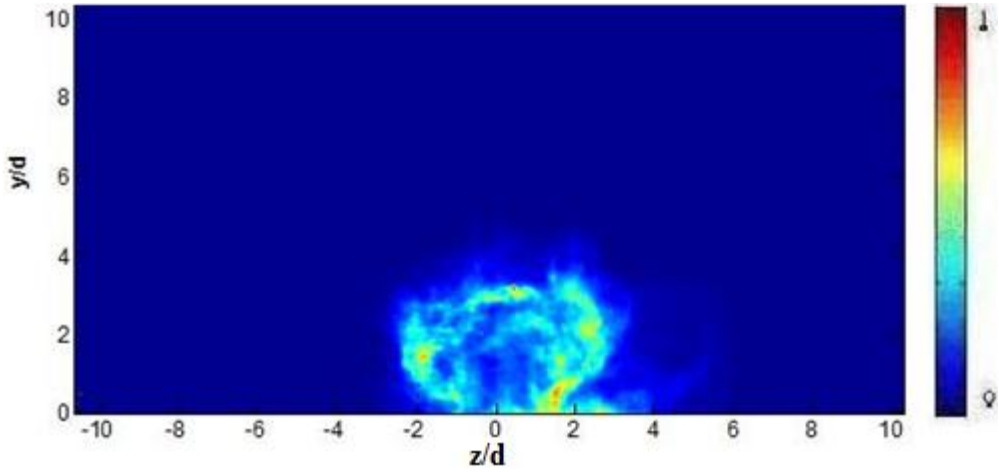

Figure 3.32. Instantaneous (C/C_{max})PLMS end view image. δ/d =7.5, J=1.2, and x/d=10.

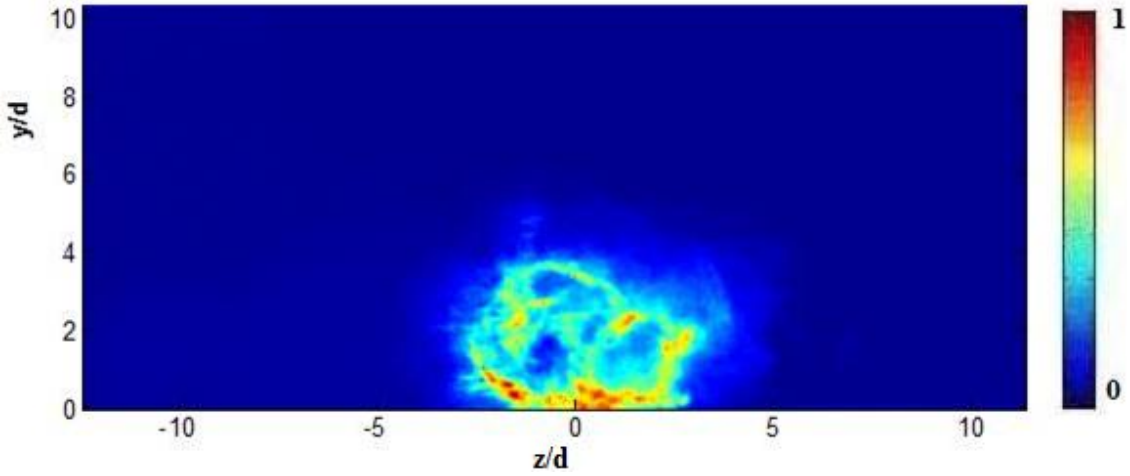

Figure 3.33. Instantaneous (C/C_{max})PLMS end view image. δ/d =7.5, J=1.2, and x/d=20.

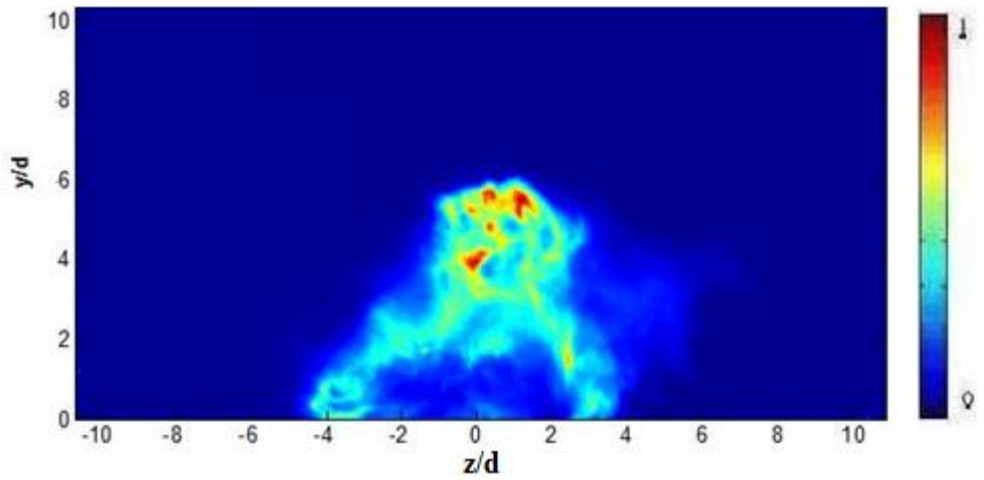

Figure 3.34. Instantaneous (C/C_{max})PLMS end view image. δ/d =7.5, J=2.7, and x/d=5.

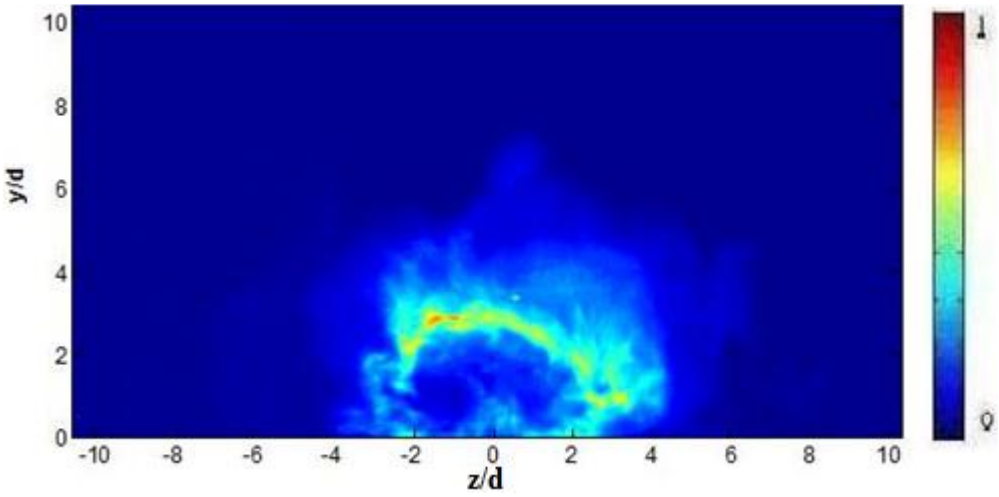

Figure 3.35 Instantaneous (C/C_{max})PLMS end view image. δ/d =7.5, J=2.7, and x/d=10.

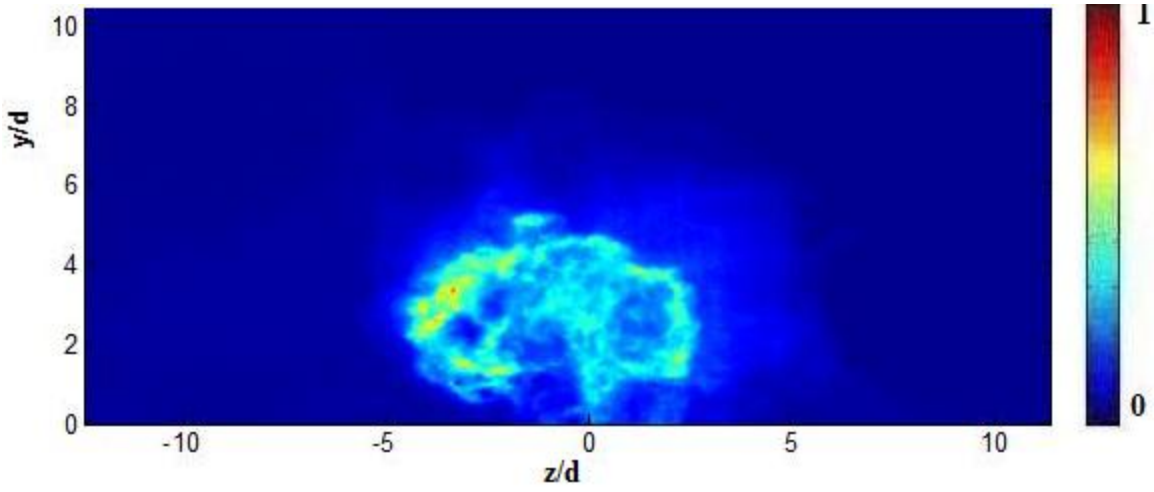

Figure 3.36. Instantaneous (C/C_{max})PLMS end view image. δ/d =7.5, J=2.7, and x/d=20.

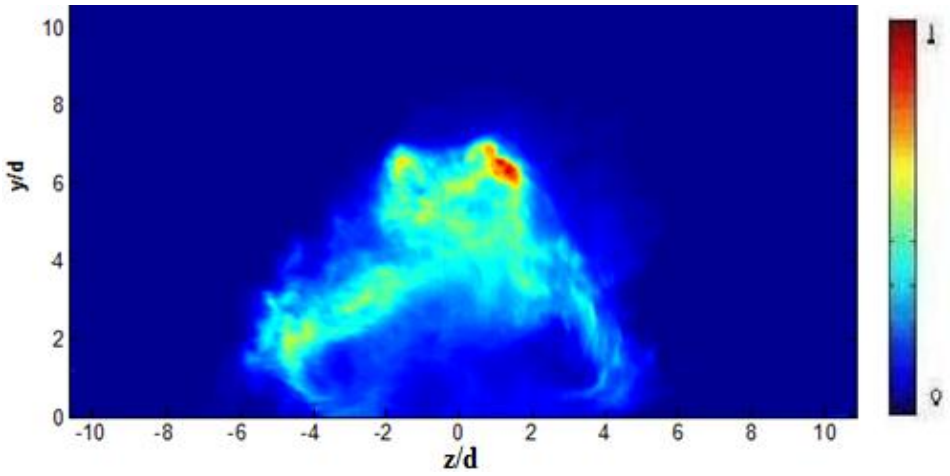

Figure 3.37. Instantaneous (C/C_{max})PLMS end view image. δ/d =7.5, J=5.2, and x/d=5.

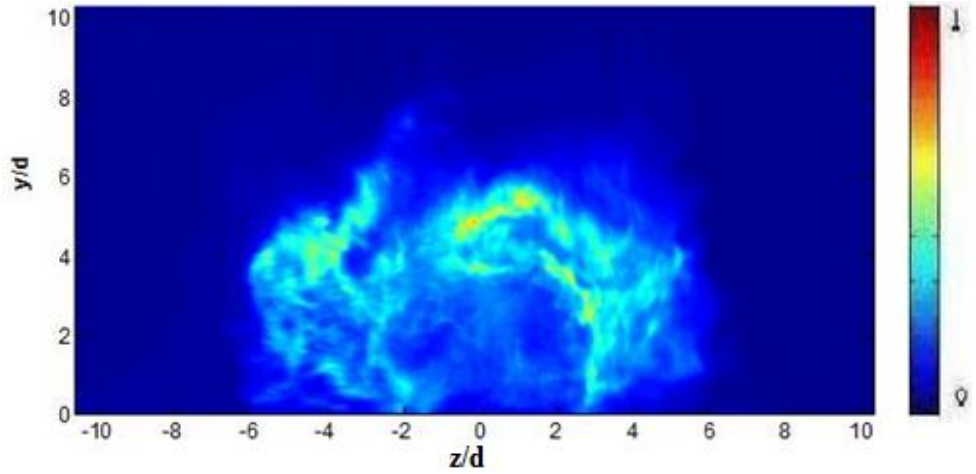

Figure 3.38. Instantaneous (C/C_{max})PLMS end view image. δ/d =7.5, J=5.2, and x/d=10.

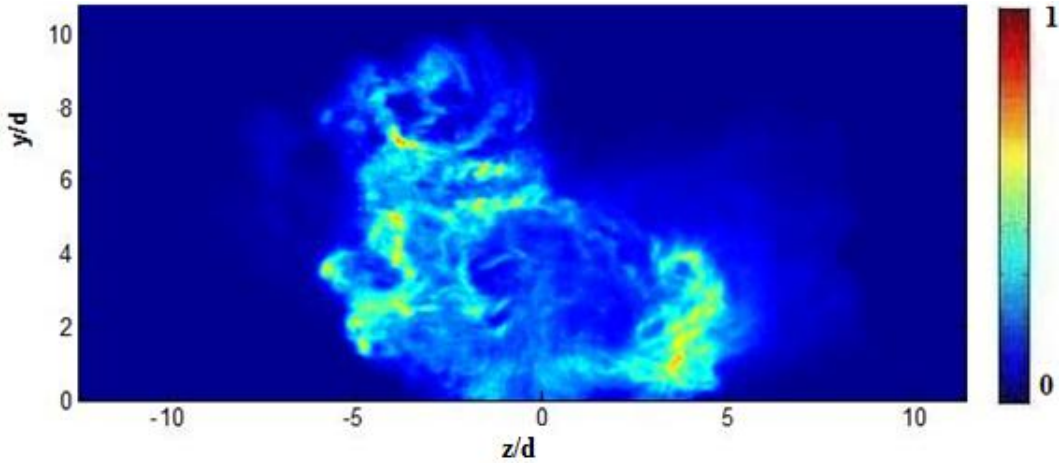

Figure 3.39. Instantaneous (C/C_{max})PLMS end view image. δ/d =7.5, J=5.2, and x/d=20.

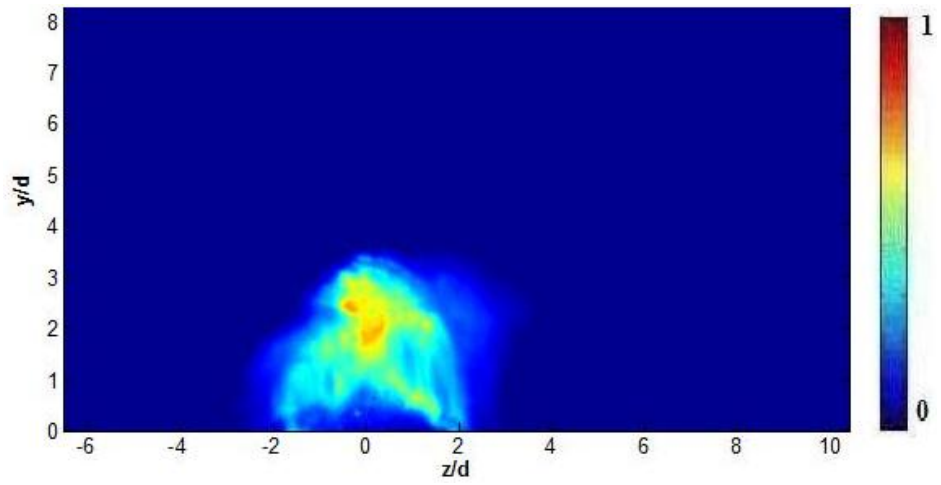

Figure 3.40. Instantaneous (C/C_{max})PLMS end view image. δ/d ~0.7, J=1.2, and x/d=5.

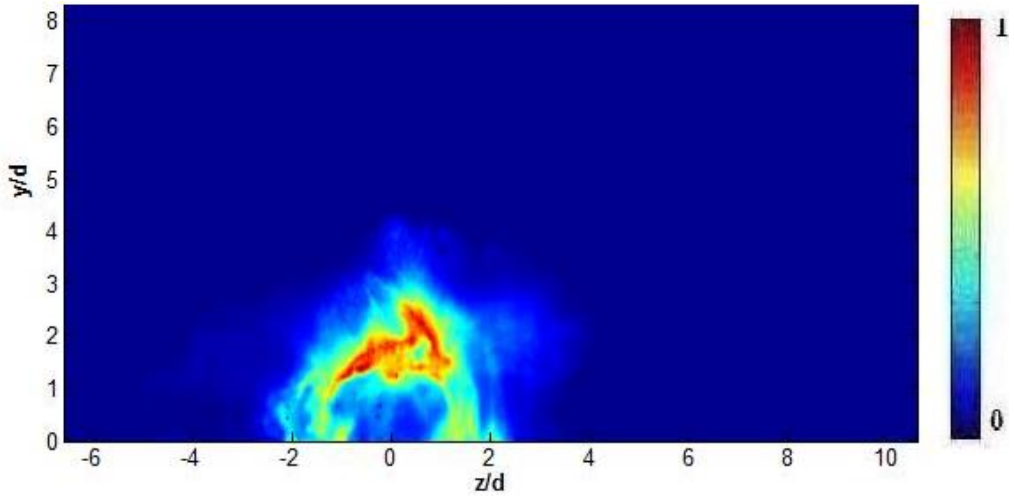

Figure 3.41. Instantaneous (C/C_{max})PLMS end view image. δ/d ~0.7, J=1.2, and x/d=10.

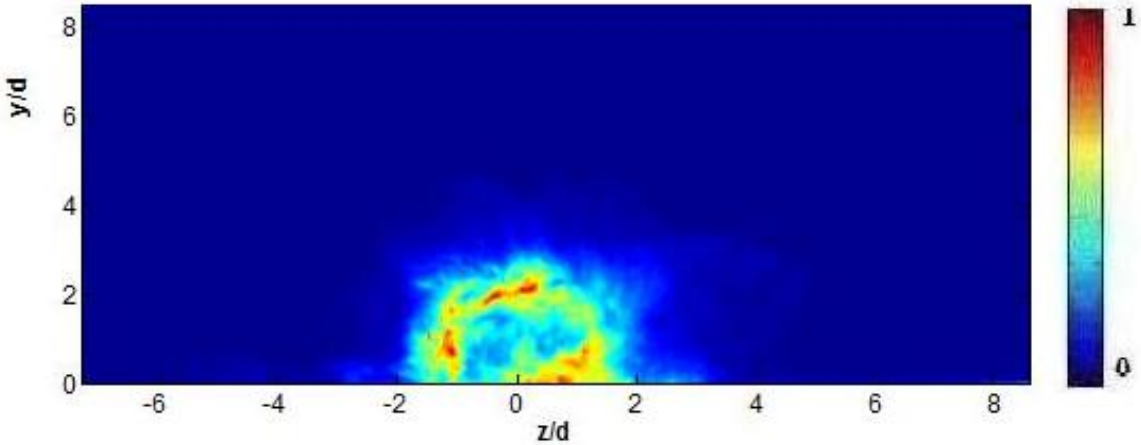

Figure 3.42. Instantaneous (C/C_{max})PLMS end view image. δ/d ~0.7, J=1.2, and x/d=20.

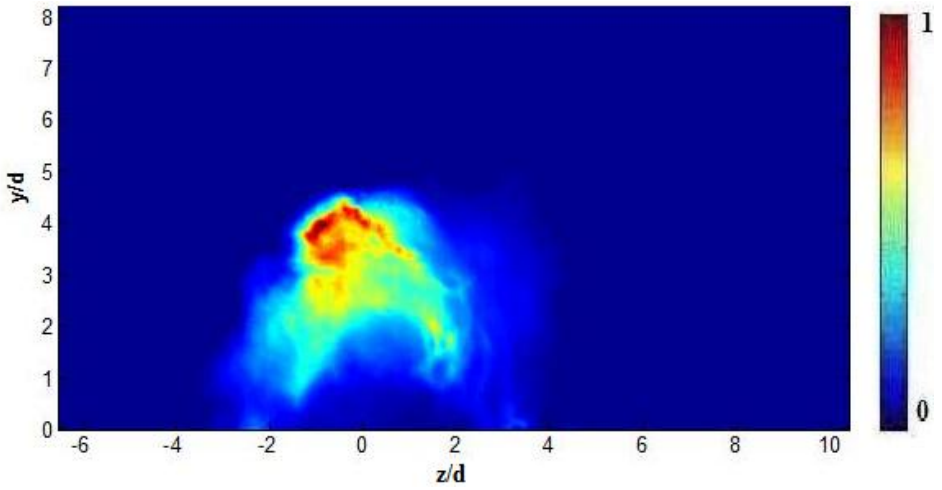

Figure 3.43. Instantaneous (C/C_{max})PLMS end view image. δ/d ~0.7, J=2.7, and x/d=5.

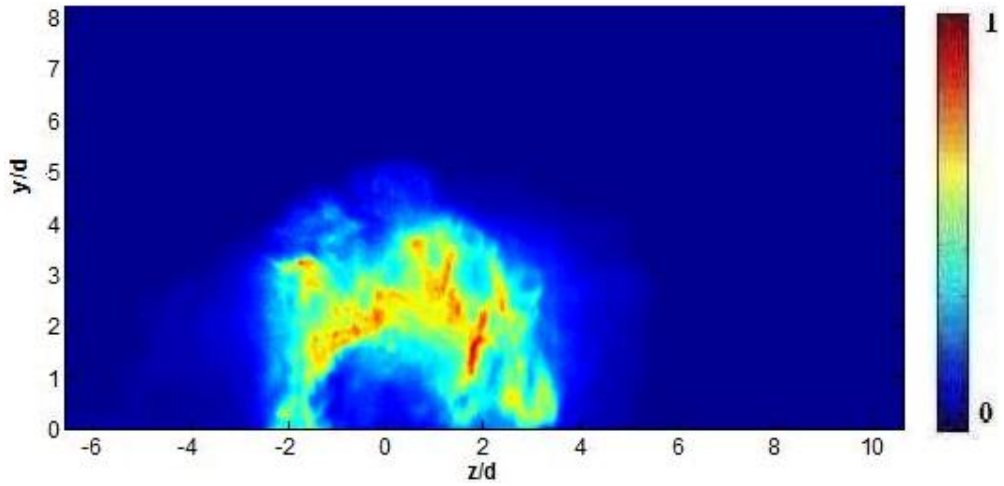

Figure 3.44. Instantaneous (C/C_{max})PLMS end view image. δ/d ~0.7, J=2.7, and x/d=10.

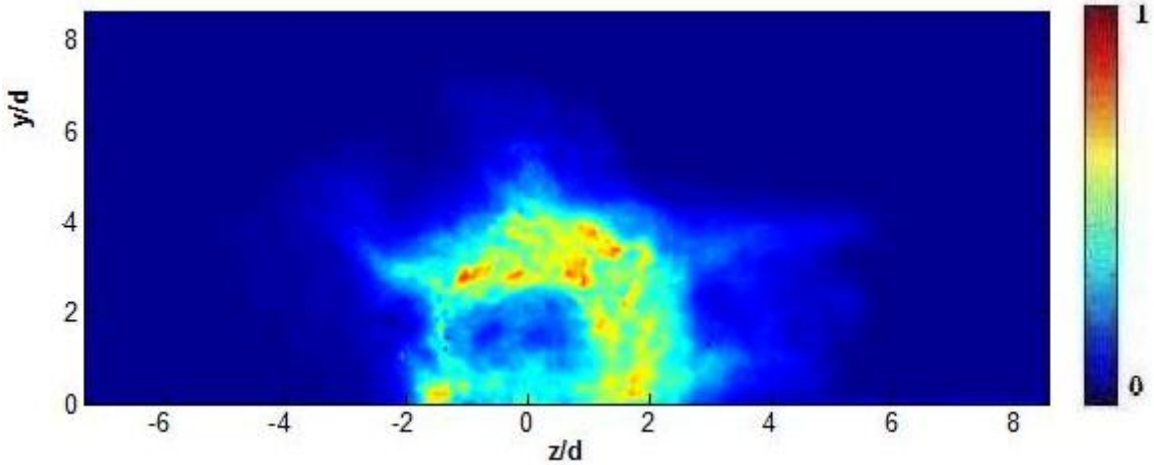

Figure 3.45. Instantaneous (C/C_{max})PLMS end view image. δ/d ~0.7, J=2.7, and x/d=20.

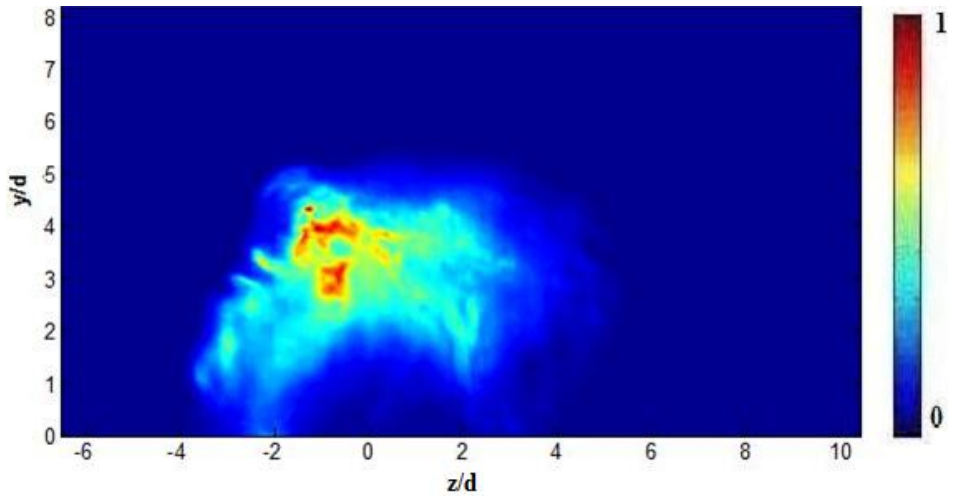

Figure 3.46. Instantaneous (C/C_{max})PLMS end view image. δ/d ~0.7, J=5.2, and x/d=5.

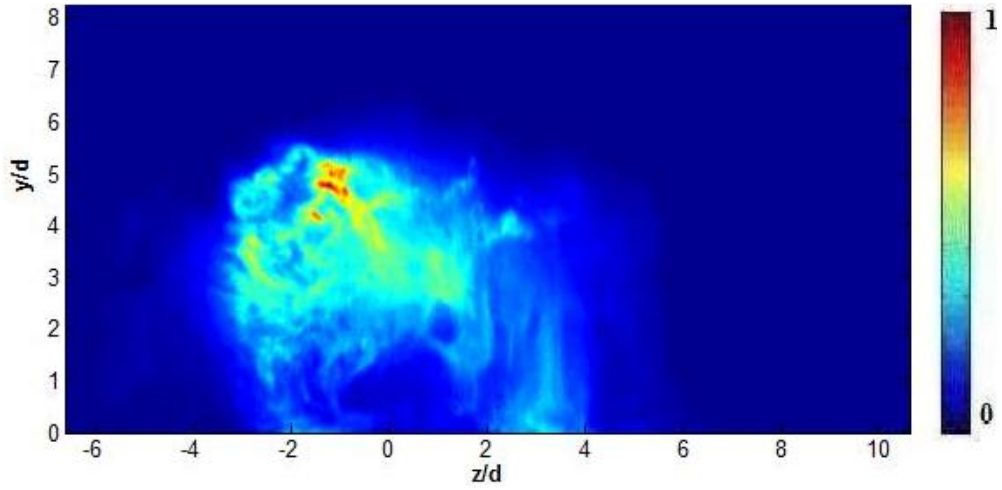

Figure 3.47. Instantaneous (C/C_{max})PLMS end view image. δ/d ~.7, J=5.2, and x/d=10.

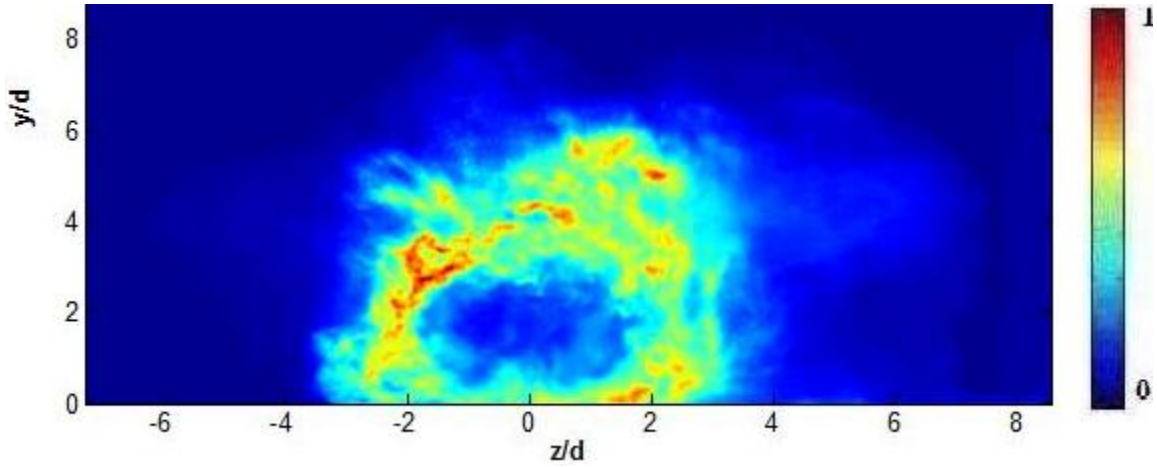

Figure 3.48. Instantaneous (C/C_{max})PLMS end view image. δ/d ~0.7, J=5.2, and x/d=20.

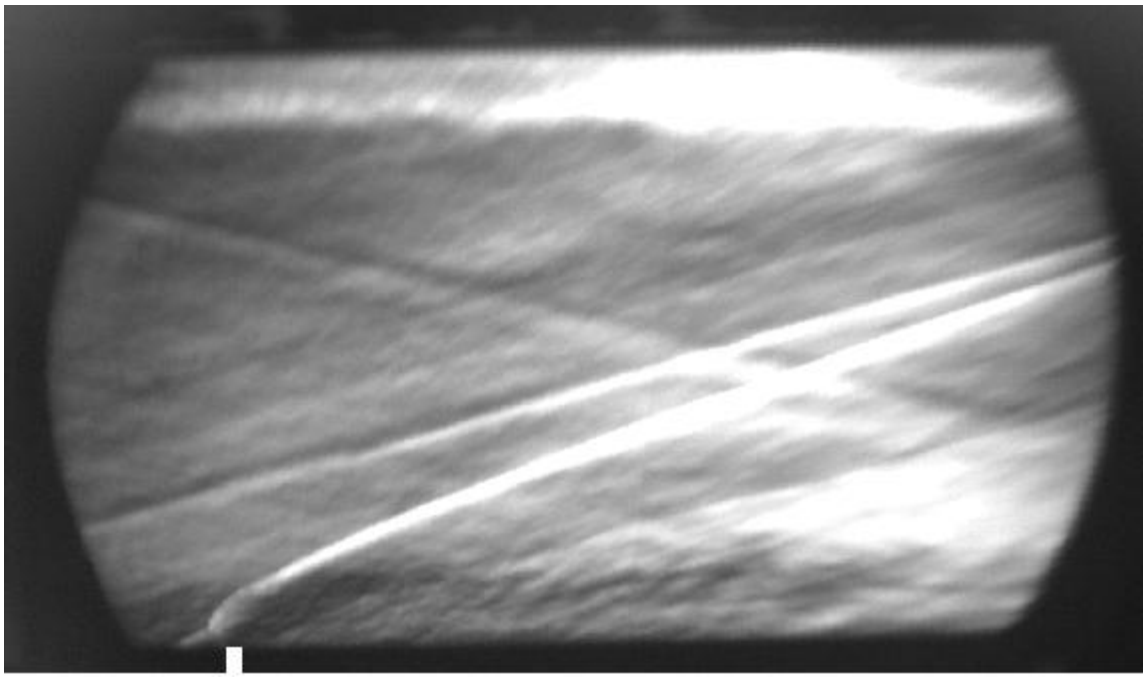

Figure 3.49 Instantaneous schlieren side-view image. δ/d=7.5 and J=5.2

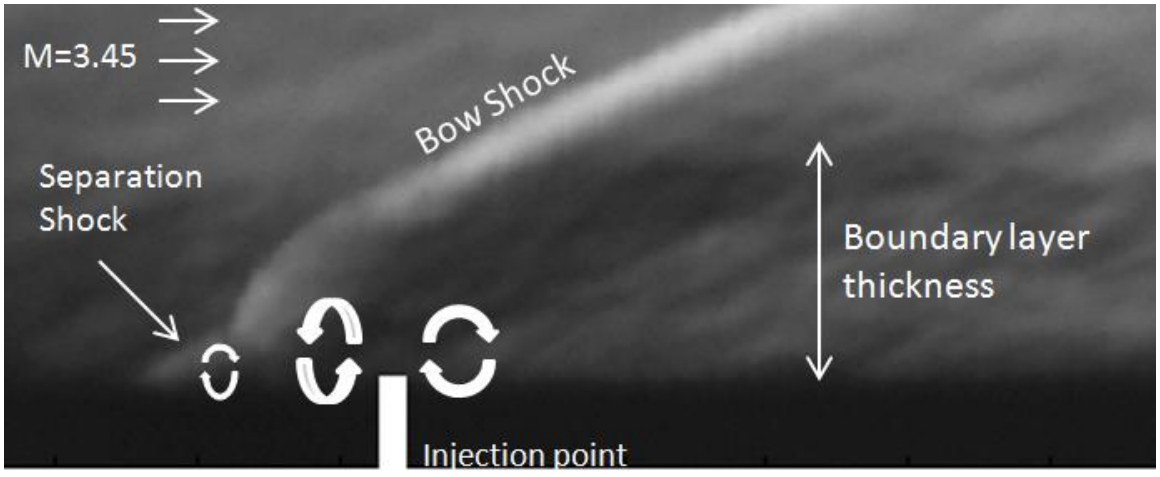

Figure 3.50 Zoomed in instantaneous schlieren side-view image. δ/d=7.5 and J=5.2

Chapter 4 Quantitative Analysis

4.1 Side View Measurements

4.1.1 Jet Trajectories

Jet measurements can be scaled by different normalization constants. Three common length scales are used by researchers to scale the jet in crossflow. The jet can be scaled by jet diameter (d), the product of the jet crossflow velocity ratio and jet diameter (rd) (Broadwell and Breidenthal 1984) and by (r^2d) (Keffler and Baines 1963). Having the use of three length scales can provide flexibility when trying to collapse jet trajectories and trying to claim trends. Throughout the paper, the jet will be normalized by the jet diameter. An often correlated measurement of the jet in crossflow by jet diameter is the jet centerline trajectory (Smith and Mungal 1998). Equation 4.1 is the power law for the jet centerline trajectory where "A" and "n" are both constants obtained from a curve fit.

$$\frac{y}{d} = A\left(\frac{x}{d}\right)^n \qquad 4.1$$

Figures 4.1 through 4.4 are plots of the jet trajectories. The centerline points plotted on top of the PLMS image for the J=5.2 jet injected into the thick boundary layer is shown in Figure 1. Figure 4.2 contains the jet trajectory profiles of the J=1.2, 2.7, and 5.2 jets injected into the thick boundary layer. The jets are power fitted to the length scale of equation 4.2. For the first couple of jet diameters downstream of the jet exit, the power

law correctly fits the centerline trajectories of the jets. However for each jet there comes a streamwise distance where the power law fails to scale the centerline trajectory and over predicts the trajectory. An imaginary black dash curve is drawn to show where the power law deviates completely from the centerline trajectories. The region left of the black dash line is termed the near field region and the region right of the black dash line is termed the far field region. In physical terms there is no clear distinct line between the near and far field region, the curve is used as a guide. The jet *y*-momentum significantly impacts the jet trajectory in the near field while the crossflow dominantly governs the trajectory of the mixed fluid in the far field. The trend in Fig. 4.2 suggests that the higher the *J* value of the jet, the better the jet centerline fits the power law. The higher the *J* value, the more resilience the jet has in retaining jet growth behavior characteristics against the high momentum crossflow. Figure 4.3 contains the jet trajectory profiles of the *J*=1.2, 2.7, and 5.2 jets injected into the thin wedge boundary layer. The profiles were found from the time averaged images. A comparison with Fig. 4.3 shows that for a particular *J* value, the thicker boundary layer fits the jet trajectory profile better than the thin boundary layer. With the help of Fig. 4.4, the centerline trajectories quantitatively show that jets injected into a thicker boundary layer have centerline trajectories farther out into the crossflow than jets injected into thin boundary layer. The effect of the boundary layer is so significant on jet penetration, that the *J*=1.2 jet injected into a thick boundary layer has its centerline farther out into the crossflow than the *J*=2.7 jet injected into the thin boundary layer.

The standard deviation was calculated for the side-view centerline trajectories profiles. The purpose of the following calculation was to measure the dispersion of the

centerline data points from the power law fit. In equation 4.2, the sample standard deviation *s* for the trajectory profile is given.

$$s = \sqrt{\frac{1}{N-1}\sum_{i=1}^{N}\left((y/d)_i - \overline{(y/d)_\iota}\right)^2} \qquad 4.2$$

In equation 4.1, the variable *N* is the total number of points that make up the trajectory profile of the jet. The variable $(y/d)_i$ is the centerline point location found in the average image by a MATLAB code. The variable *i* is a dummy index. The variable $\overline{(y/d)_\iota}$ is the power law trajectory of the jet calculated from equation 4.1. The standard deviation results are tabulated in Table 4.1 with units of jet diameters. The *J*=5.2 jet injected into the thick boundary layer has a smaller standard deviation than the lower jet momentum flux ratios jets injected into the same boundary layer thickness. However, for the jets injected into the thin boundary layer, the *J*=5.2 jet has the largest standard deviation than the other jets injected into the same boundary layer thickness. The larger the standard deviation calculation, the more the jet centerline measurements deviate from the power law trajectory in the far field. The error in calculating the centerline trajectory will be discussed in section 4.5

4.1.2 Jet Spread

A way to measure jet growth is to analyze its spread as it mixes downstream from the averaged data. The jet spread is measured from the orifice plane to the 5% pixel value curve located on the windward side of the jet. Figure 4.1 shows the centerline trajectory and the 5% pixel value curve plotted on top of the PLMS image of the J=5.2 jet injected into the thick boundary layer. All the values on the 5% curve are 5% of the centerline

pixel value from the averaged image. Figures 4.5 and 4.6 show jet spread for all jet momentum flux ratios for the thick and thin boundary layer injections, respectively. In Fig.4.5, the wall boundary layer spreads are plotted with a linear curve fit in the near field. The curve fits show that the jets grow linearly for up to 4 jet diameters downstream of the injection point before they grow nonlinearly with a slope less than 1. The J=5.2 jet has a steeper spread slope than the J=2.7 and J=1.2 jet. The J=2.7 jet should have a steeper slope than the J=1.2 jet but the thick boundary layer interaction causes the slopes to be nearly equal. In the near field, the penetration of the J=1.2 and J=2.7 jets is less than the boundary layer thickness. In contrast, for the thin boundary layer injections all jets make it out of the boundary layer and the J=2.7 jet has a steeper growth spread in the near field than the J=1.2 jet. The jet entrains crossflow fluid in the near field and eventually loses all y momentum in the far field so the slope of the curves is close to zero in the far field for all jet injections. In terms of the near field, the jets injected into the thick boundary layer have steeper spread slopes than the jets injected into the thin boundary layer. In the wall injection boundary layer, the J=5.2 jet spreads the farthest into the crossflow, reaching almost 11.5 jet diameters in the transverse direction at 15 jet diameters downstream. In contrast, the jet centerline trajectory of the J=5.2 jet in Fig.4.2 shows that the J=5.2 jet's centerline stops growing at 10 jet diameters downstream. So the spreading results of Fig. 4.6 indicate the jets continue to grow in the transverse direction although the centerline of the jets stops growing. This trend can be seen for all jets in both the wall and wedge injection boundary layers.

4.1.3 Concentration Decay

The jet concentration decay plots provide an indication of how fast the jet centerline is mixing with streamwise distance. Figures 4.7 through 4.9 are normalized by the pixel values located immediately at the jet exit. The centerline of the jet is determined by the maximum concentration at a given distance *x/d*. The plots show that as the jet mixes downstream the initial pixel intensity exponentially decays to smaller values. Figure 4.7 shows that by five jet diameters downstream, all jets regardless of the boundary layer they are injected into have already lost on average 60% of the initial jet concentration. This demonstrates the effectiveness of turbulent mixing of the jet in the crossflow. Figure 4.7 shows that the jets injected into the wedge boundary layer decay to lower values than for the thick boundary layer in the near field. However in the far field, the jets in the thick boundary layer collapse to smaller concentration values than for the wedge. In the thin boundary layer, the jets are able to interact with high speed flow easier than for the thick boundary layer. In regards to jets injected into the thick boundary layer, in the far field the jets are able to interact with the turbulent fluctuations and vortical structures that the thin boundary layer does not contain. When the pixel intensity decay profiles for the wall and wedge injected jets are broken up into two figures (Fig. 4.8 and Fig. 4.9), clearer trends can be seen in each boundary layer. The jets injected into the thin boundary layer do not get much time to interact with the boundary layer before penetrating through it. So the jet that mixes best will be the one that has stronger vortical elements in it. In regard to the jets injected into the thin boundary layer, the J=5.2 jet is more powerful than the lower value J value jets. It will have stronger vortices within it to break down any high jet concentration values. The wall injected jets in Fig. 4.9 shows

that the decay rates between each *J* value are quite different in the near field. The plot reveals that lower *J* value jets decay faster than higher *J* value jets. The results shown in Fig. 4.9 are not intuitive at first. The *J*=5.2 jet should have stronger vortical elements within it which would cause it to mix faster than the lower *J* values in the thick boundary layer. However the *J*=5.2 jet is actually further out from the thick boundary layer, so it doesn't get to work with as much of the boundary layer vorticity as does the *J*=1.2 jet. Thus the boundary layer vortical structures are helping the *J*=1.2 jet mix faster than it should.

Figures 4.10 through 4.14 show log-log plots of the decay results of the jets in crossflow. Log-log plot show the decay rates of the jets. Figure 4.10 shows the *J*=1.2 wedge injected jet with a -1.2 concentration decay rate slope in the far field before branching off to a -2/3 slope. This result is similar to what Smith (1996) recorded in his experiments with *d*- length scaling for various *J* value jets. Figure 4.11shows the *J*=5.2 jet injected into the wall boundary layer. The thick boundary layer helps the jet decay at a fast rate so the slopes are steeper. In the subsonic experiments of Smith and Mungal (1997) jet slopes ranging from -1 branching to -2/3 for different velocity ratios were recorded in the far field. The results in Fig. 4.10 and Fig. 4.13 for the jets injected into thin boundary layers have slopes similar to Smith. Toward the end of the branches in Fig. 4.13, the slopes become shallower to -2/3 which agrees well with the trends by Smith and Mungal. The points where the slopes branch to a shallower slope are known as the branch points and are denoted by asterisks in Figures 4.10 through 4.13. Smith and Mungal showed that the branch points are delayed for the higher *J* values as does the results of Fig. 4.12 and Fig. 4.13 for thick and thin boundary layers. In addition, the results in Fig.

4.14 show that the delay in the branch points will occur earlier for the wedge injection cases than for the wall injections. Much interest in the transverse jet results from its enhanced mixing properties, making the regions before and just after the branch points important areas of study (Smith and Mungal 1997).

4.2 Probability Density Functions

Probability density functions (PDF's) were developed to calculate mixing quantities. Koochesfahani and Dimotakis (1986) showed the importance of PDF's in mixing studies. They conducted mixing studies with parallel high speed and low speed mixing layers. As noted in (Koochesfahani and Dimotakis 1986) the width ($\boldsymbol{\epsilon}$) of each bin in the histograms are dictated by the signal to noise ratio. Fig. 4.15 shows an image of a typical histogram. The width $\boldsymbol{\epsilon}$ was 0.05 in the following PDF's. There were no intensity values in any of the experiments that ranged larger than three times the average maximum pixel value in any paths of the instantaneous images. So the values of the bins ranged from 0 to 3 which make 60 intervals. The PDF's in Figs. 4.16-4.29 are constructed similar to their methods. An Eulerian approach is carried out by constructing a surface of 3 by 3 pixels at a certain location and recording the signal of the pixels in each set of images. The 9 pixels are averaged to reduce noise and that sample is saved in a matrix. A series of 3 by 3 pixels will stretch from the windward surface of the jet, pass through the center of the jet, and end at the wind tunnel wall. After a set of (n) number of images are collected, there will be (n) number of samples to be placed in each (m) number histograms for each (m) number of 3 by 3 pixel constructed surfaces. The histograms were normalized so that the integral of equation 4.3 equaled unity.

$$\int_0^3 p(c,y)dc = 1 \qquad (4.3)$$

In the PDF's, the path in the transverse direction was normalized by the vertical distance measured from the wall to the 5% signal boundary as shown in equation 4.4

$$\eta = \frac{\delta_{5\%} - y}{\delta_{5\%}} \qquad (4.4)$$

The variable (y) is the transverse distance measured from the wall. ($\delta_{5\%}$) is the vertical distance measured from the wall to the 5% signal boundary on the windward side of the jet at z/d=0 and (η) is the normalized dimension.

The PDF's in Figures 4.16-4.29 are grouped together by the J-value of the jet. The colors of the bins are correlated to the colors of the circles in the jet trajectory profile in each figure. Each PDF is normalized by the maximum value (C/C_{cl}) on their respective paths. The paths start from the windward side of the jet and move towards the orifice plane. For each PDF, nine equally distant locations were observed. In each J value case, the side-view PDF's are preceded by the end-view PDF's for comparison. For example, Fig. 4.16 shows the jet trajectory profile for the J=5.2 wall injected jet and three side-view plane PDF's correlated to the paths in the jet trajectory profile. These paths are of particular interest since they are on the common line that the side-view and end-view planes share. Following the side-view plane PDF's are the end view PDF's for the same paths in Fig. 4.17. The x/d=5 PDF's calculated in the side-view plane in Fig. 4.16 compares well with the x/d=5 PDF's in the end-view plane in Fig. 4.17. Each begins on the windward surface of the jet, where unmixed fluid is dominant in the shear layer. As the paths make their way through the core of the jet, the PDF's march toward the center.

After the paths pass through the centerline of the jet, the PDF's begin to march toward lower concentration values again. The trend of marching PDF's from low pixel values to high values and back to low values can be clearly seen in the *x/d*=5 PDF's for all *J* values in the end and side view planes except in the side view plane of the *J*=1.2. In both the wedge (Fig. 4.26) and wall (Fig. 4.20) boundary layers, the *J*=1.2 jet shows a PDF in the side view plane that can be argued is non marching as it passes through the core of the jet. The non marching trends in the side-view planes for the *J*=1.2 jets is opposed to the clear marching trends in the end-view plane.

As one compares the side-view and end-view PDF's for the *x/d*=10 streamwise distance for each *J* value, the trends become more difficult to define. For Fig. 4.16, the *J*=5.2 side-view plane PDF at *x/d*=10 looks like it is marching toward the center and then marches back to lower values. This compares well with the trend for the end view path in Fig. 4.17. However for the *J*=2.7 jet in Fig. 4.18, the *x/d*=10 PDF in the side-view plane shows sign of aliasing, while the PDF in the end-view plane in Fig. 4.19 is clear and marching. The error of aliasing, when it occurs, takes place in the side-view plane PDF's for *x/d*=10 and *x/d*=20. This error will be further discussed in the end of chapter 4, but could be the result of a large dynamic range issue. The clearest PDF in the side-view plane at the *x/d*=10 stream-wise distance is the one located in Fig. 4.26. Figure 4.26 is the *J*=1.2 jet injected into the thin boundary layer. At *x/d*=10, Fig. 4.26 shows the jet marching to the center and after the jet passes through the core of the jet, the jet becomes non-marching. This trend also occurs in the end-view plane of Fig. 4.26 for the same path to about half way through the jet core. After the path passes through the jet core, the PDF goes to a non-marching status. The end view PDF's for all the jets at *x/d*=10 are quite

clear. The end-view PDF's, except Fig. 4.21, march from the low pixel values to around unity and march back down to around 20% of unity. In Fig. 4.21, the J=1.2 jet injected into the thick boundary layer shows the trend of marching to the center and as the path continues from the center of the jet to the wall, the PDF becomes non marching.

For x/d=20 in the side view Figures of 4.16, 4.18, 4.20, and 4.22 there is clearly aliasing going on. No conclusion of how the PDF's in the side-view compare to the end view PDF's can be made definitively for those plots. However the side-view PDF for the J=1.2 jet in Fig. 4.26 at x/d=20 shows a degree of sufficient clarity. Just like the x/d=20 PDF in the end-view plane in Fig. 4.27, the jet shows the trend of marching to the center. In addition, as the path continues from the center of the jet to the wall, the PDF's become non-marching. Overall, the PDF's calculated in the end-view plane provide better trends than the side-view for x/d=20. At x/d=20, the end-view planes tend to be marching from the windward side of the jet to the core of the jet. From the core of the jet to the wall at x/d=20, the Figures of 4.23 and 4.25 show a degree of marching while Figures 4.17, 4.19, 4.21 and 4.27 can be argued to be non marching.

4.3 Mixing measurements

The construction of the PDF's provide avenues for other mixing calculations. The true mean (TM) is a calculation that takes all the values in a histogram and calculates the average. The mixed mean (MM) calculates the average of the values in each histogram but excludes crossflow fluid in the calculation. The unmixed crossflow fluid is considered to be any value that is below the 5% threshold value. Any signal higher than

5% is considered mixed fluid. The mixed mean measurement was used in Koochesfahani and Dimotakis (1986) and was termed average *mixed* fluid concentration. The true mixed fraction (TMF) is the amount fluid that exists in a mixed state. If the TMF is equal to unity, then the true mean and mixed mean values are the same. Any value less than unity signify the presence of unmixed cross flow fluid. The denominator of equation 4.6 is shown in equation 4.8. Equation 4.8 is the probability (*P*) of finding mixed fluid at any concentration (Koochesfahani and Dimotakis, 1986). The total mixed fluid concentration (TMFC) for the entire path is shown in equation 4.9. Equation 4.9 integrates the mixed mean across the path into a single discrete number. The equation gives a value of what concentration the mixed fluid is mixed at as the fluid comes by. A value close to 1 indicates that the average is close to the jet centerline concentration. Likewise a value close to zero indicates the total mixed fluid concentration has a numerical value close to that of unmixed fluid. It does not indicate how mixed the jet is across the layer. The true mean, mixed mean, and true mixed fraction are shown in equations 4.5, 4.6, and 4.7 respectively. The term *p(c,y)* is the probability of finding fluid at a certain concentration and location on the path. If the true jet concentration signal was being measured, the concentration value would be assigned to the variable *c*. However, as will be discussed in section 4.5, the true jet concentration signal *c* is very difficult to obtain. The variable *c* in this report should be interpreted as the resultant signal value of the image processing carried out in section 2.5. The variable $\delta_{5\%}$ is the distance from the orifice plane to the 5% concentration boundary on the windward side of the jet at *z/d*=0.

$$\mathrm{TM(y)} = \frac{\int_0^3 p(c,y) * c \, dc}{\int_0^3 p(c,y) dc} \qquad 4.5$$

$$\mathrm{MM(y)} = \frac{\int_{0.05}^{3} p(c,y) * c \, dc}{\int_{0.05}^{3} p(c,y) dc} \qquad 4.6$$

$$\mathrm{TMF(y)} = \frac{\int_{0.05.}^{3} p(c,y) \, dc}{\int_{0}^{3} p(c,y) dc} \qquad 4.7$$

$$\mathrm{P(y)} = \int_{.05}^{3} p(c,y) \, dc \qquad 4.8$$

$$\mathrm{TMFC} = \frac{\int_{0}^{\delta_{5\%}} P(y) * MM(y) dy}{\int_{0}^{\delta_{5\%}} P(y) dy} \qquad 4.9$$

4.3.1 Mean Comparisons

4.3.1.1 Side View and End View Mean Comparisons at z/d=0

Figs. 4.30 through 4.83 contain figures of true mean, mixed mean, and true mixed fractions. The figures compare the side-view and end-view plane calculations at *z/d*=0 for *x/d*= 5, 10, and 20. From the mixed mean and true mean plots, the true mean values for side and end-view start off at around 5% of the centerline signal in their respective planes. In both the end-view and side-view plane, the calculated mixed mean and true mean averages near the windward side of the jet are not equal. At the windward side of the jet, there is unmixed crossflow fluid being entrained into the jet. The probability of finding unmixed fluid at the windward side of the jet is more probable than finding unmixed fluid toward the center. As the path continues through the core of the jet, the true and mixed mean profiles come together, more so for the end-view profiles than for

the side-view profiles. At the locations where the true mean and mixed mean profiles lay close together, that is where the fluid is well mixed along the path. The true mixed fraction results for the end-view profiles converge to unity indicating that there is little to essentially no unmixed fluid samples immediately before and after passing transversely through the centerline of the jet. However the side-view results tell a different story.

The side-view mean profiles show a different trend than the end-view profiles for both thick and thin boundary layers. A few generalizations can be made about the side-view plots. The gap between the true mean and mixed mean profiles starting at the windward side of the jet are much larger when compared to the end-view profiles for all cases. In other words, the true mixed fraction values near the windward side of the jets are smaller when calculated in the side-view plane as opposed to calculating the values in the end-view plane. The gap between the true and mixed mean profiles begins to narrow as the path makes its way through the center of the jet. In the thick boundary layer, the true mixed fraction approaches and meanders near unity in the side-view plane at x/d=5 for J=5.2 (Fig. 4.30), J=2.7 (Fig. 4.32), and at x/d=10 for J=5.2 (Fig. 4.37). For all other cases in the thick boundary layer, when looking at the side-view results (Fig. 4.34, 4.38-4.46) , the true mean and mixed mean do not fall onto each indicating that the jet does not become fully mixed. The results in (Fig. 4.34, 4.38-4.46) are contrary to the end-view results in the same figures because the end-view results indicate that at the center of the jet, the jet is fully mixed and remains mixed along the transverse path to the wall. The side-view results in the thick boundary layer also show that the jet becomes less mixed near the wall while the end-view results do not show the same indication. For the thin boundary layer cases, the side-view results correlate better with the end-view results in

terms of mixedness. For all three *J*-values from *x/d*=5 to 10 (Figures 4.48-4.59), the true mean and mixed mean profiles at one point or another become equal. However the true mean and mixed mean for (Figures 4.48-4.59) show that near the wall the mixedness decreases, which is in contrary to what the end-view results show in the same figures. For *x/d*=20(Figures 4.60-4.65) the side view results indicate that the jet has its maximum intensity values on its path near the wall as opposed to the centerline which the end-view plots suggest. At *x/d*=20 in the thin boundary layer, the side-view results suggest that the mixedness increases near the wall again and has true mixed fraction values at 1. Once again, the side-view results for the stream wise distance at *x/d*=20 are very susceptible to aliasing problems to do the low signal levels of the fluid far downstream.

4.3.1.2 End view mean Comparisons at *z/d*=0

The end view results seem to be more promising. They do not have the dynamic range and aliasing problems that the side view results are susceptible to. A further analysis was carried out on the end-view images to see how boundary layer thickness affected the mixing. Figs. 4.66 through 4.83 contain the end-view plots of true mean, mixed mean, and true mixed fraction for each *J*-value jet injected into two boundary layers of different thickness. As one can see, the true mean and mixed mean profiles are close together. The true mixed fraction plots provide better clarity for comparison. For all cases except the *J*=5.2 (Fig. 4.73) and *J*=2.7 (Fig. 4.75) at *x/d*=10 it is quite clear that the jet injected into the thinner boundary layer mixes faster at its windward edge than in the thick boundary layer. This makes sense since the jet is interacting with greater shearing speeds at the windward side in the small boundary layer case than in the thick turbulent boundary layer. Although the wedge boundary layer exposes the top of the jet to the

higher shearing velocity to mix better on top, the thick boundary layer is able to work with the jet at the wall. For the tested *J* values and stream-wise stations, the jets injected into the wall boundary layer had higher mean values near the wall than the jets injected into the wedge boundary layer. The thick boundary layer is very turbulent and is able to move and mix jet fluid around near the wall easier than the thin boundary layer.

4.3.1.3 End View Mean Comparisons and PDF's in Non-Zero *z/d* Planes

Up to this point, much of the analysis had been conducted on the *z/d*=0 plane for both the side-view and end-view planes. This section investigates the mixing on other non-zero *z/d* planes. Figures 4.84 through 4.119 show true mean, mixed mean and true mixed fraction profiles selected at different *z/d* locations in the end-view plane. Five paths, equal distance from each other, were extracted from the end-view images. The range of the extracted paths in the *z/d* span wise direction depended on the size of the end-view plume. Immediately upon investigating the true mean and mixed mean plots, one can see that the jet is asymmetric quantitatively. The numerical results of the *J*=5.2jet at *x/d*=20 (Fig. 4.96) injected into the thick boundary layer and the *J*=2.7 jet at *x/d*=10 (Fig. 4.110) injected into the thin boundary layer agree with the qualitative discussion in section 3.1.2. Those particular jets show symmetrical trends in the mean profiles at locations off the centerline axis. The mean profiles at different *z/d* locations show, as noted in section 3.1.2, that jets injected into the wedge boundary layer show better symmetrical behavior than jets injected into the wall boundary layer. Visually from inspection, the rate at which each true mixed fraction goes to unity is quite the same. There are instances where the slopes for the non-zero *z/d* planes are shallower than the

z/d=0 profile. The profiles show that toward the center of the jet, the jets mix better than the sides of the jet.

PDF's at non zero *z/d* locations were made for the *J*=5.2 jet injected into the thick boundary layer at *x/d*=20 (Fig. 4.28) and the *J*=5.2 jet injected into the thin boundary layer at *x/d*=10 (Fig. 4.29). In Fig. 4.28 at *z/d*=-5 and *z/d*=5, the PDF's appear to be non-marching. The PDF's are at the outer edge of the jet and are sampling mixed but mostly unmixed fluid. Moving closer to the center at *z/d*=-3 and z/d=+3 the PDF's appear to go from marching to about 75% of the centerline signal value before marching back down to lower signal values. Often the maximum jet concentration in the jet are near *z/d*=0 location so the PDF's off of that plane will not usually have histograms averaging around unity. The spatial trends in Fig. 4.28 are similar to the trends seen in figure 4.29 but with a different lateral range.

4.3.2 Total Mixed Fluid Concentration and True Mixed Fraction

The total mixed fluid concentration for the entire path (eq. 4.9) was calculated in the end view plane at *z/d*=0 for all three jet momentum flux ratios. The results for the thick and thin boundary layers are tabulated in Table 4.2 and Table 4.3, respectively. The numerical values indicate whether the total average across the layer is closer to that of the jet centerline concentration or to the value of unmixed fluid. It does not conclude how well mixed the jet is. Overall the results show that the total mixed fluid concentration values are greater for the jets injected into the thick boundary layer as opposed to the thin boundary layers. For all cases, the total mixed fluid concentration values in Tables 4.2 and 4.3 are greater than 0 .5. The average calculated concentration across the paths seems

to lean closer to the centerline jet fluid signal value as opposed to the unmixed fluid signal value. It should be noted that the error bars have not been calculated.

The true mixed fraction for the entire jet within the 5% contours in the end-view plane was calculated. The results for the thick and thin boundary layers are tabulated in Table 4.4 and Table 4.5, respectively. The true mixed fraction for the entire jet calculates how well mixed the jet is from the perspective of the end view plane at a particular stream wise distance of interest. A value closer to unity indicates a well mixed jet. A value close to zero indicates a jet not so well mixed. The results are tabulated in Table 4.4 and Table 4.5. The values in both tables show jets that are all well mixed. As stream wise distance increases downstream, the jet remains consistently mixed around the same values. It is also noticeable that the jets injected into the wedge boundary layer have in general higher true mixed fraction values than the jets injected into the thick boundary layer. The error is on the order of the uncertainty in the measurement.

4.4 Plume Area Calculation

The plume area of the jet was calculated in Tables 4.6 and 4.7 for the two boundary layers the jets were injected into. The units of area are in terms of jet diameter. The plume area was calculated by considering all the mixed fluid contained in the 5% contour line in the end-view plane. The jet area increases as the *J*-value and stream wise distance increases. The results show that the jet plume area is greater for the thick boundary layer cases than for the thin boundary layer cases.

4.5 Error

There were a couple sources of error in the experiments. The first source of error was the limitation of the resolution of the camera to record the smallest scale eddy. The Batchelor scale in equation 4.10 is used to determine the size of the smallest scale eddy (Smith 1996).

$$\lambda_B = \beta\delta Re^{-.75}Sc^{-.5} \qquad 4.10$$

In equation 4.10, λ_B is the size of the smallest eddy, β is a constant, δ is the local jet width, *Re* is the local jet Reynolds number, and Sc is the Schmidt number. With $\beta = 1$ and Sc = 1.5, the Batchelor scale was calculated to be less than 1 micrometer. This value is much smaller than the size of the smallest pixel length. Therefore the probe dimensions in the experiments are considered under resolved and the fluid measured in the experiments may not be mixed on the molecular scale but instead be well stirred.

The PLMS technique is sensitive to the ethanol density of the particles. The density of the particles is affected by changes in pressure and temperature fluctuations in the flow. All particles are created at the jet exit and could be conglomerating as they head downstream. If the particles are conglomerating, this phenomenon could increase the intensity of the recorded signal which is undesirable effect. No definitive study has been conducted on this theory in the lab. However end-view images should not be affected by that physical phenomenon if it is occurring.

The BETE PJ-40 nozzle did not perform to the highest of standards at the *J*=1.2 value. There was a problem of the ethanol vapor not condensing into infinitesimal fine particles for some of the images. Occasionally the images contained large discrete

droplets in the flow. Those images had to be discarded since the intensity value did not accurately describe the flow field. There were 200 images recorded in each wind tunnel run. Unfortunately for some of the lower *J* value jets, in a number of cases, a majority of the images had to be discarded. The smallest data set was around 80 images. The pressure of the jet was set to the desired jet momentum flux ratio in the beginning of the run. Occasionally, the jet was found to decrease by 5 psi at the end of the 15 second wind tunnel run. The cause was due to the decreasing stagnation pressure in the storage tanks.

The low levels of signal in the far field area of the jet in crossflow in the side-view image plane seemed to be a problem. The digitized noise in the side-view image was brought to attention when the PDF's were constructed. The raw tiff images were taken from a 16383 count resolution camera. The images were uploaded to Matlab and were converted to 8 bit integer images. This means the pixels values no longer had the long range of 0 to16383 to be assigned to but instead the signal had been assigned to a shorter range of values from 0 to 256. The lower value pixels that were less than 1 had to pick a digitized integer. This is a possible explanation for why the bins appeared to be grouped for particular stream wise distance especially at the lower signal range at x/d=20. In the results for the side view image, the calculated mixed mean was of poor quality for some of the side-view images because there was poor accuracy around zero in assigning pixel values. The error bars increase in the far field regions in the side-view images.

The standard deviation for the centerline trajectories was larger in the far field regions when compared to the near field regions as was discussed in section 4.1. The centerline was found by locating the maximum pixel intensity values in each of the column in the corrected averaged imaged. The raw instantaneous images for the side-

view and end-view had background noise levels of around 4% of the maximum pixels values in the image. Therefore there could be at least 4% error bars in determining the centerlines or thickness of the jets.

Other sources of error in the experiment include smoothing of the laser sheet profile, off axis transformation distorting, and correcting unwanted reflections in raw images. All those changes affect the original signal of the samples. In addition, an optical density filter was used that changed the incoming signal nonlinearly. Throughout the report, the terms *jet concentration* and *pixel intensity* are used interchangeably. One should understand the term *jet concentration* mentioned in the report is not the absolute true signal of the jet concentration in the crossflow due to the sources of error previously mentioned in extracting the true concentration signal, Changes in day to day operation of the wind tunnel, seasonal changes in ambient conditions such as temperature of the air, and keeping a consistent wind tunnel stagnation pressure affect the outcome of the results.

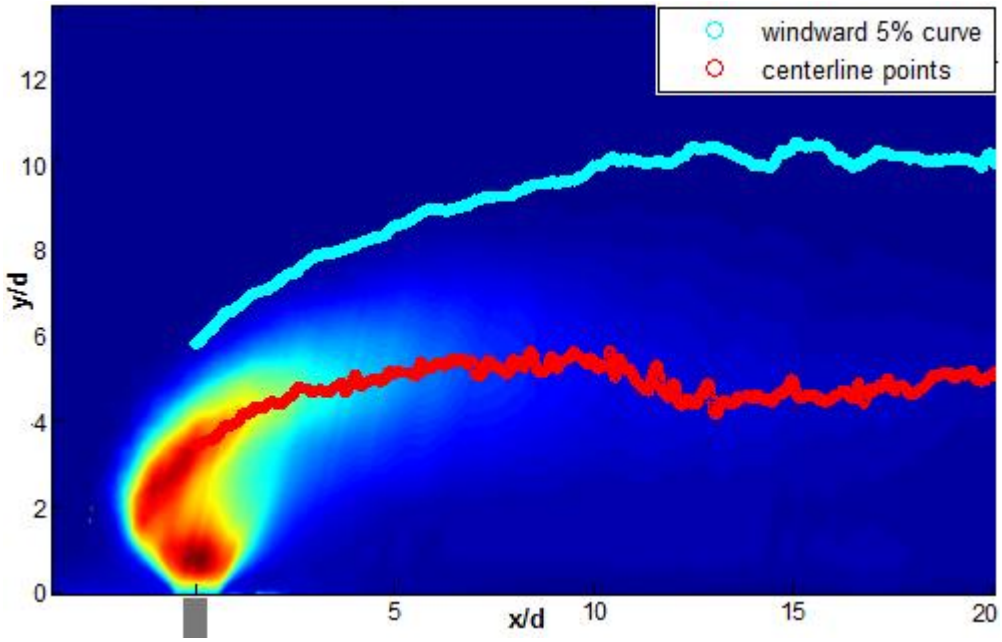

Figure 4.1. Time averaged (C/C_0). PLMS side view image. δ/d =7.5 and J=5.2. Gray line is the injection point. Centerline trajectory and jet spread.

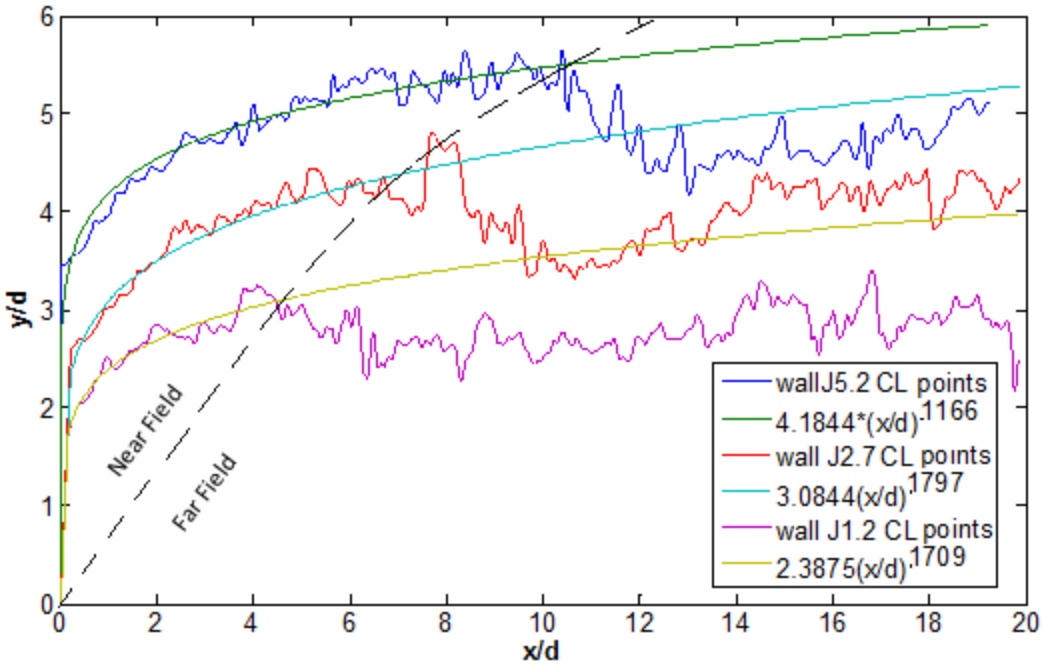

Figure 4.2. Time averaged data. Wall (δ/d=7.5) injection centerline trajectories. Scaled trajectories with power law fit. Black dash curve is the boundary between near and far field regions.

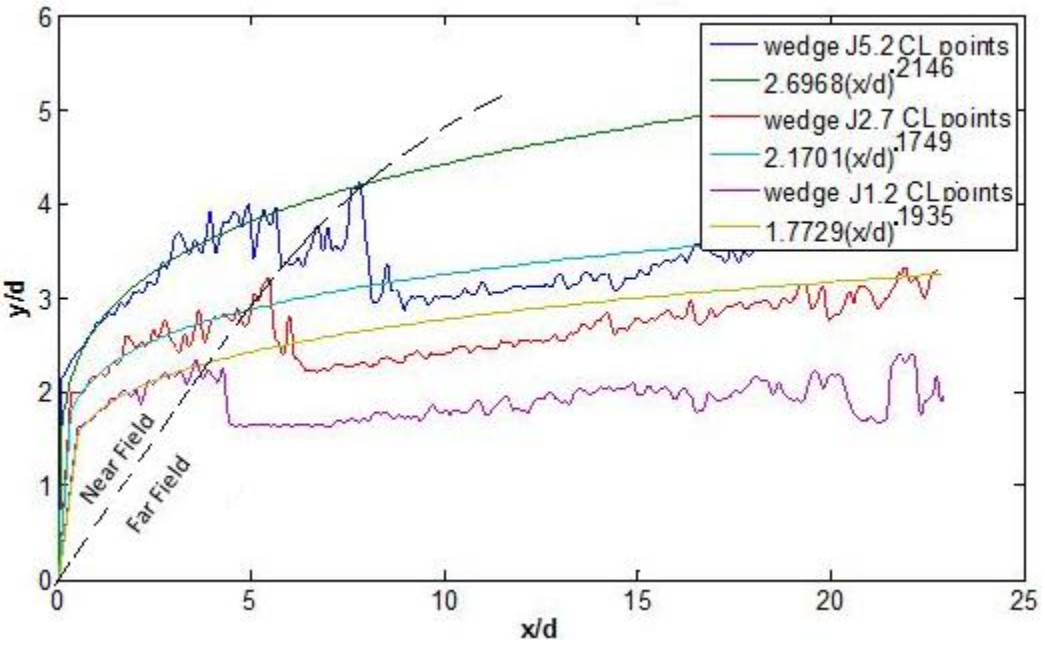

Figure 4.3. Time averaged data. Wedge (δ/d~0.7) injection centerline trajectories. Scaled trajectories with power law fit. Black dash curve is the boundary between near and far field regions.

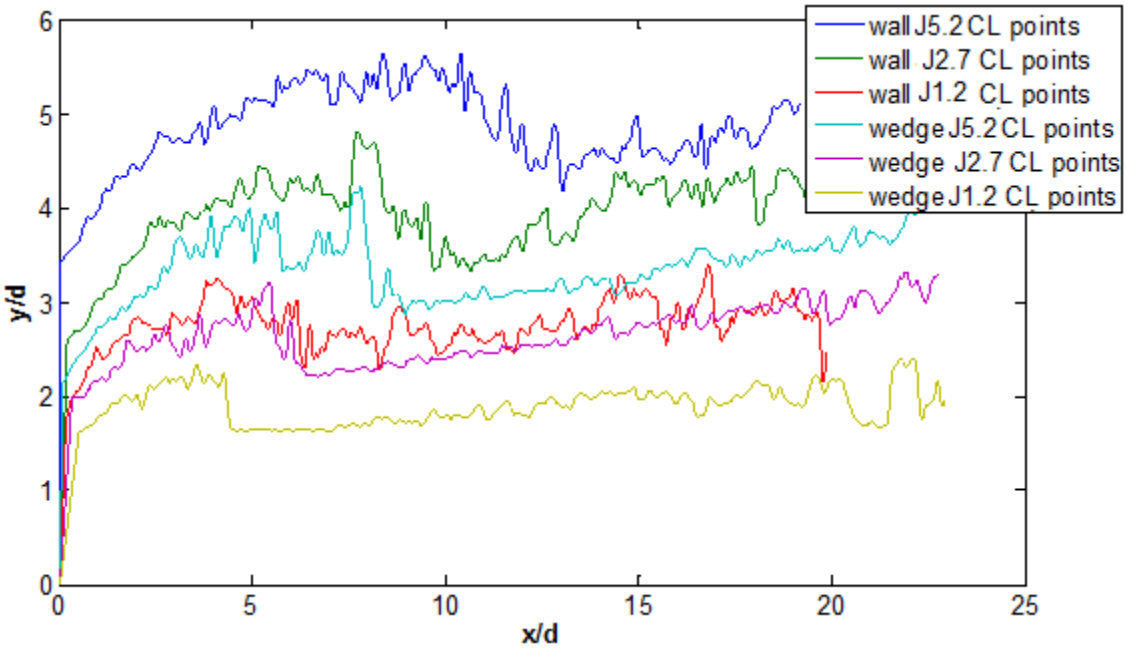

Figure 4.4. Time averaged data. A comparison of Wall (δ/d=7.5) and Wedge (δ/d~0.7) injection centerline trajectories.

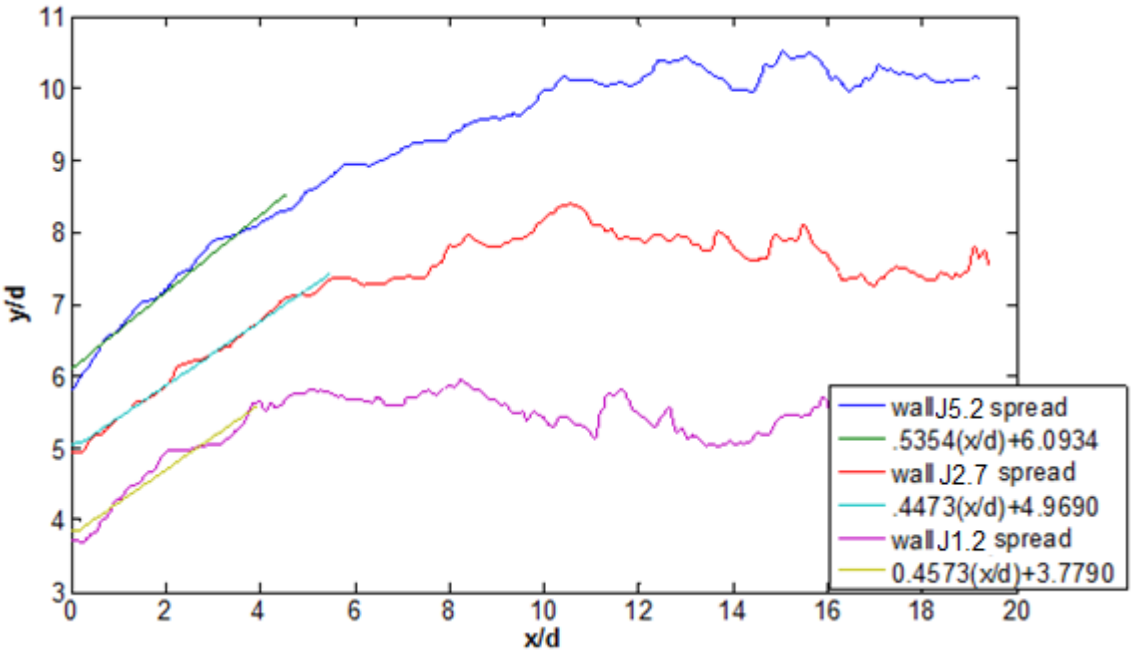

Figure 4.5. Time averaged data. Wall (δ/d=7.5) injection jet spread with line fit in the linear regions

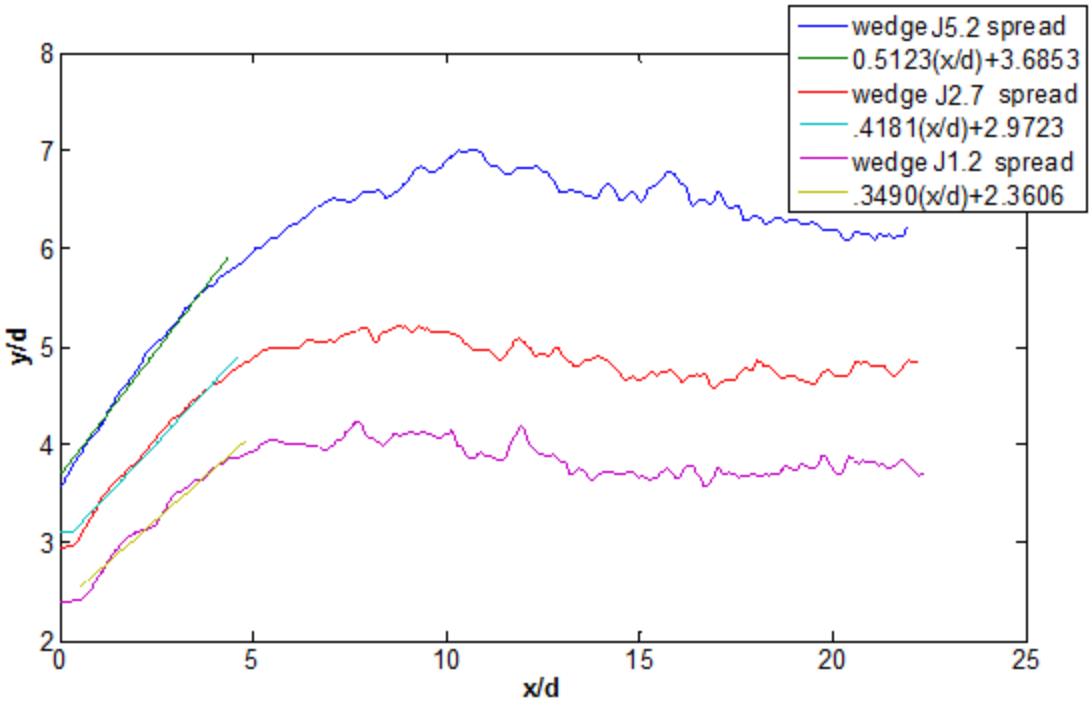

Figure 4.6. Time averaged data. Wedge (δ/d~0.7) injection jet spread with line fit in the linear regions

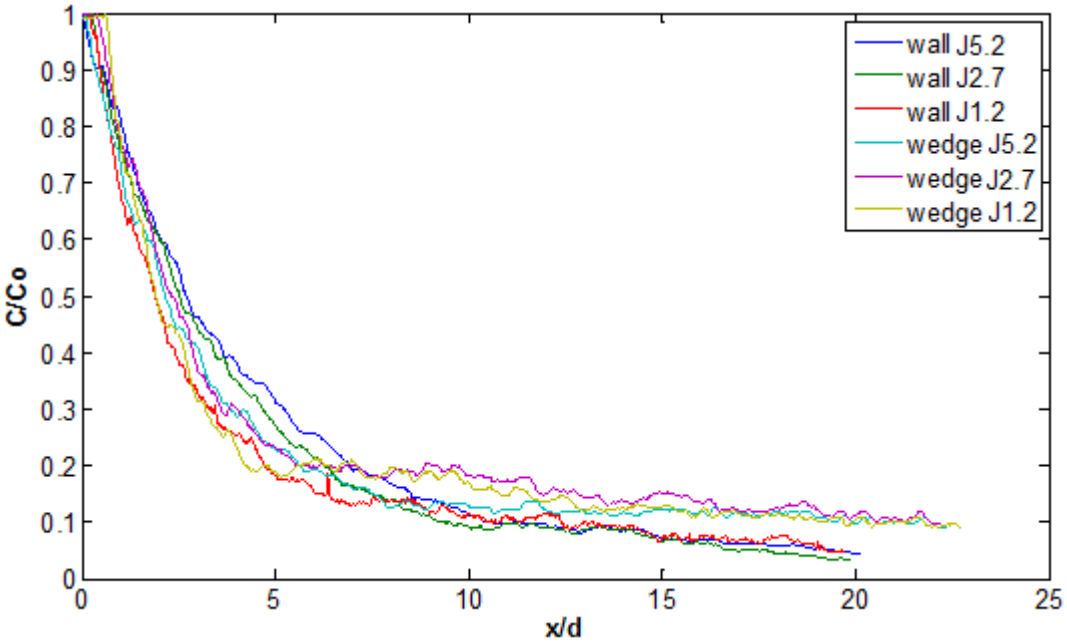

Figure 4.7. Time averaged data. Comparison of Intensity decays of wall (δ/d=7.5) and wedge(δ/d~0.7) injected jets

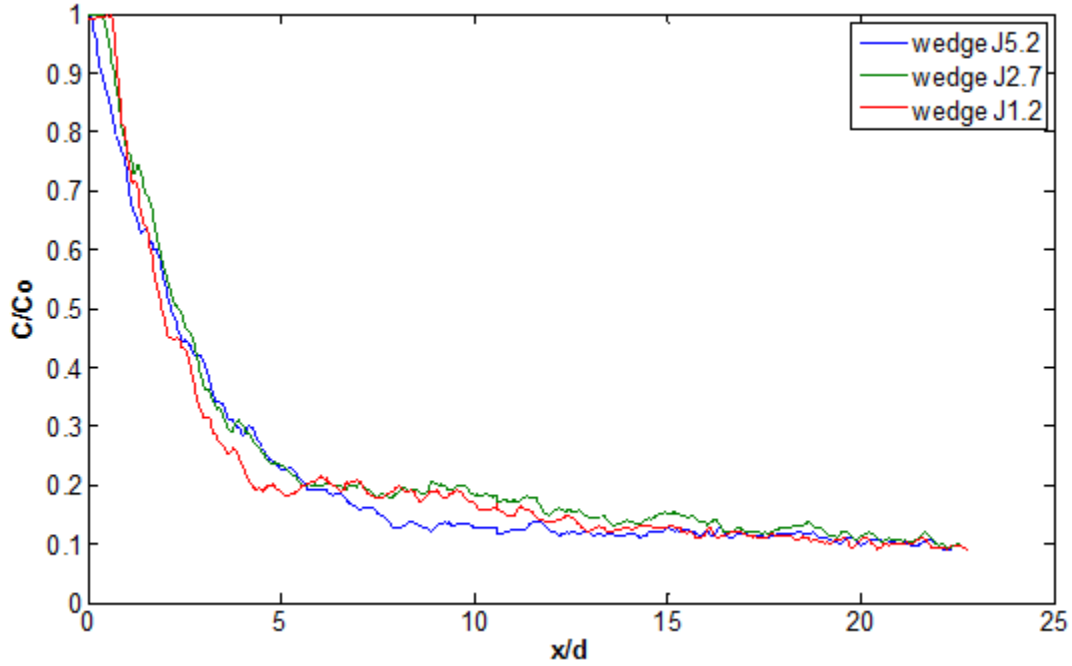

Figure 4.8. Time averaged data. Intensity decays of wedge (δ/d~0.7) injected jets

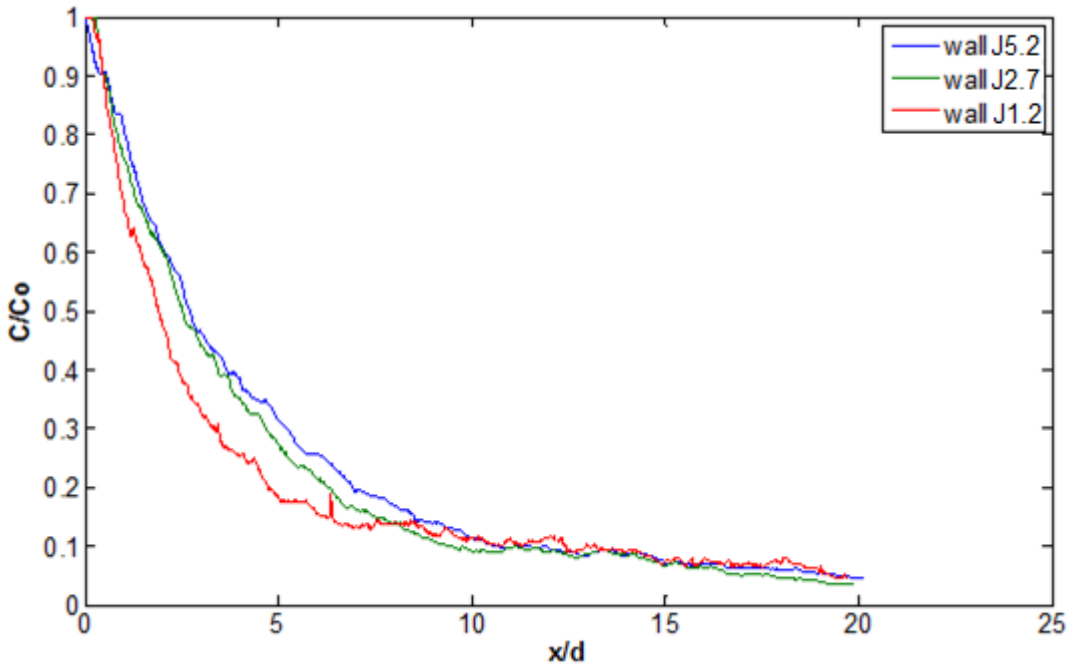

Figure 4.9. Time averaged data. Intensity decays of wall (δ/d=7.5) injected jets

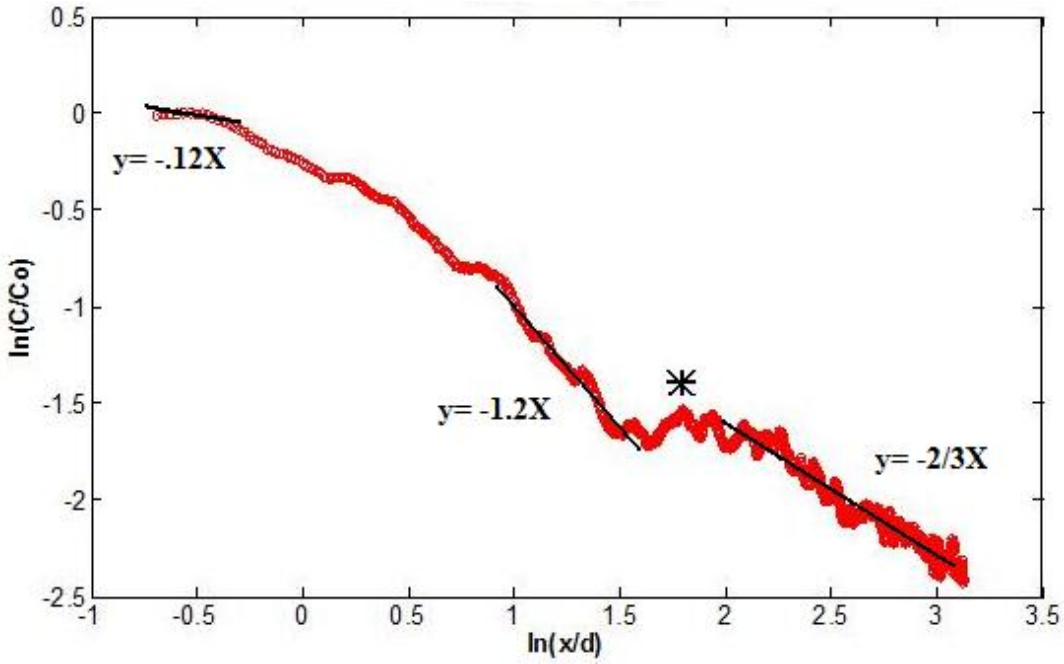

Figure 4.10. Time averaged data. ln(C/C_0) vs ln(x/d) plot of wall(δ/d~0.7) injected J=1.2 jet

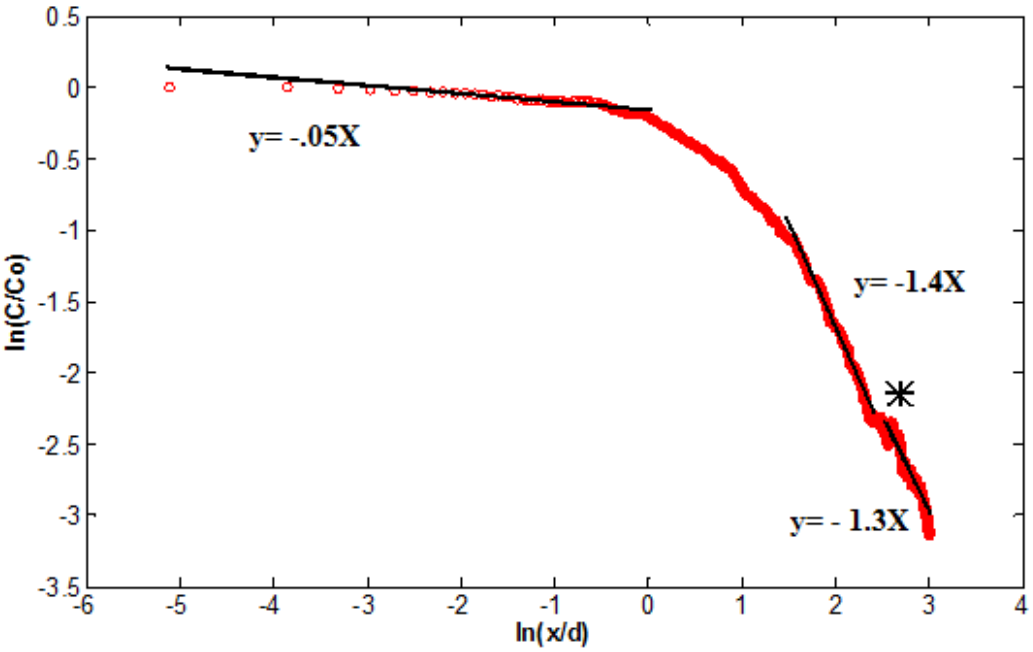

Figure 4.11. Time averaged data. $\ln(C/C_0)$ vs $\ln(x/d)$ plot of wall($\delta/d=7.5$) injected J=5.2 jet

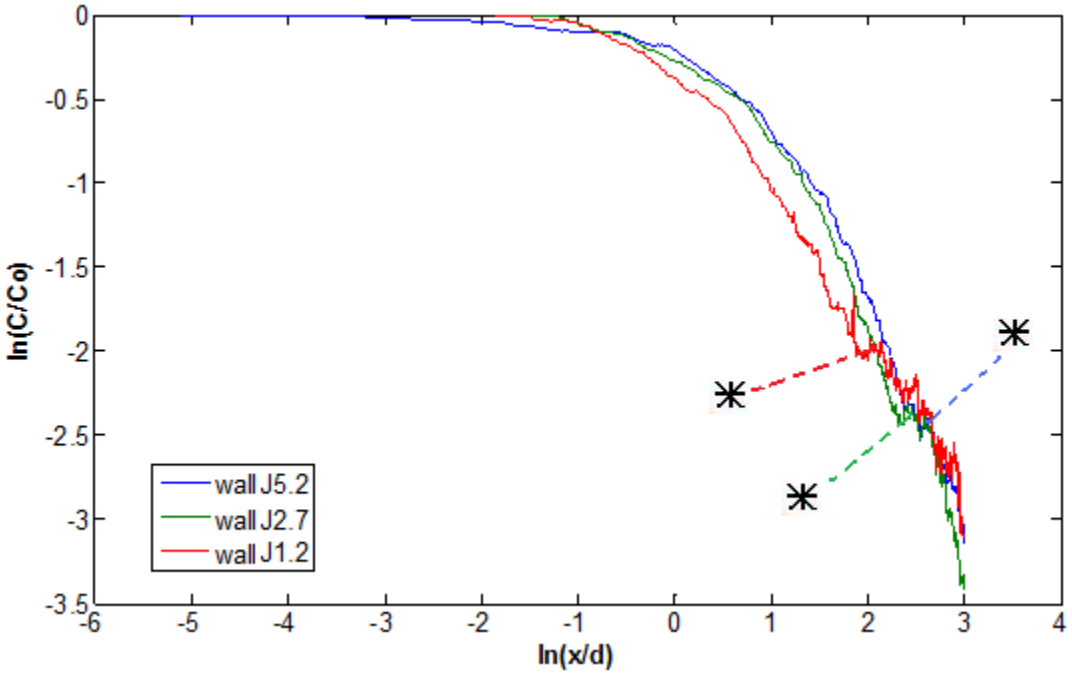

Figure 4.12. Time averaged data. $\ln(C/C_0)$ vs $\ln(x/d)$ plot of wall($\delta/d=7.5$) injected jets

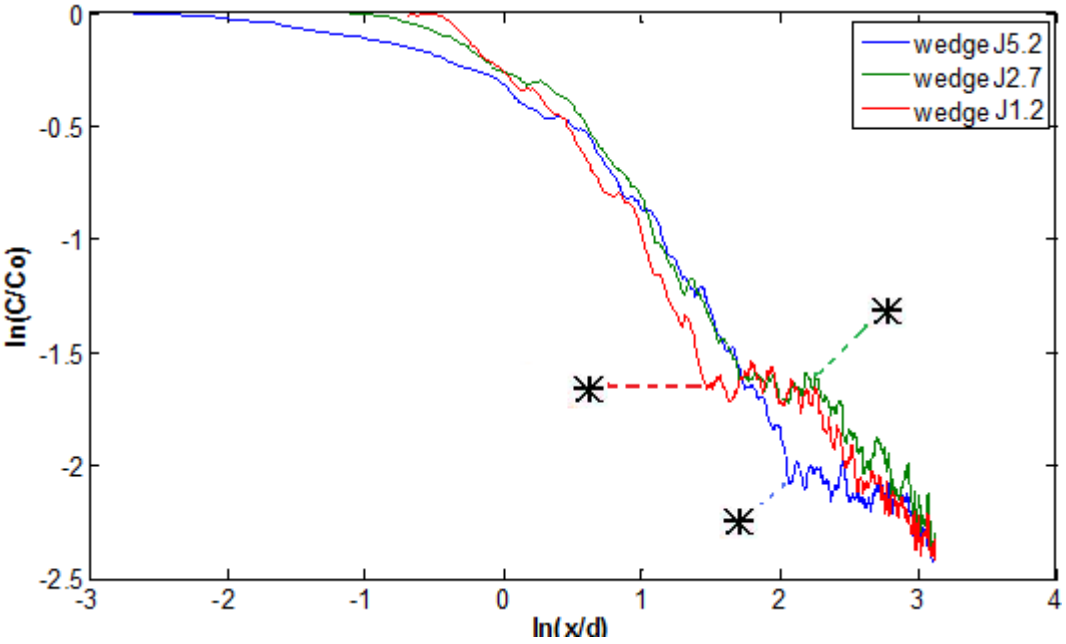

Figure 4.13. Time averaged data. $\ln(C/C_0)$ vs $\ln(x/d)$ plot of wedge(δ/d~0.7) injected jets

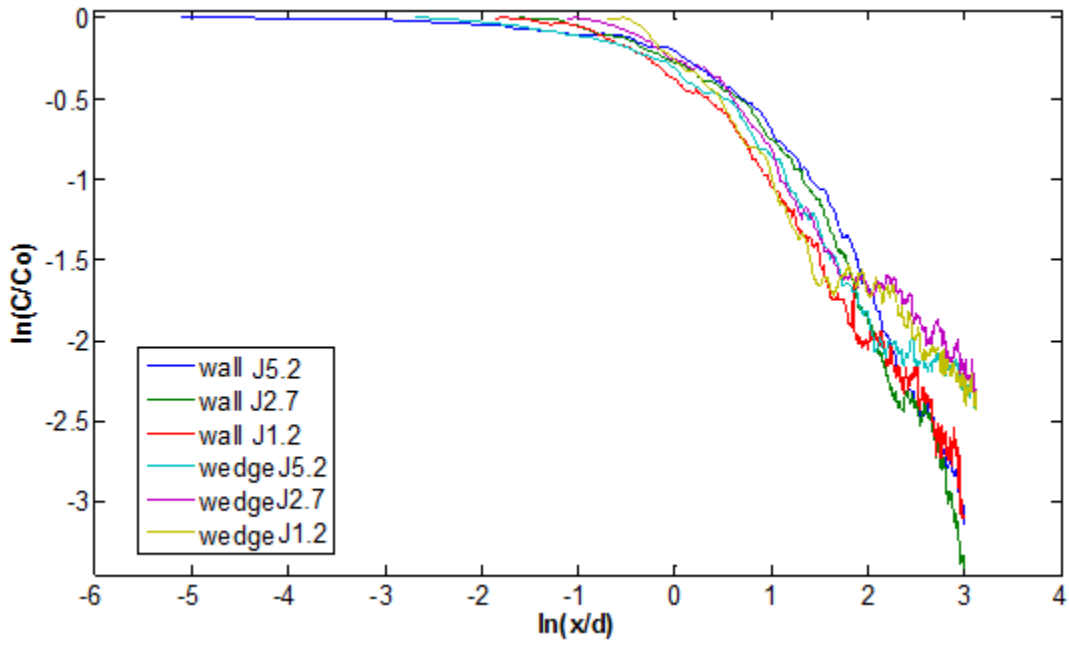

Figure 4.14 Time averaged data. A comparison of $\ln(C/C_0)$ vs $\ln(x/d)$ wall(δ/d=7.5) and wedge(δ/d~0.7) injected jets.

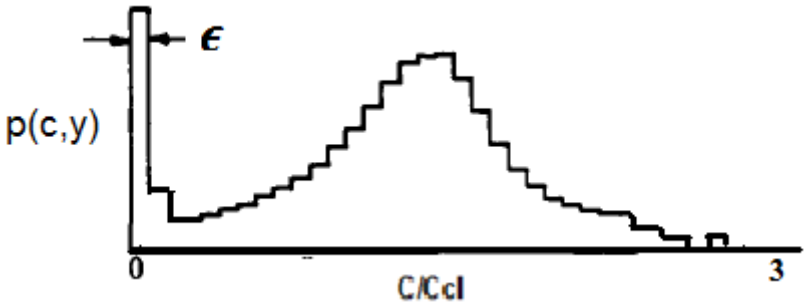

Figure 4.15 A sample histogram.

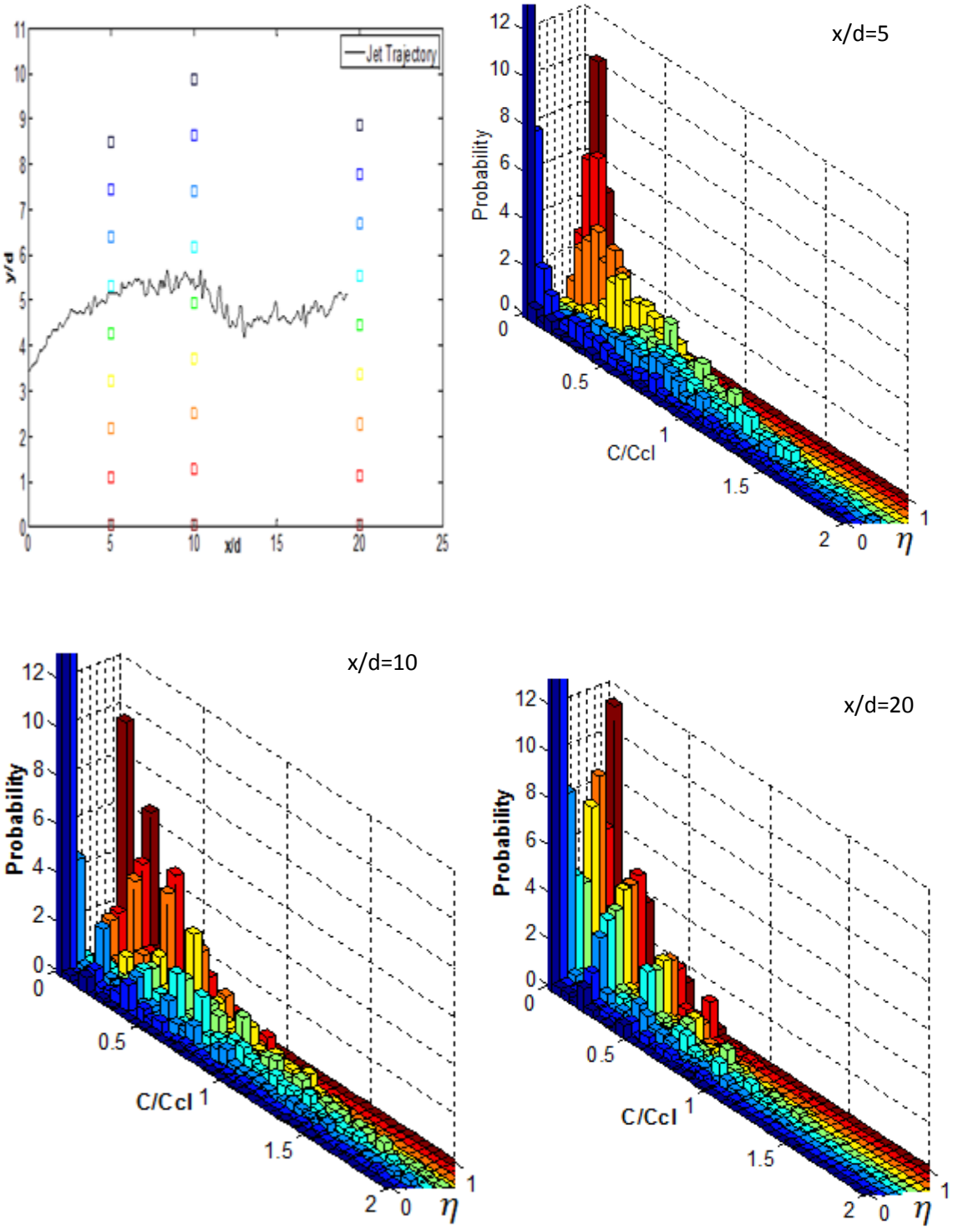

Figure 4.16. Side view PDF's for wall(δ/d=7.5) injected J=5.2 jet.

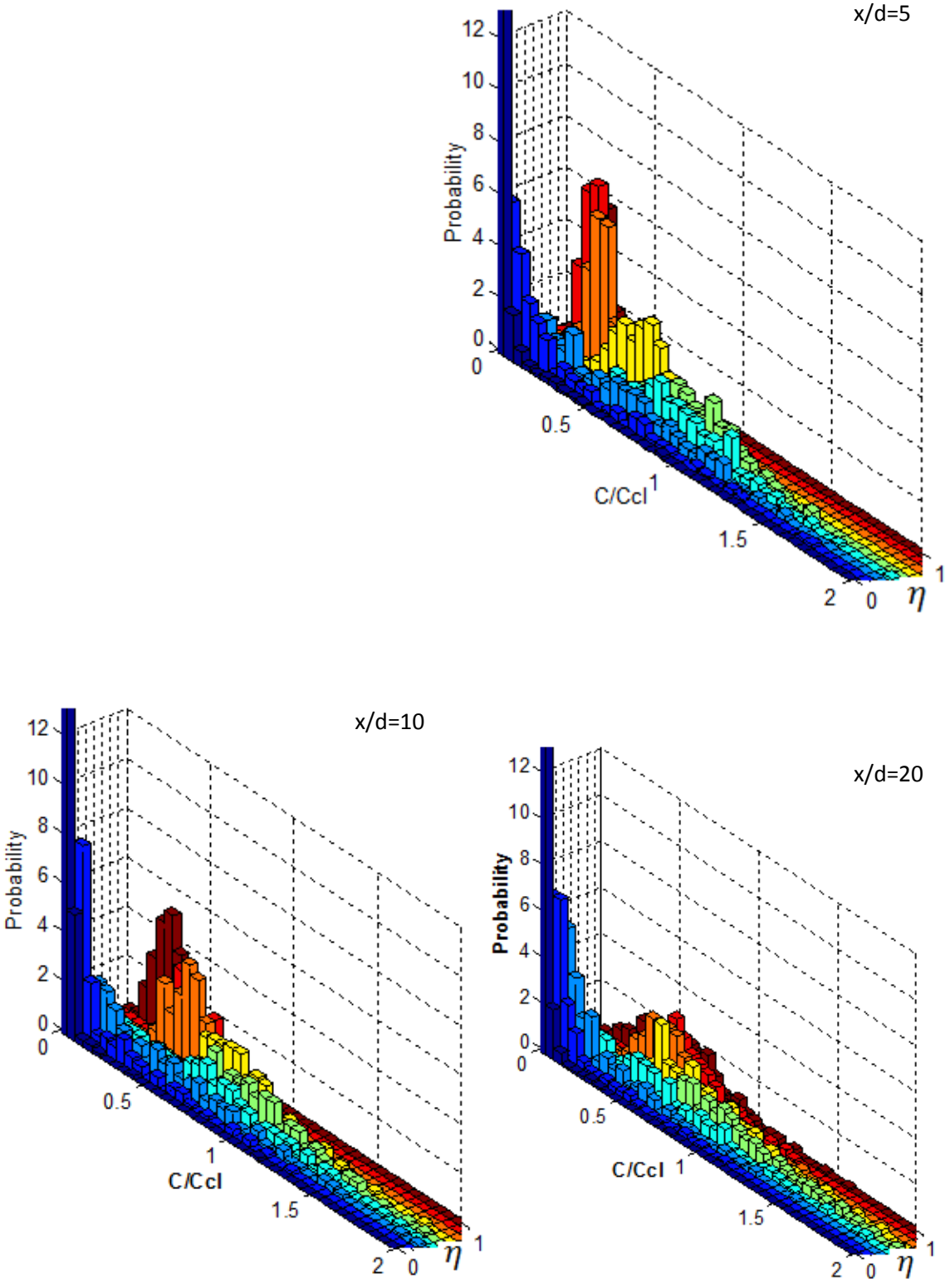

Figure 4.17. End view PDF's for wall(δ/d=7.5) injected J=5.2 jet.

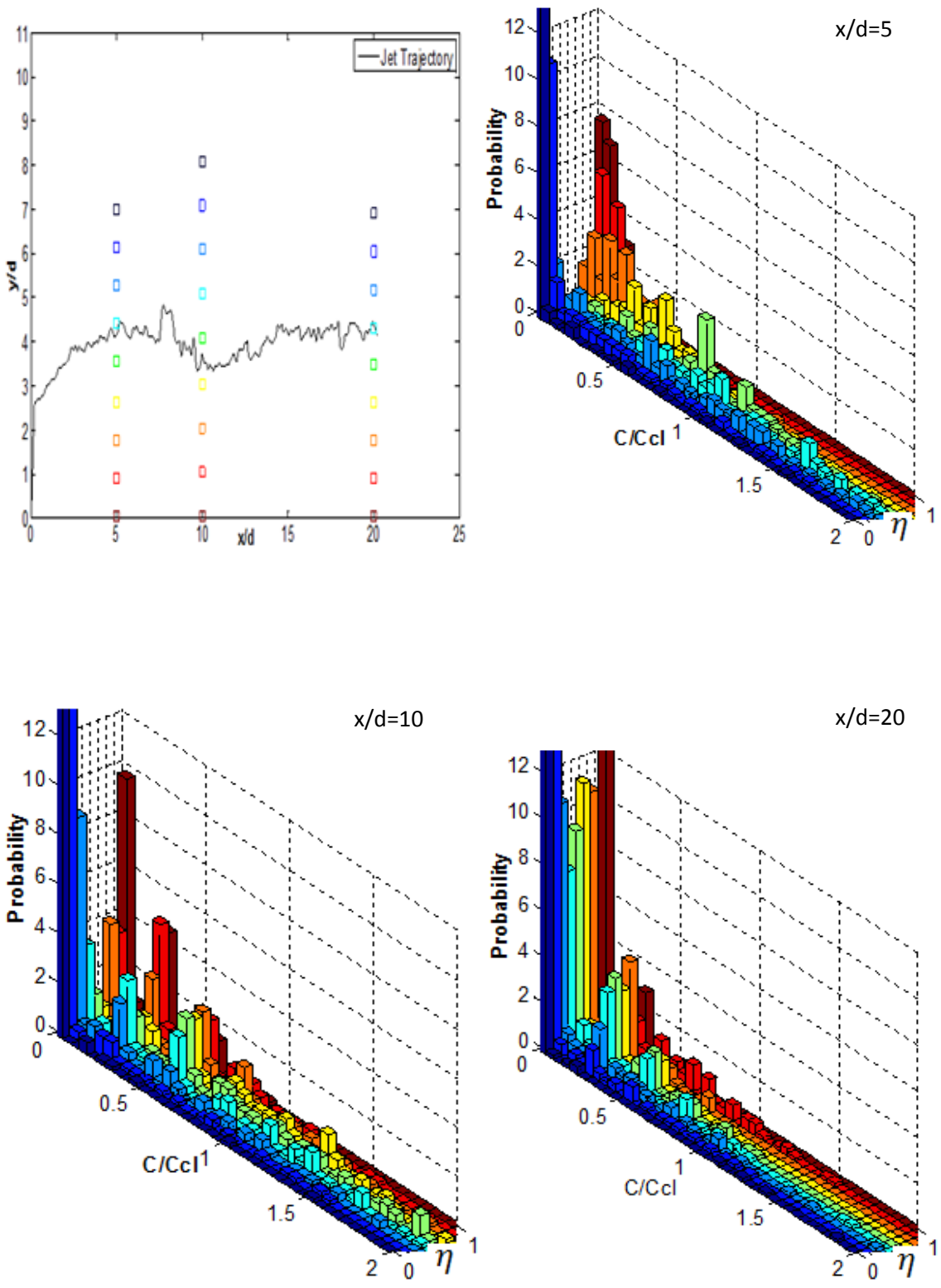

Figure 4.18. Side view PDF's for wall(δ/d=7.5) injected J=2.7 jet.

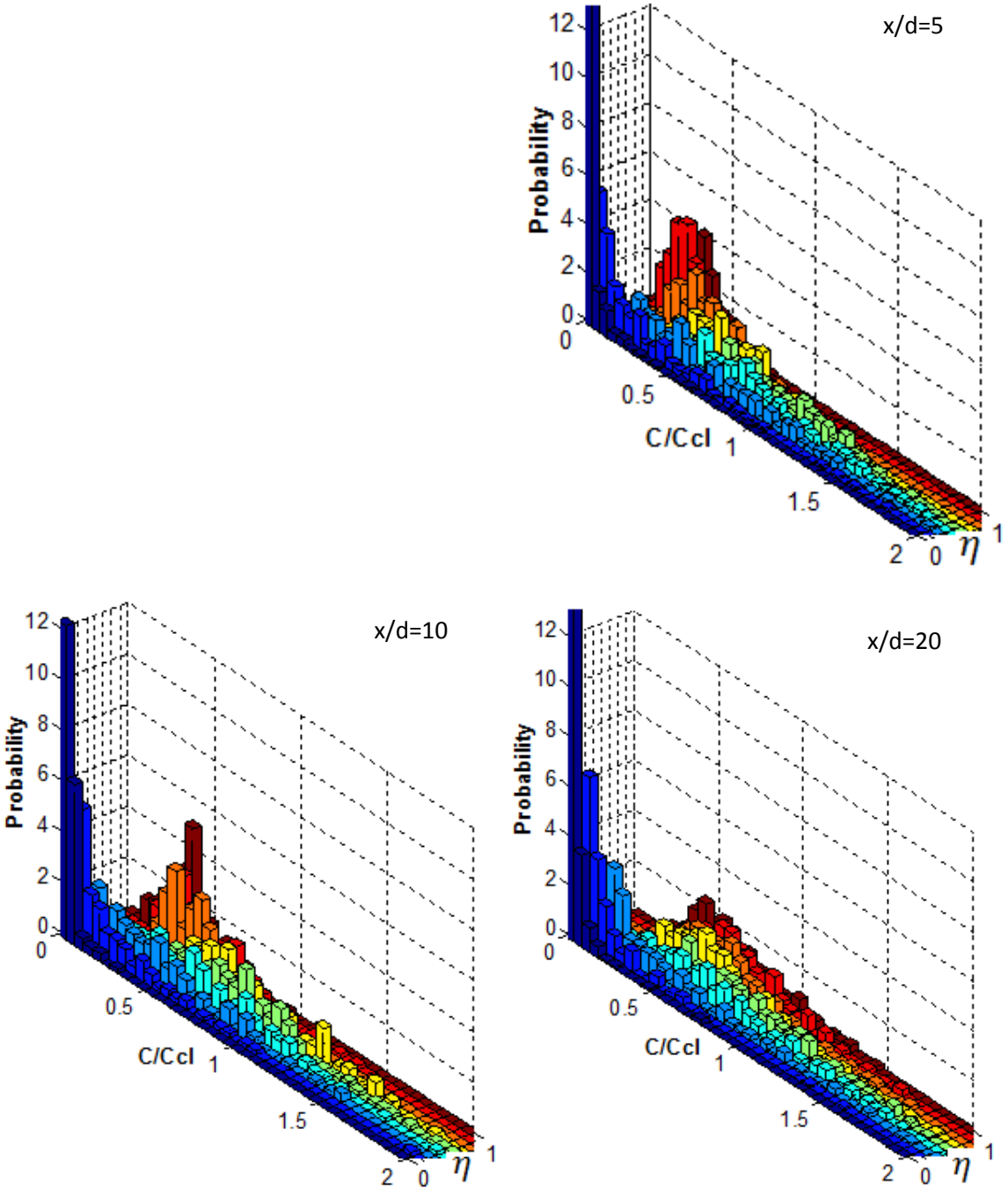

Figure 4.19. End view PDF's for wall(δ/d=7.5) injected J=2.7 jet.

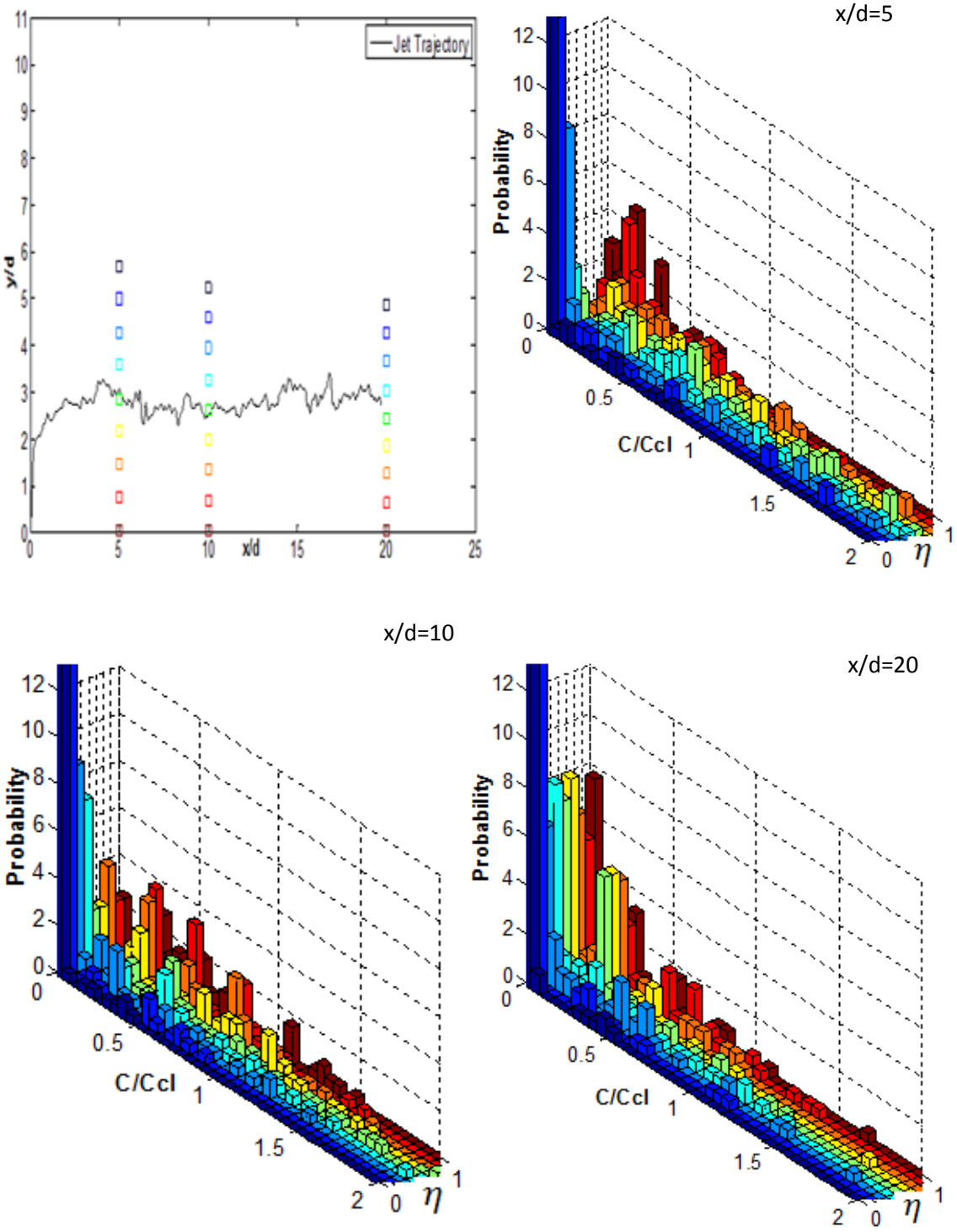

Figure 4.20. Side view PDF's for wall(δ/d=7.5) injected J=1.2 jet.

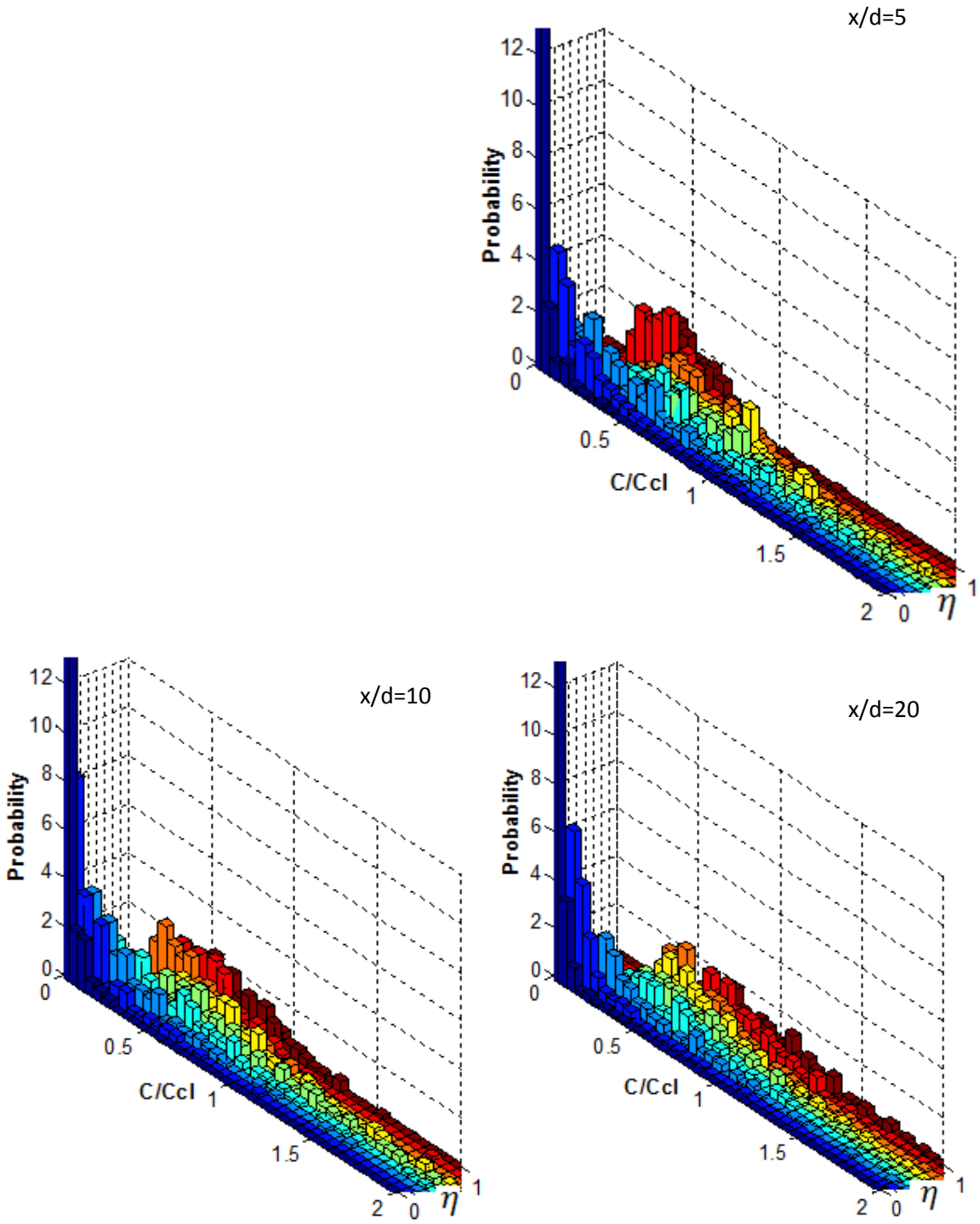

Figure 4.21. End view PDF's for wall(δ/d=7.5) injected J=1.2 jet.

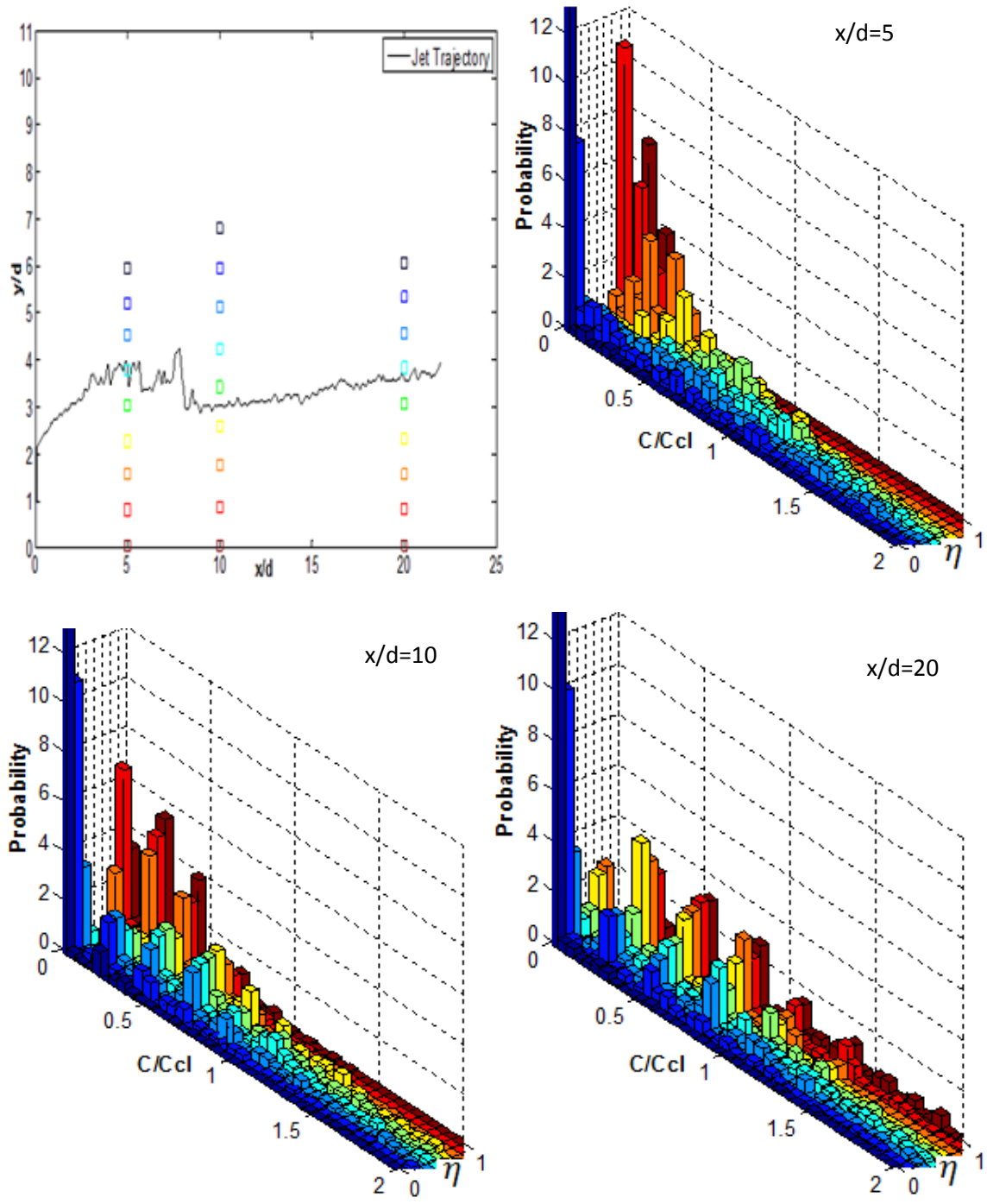

Figure 4.22. Side view PDF's for wedge(δ/d~0.7) injected J=5.2 jet.

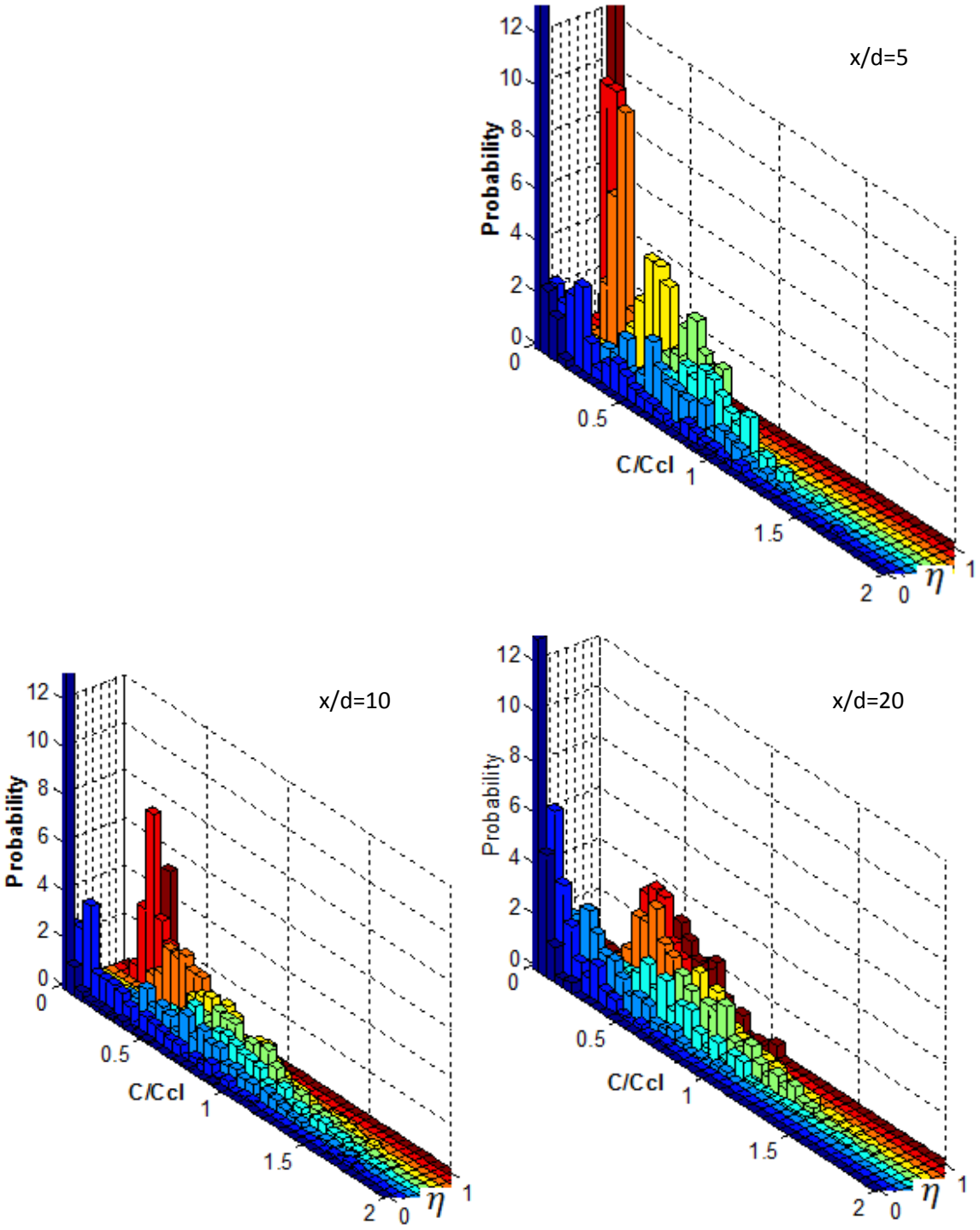

Figure 4.23. End view PDF's for wedge(δ/d~0.7) injected J=5.2 jet.

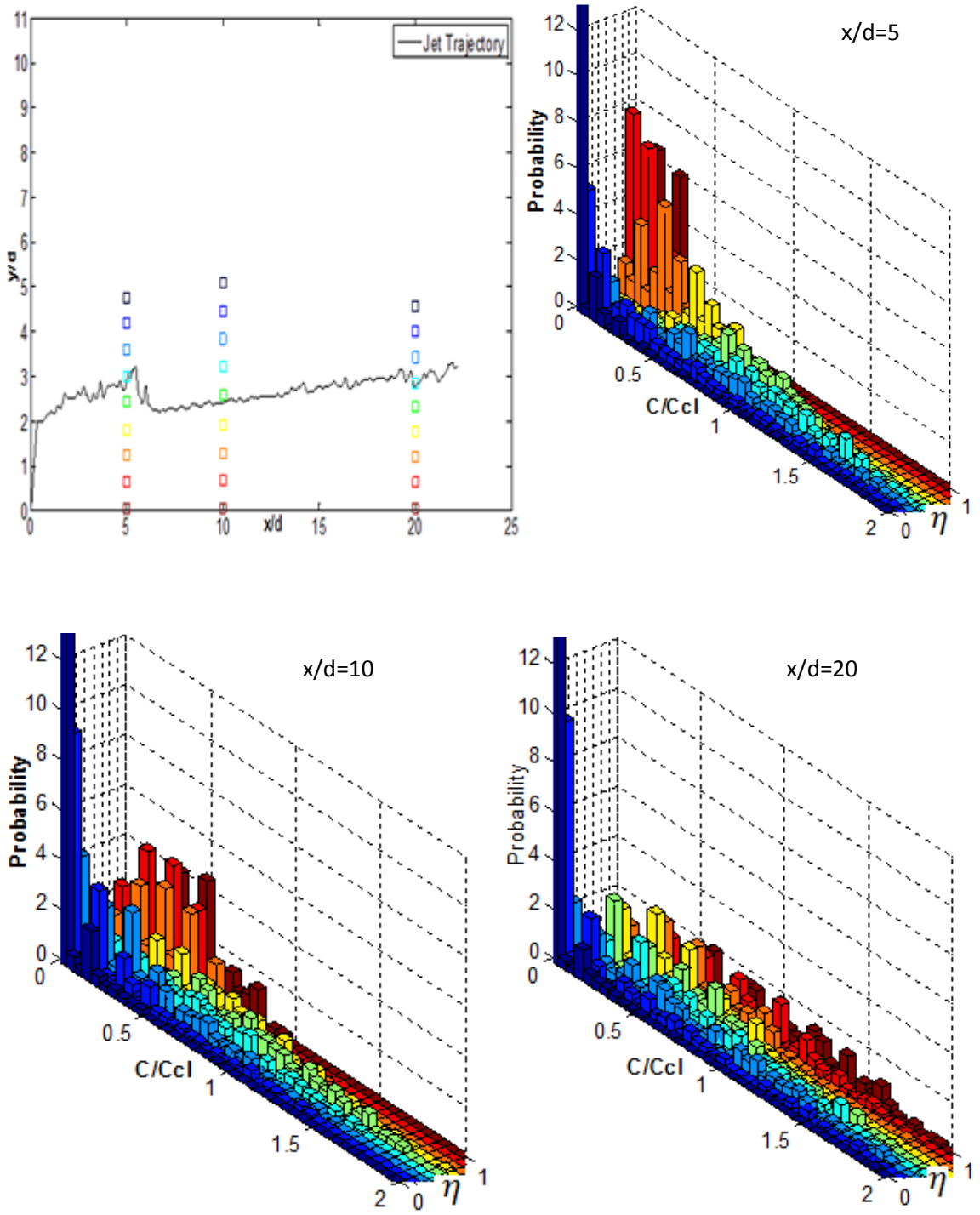

Figure 4.24. Side view PDF's for wedge(δ/d~0.7) injected J=2.7 jet.

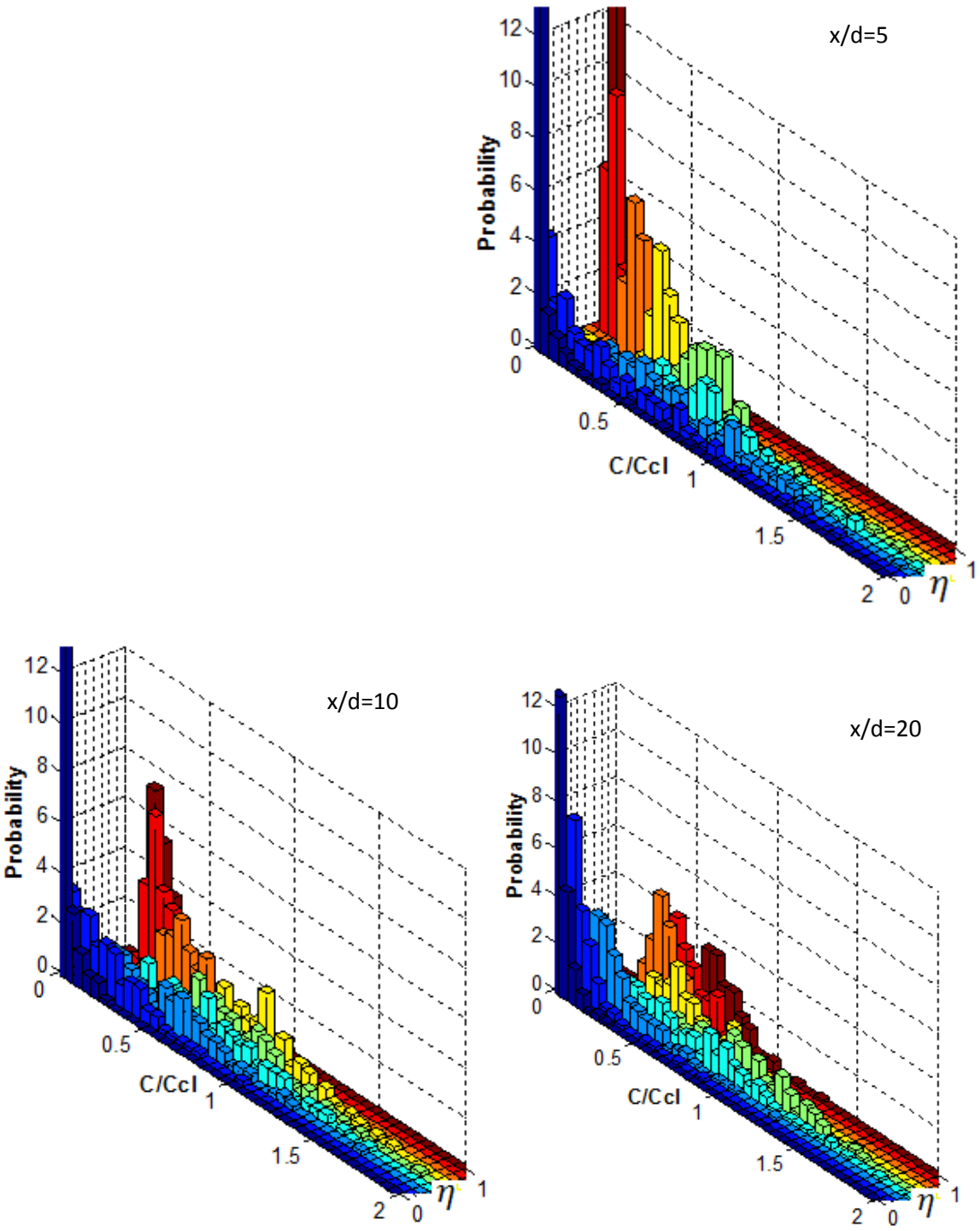

Figure 4.25. End view PDF's for wedge(δ/d~0.7) injected J=2.7 jet.

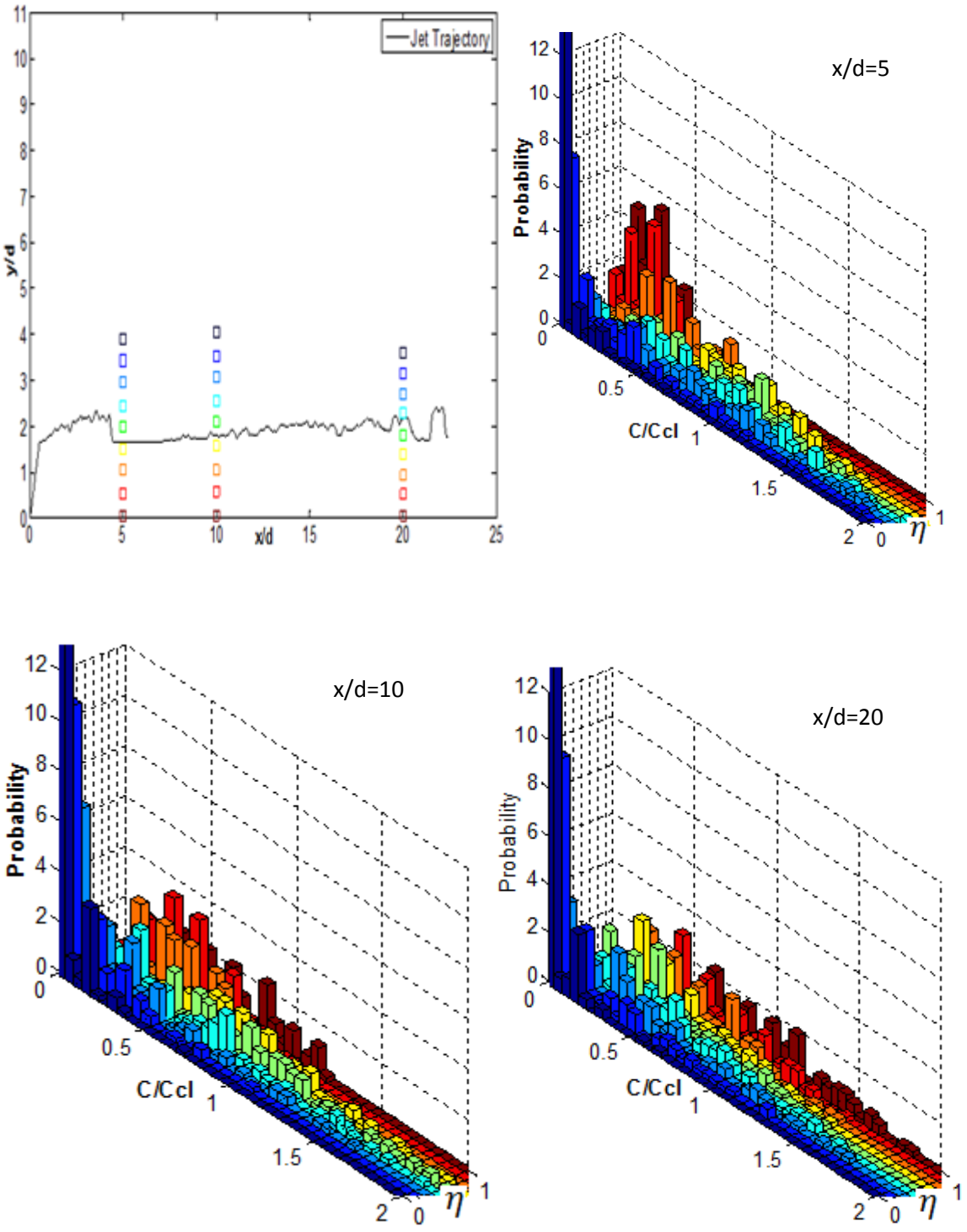

Figure 4.26. Side view PDF's for wedge(δ/d~0.7) injected J=1.2 jet.

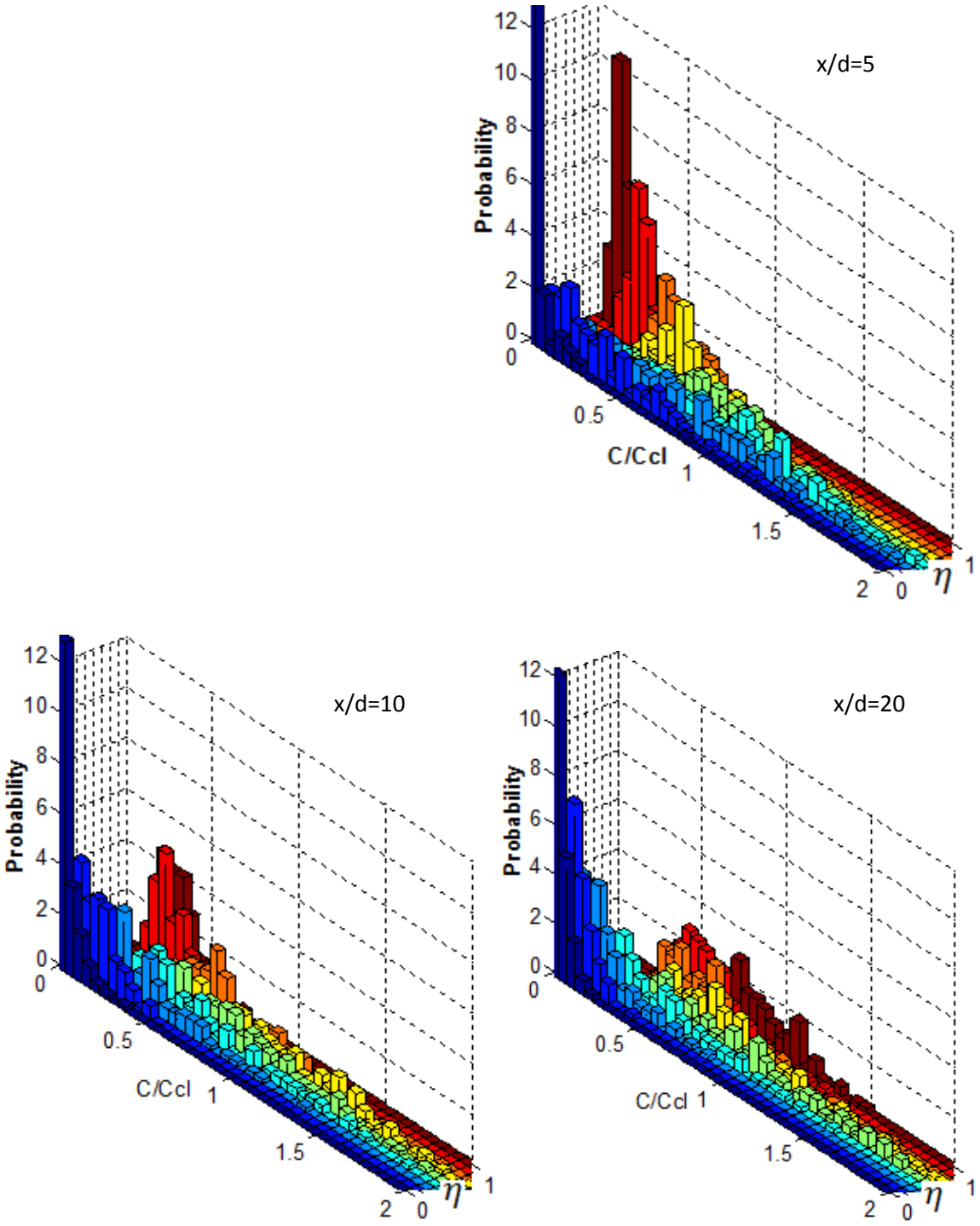

Figure 4.27. End view PDF's for wedge(δ/d~0.7) injected J=1.2 jet.

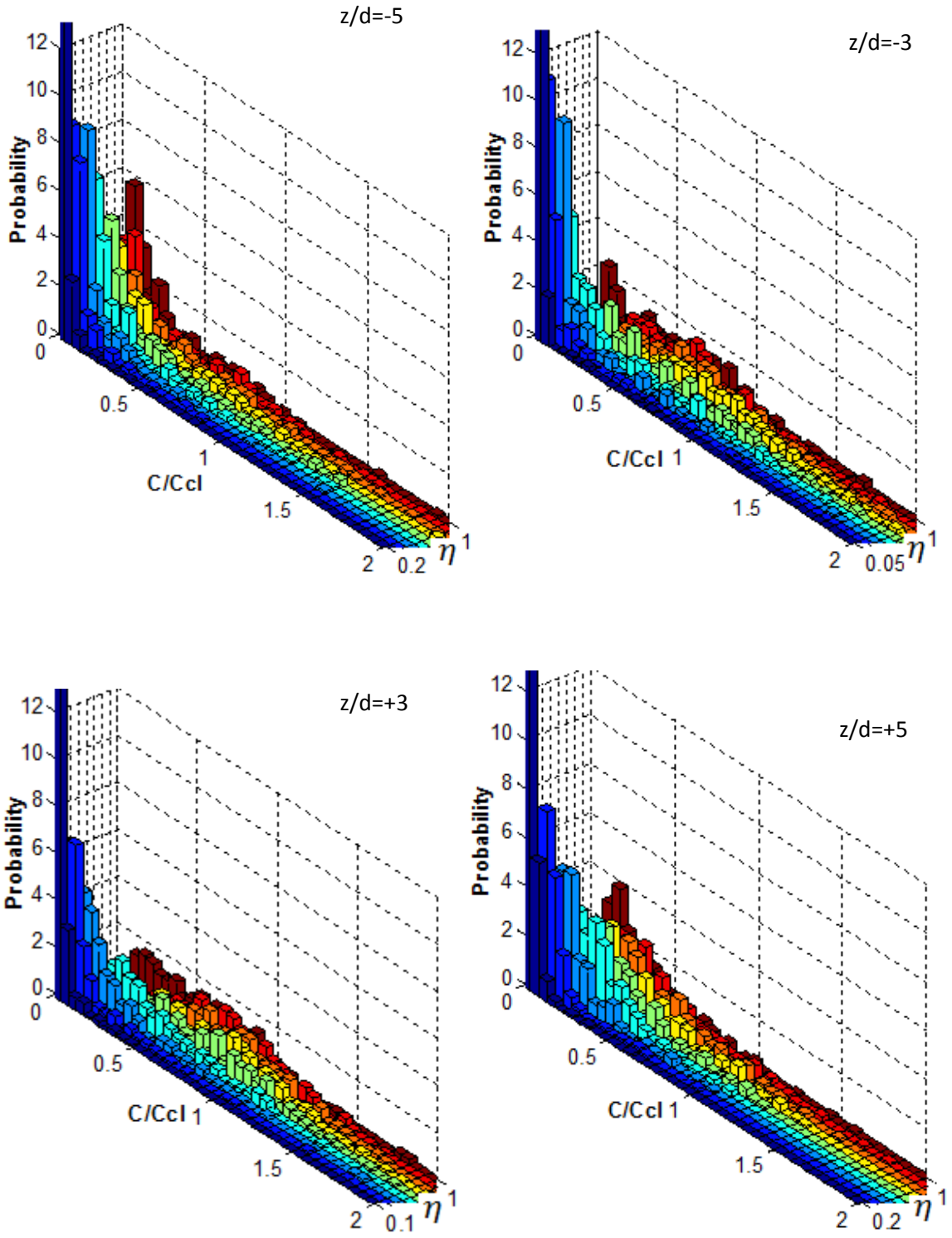

Figure 4.28. z/d=-5, -3, +3, and +5 end view PDF's for wall (δ/d=7.5) injected J=5.2 jet at x/d=20.

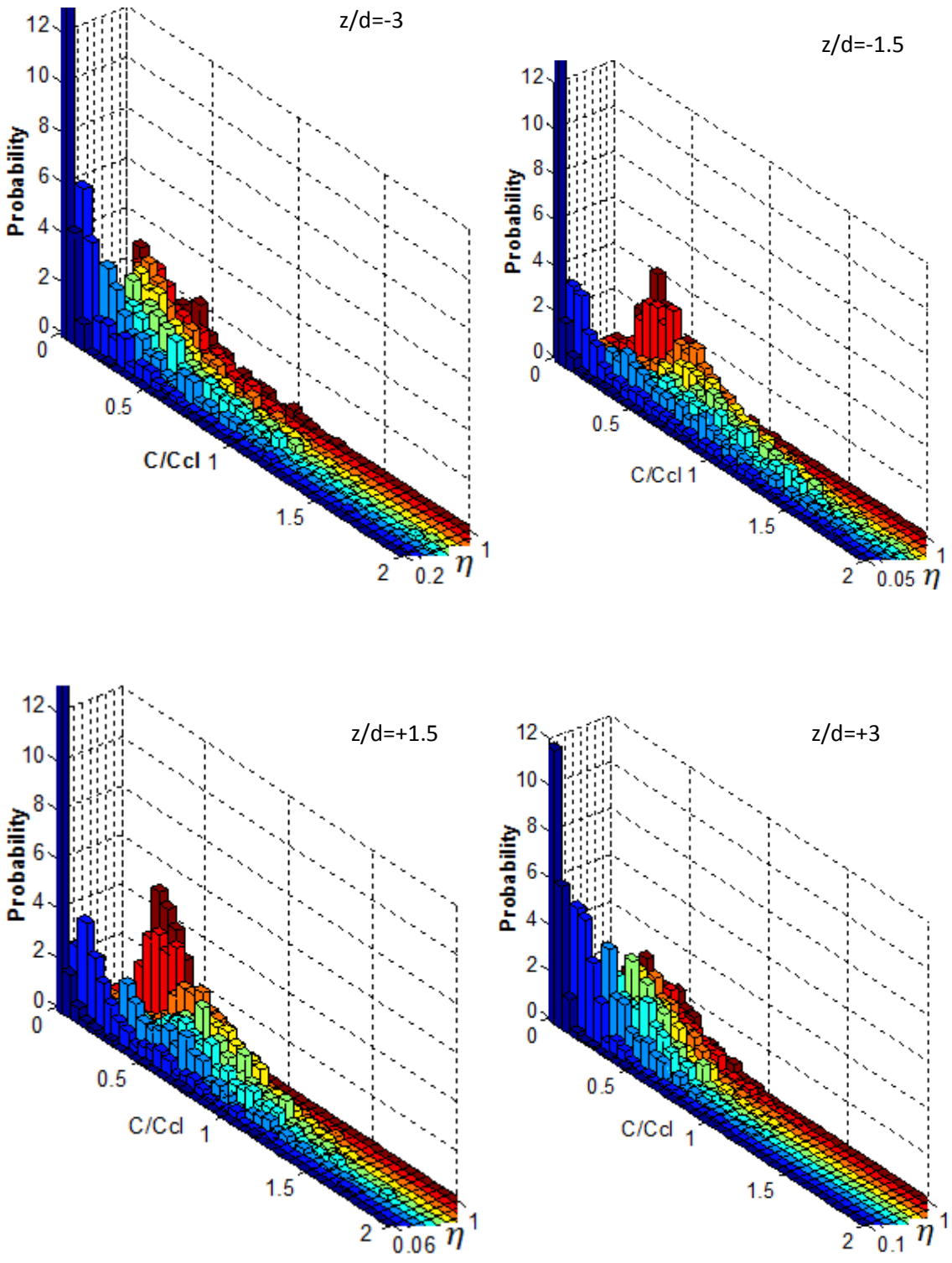

Figure 4.29. z/d=-3, -1.5, +1.5, and +3 end view PDF's for wedge (δ/d~0.7) injected J=5.2 jet at x/d=10.

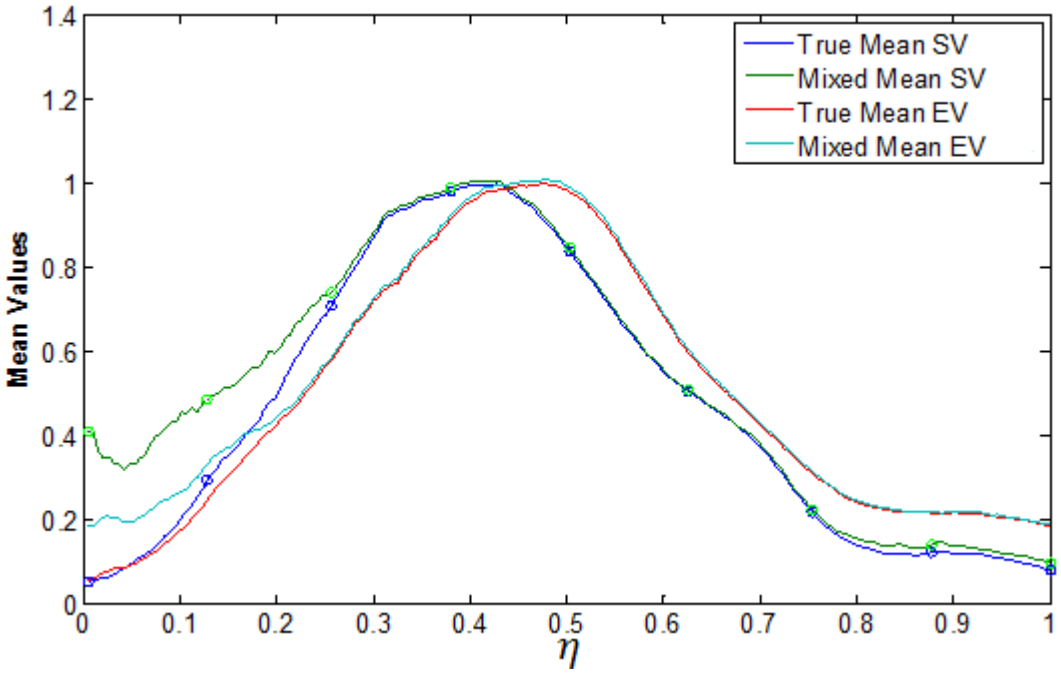

Figure 4.30. Side and end view mean comparisons for wall (δ/d=7.5) injected J=5.2 jet at x/d=5.

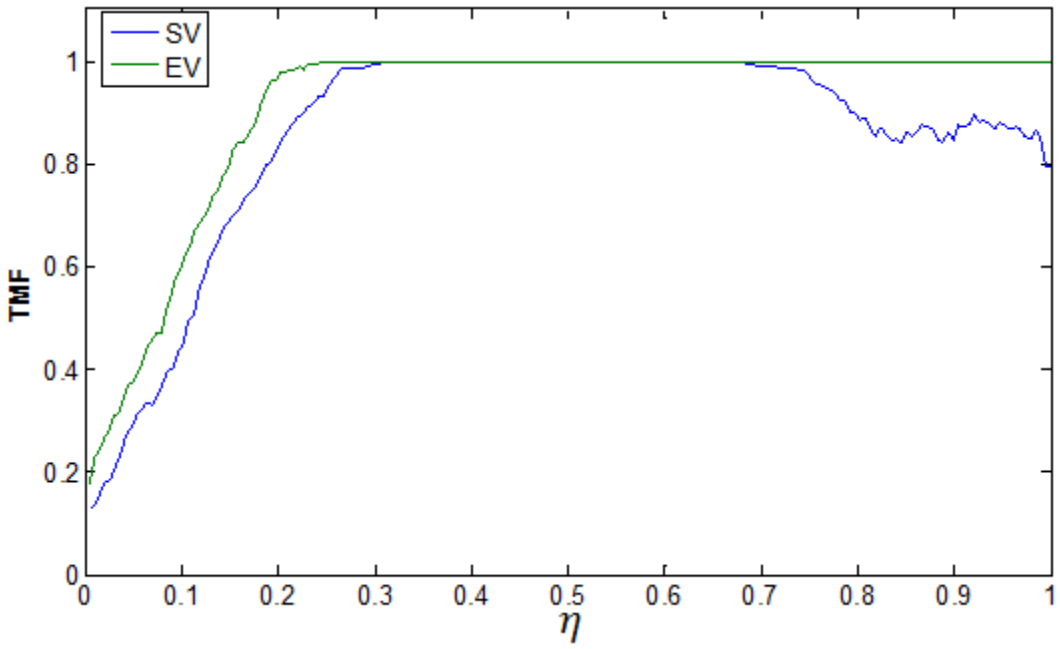

Figure 4.31. Side and end view True Mixed Fraction comparisons for wall (δ/d=7.5) injected J=5.2 jet at x/d=5.

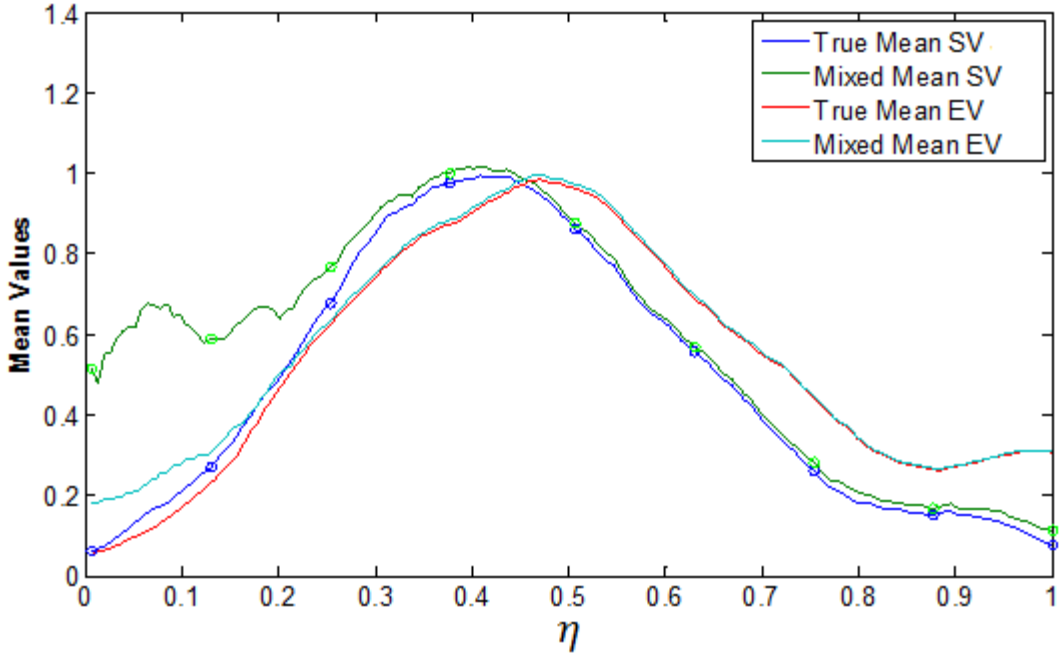

Figure 4.32. Side and end view mean comparisons for wall (δ/d=7.5) injected J=2.7 jet at x/d=5.

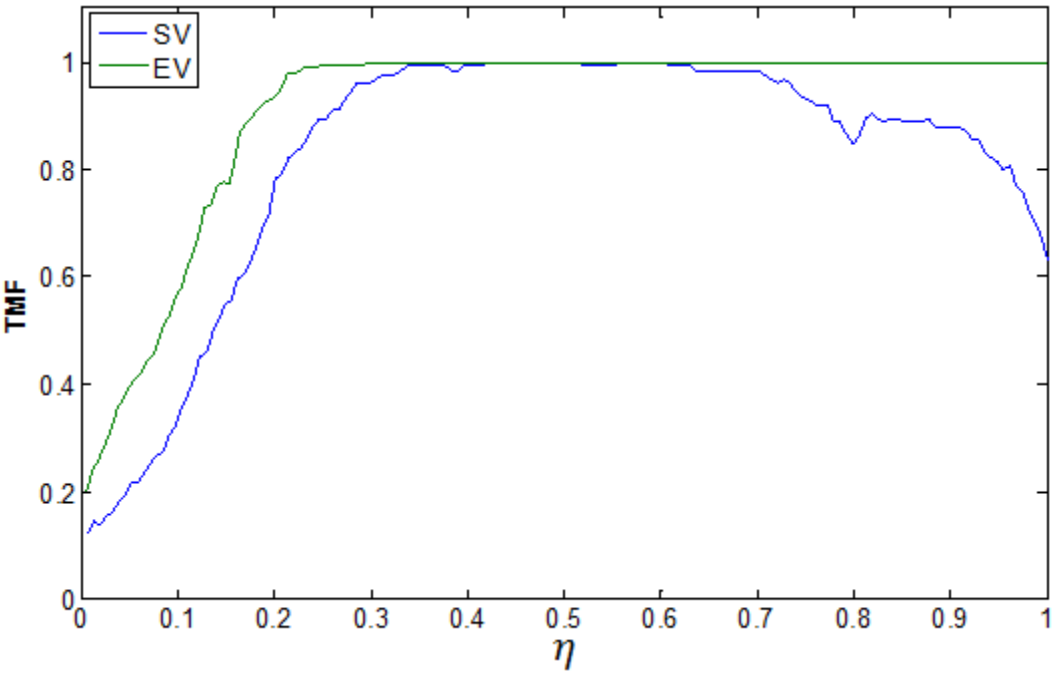

Figure 4.33. Side and end view True Mixed Fraction comparisons for wall (δ/d=7.5) injected J=2.7 jet at x/d=5.

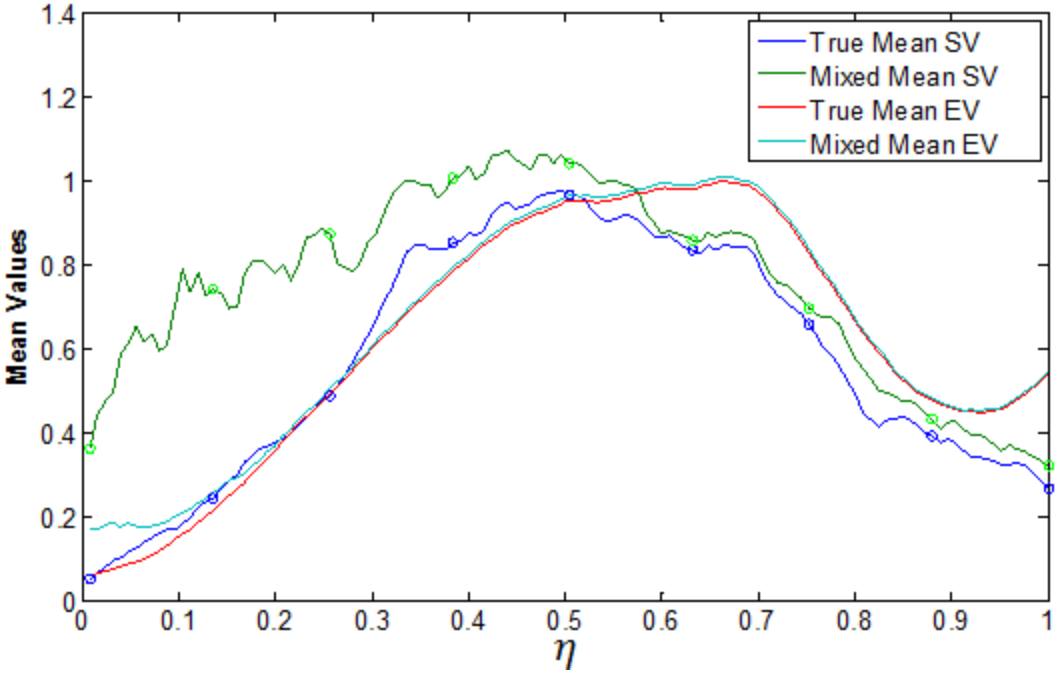

Figure 4.34. Side and end view mean comparisons for wall (δ/d=7.5) injected J=1.2 jet at x/d=5.

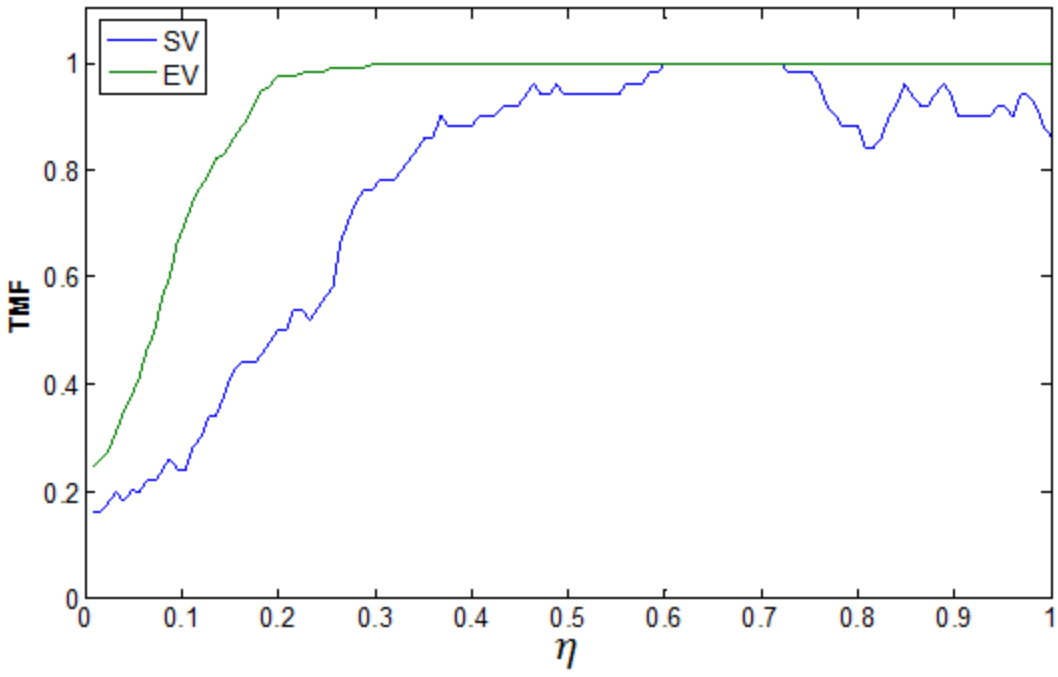

Figure 4.35. Side and end view True Mixed Fraction comparisons for wall (δ/d=7.5) injected J=1.2 jet at x/d=5.

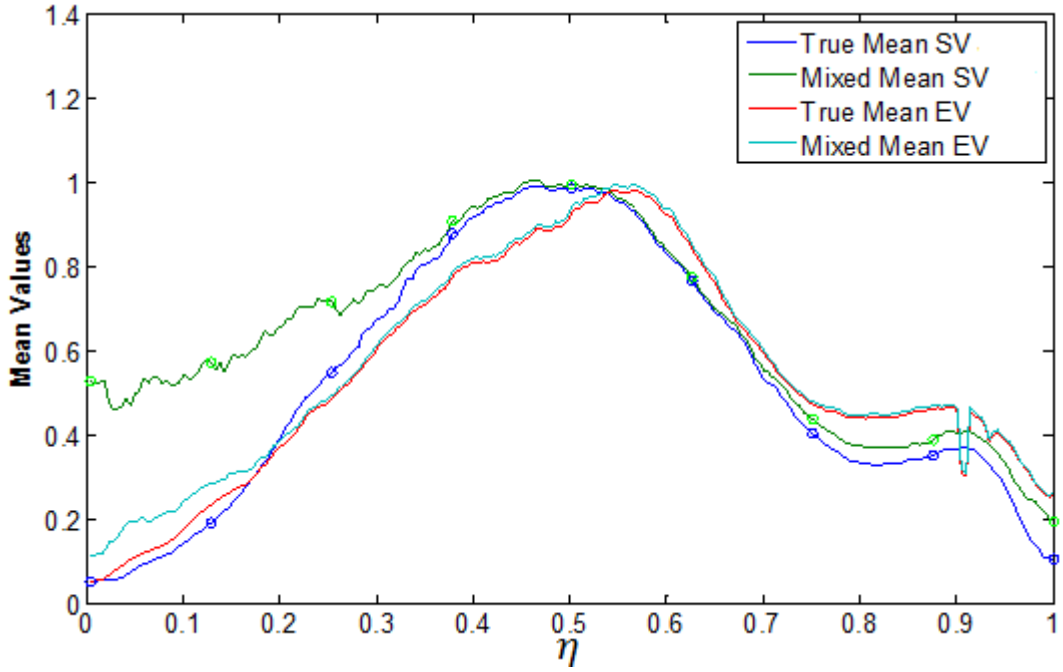

Figure 4.36. Side and end view mean comparisons for wall (δ/d=7.5) injected J=5.2 jet at x/d=10.

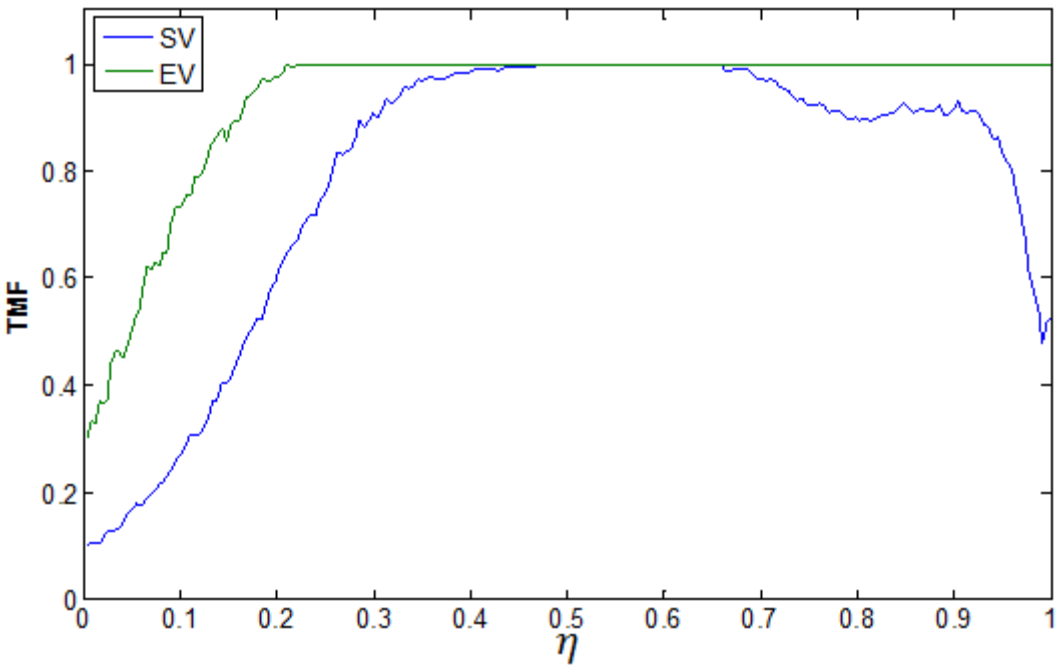

Figure 4.37. Side and end view True Mixed Fraction comparisons for wall (δ/d=7.5) injected J=5.2 jet at x/d=10.

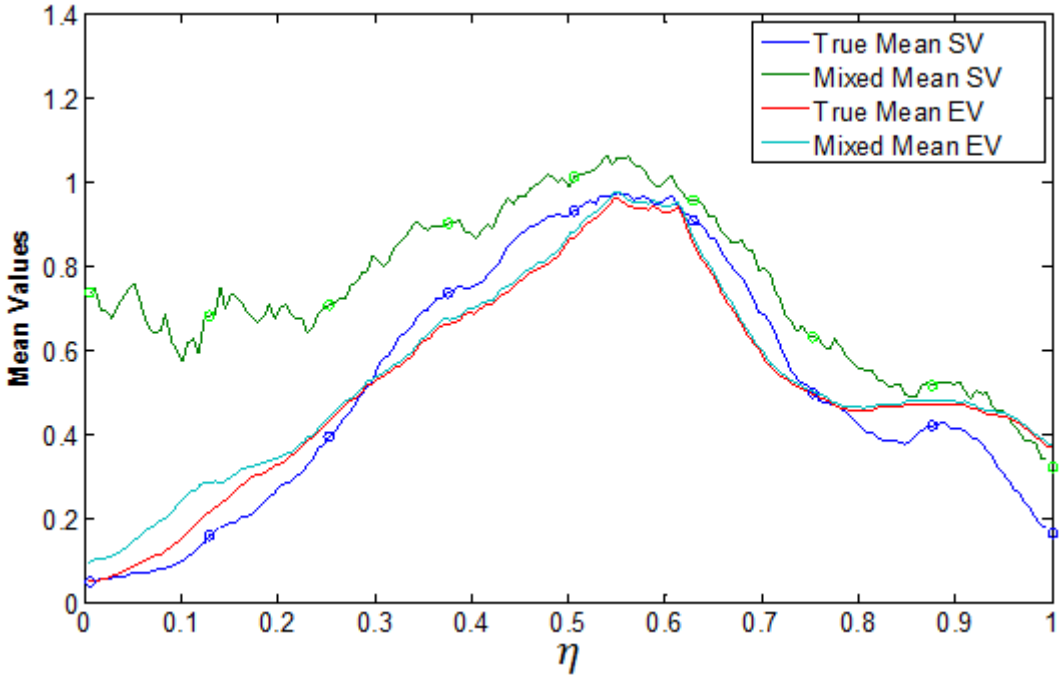

Figure 4.38. Side and end view mean comparisons for wall (δ/d=7.5) injected J=2.7 jet at x/d=10.

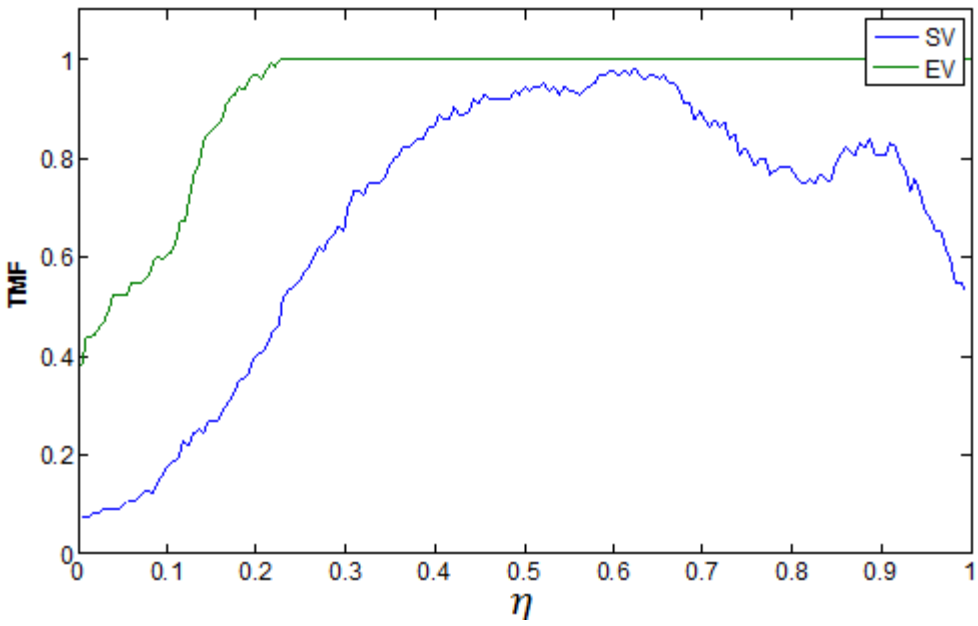

Figure 4.39. Side and end view True Mixed Fraction comparisons for wall (δ/d=7.5) injected J=2.7 jet at x/d=10.

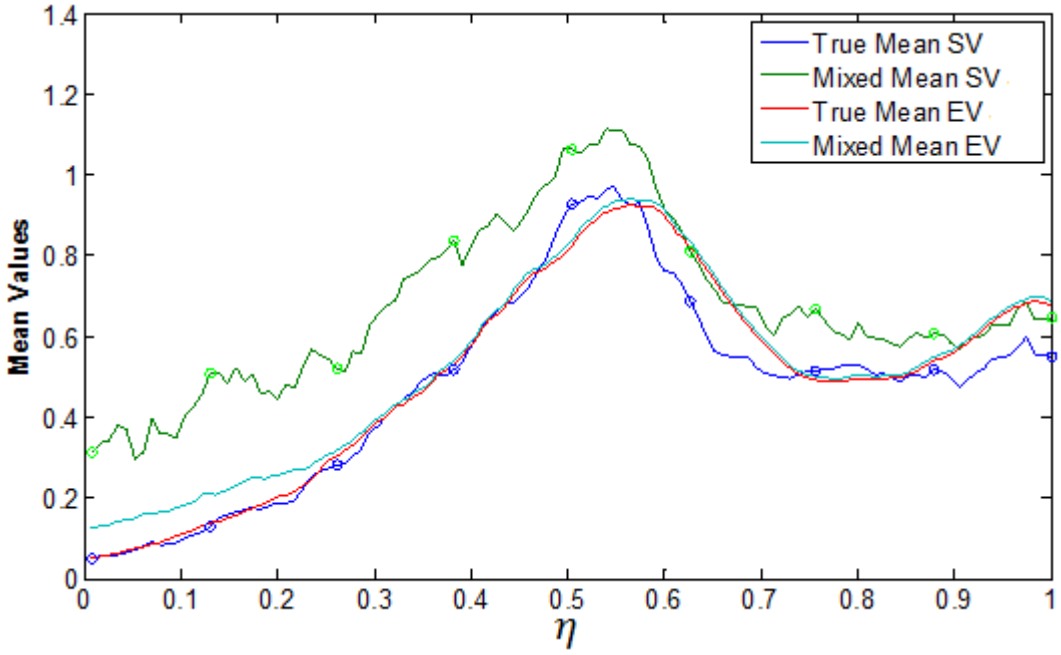

Figure 4.40. Side and end view mean comparisons for wall (δ/d=7.5) injected J=1.2 jet at x/d=10.

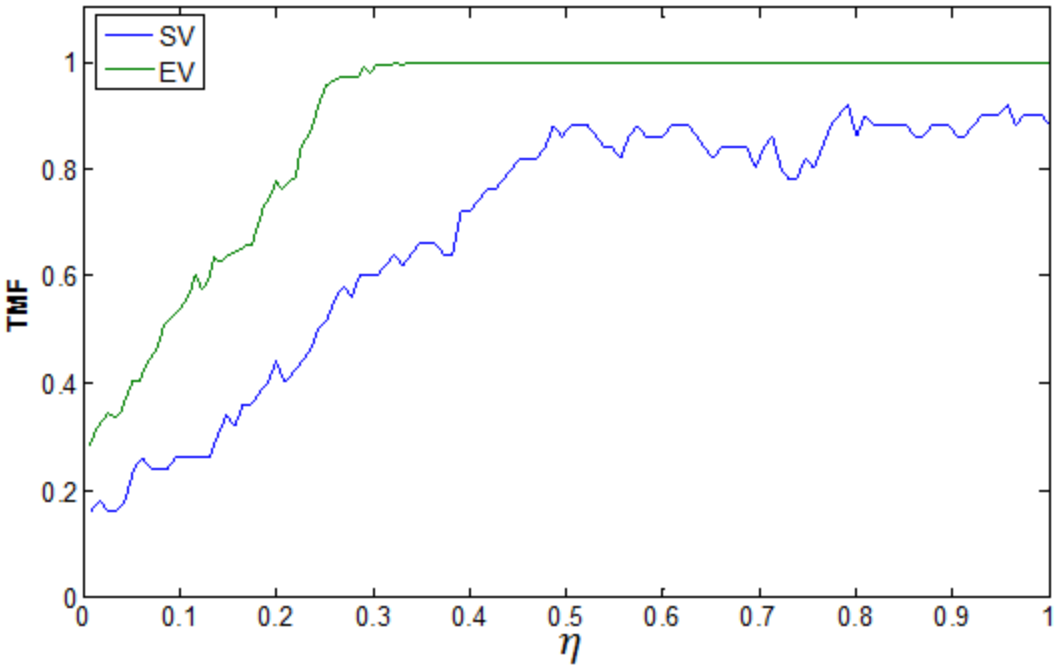

Figure 4.41. Side and end view True Mixed Fraction comparisons for wall (δ/d=7.5) injected J=1.2 jet at x/d=10.

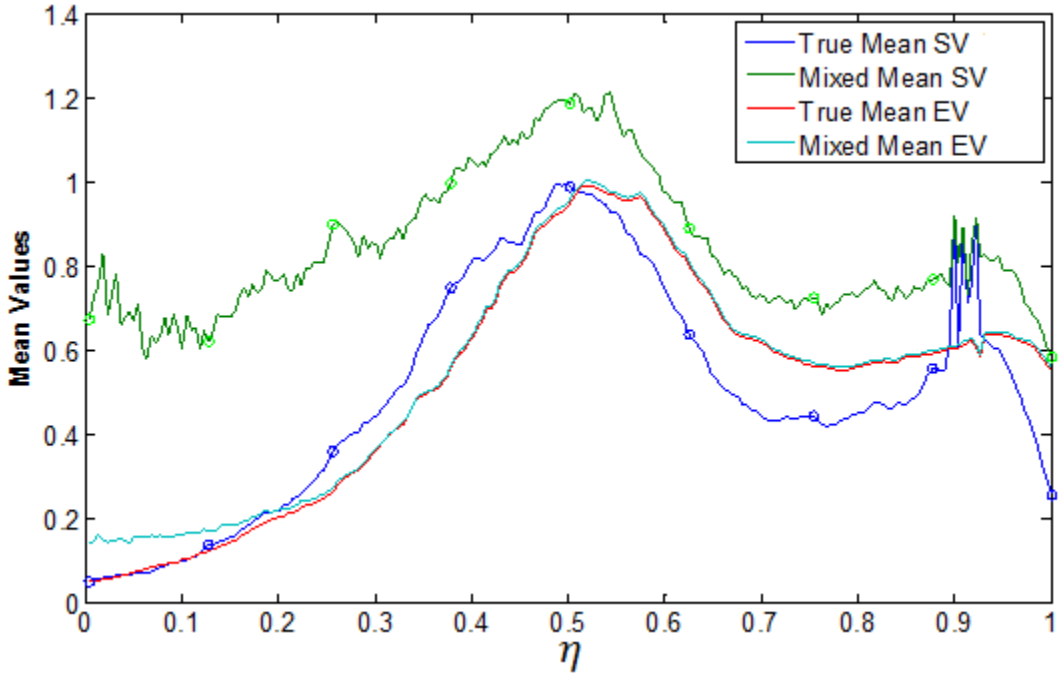

Figure 4.42. Side and end view mean comparisons for wall (δ/d=7.5) injected J=5.2 jet at x/d=20.

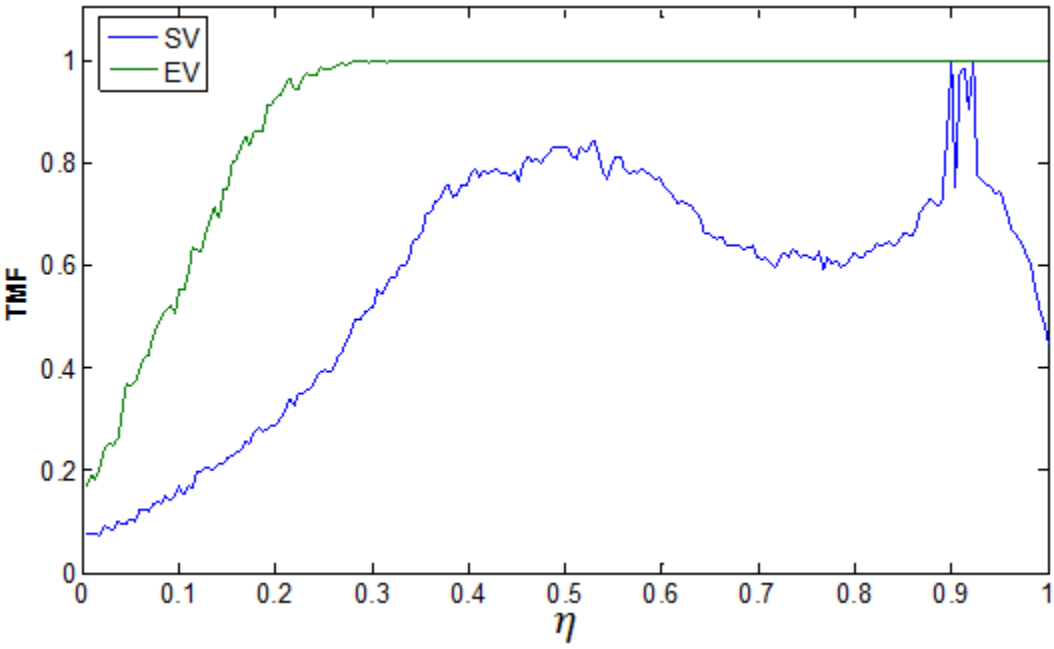

Figure 4.43. Side and end view True Mixed Fraction comparisons for wall (δ/d=7.5) injected J=5.2 jet at x/d=20.

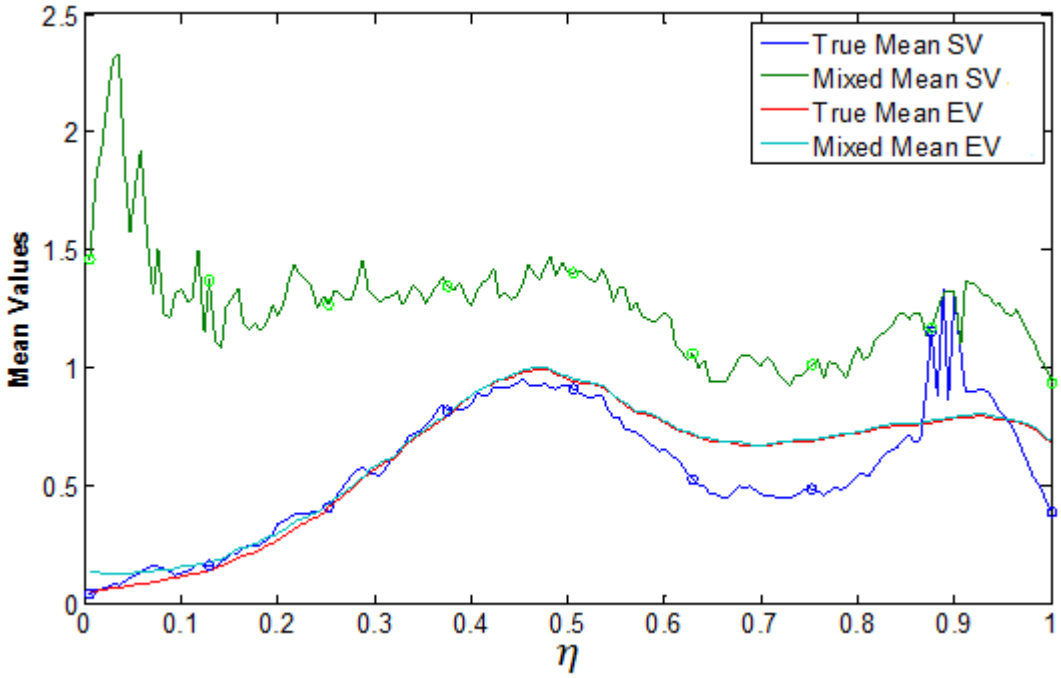

Figure 4.44. Side and end view mean comparisons for wall (δ/d=7.5) injected J=2.7 jet at x/d=20.

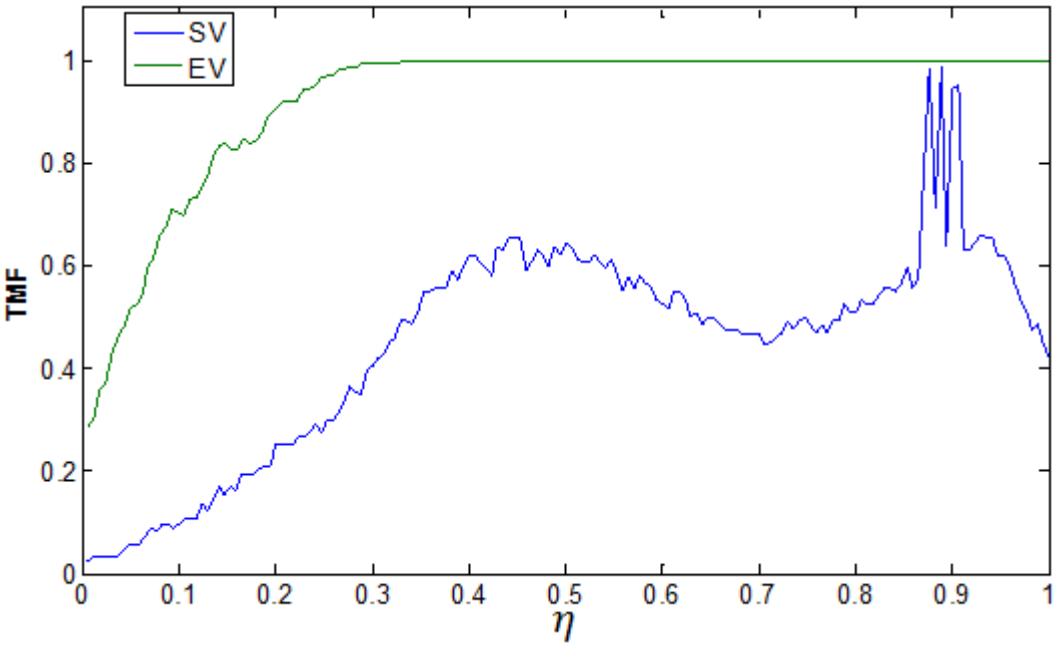

Figure 4.45. Side and end view True Mixed Fraction comparisons for wall (δ/d=7.5) injected J=2.7 jet at x/d=20.

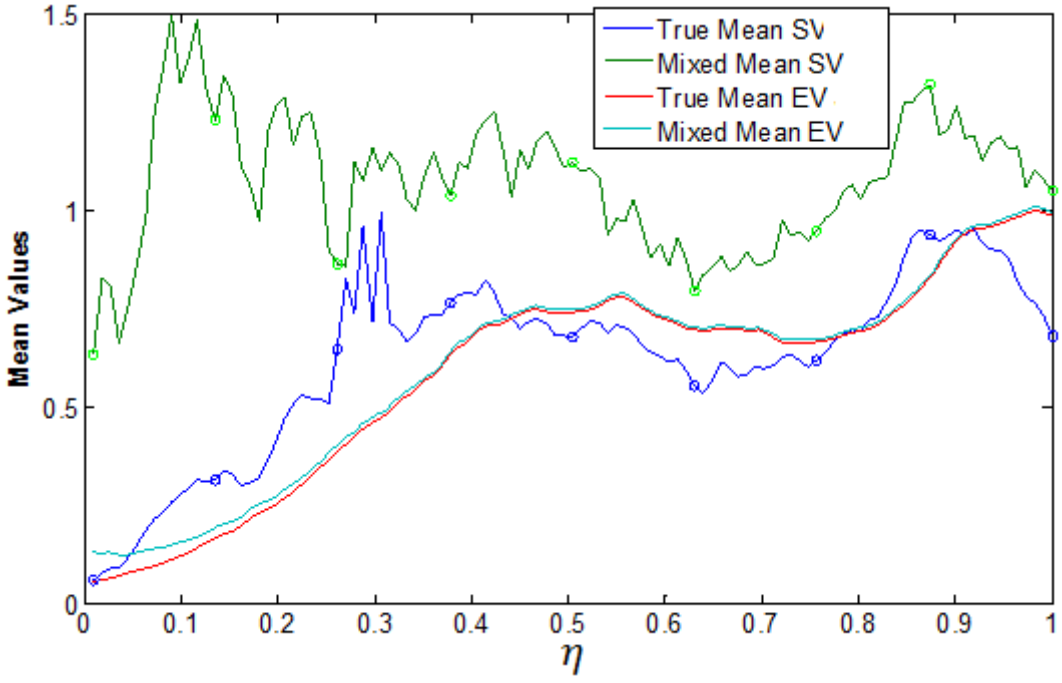

Figure 4.46. Side and end view mean comparisons for wall (δ/d=7.5) injected J=1.2 jet at x/d=20.

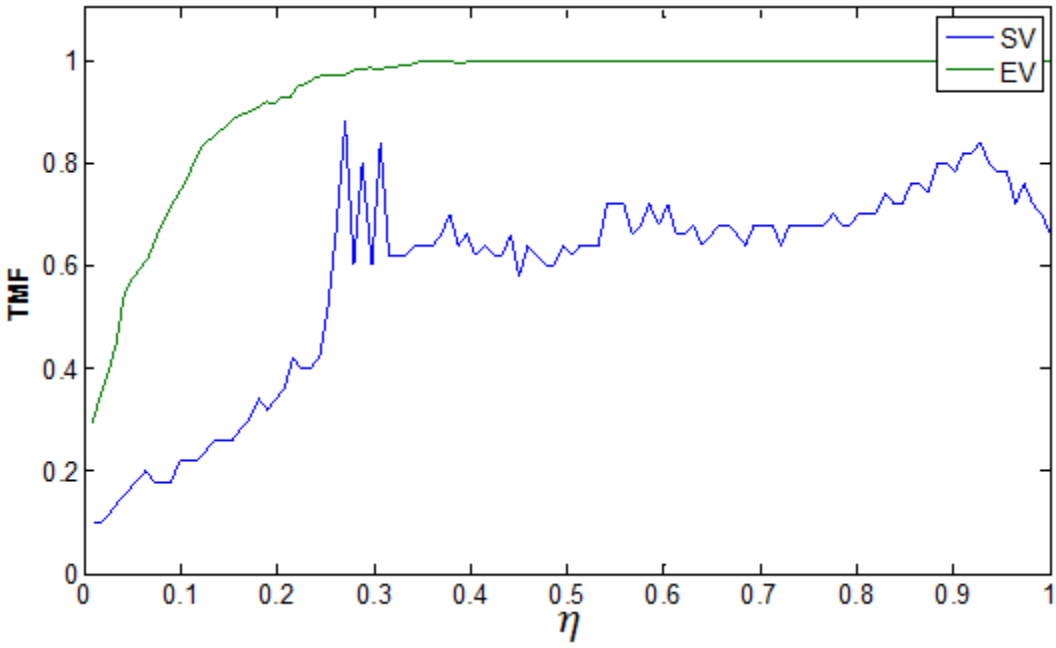

Figure 4.47. Side and end view True Mixed Fraction comparisons for wall (δ/d=7.5) injected J=1.2 jet at x/d=20.

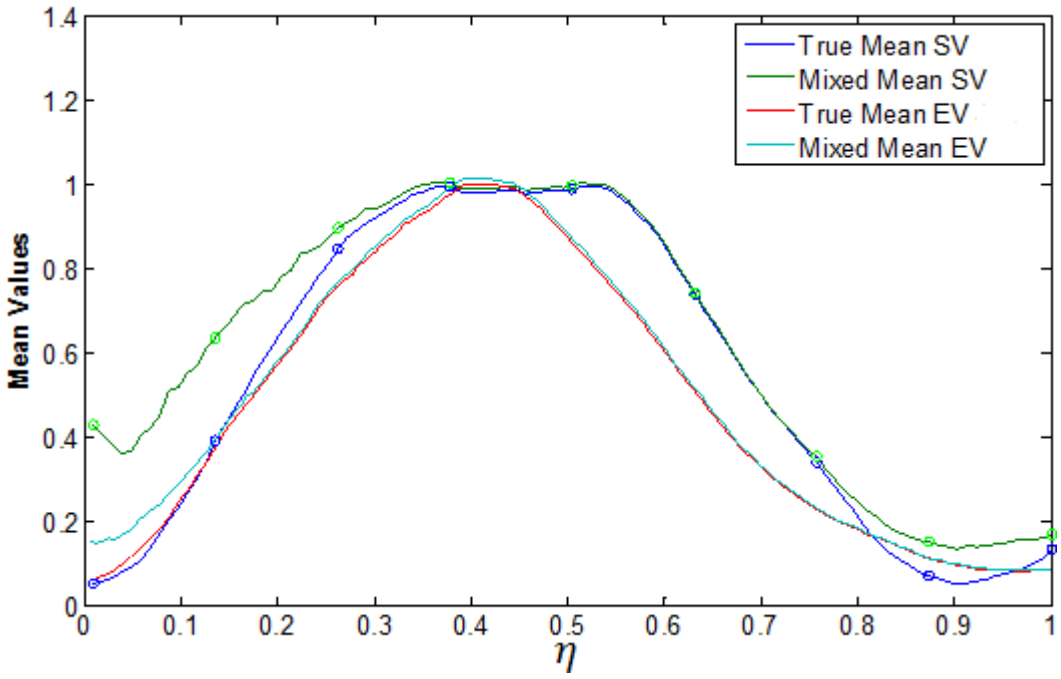

Figure 4.48. Side and end view mean comparisons for wedge (δ/d~0.7) injected J=5.2 jet at x/d=5

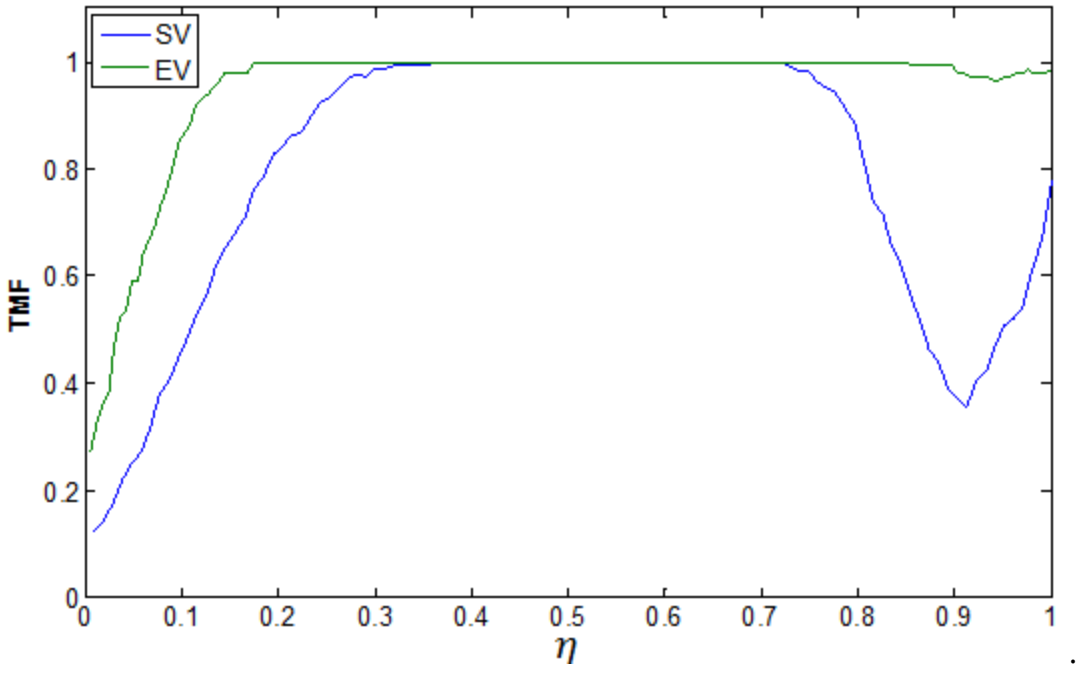

Figure 4.49. Side and end view True Mixed Fraction comparisons for wedge (δ/d~0.7) injected J=5.2 jet at x/d=5.

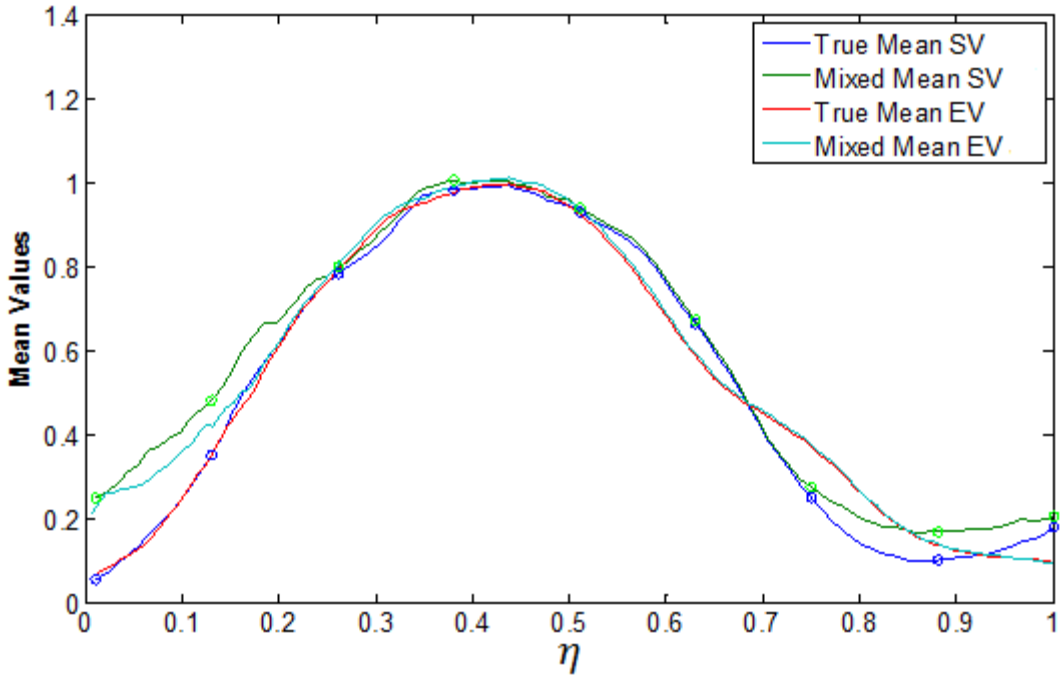

Figure 4.50. Side and end view mean comparisons for wedge (δ/d~0.7) injected J=2.7 jet at x/d=5

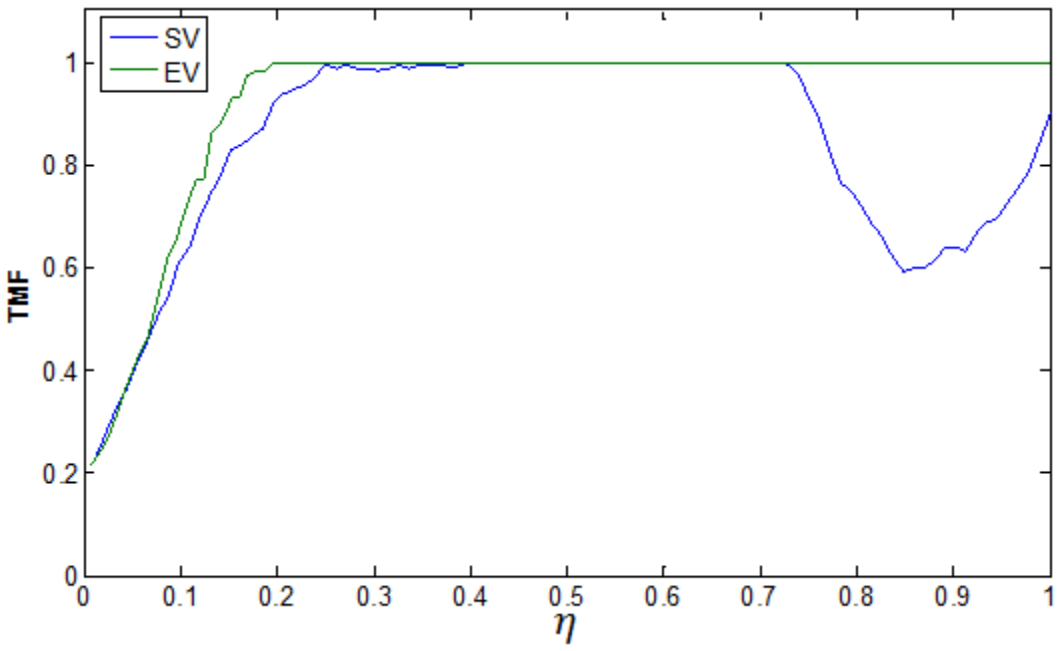

Figure 4.51. Side and end view True Mixed Fraction comparisons for wedge (δ/d~0.7) injected J=2.7 jet at x/d=5.

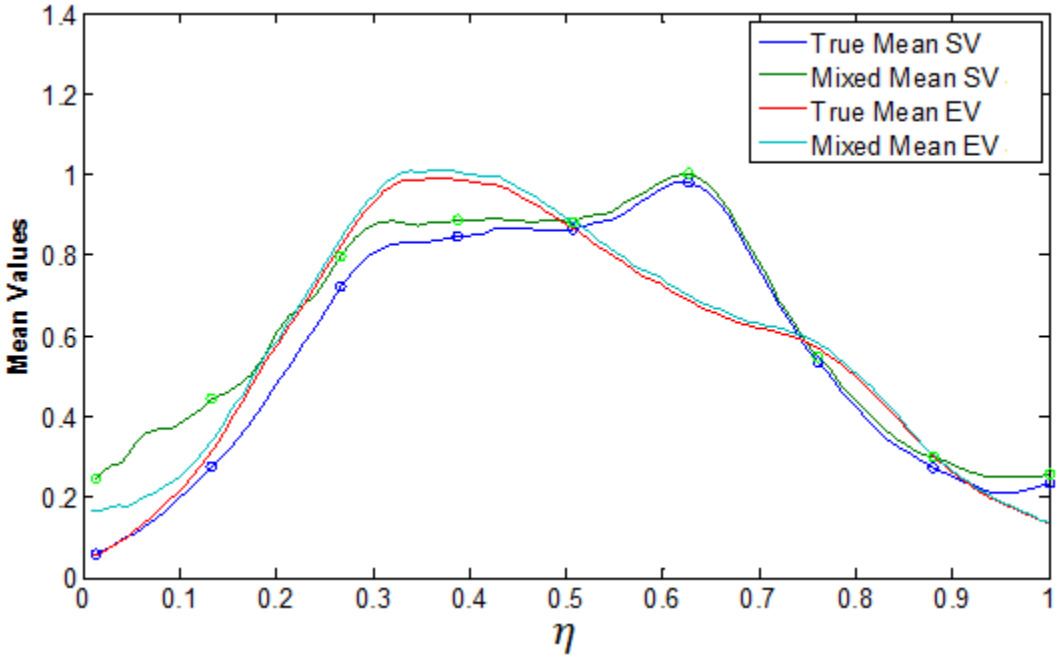

Figure 4.52. Side and end view mean comparisons for wedge (δ/d~0.7) injected J=1.2 jet at x/d=5

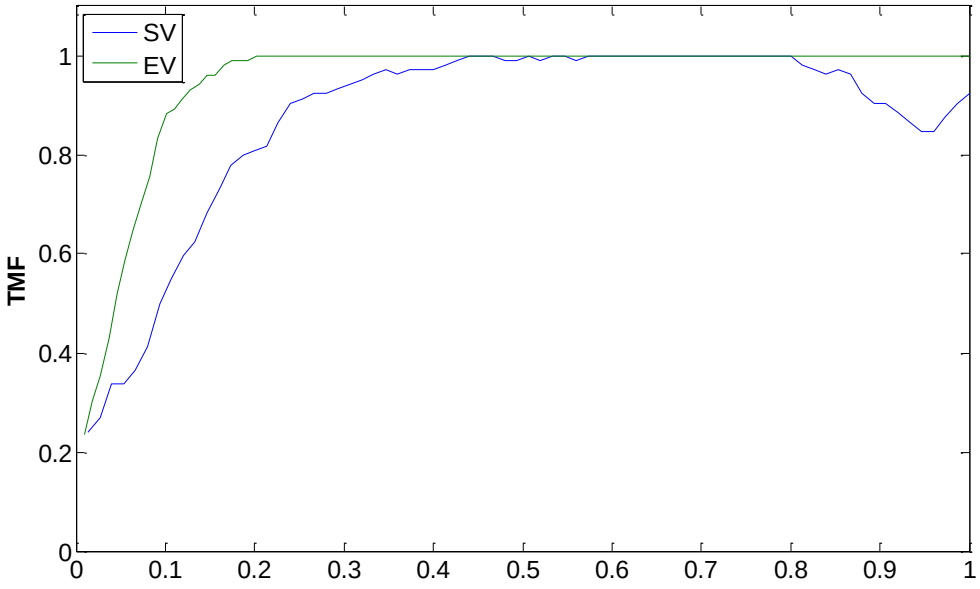

Figure 4.53. Side and end view True Mixed Fraction comparisons for wedge (δ/d~0.7) injected J=1.2 jet at x/d=5.

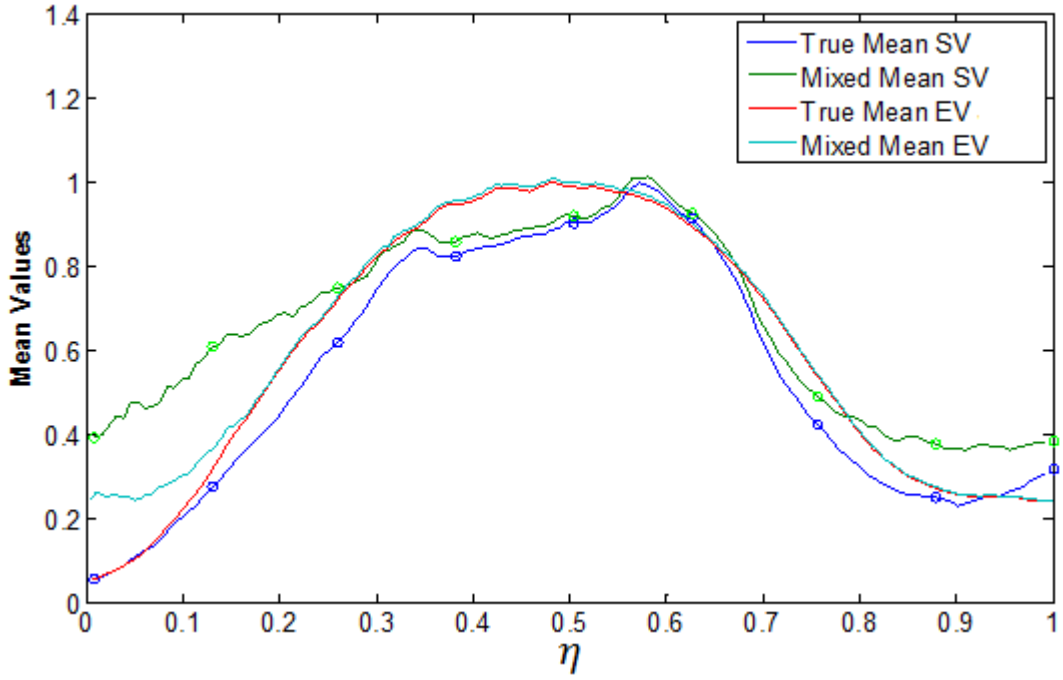

Figure 4.54. Side and end view mean comparisons for wedge (δ/d~0.7) injected J=5.2 jet at x/d=10

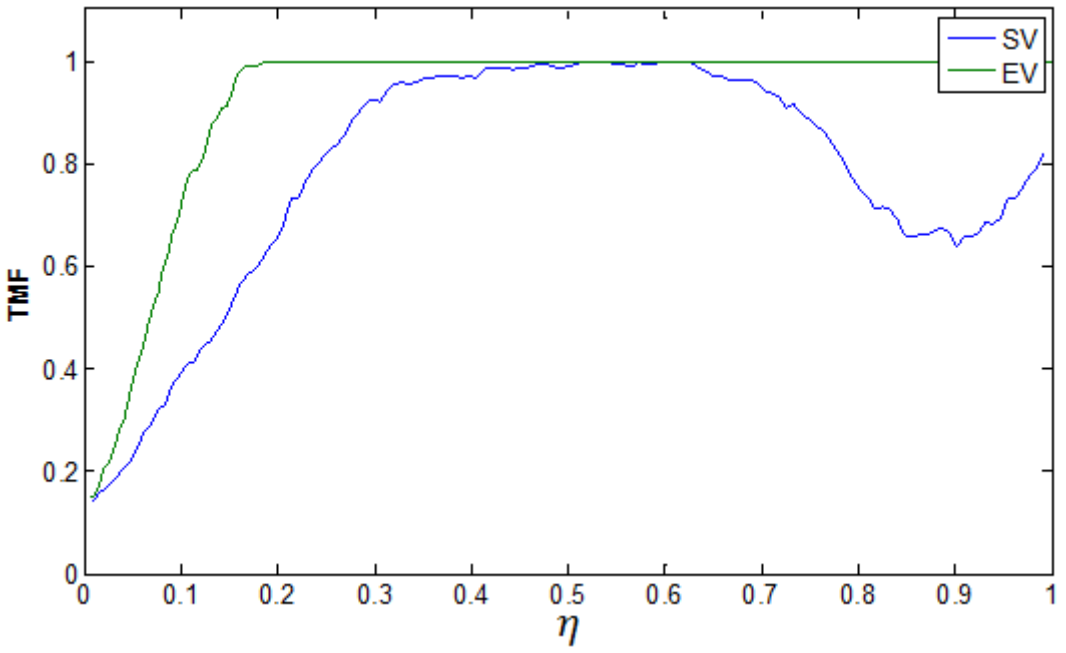

Figure 4.55. Side and end view True Mixed Fraction comparisons for wedge (δ/d~0.7) injected J=5.2 jet at x/d=10.

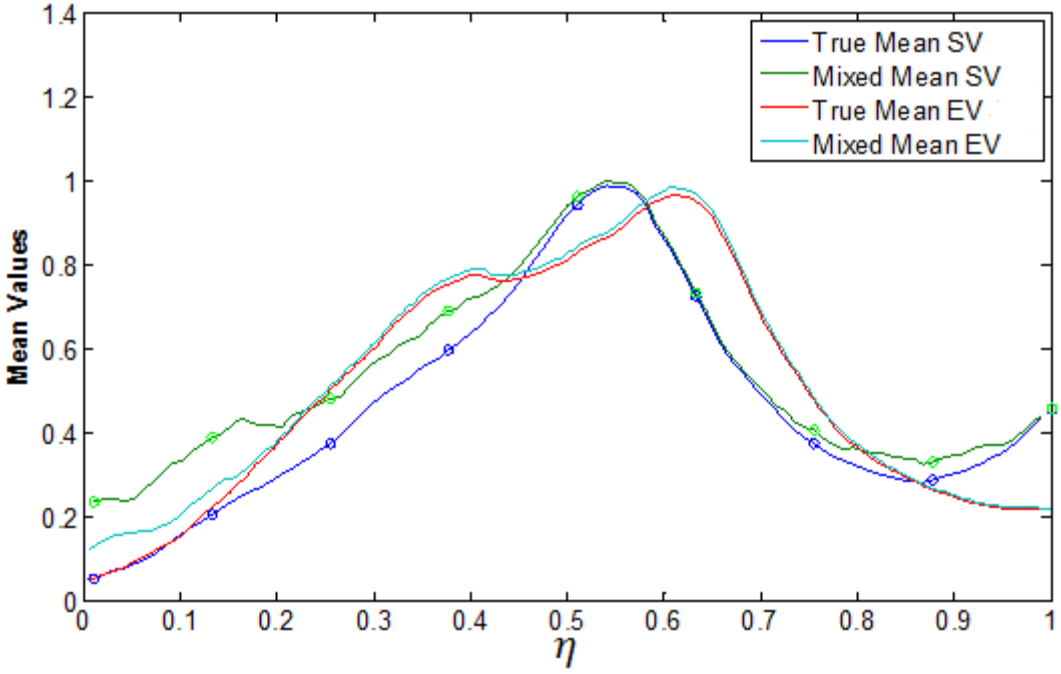

Figure 4.56. Side and end view mean comparisons for wedge (δ/d~0.7) injected J=2.7 jet at x/d=10

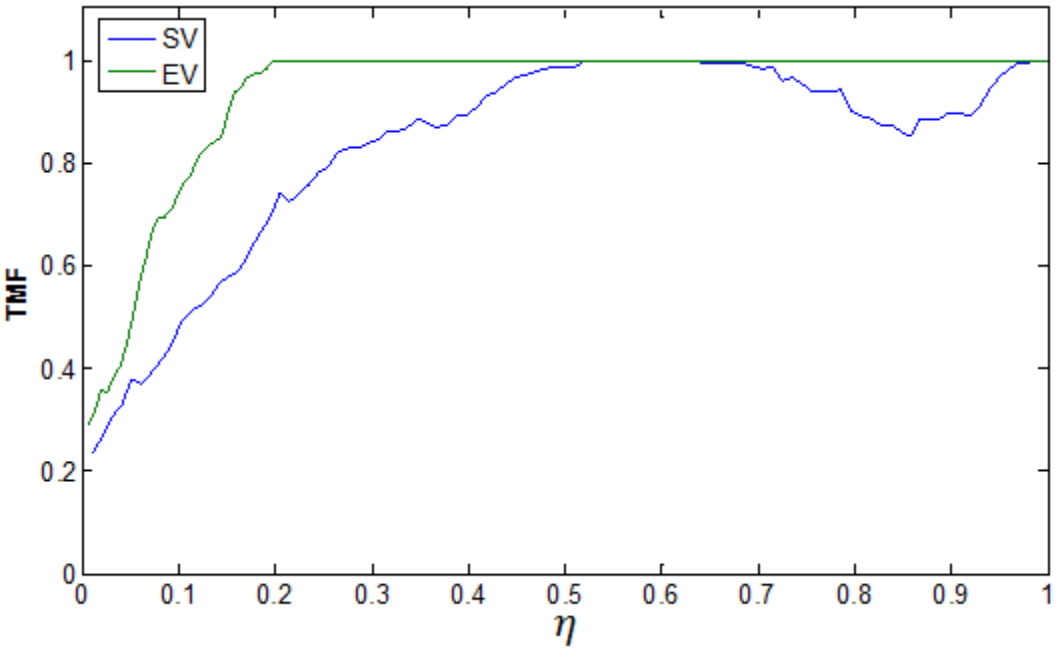

Figure 4.57. Side and end view True Mixed Fraction comparisons for wedge (δ/d~0.7) injected J=2.7 jet at x/d=10.

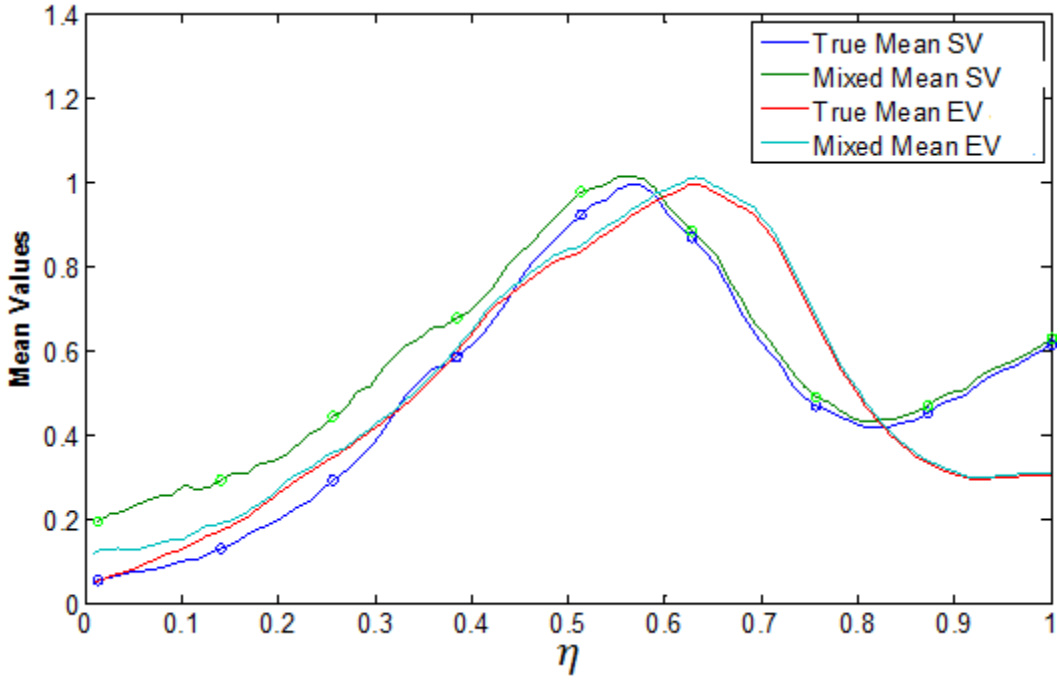

Figure 4.58. Side and end view mean comparisons for wedge (δ/d~0.7) injected J=1.2 jet at x/d=10

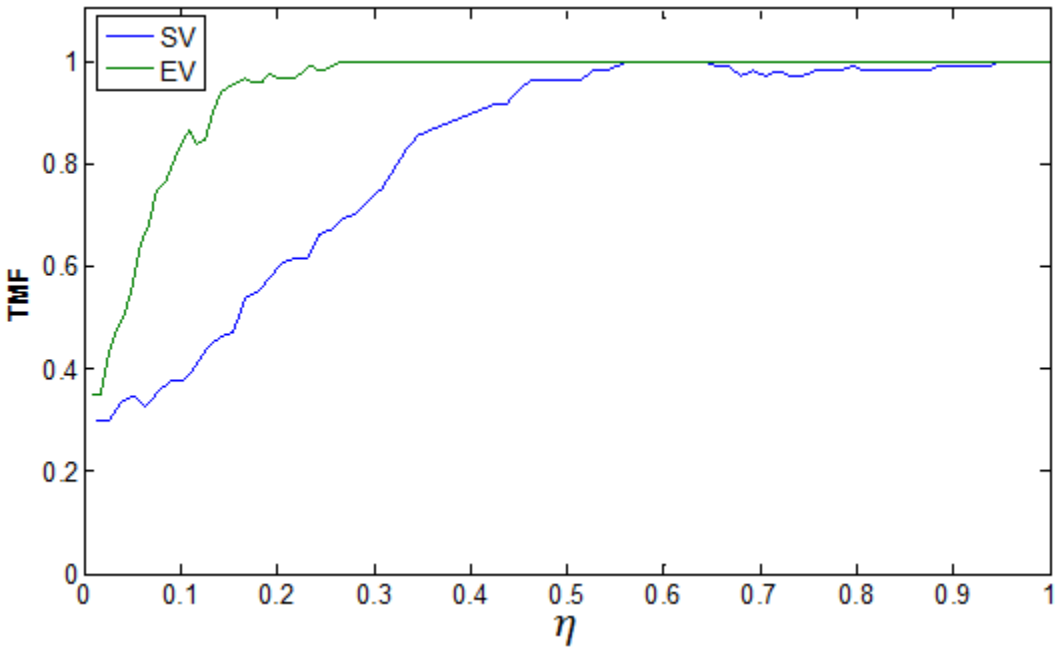

Figure 4.59. Side and end view True Mixed Fraction comparisons for wedge (δ/d~0.7) injected J=1.2 jet at x/d=10.

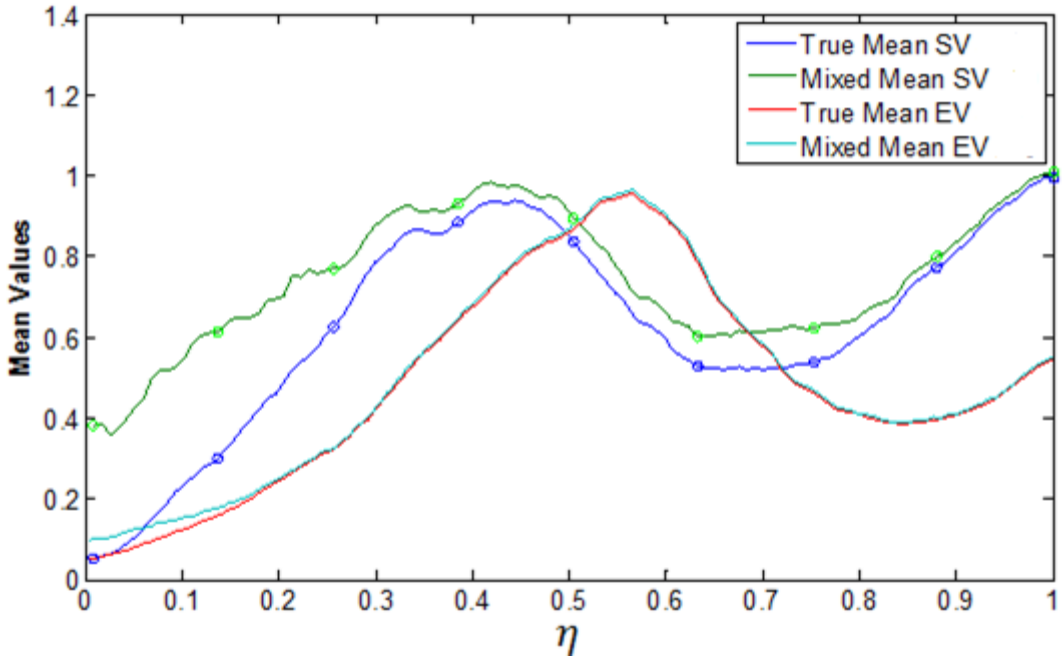

Figure 4.60. Side and end view mean comparisons for wedge (δ/d~0.7) injected J=5.2 jet at x/d=20

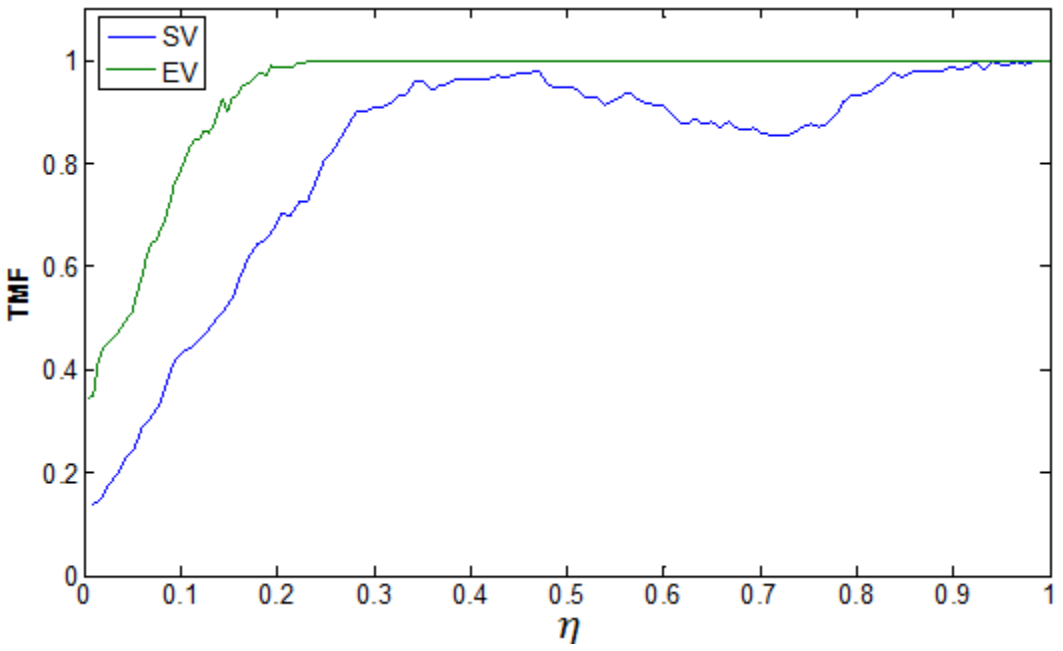

Figure 4.61. Side and end view True Mixed Fraction comparisons for wedge (δ/d~0.7) injected J=5.2 jet at x/d=20.

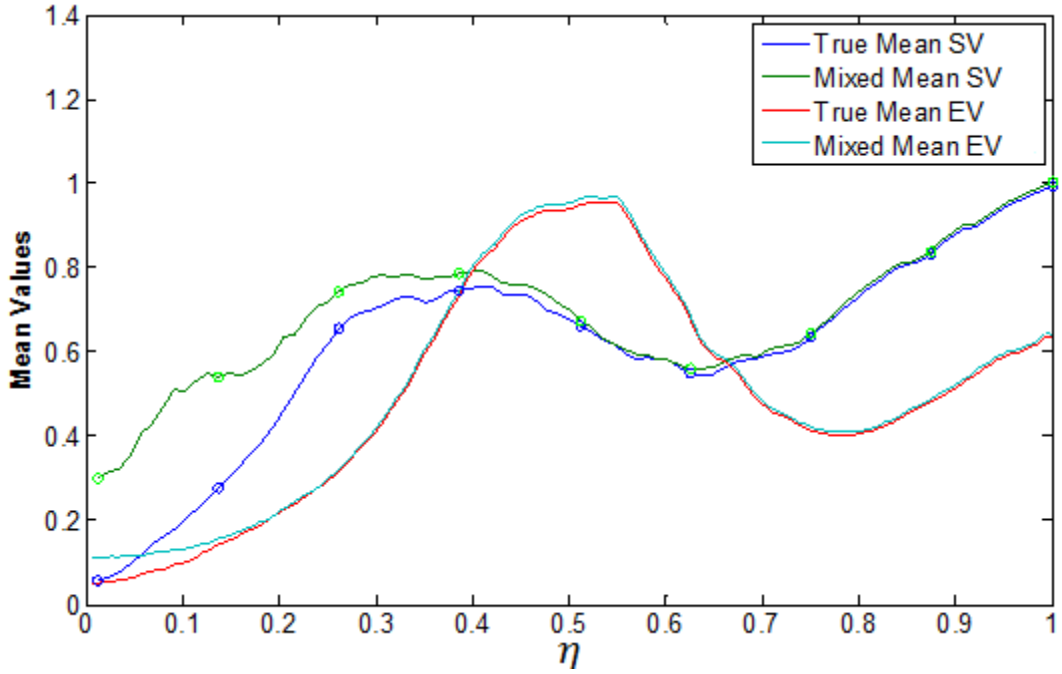

Figure 4.62. Side and end view mean comparisons for wedge (δ/d~0.7) injected J=2.7 jet at x/d=20

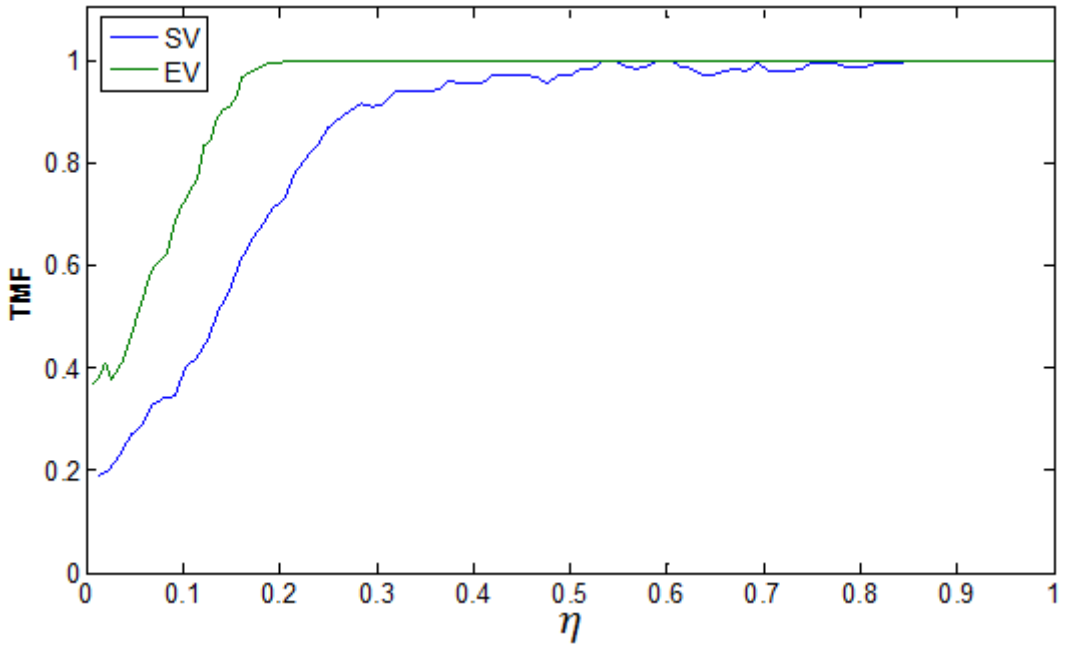

Figure 4.63. Side and end view True Mixed Fraction comparisons for wedge (δ/d~0.7) injected J=2.7 jet at x/d=20.

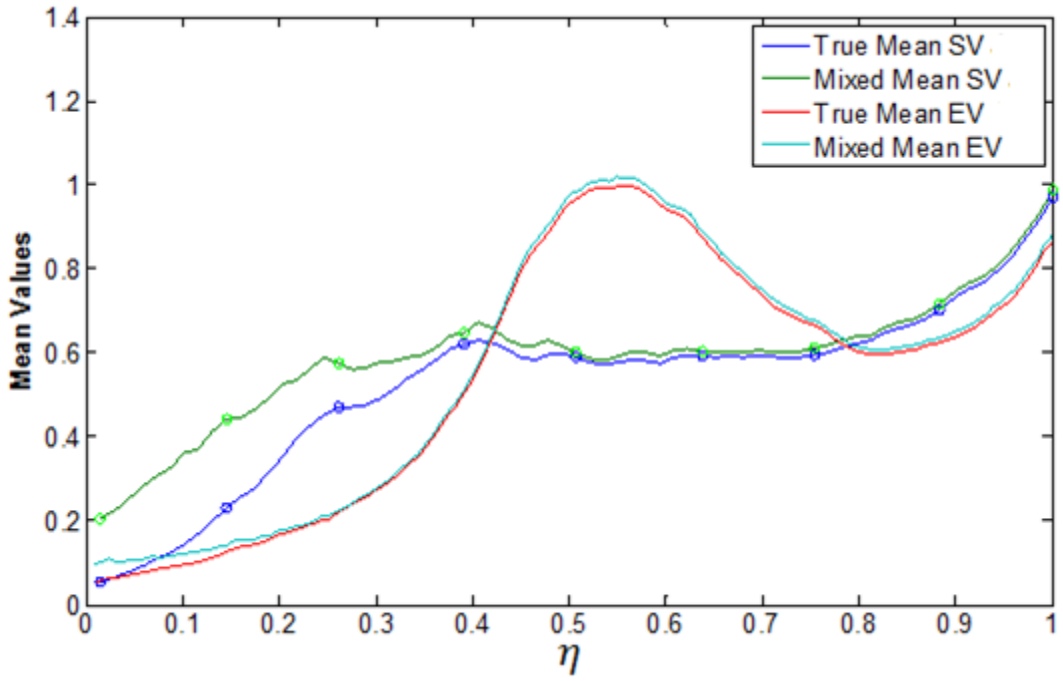

Figure 4.64. Side and end view mean comparisons for wedge (δ/d~0.7) injected J=1.2 jet at x/d=20

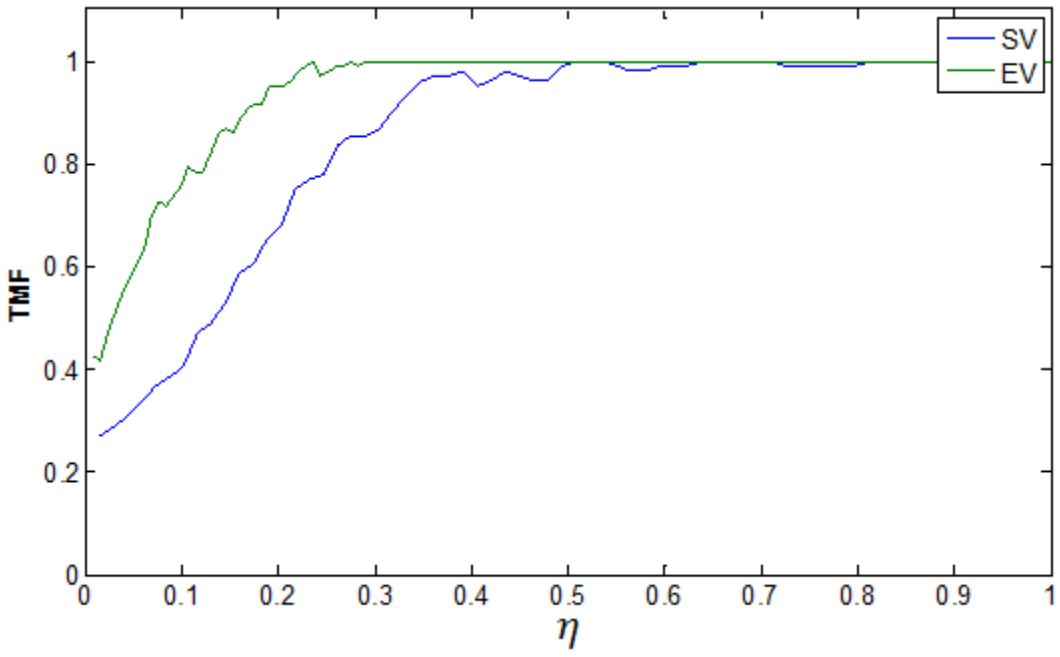

Figure 4.65. Side and end view True Mixed Fraction comparisons for wedge (δ/d~0.7) injected J=1.2 jet at x/d=20.

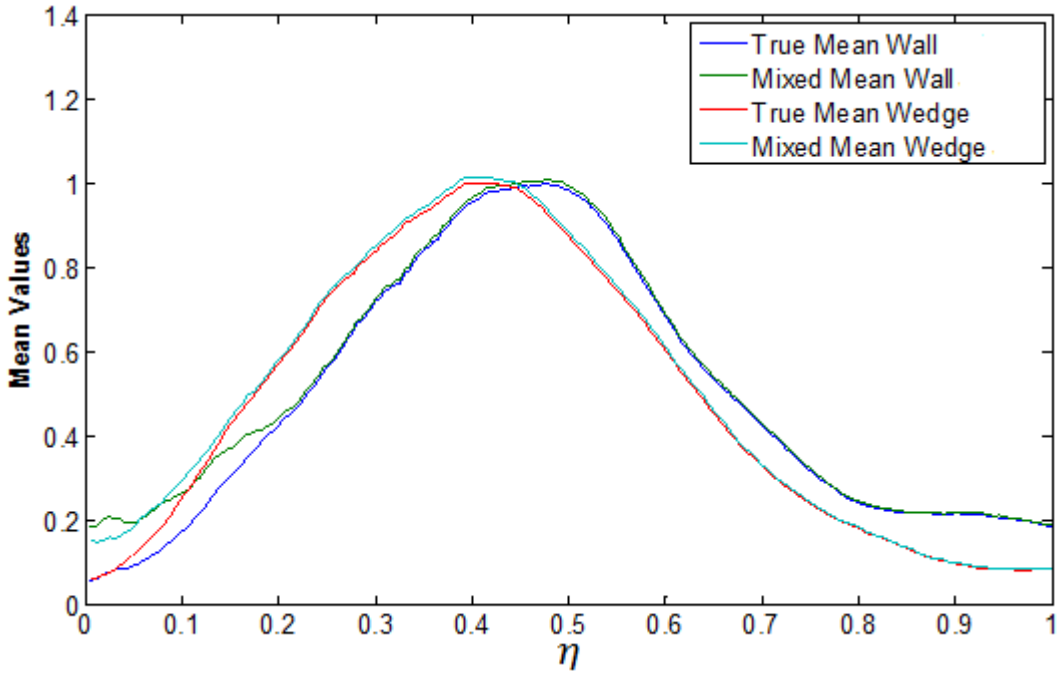

Figure 4.66. End view mean comparisons for wedge (δ/d~0.7) and wall (δ/d=7.5) injected J=5.2 jet at x/d=5

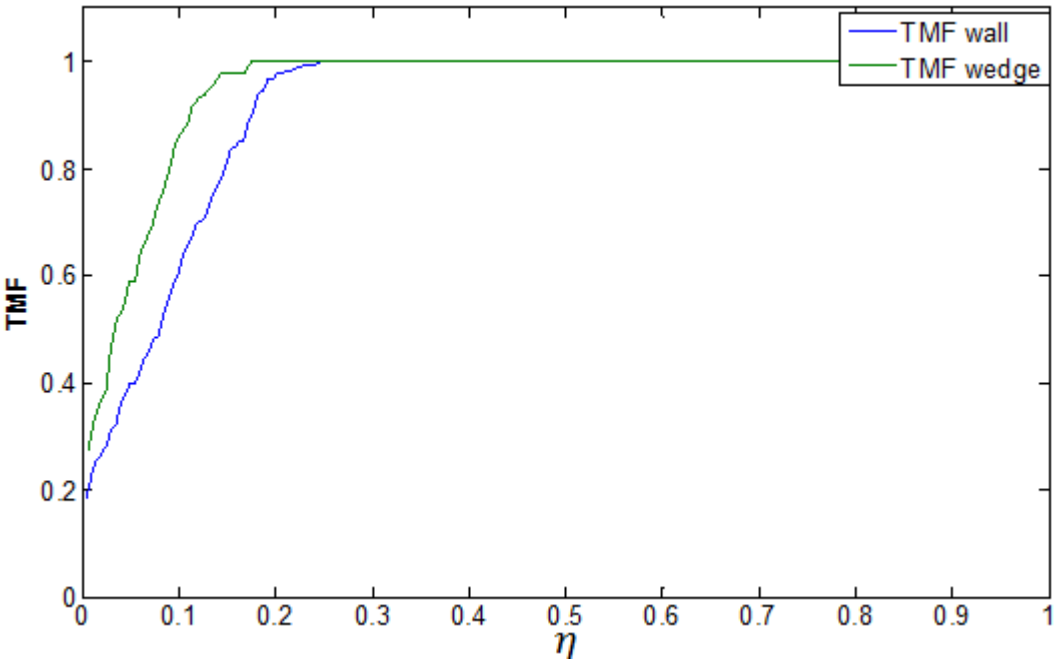

Figure 4.67. End view True Mixed Fraction comparison for wedge (δ/d~0.7) and wall (δ/d=7.5) injected J=5.2 jet at x/d=5

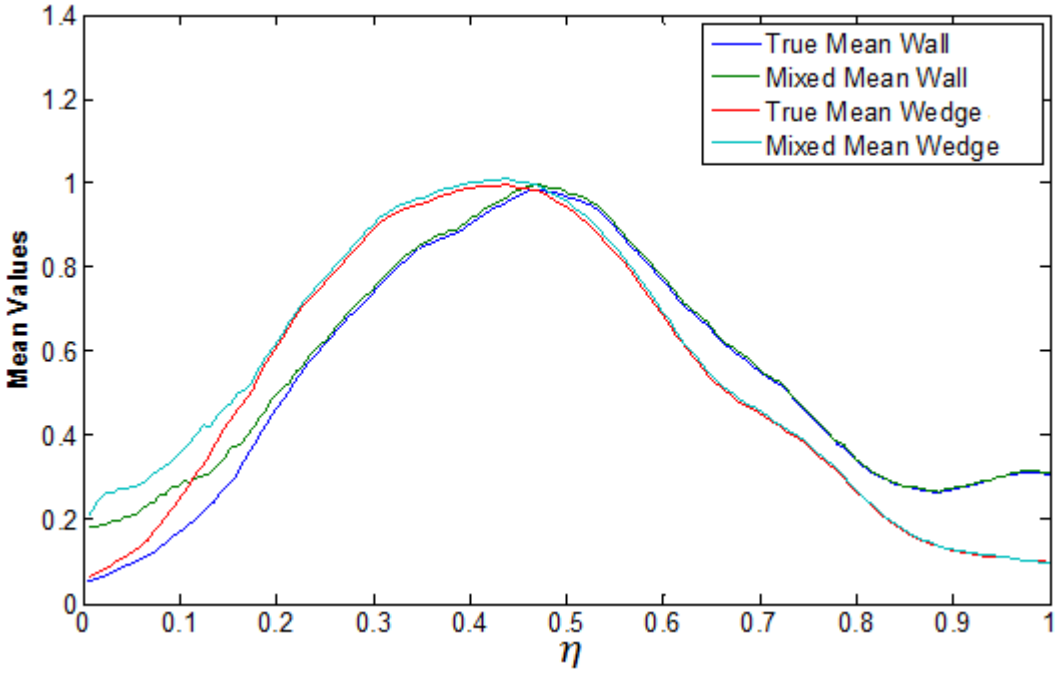

Figure 4.68. End view mean comparisons for wedge (δ/d~0.7) and wall (δ/d=7.5) injected J=2.7 jet at x/d=5

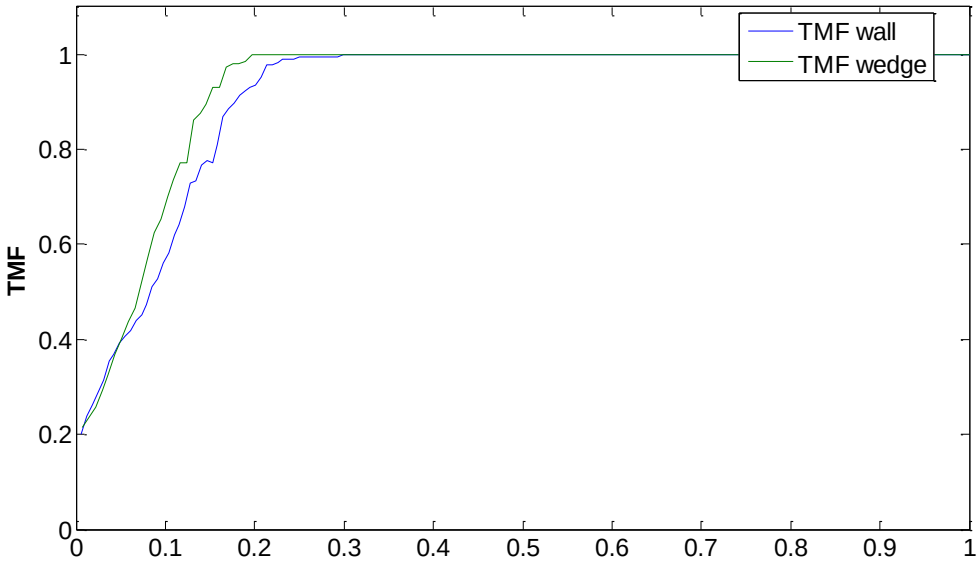

Figure 4.69. End view True Mixed Fraction comparison for wedge (δ/d~0.7) and wall (δ/d=7.5) injected J=2.7 jet at x/d=5

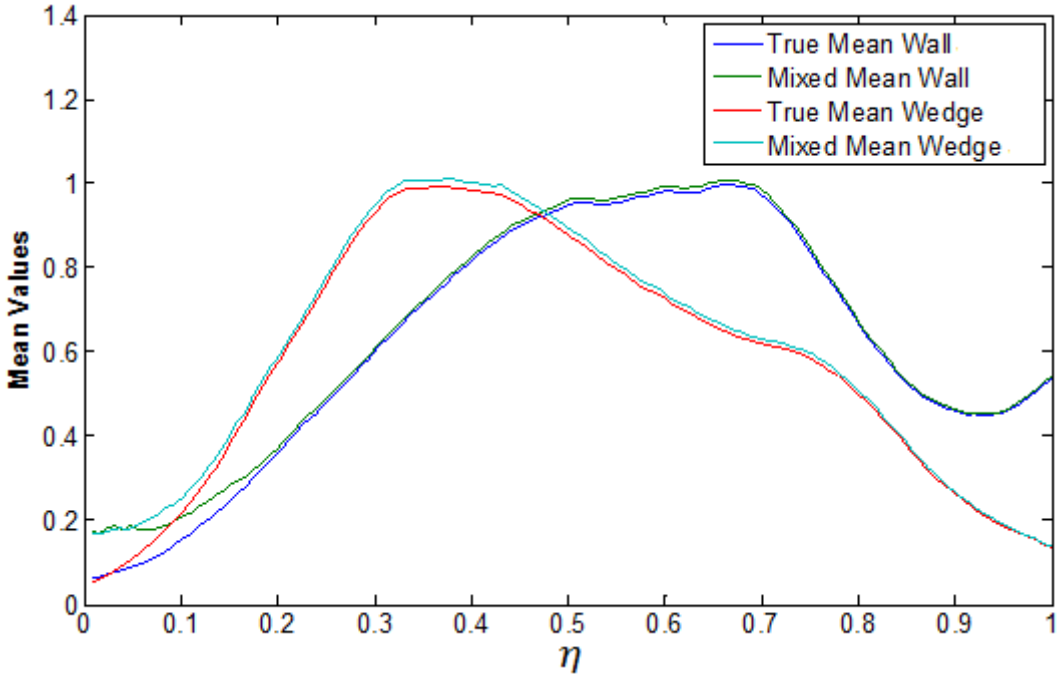

Figure 4.70. End view mean comparisons for wedge (δ/d~0.7) and wall (δ/d=7.5) injected J=1.2 jet at x/d=5

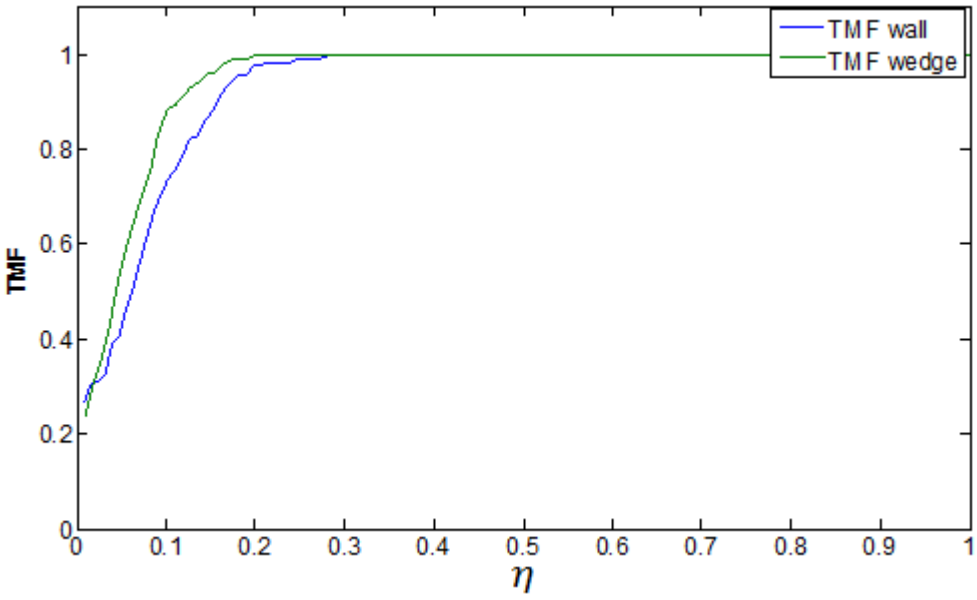

Figure 4.71. End view True Mixed Fraction comparison for wedge (δ/d~0.7) and wall (δ/d=7.5) injected J=1.2 jet at x/d=5

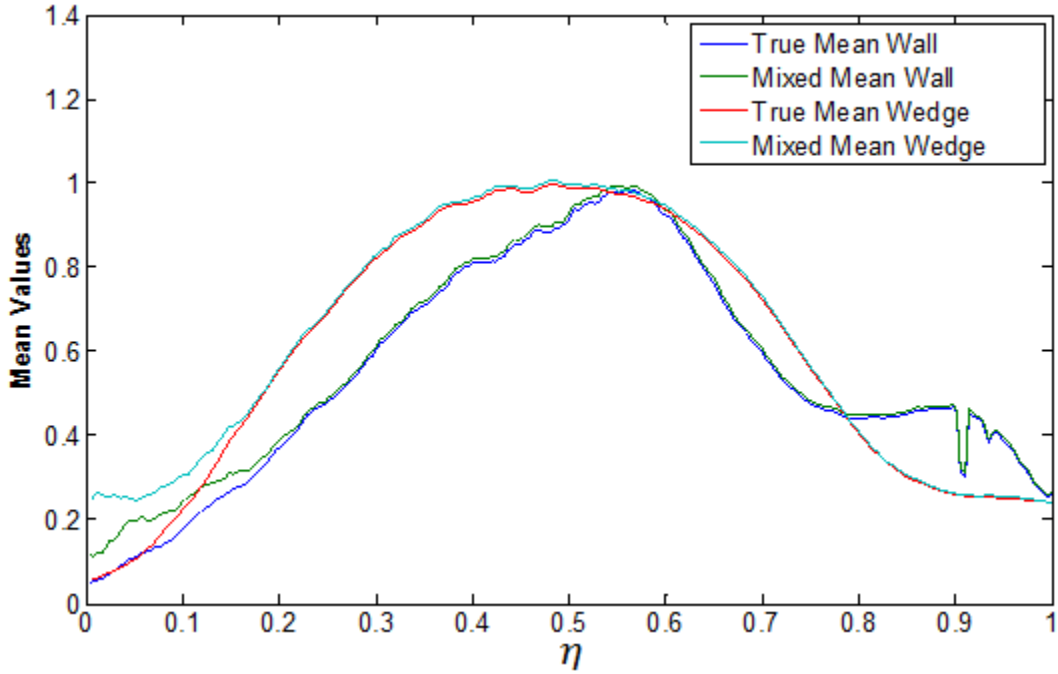

Figure 4.72. End view mean comparisons for wedge (δ/d~0.7) and wall (δ/d=7.5) injected J=5.2 jet at x/d=10

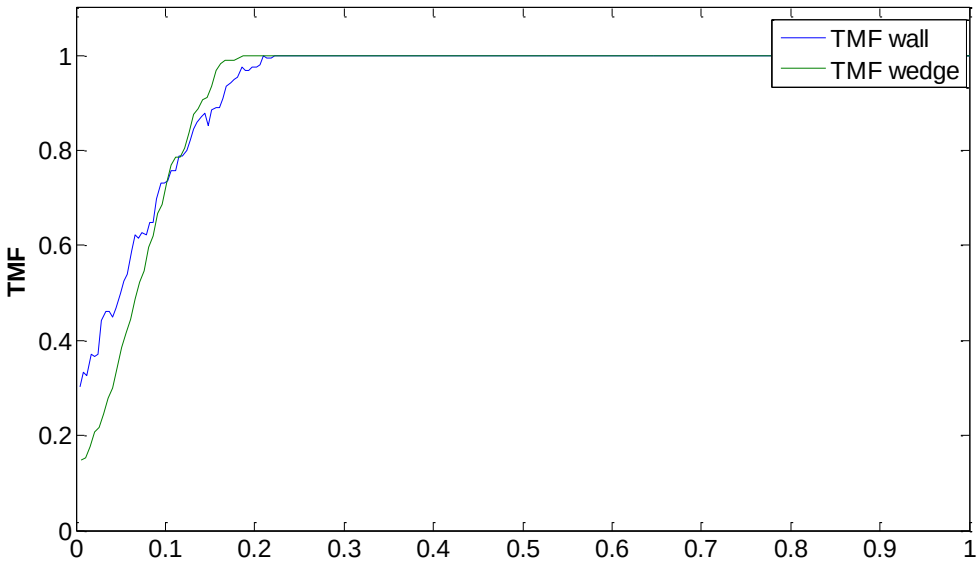

Figure 4.73. End view True Mixed Fraction comparison for wedge (δ/d~0.7) and wall (δ/d=7.5) injected J=5.2 jet at x/d=10

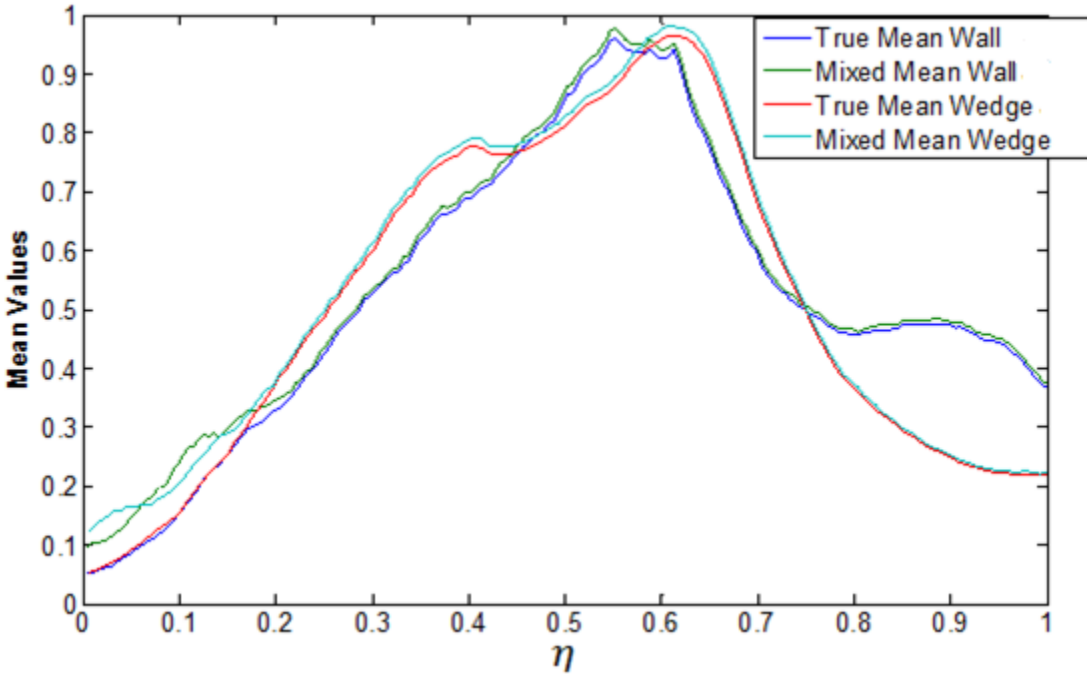

Figure 4.74. End view mean comparisons for wedge (δ/d~0.7) and wall (δ/d=7.5) injected J=2.7 jet at x/d=10

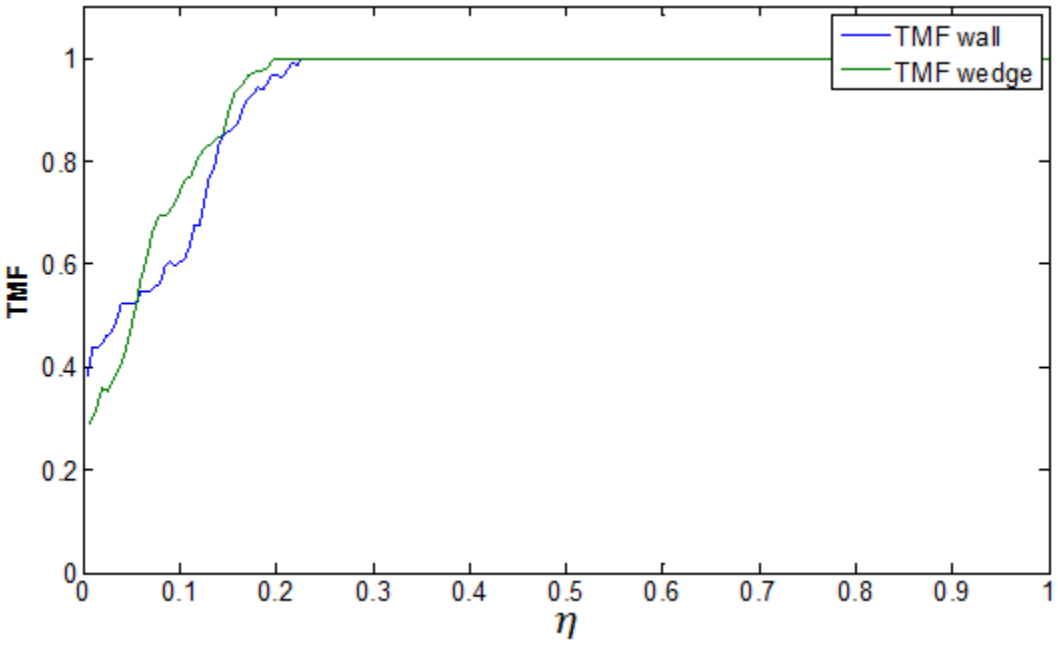

Figure 4.75. End view True Mixed Fraction comparison for wedge (δ/d~0.7) and wall (δ/d=7.5) injected J=2.7 jet at x/d=10

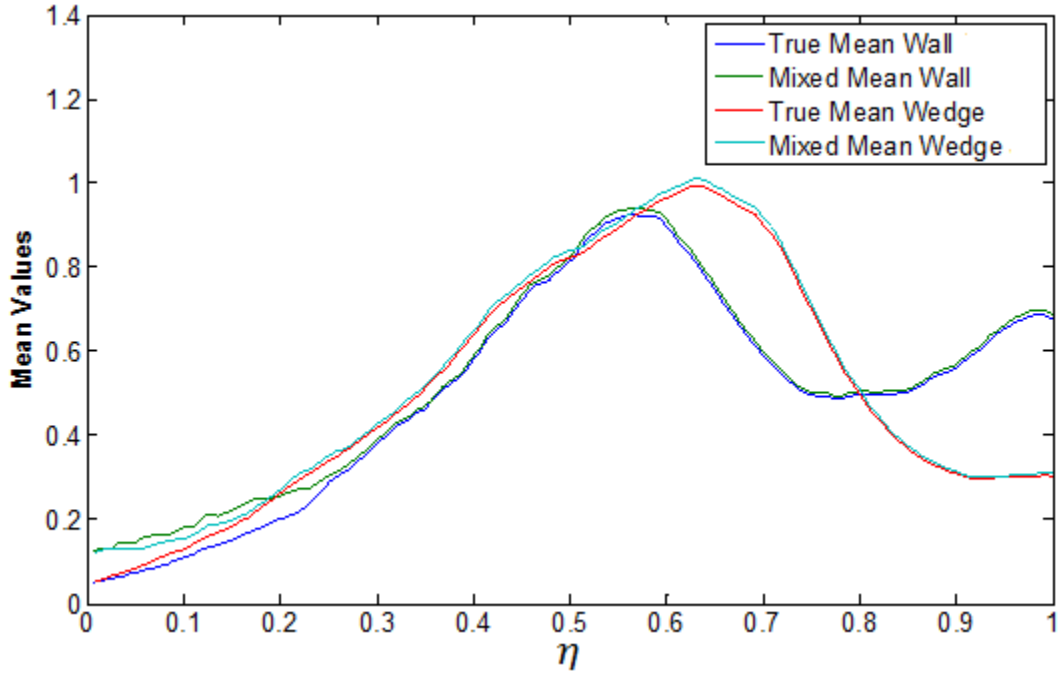

Figure 4.76. End view mean comparisons for wedge (δ/d~0.7) and wall (δ/d=7.5) injected J=1.2 jet at x/d=10

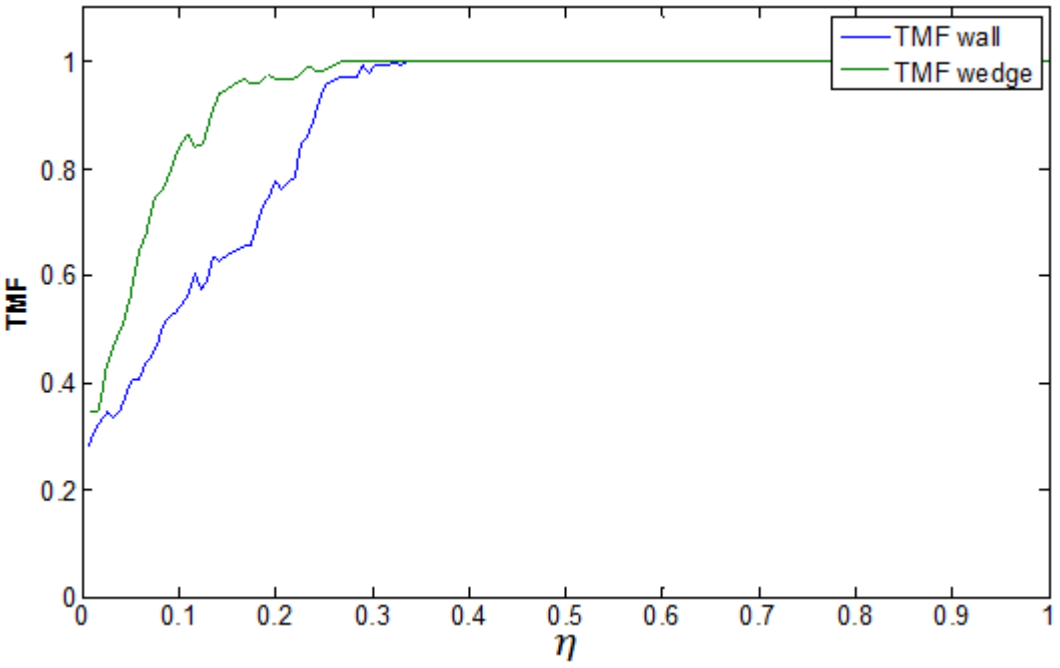

Figure 4.77. End view True Mixed Fraction comparison for wedge (δ/d~0.7) and wall (δ/d=7.5) injected J=1.2 jet at x/d=10

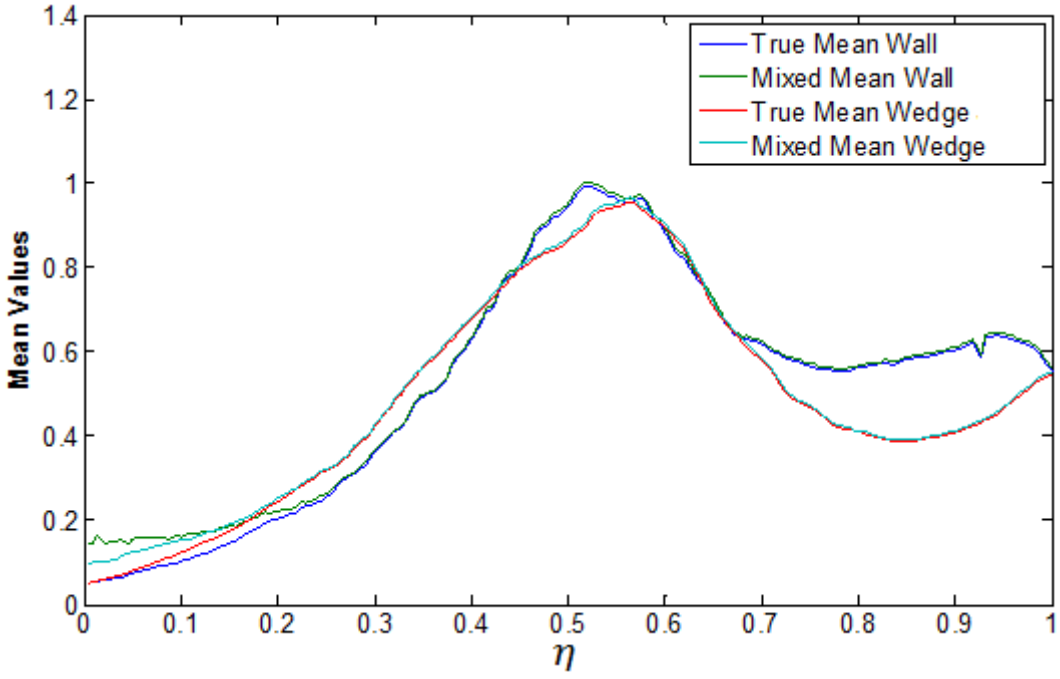

Figure 4.78. End view mean comparisons for wedge (δ/d~0.7) and wall (δ/d=7.5) injected J=5.2 jet at x/d=20

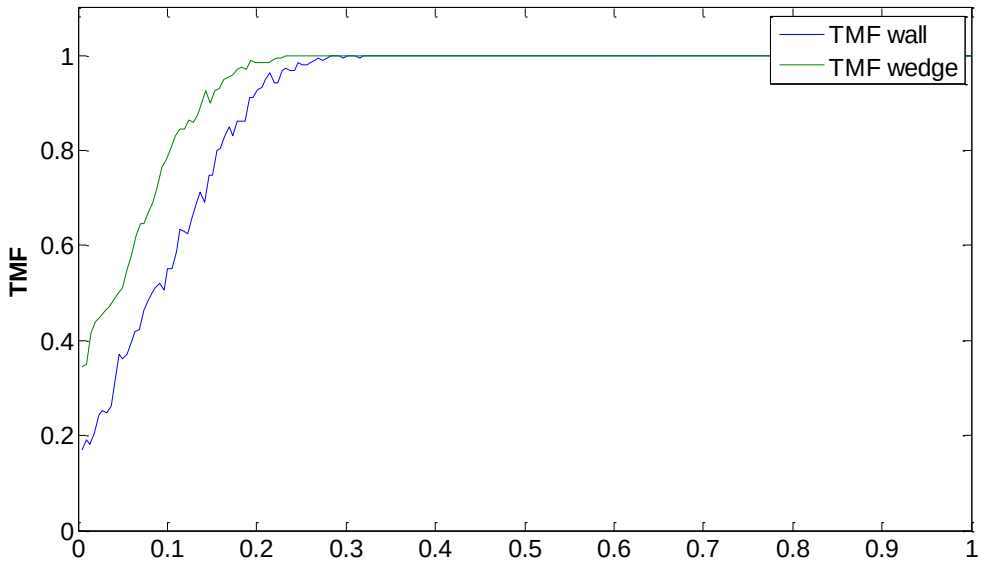

Figure 4.79. End view True Mixed Fraction comparison for wedge (δ/d~0.7) and wall (δ/d=7.5) injected J=5.2 jet at x/d=20

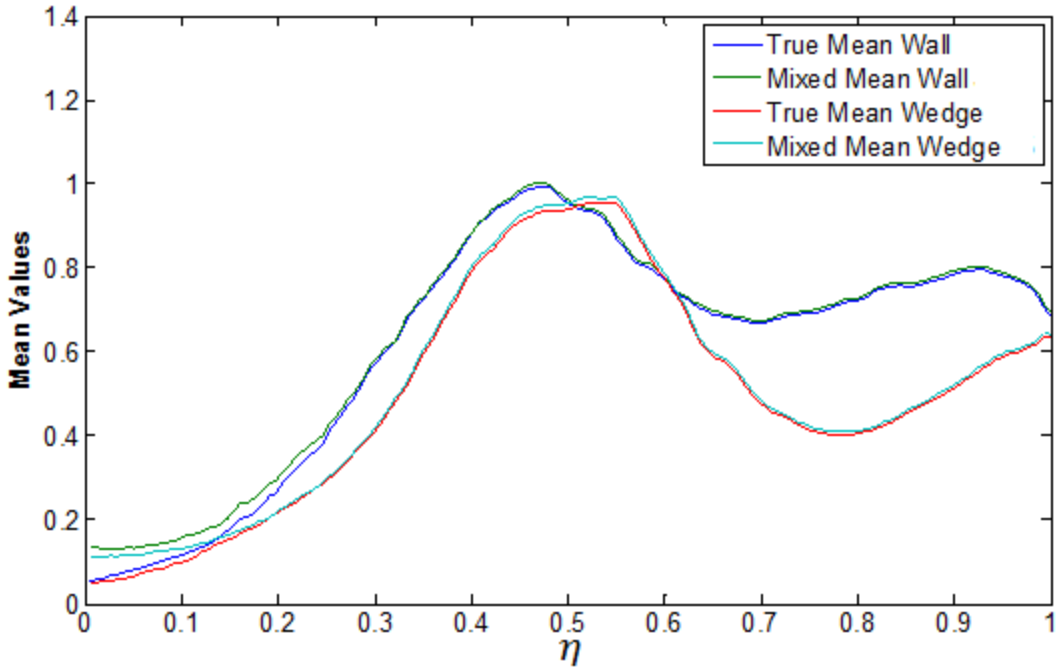

Figure 4.80. End view mean comparisons for wedge (δ/d~0.7) and wall (δ/d=7.5) injected J=2.7 jet at x/d=20

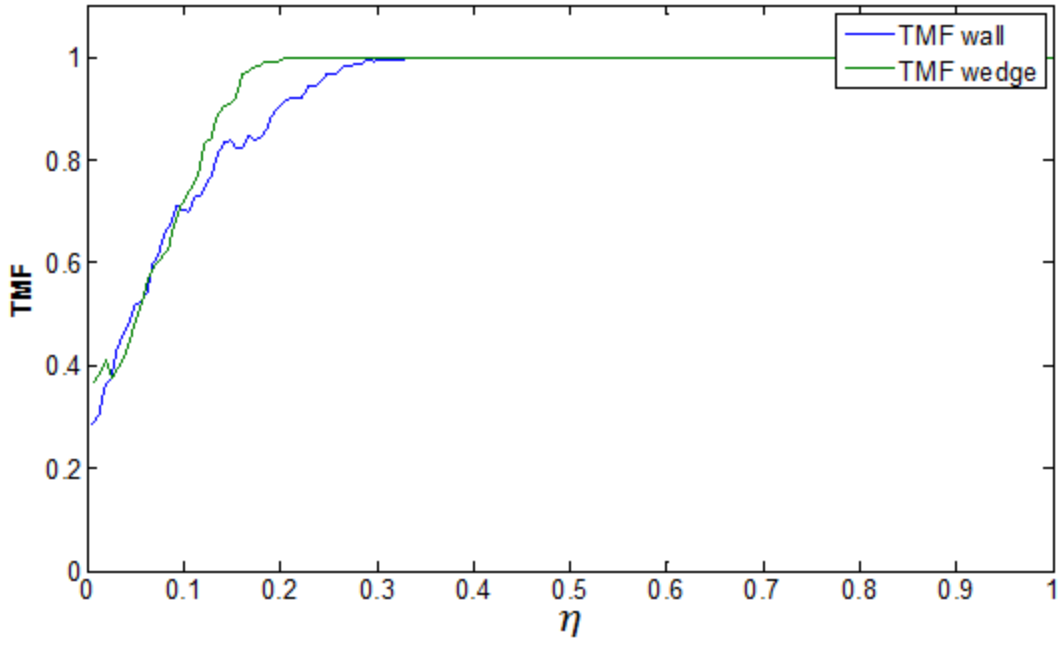

Figure 4.81. End view True Mixed Fraction comparison for wedge (δ/d~0.7) and wall (δ/d=7.5) injected J=2.7 jet at x/d=20

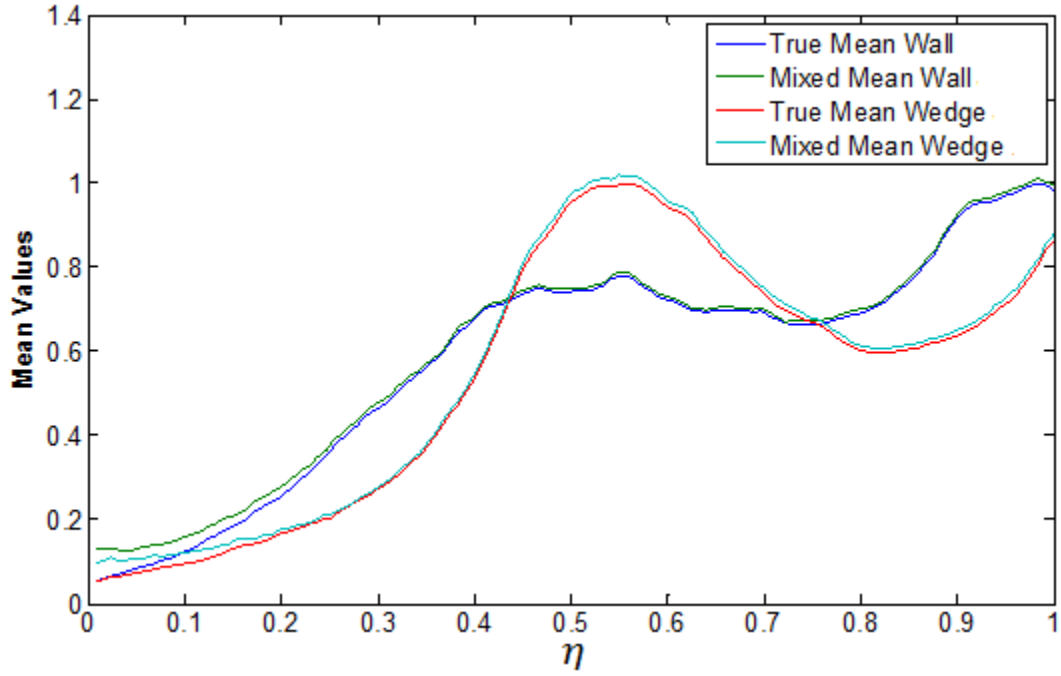

Figure 4.82. End view mean comparisons for wedge (δ/d~0.7) and wall (δ/d=7.5) injected J=1.2 jet at x/d=20

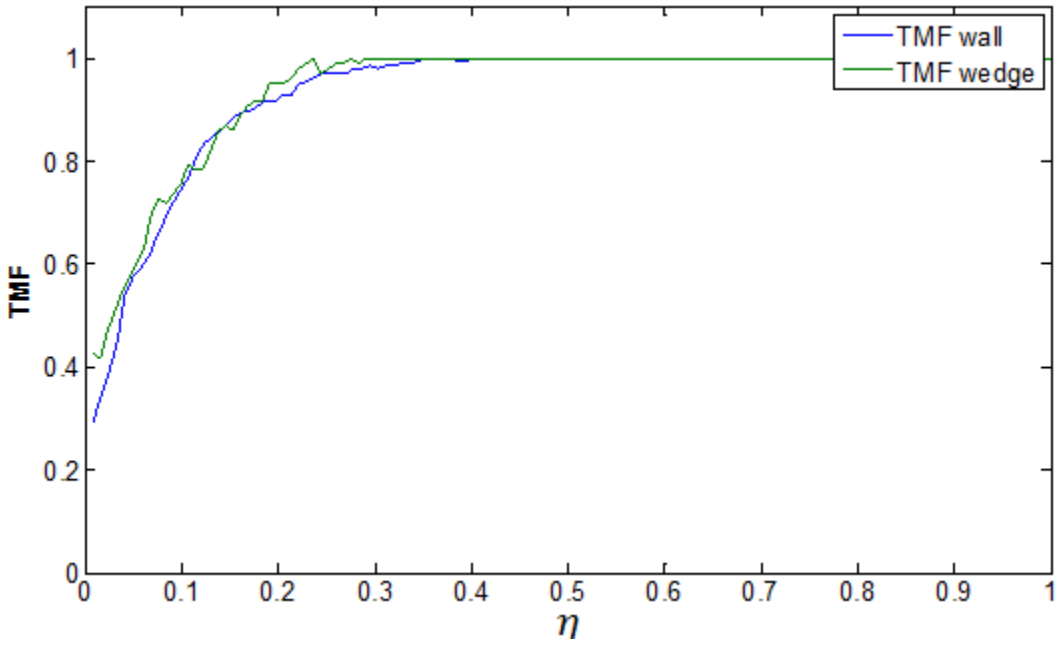

Figure 4.83. End view True Mixed Fraction comparison for wedge (δ/d~0.7) and wall (δ/d=7.5) injected J=1.2 jet at x/d=20

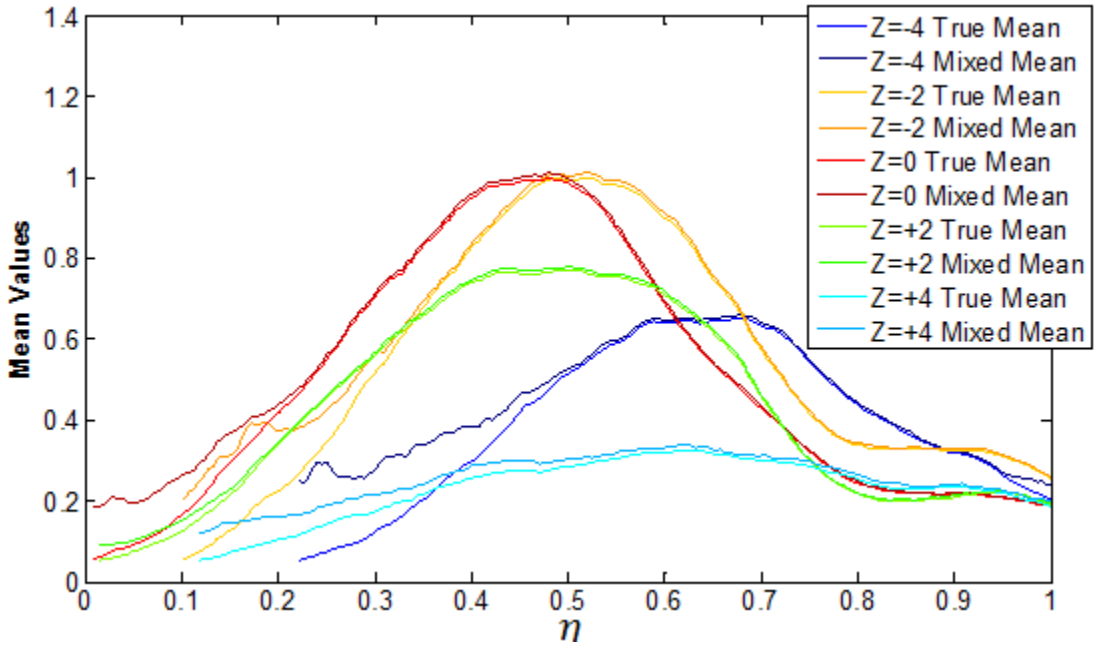

Figure 4.84. x/d=5 end view mean comparisons for wall (δ/d=7.5) injected J=5.2 jet at z/d = -4, -2, 0, +2, +4

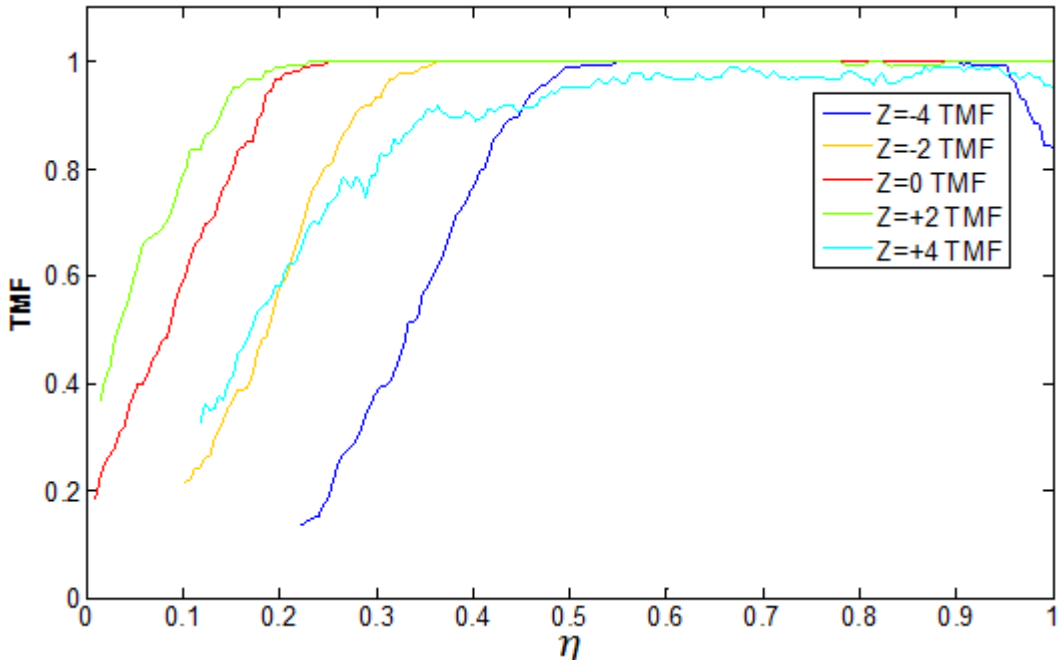

Figure 4.85. x/d=5 end view True Mixed Fraction comparisons for wall (δ/d=7.5) injected J=5.2 jet at z/d = -4, -2, 0, +2, +4

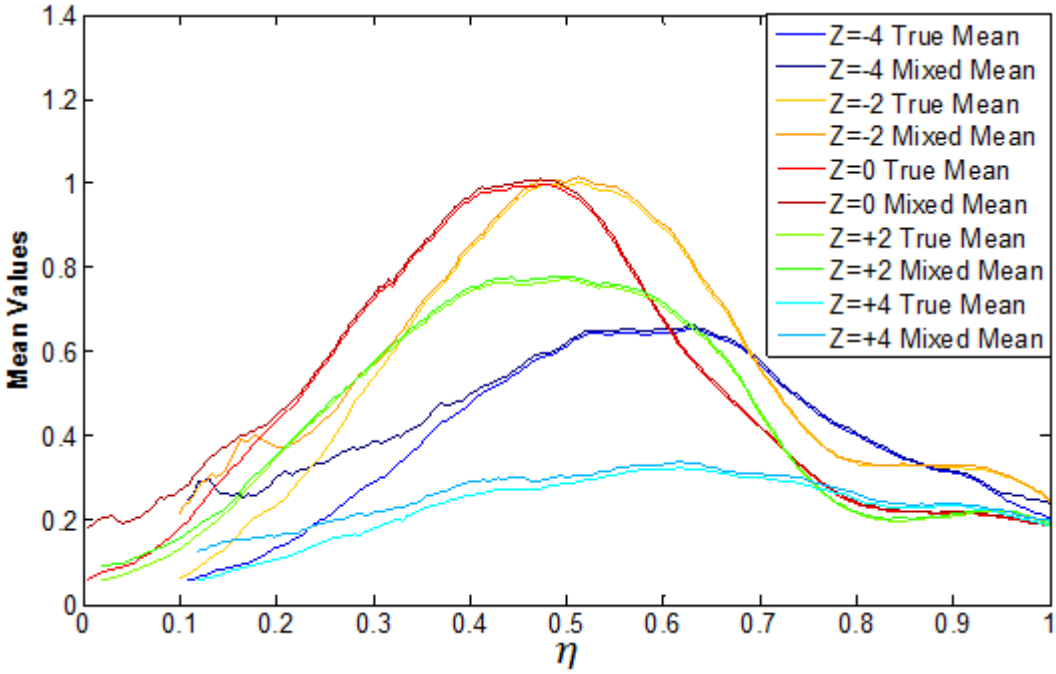

Figure 4.86. x/d=5 end view mean comparisons for wall (δ/d=7.5) injected J=2.7 jet at z/d = -4, -2, 0, +2, +4

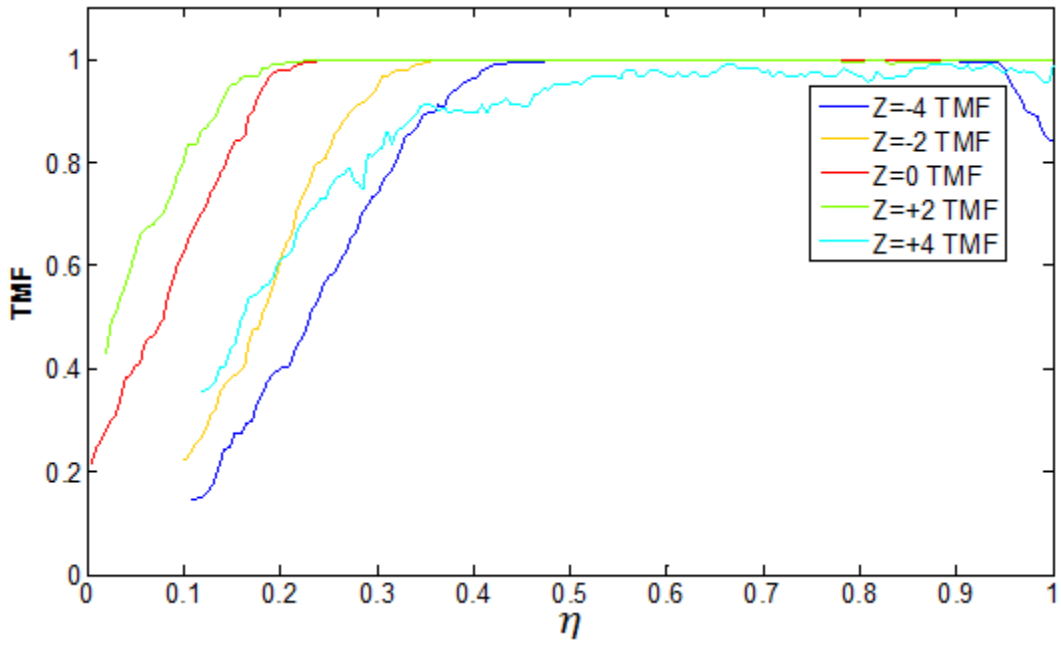

Figure 4.87. x/d=5 end view True Mixed Fraction comparisons for wall (δ/d=7.5) injected J=2.7 jet at z/d = -4, -2, 0, +2, +4

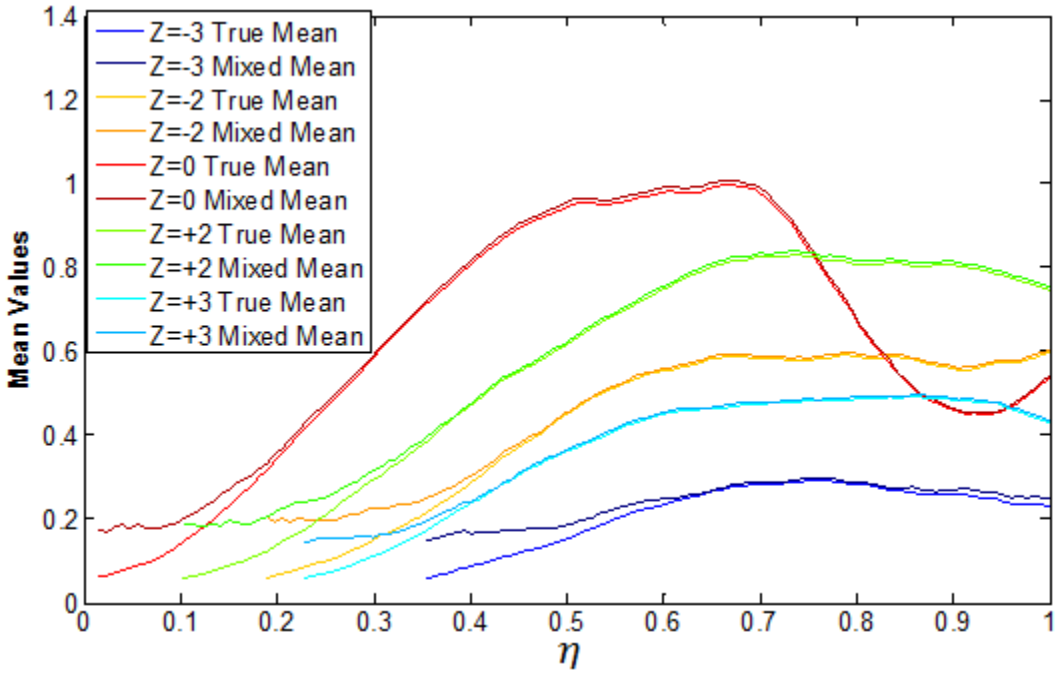

Figure 4.88. x/d=5 end view mean comparisons for wall (δ/d=7.5) injected J=1.2 jet at z/d = -3, -2, 0, +2, +3

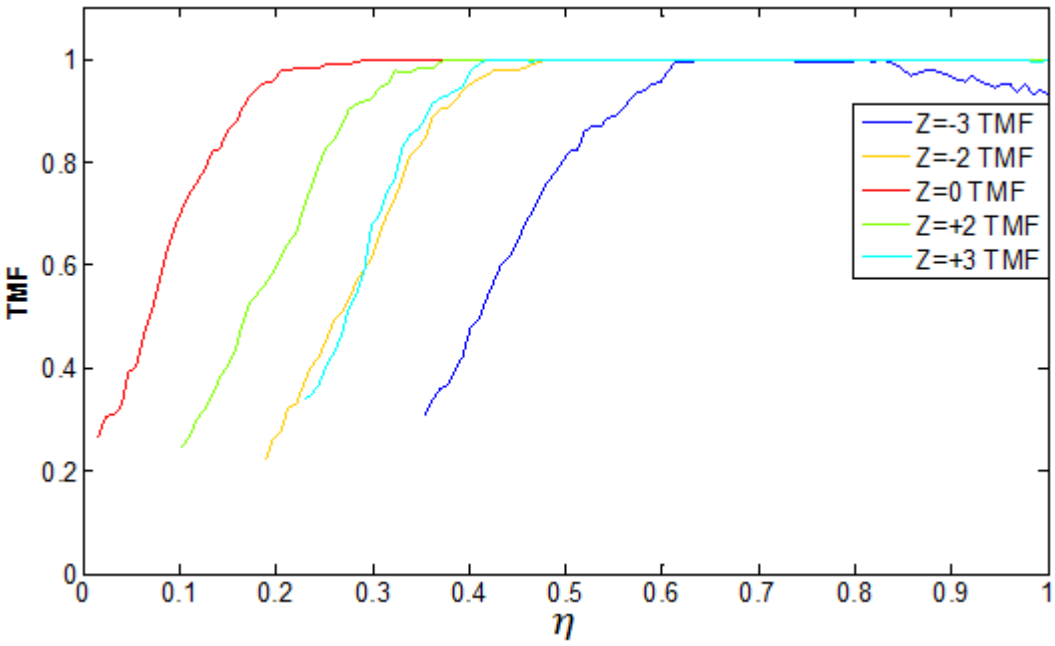

Figure 4.89. x/d=5 end view True Mixed Fraction comparisons for wall (δ/d=7.5) injected J=1.2 jet at z/d = -3, -2, 0, +2, +3

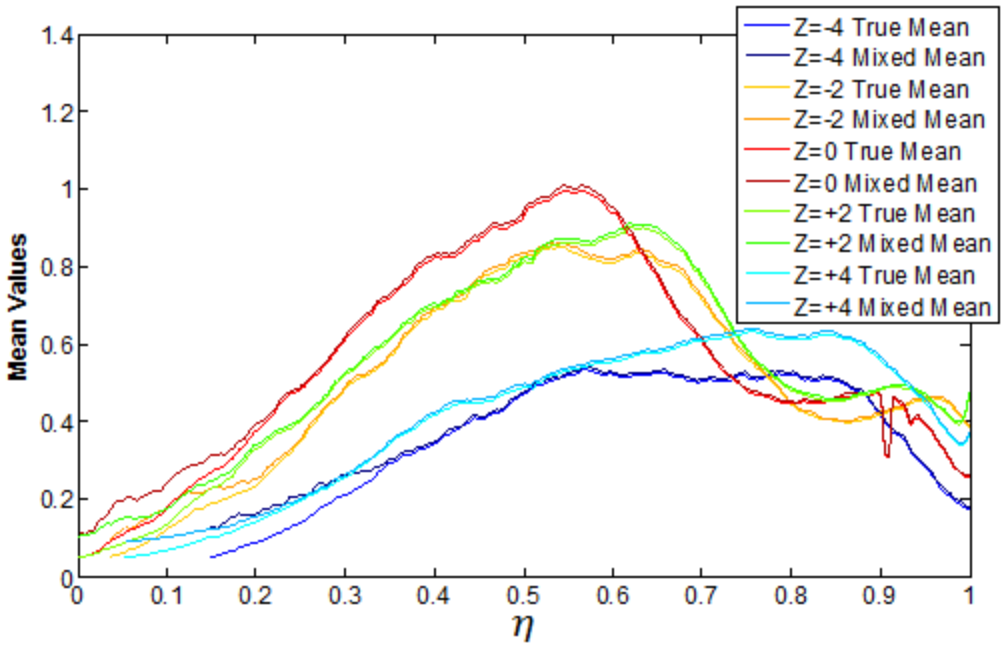

Figure 4.90. x/d=10 end view mean comparisons for wall (δ/d=7.5) injected J=5.2 jet at z/d = -4, -2, 0, +2, +4

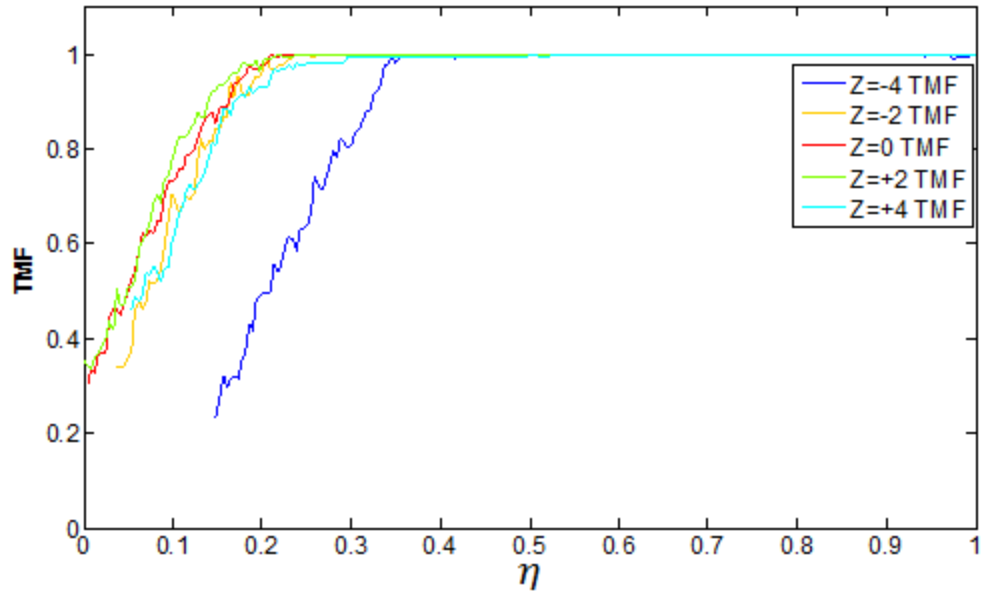

Figure 4.91. x/d=10 end view True Mixed Fraction comparisons for wall (δ/d=7.5) injected J=5.2 jet at z/d = -4, -2, 0, +2, +4

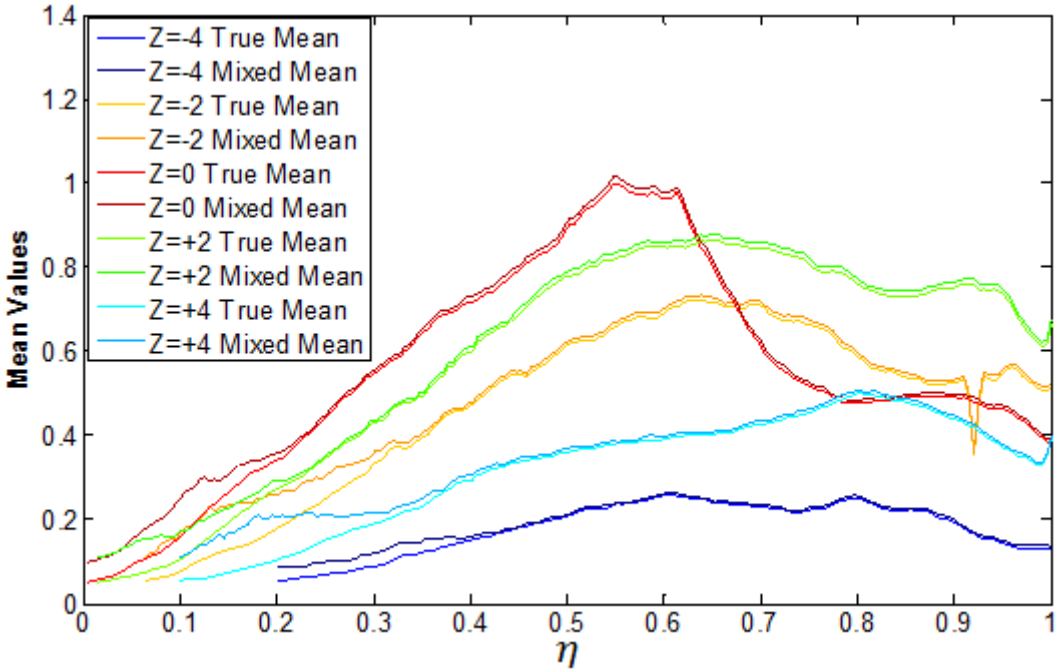

Figure 4.92. x/d=10 end view mean comparisons for wall (δ/d=7.5) injected J=2.7 jet at z/d = -4, -2, 0, +2, +4

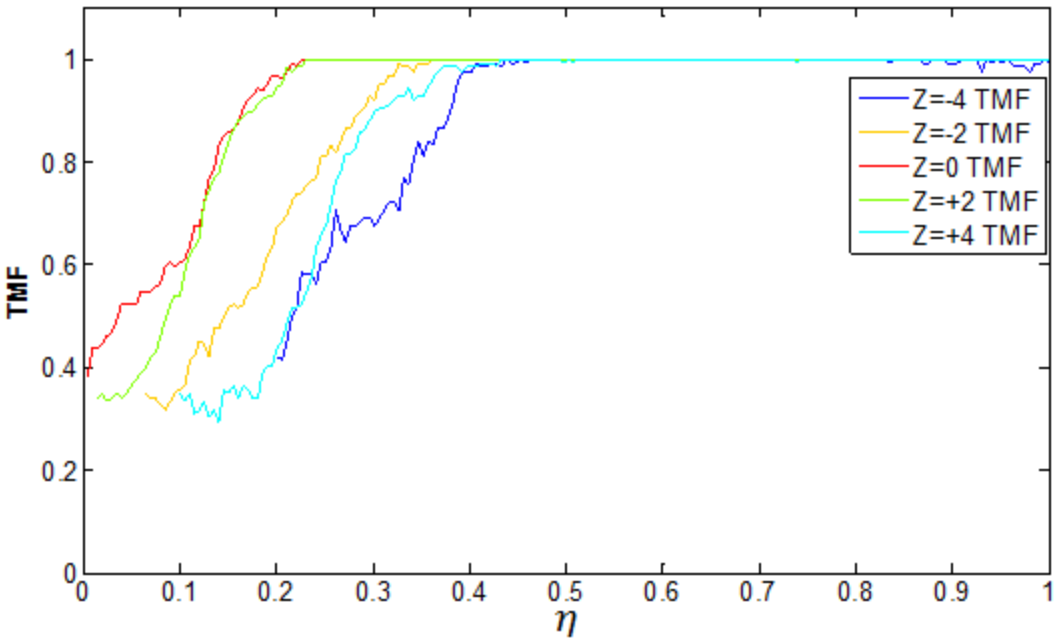

Figure 4.93. x/d=10 end view True Mixed Fraction comparisons for wall (δ/d=7.5) injected J=2.7 jet at z/d = -4, -2, 0, +2, +4

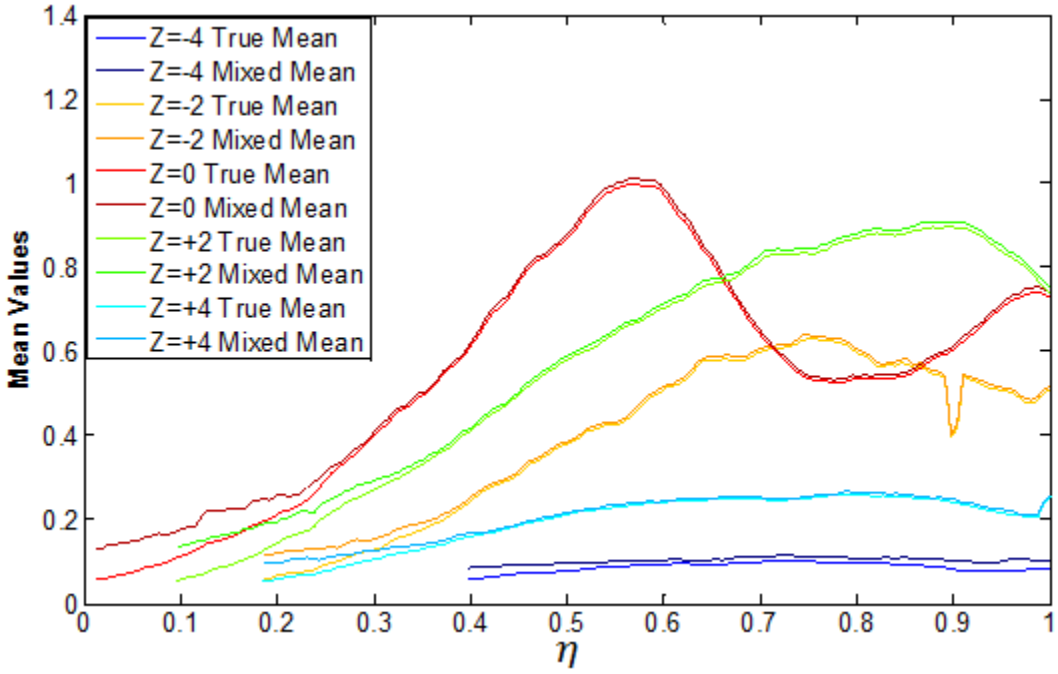

Figure 4.94. x/d=10 end view mean comparisons for wall (δ/d=7.5) injected J=1.2 jet at z/d = -4, -2, 0, +2, +4

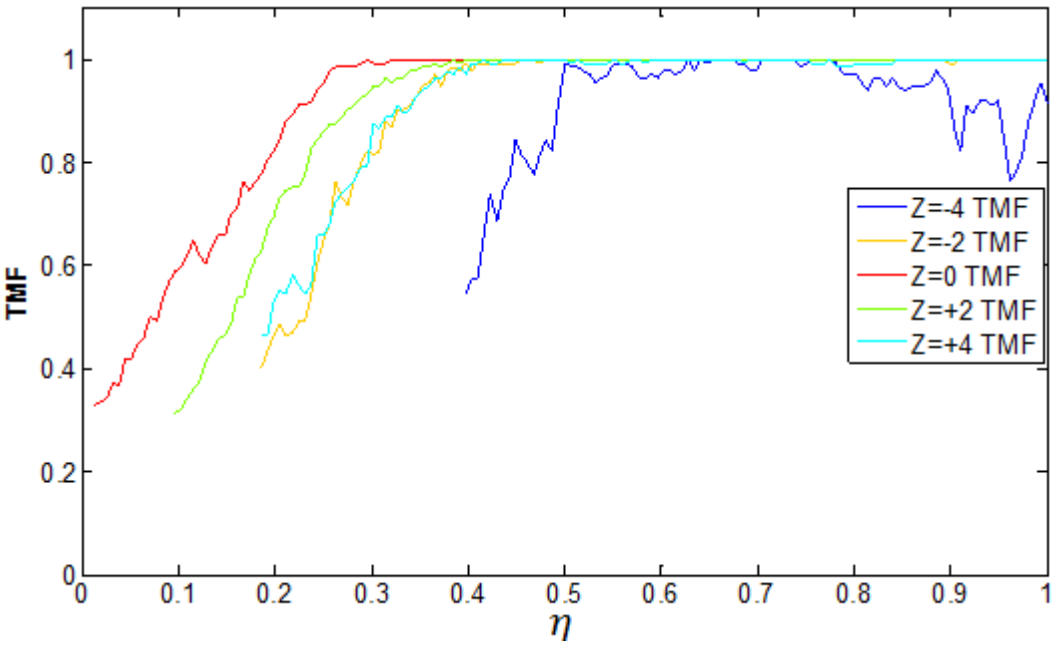

Figure 4.95. x/d=10 end view True Mixed Fraction comparisons for wall (δ/d=7.5) injected J=1.2 jet at z/d = -4, -2, 0, +2, +4

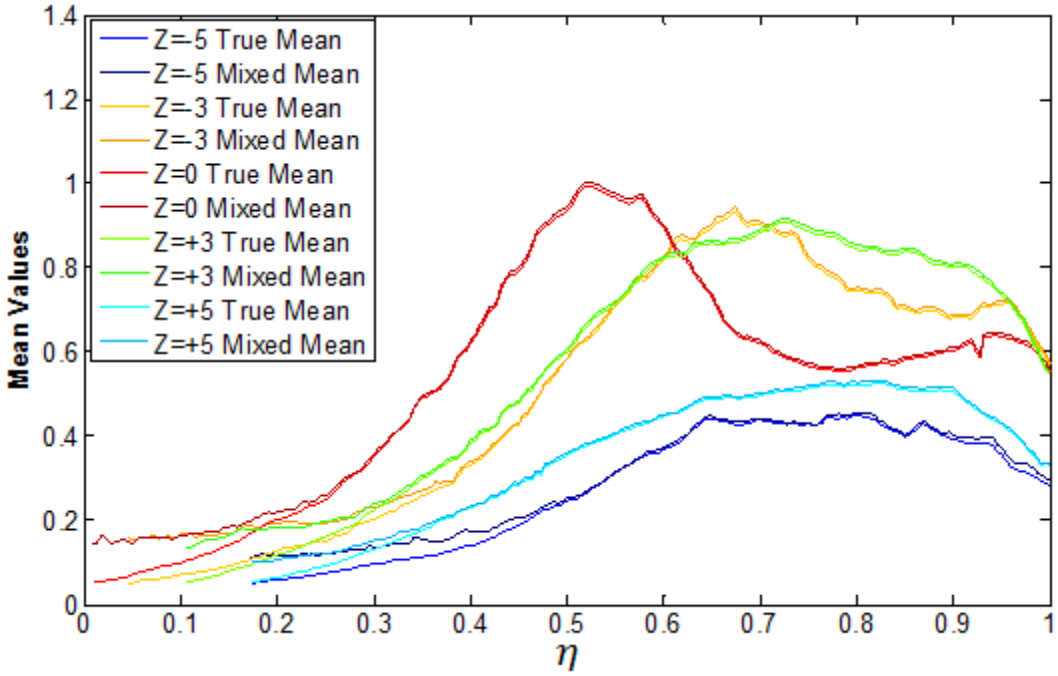

Figure 4.96. x/d=20 end view mean comparisons for wall (δ/d=7.5) injected J=5.2 jet at z/d = -5, -3, 0, +3, +5

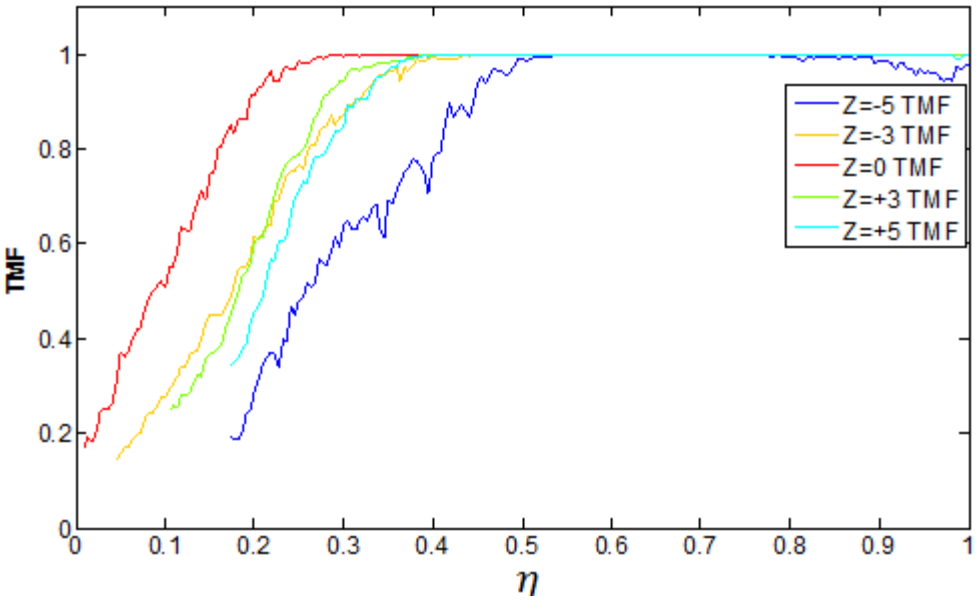

Figure 4.97. x/d=20 end view True Mixed Fraction comparisons for wall (δ/d=7.5) injected J=5.2 jet at z/d = -5, -3, 0, +3, +5

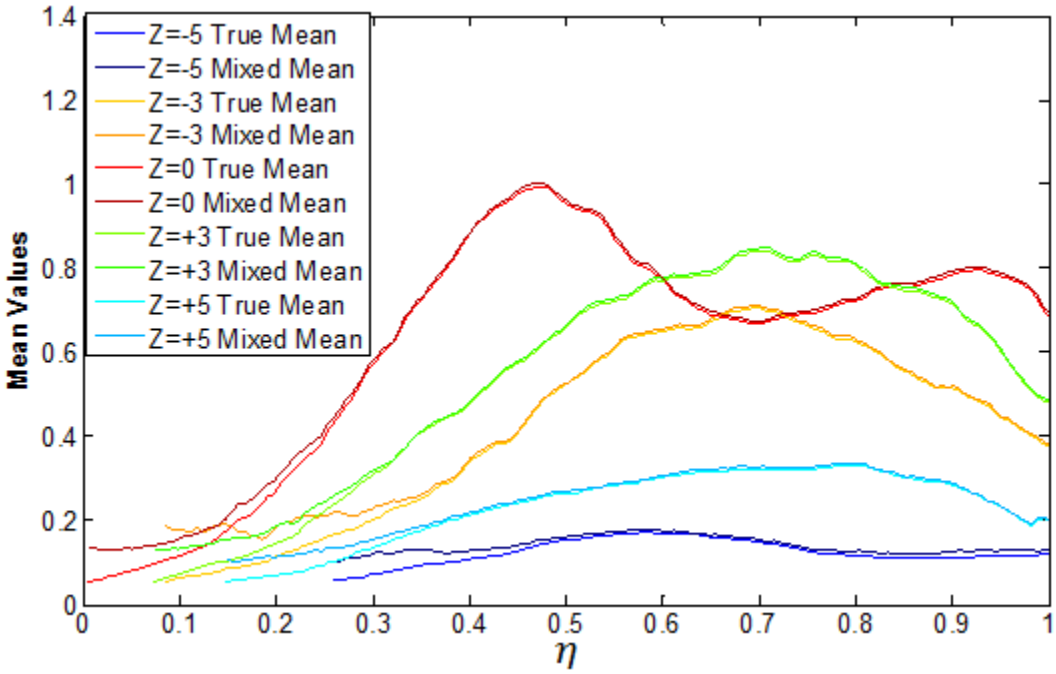

Figure 4.98. x/d=20 end view mean comparisons for wall (δ/d=7.5) injected J=2.7 jet at z/d = -5, -3, 0, +3, +5

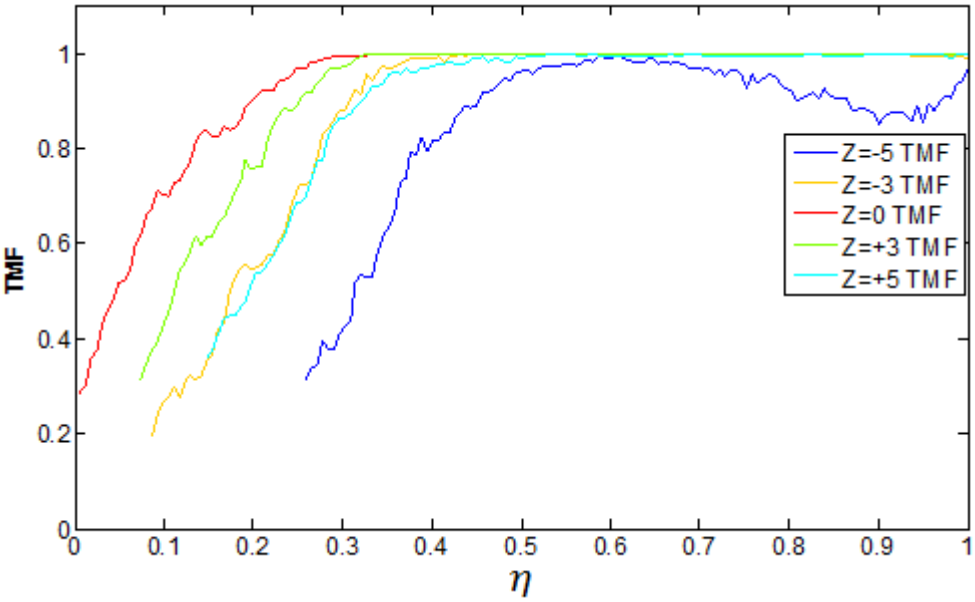

Figure 4.99. x/d=20 end view True Mixed Fraction comparisons for wall (δ/d=7.5) injected J=2.7 jet at z/d = -5, -3, 0, +3, +5

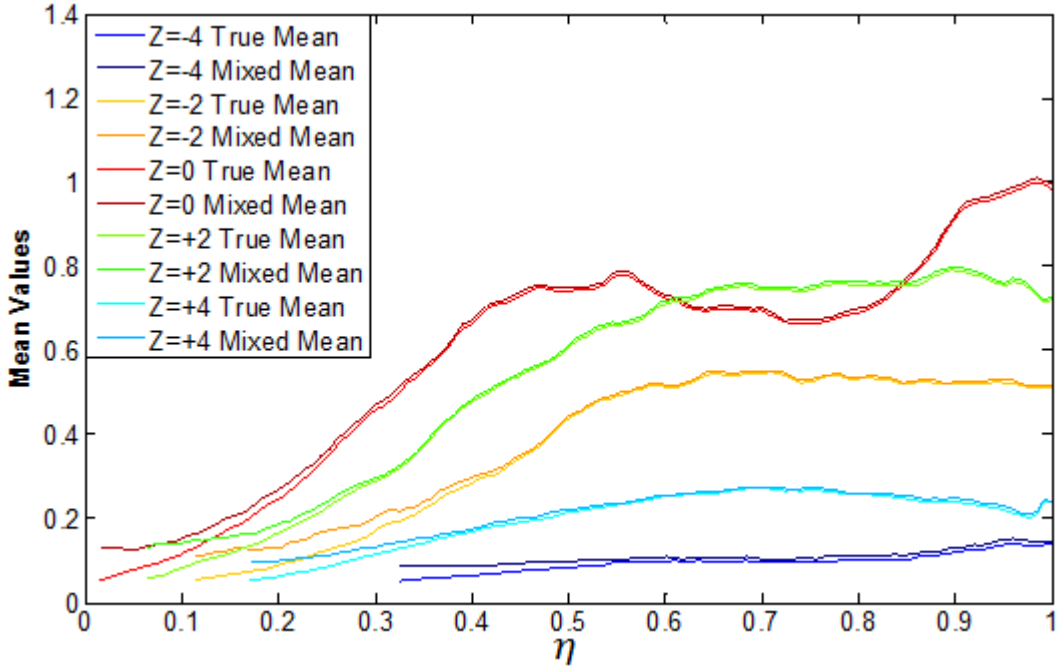

Figure 4.100. x/d=20 end view mean comparisons for wall (δ/d=7.5) injected J=1.2 jet at z/d = -4, -2, 0, +2, +4

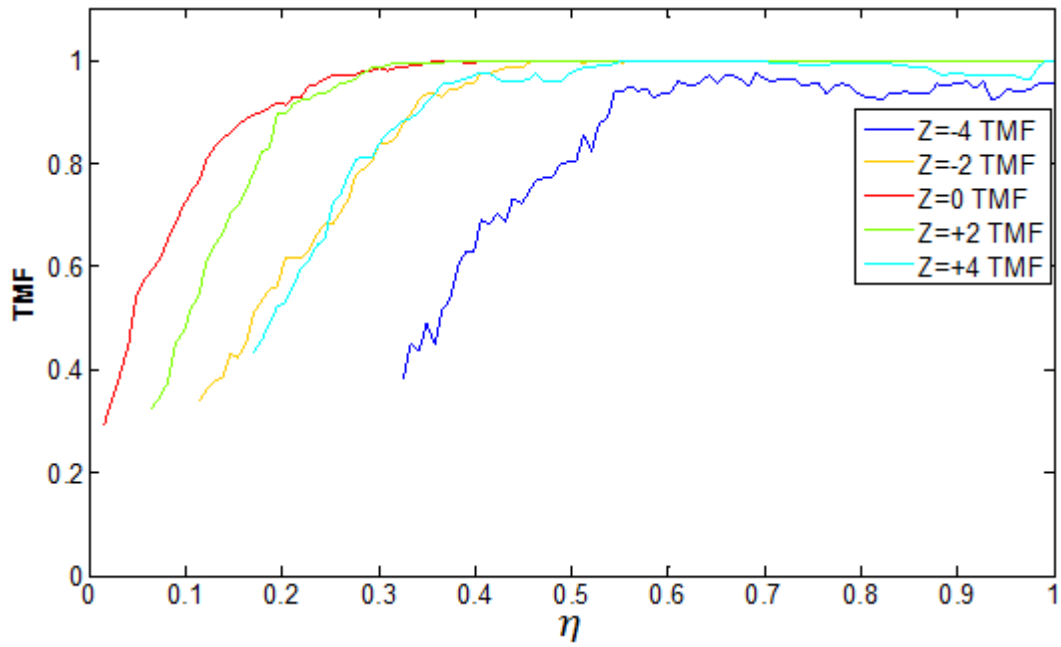

Figure 4.101. x/d=20 end view True Mixed Fraction comparisons for wall (δ/d=7.5) injected J=1.2 jet at z/d = -4 -2, 0, +2, +4

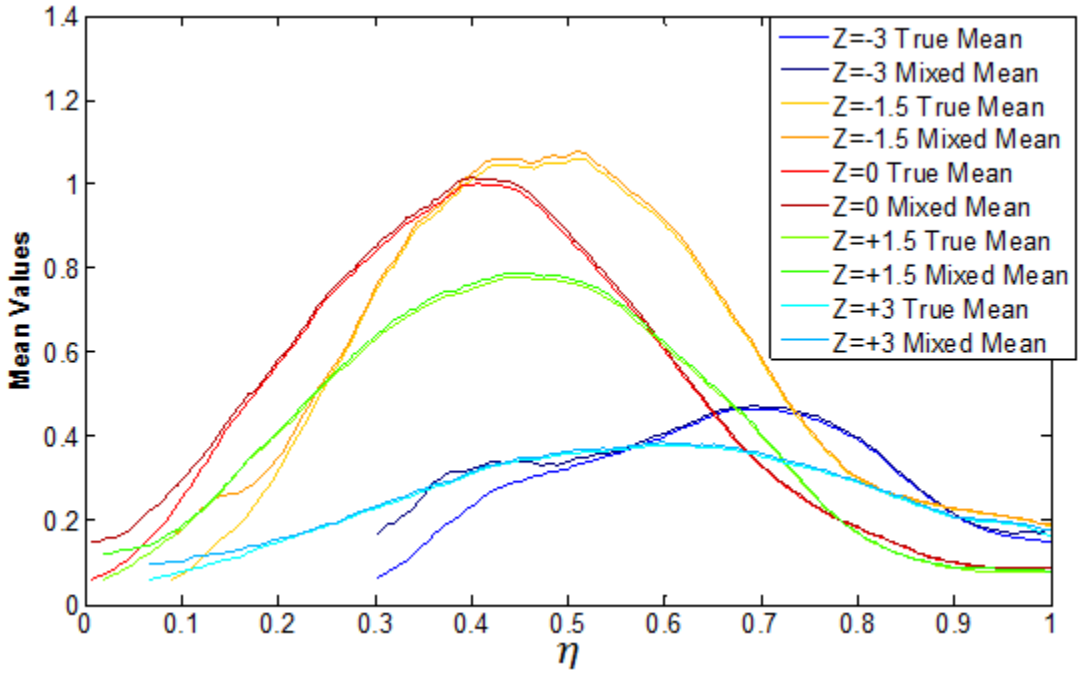

Figure 4.102. x/d=5 end view mean comparisons for wedge (δ/d~0.7) injected J=5.2 jet at z/d = -3, -1.5, 0, +1.5, +3

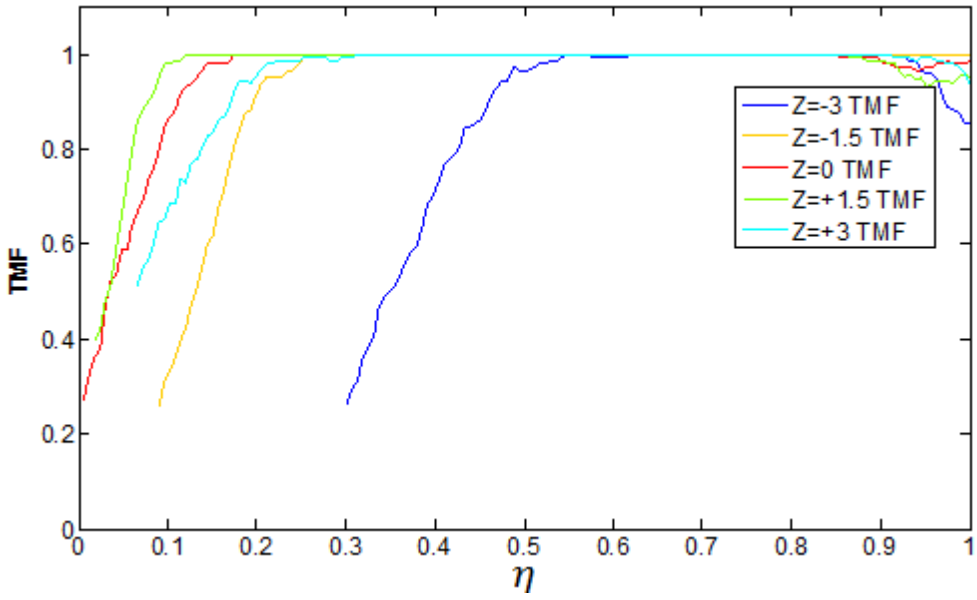

Figure 4.103. x/d=5 end view True Mixed Fraction comparisons for wedge (δ/d~0.7) injected J=5.2 jet at z/d = -3 -1.5, 0, +1.5, +3

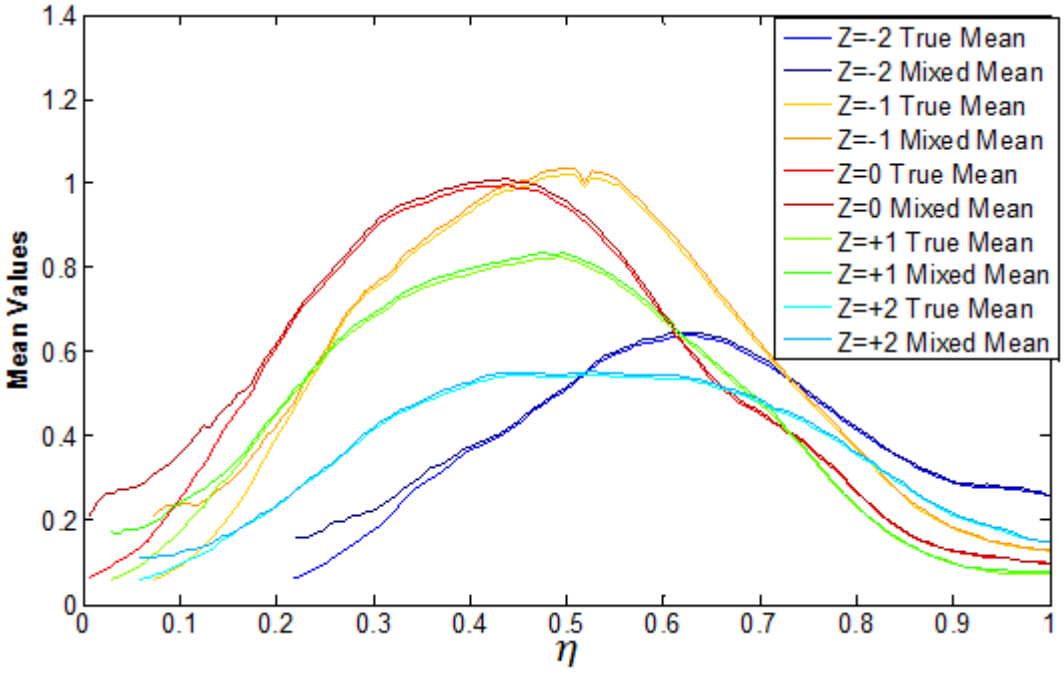

Figure 4.104. x/d=5 end view mean comparisons for wedge (δ/d~0.7) injected J=2.7 jet at z/d = -2, -1, 0, +1, +2

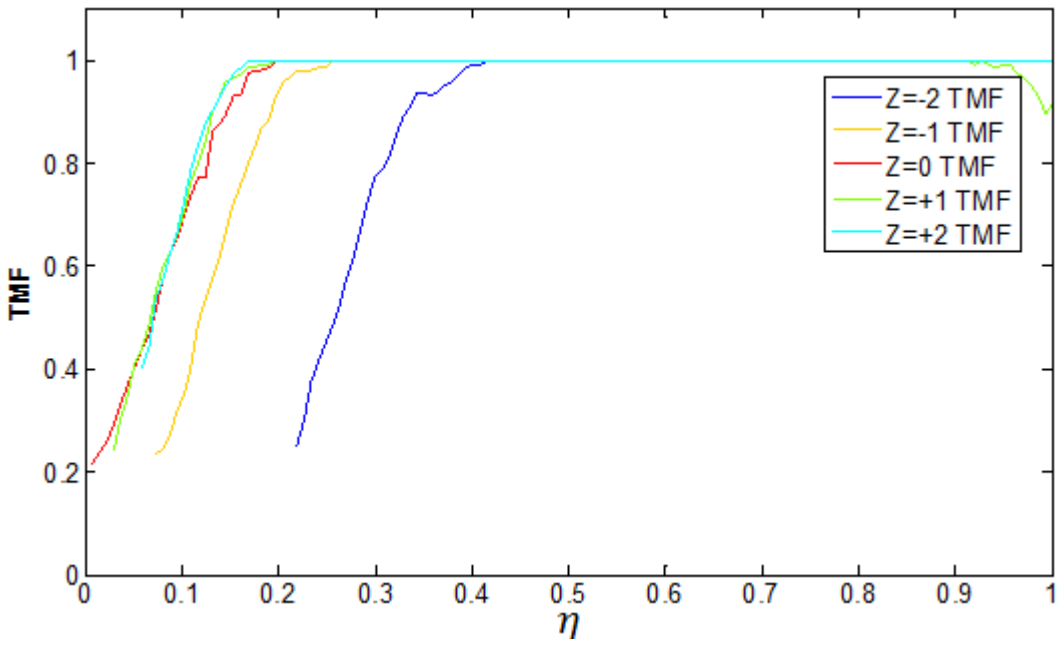

Figure 4.105. x/d=5 end view True Mixed Fraction comparisons for wedge (δ/d~0.7) injected J=2.7 jet at z/d = -2 -1, 0, +1, +2

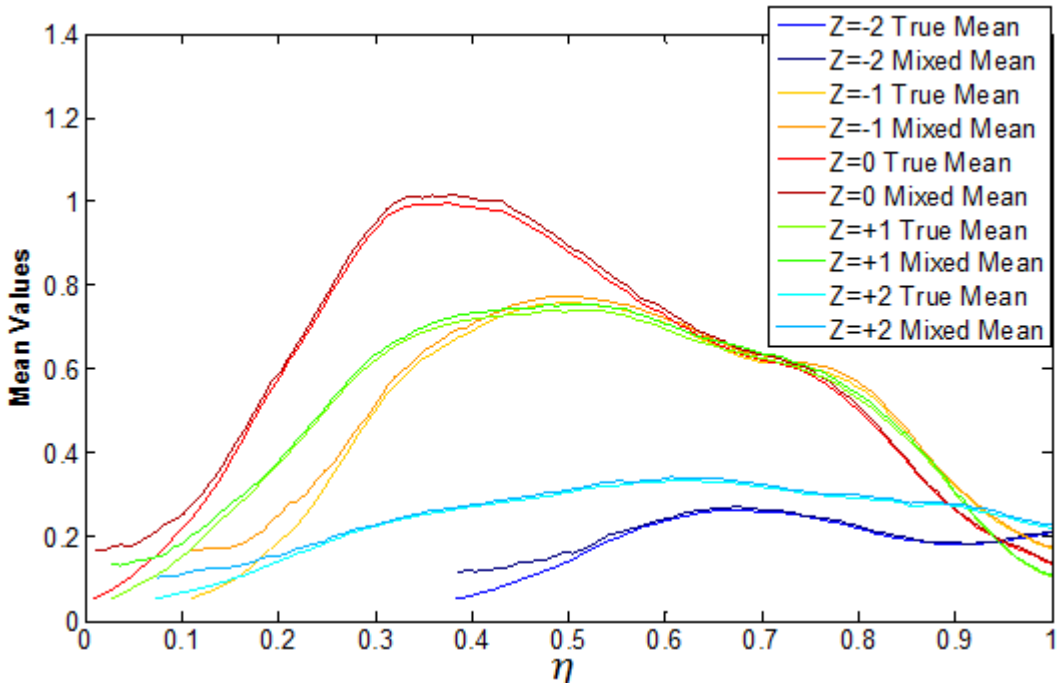

Figure 4.106. x/d=5 end view mean comparisons for wedge (δ/d~0.7) injected J=1.2 jet at z/d = -2, -1, 0, +1, +2

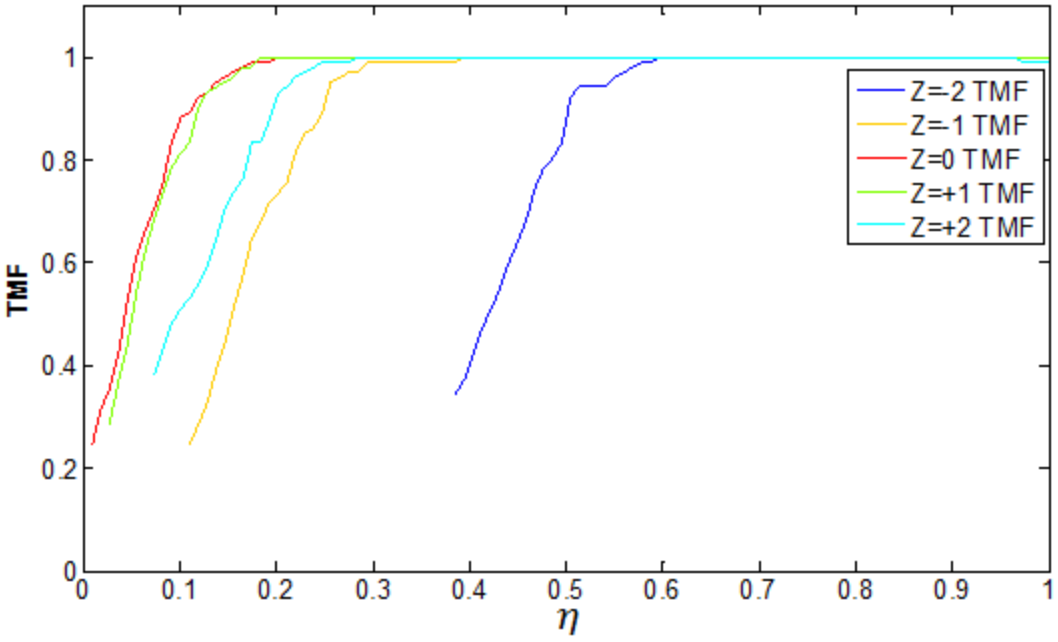

Figure 4.107. x/d=5 end view True Mixed Fraction comparisons for wedge (δ/d~0.7) injected J=1.2 jet at z/d = -2 -1, 0, +1, +2

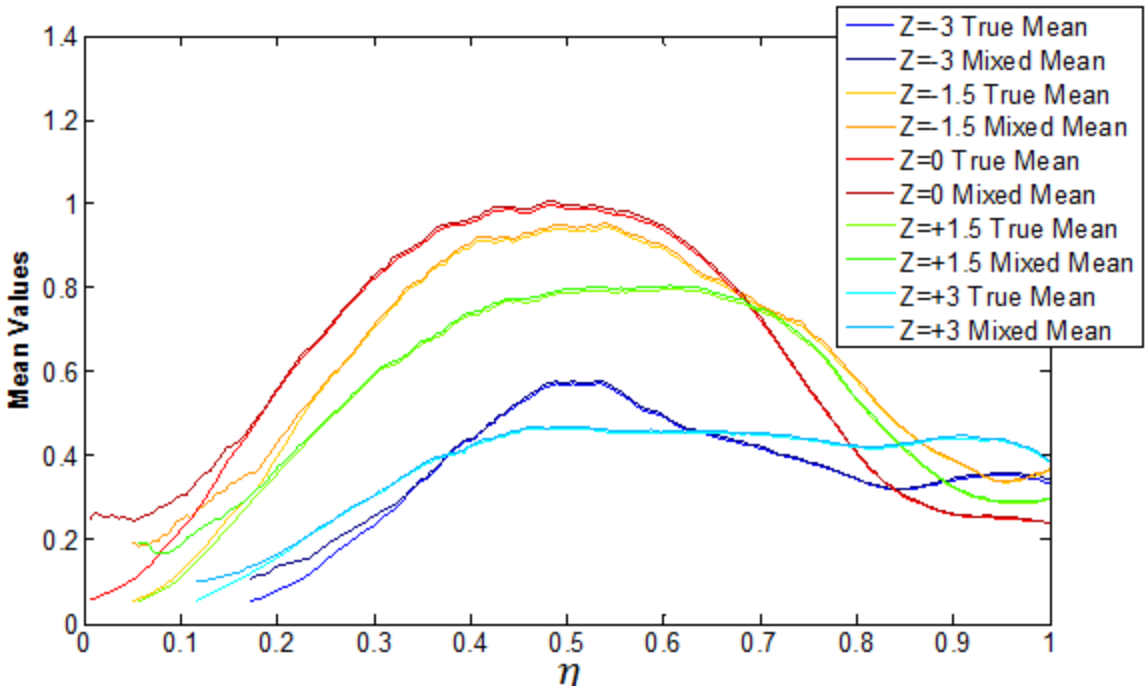

Figure 4.108. x/d=10 end view mean comparisons for wedge (δ/d~0.7) injected J=5.2 jet at z/d = -3, -1.5, 0, +1.5, +3

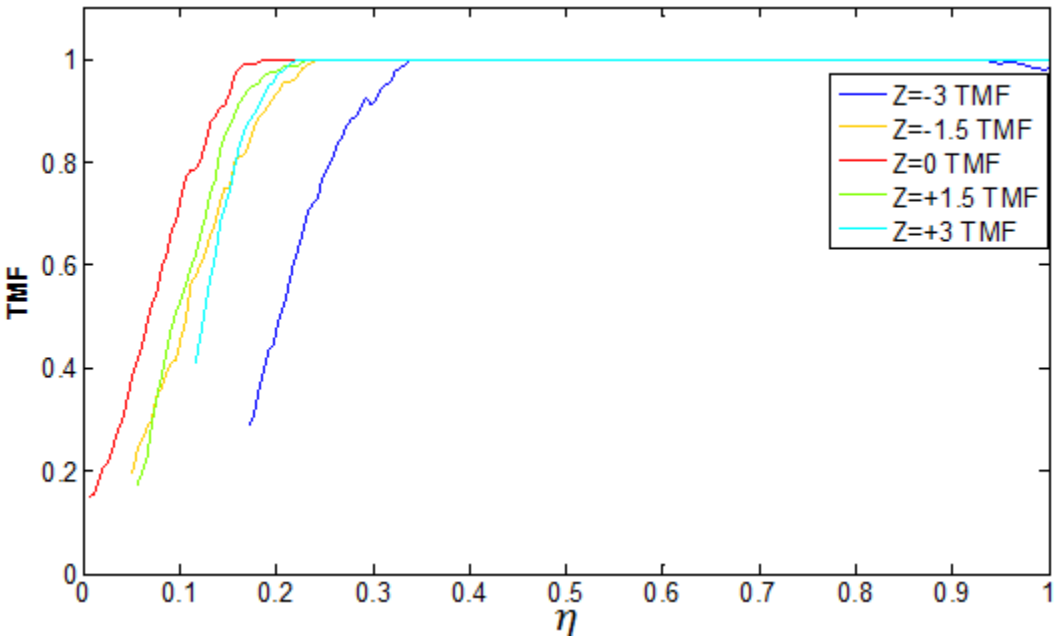

Figure 4.109. x/d=10 end view True Mixed Fraction comparisons for wedge (δ/d~0.7) injected J=5.2 jet at z/d = -3 -1.5, 0, +1.5, +3

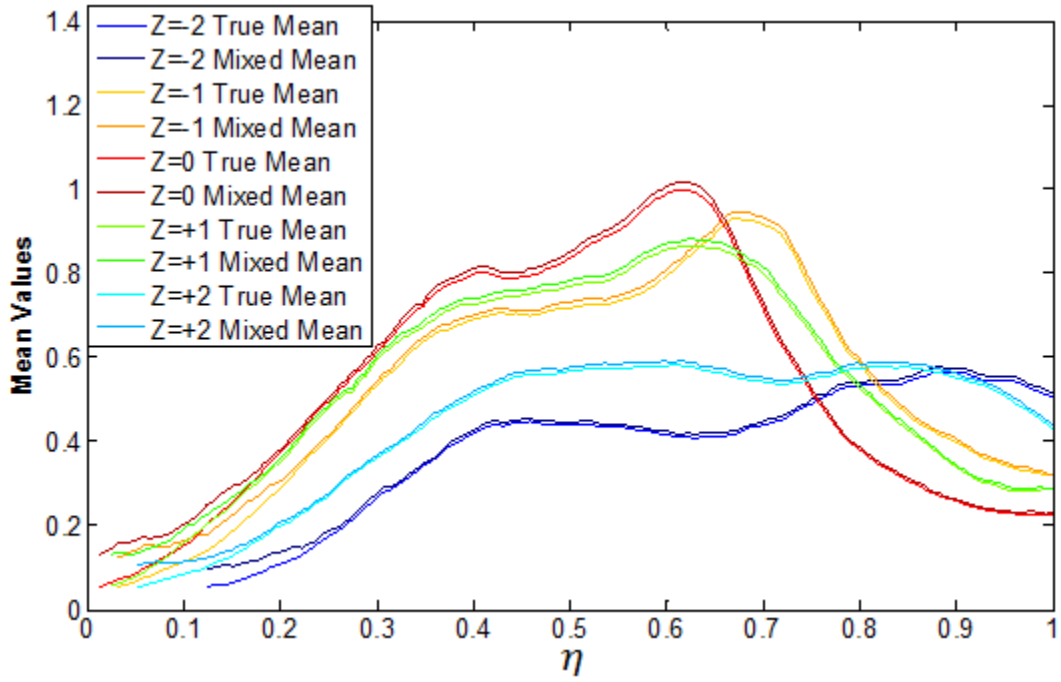

Figure 4.110. x/d=10 end view mean comparisons for wedge (δ/d~0.7) injected J=2.7 jet at z/d = -2, -1, 0, +1, +2

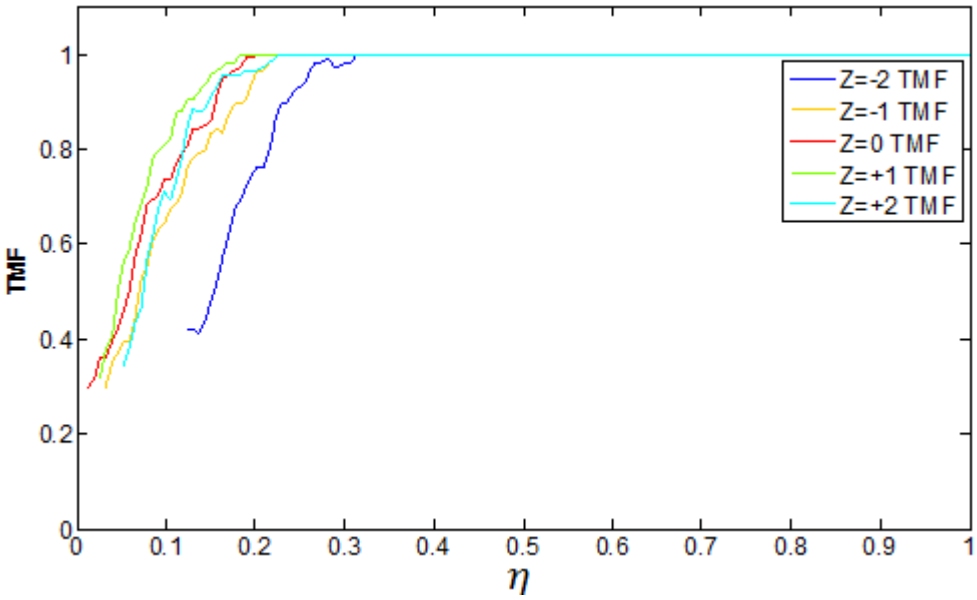

Figure 4.111. x/d=10 end view True Mixed Fraction comparisons for wedge (δ/d~0.7) injected J=2.7 jet at z/d = -2 -1, 0, +1, +2

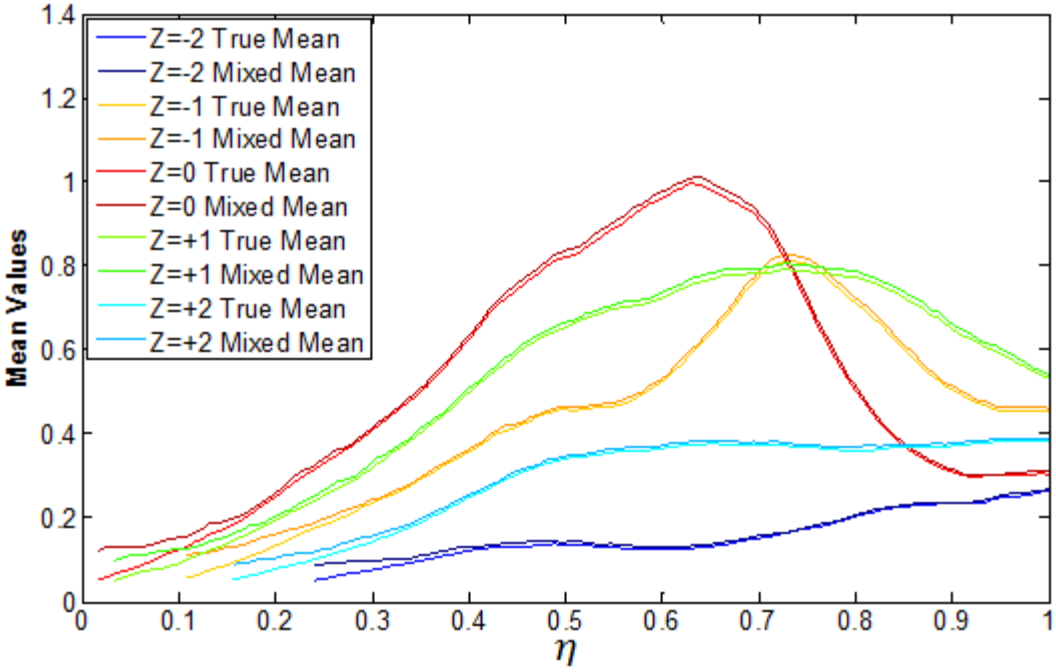

Figure 4.112. x/d=10 end view mean comparisons for wedge (δ/d~0.7) injected J=1.2 jet at z/d = -2, -1, 0, +1, +2

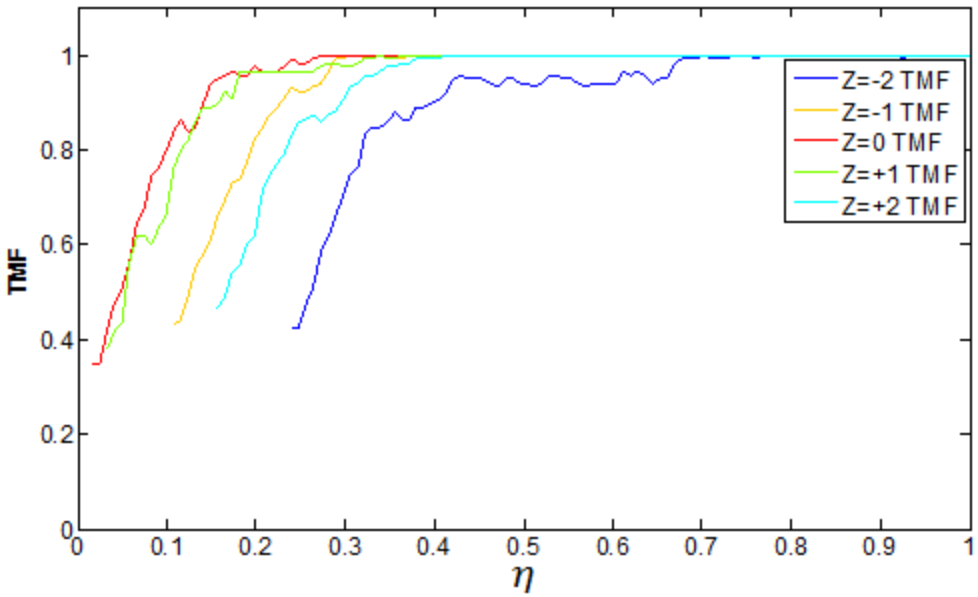

Figure 4.113. x/d=10 end view True Mixed Fraction comparisons for wedge (δ/d~0.7) injected J=1.2 jet at z/d = -2 -1, 0, +1, +2

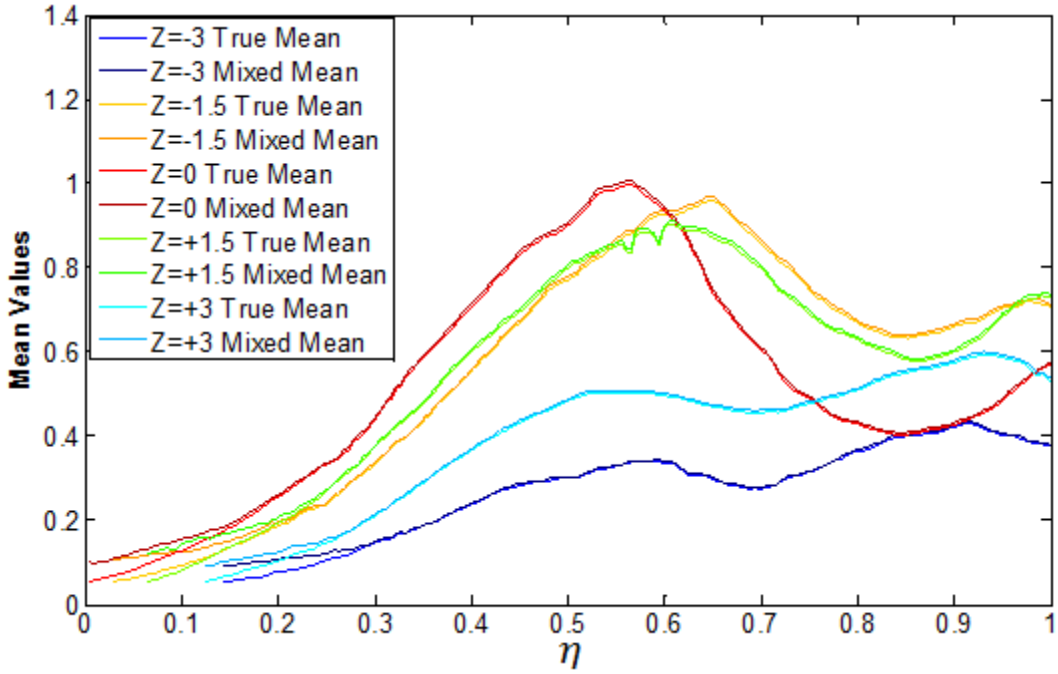

Figure 4.114. x/d=20 end view mean comparisons for wedge (δ/d~0.7) injected J=5.2 jet at z/d = -3, -1.5, 0, +1.5, +3

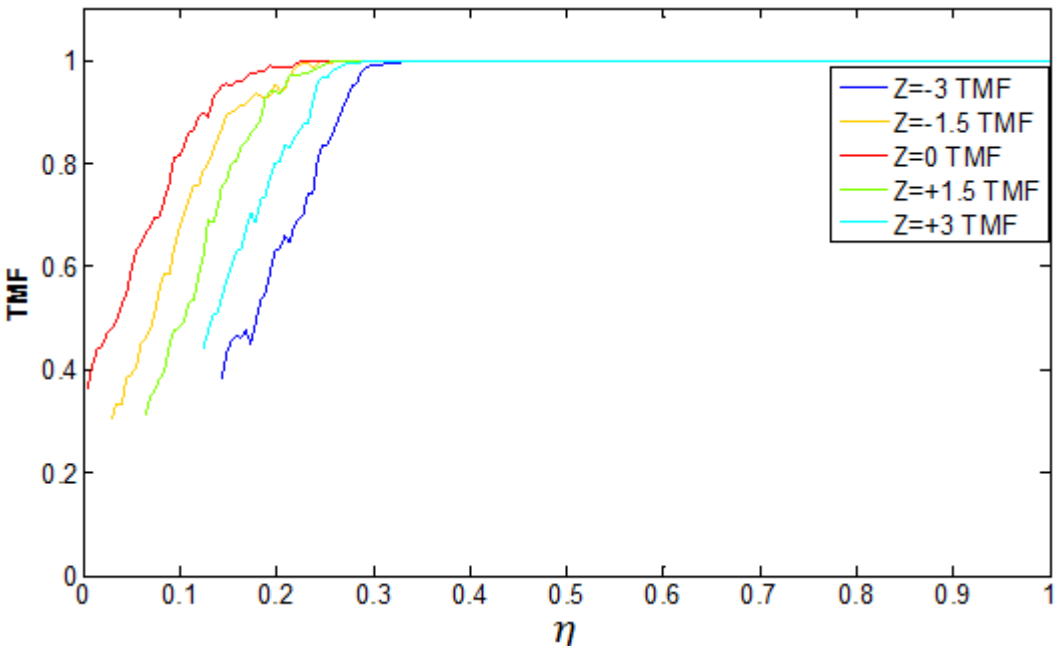

Figure 4.115. x/d=20 end view True Mixed Fraction comparisons for wedge (δ/d~0.7) injected J=5.2 jet at z/d = -3 -1.5, 0, +1.5, +3

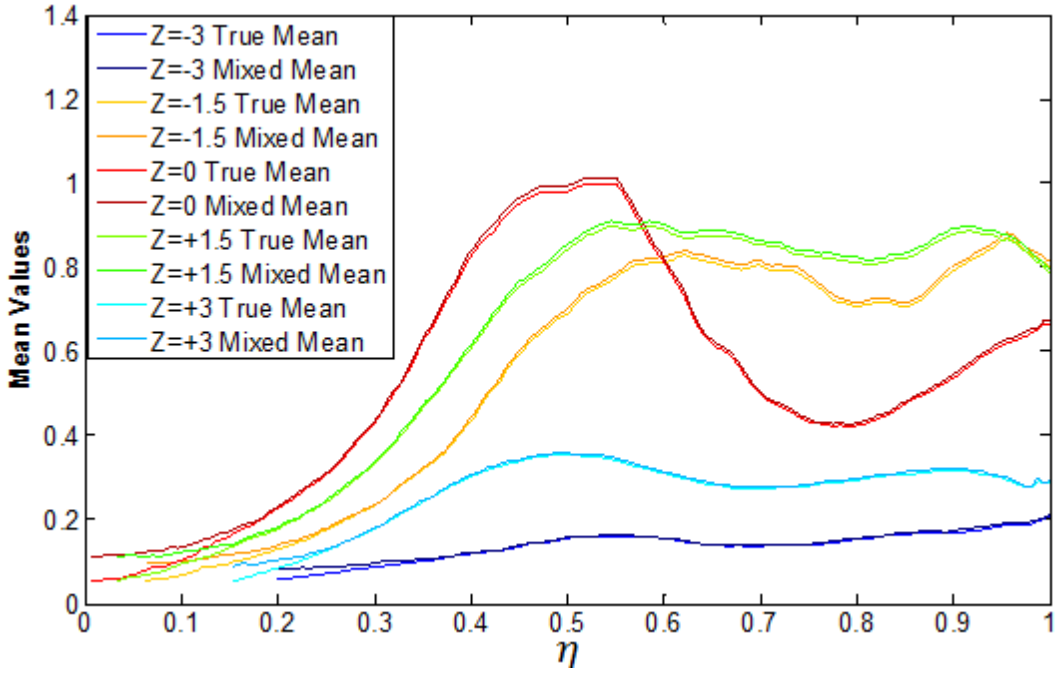

Figure 4.116. x/d=20 end view mean comparisons for wedge (δ/d~0.7) injected J=2.7 jet at z/d = -3, -1.5, 0, +1.5, +3

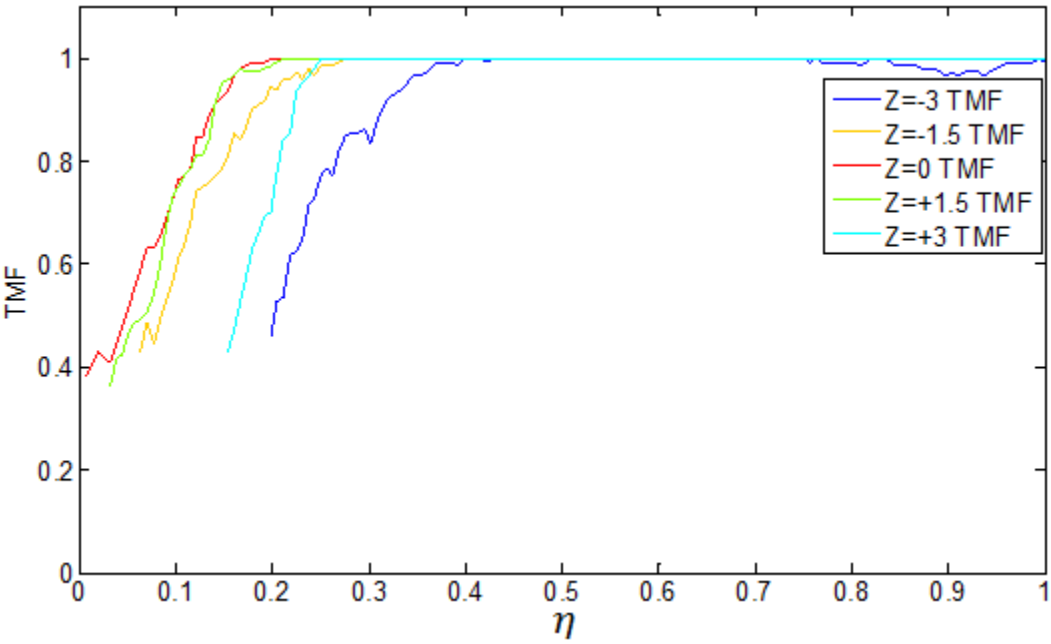

Figure 4.117. x/d=20 end view True Mixed Fraction comparisons for wedge (δ/d~0.7) injected J=2.7 jet at z/d = -3 -1.5, 0, +1.5, +3

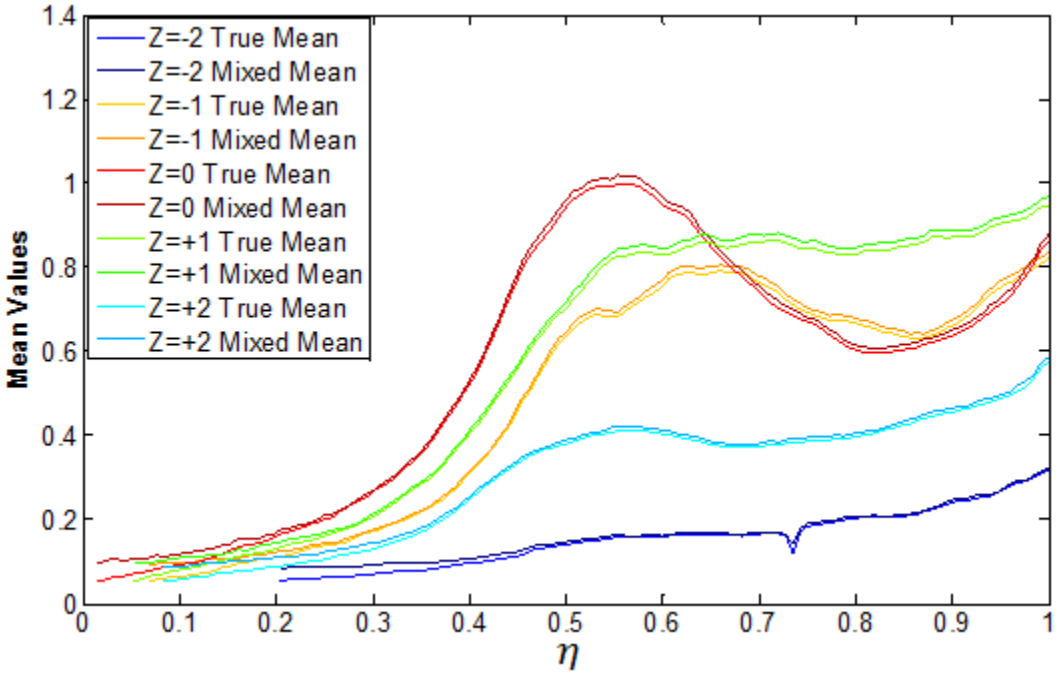

Figure 4.118. x/d=20 end view mean comparisons for wedge (δ/d~0.7) injected J=1.2 jet at z/d = -2, -1, 0, +1, +2

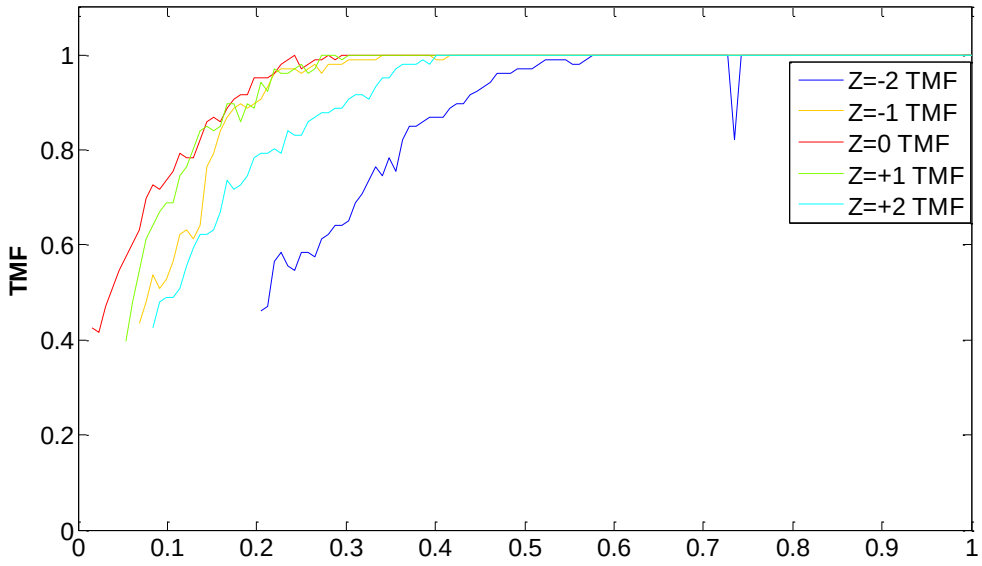

Figure 4.119. x/d=20 end view True Mixed Fraction comparisons for wedge (δ/d~0.7) injected J=1.2 jet at z/d= -2 -1, 0, +1, +2

Table 4.1 Standard deviation (d) for side view trajectory profiles.

wall_J5.2	wall_J2.7	wall_J1.2
0.48	0.60	0.59
wedge_J5.2	wedge_J2.7	wedge_J1.2
1.42	0.42	0.88

Table 4.2 Total mixed fluid concentration for z/d=0 path in end view plane. Wall (δ/d=7.5) boundary layer injection.

	J=1.2	J=2.7	J=5.2
x/d=5	0.67	0.59	0.53
x/d=10	0.59	0.58	0.59
x/d=20	0.62	0.66	0.57

Table 4.3 Total Mixed Fluid Concentration for z/d=0 path in end view plane. Wedge (δ/d~.7) boundary layer injection.

	J=1.2	J=2.7	J=5.2
x/d=5	0.62	0.57	0.51
x/d=10	0.54	0.56	0.65
x/d=20	0.58	0.55	0.54

Table 4.4 True Mixed Fraction for entire end view plane. Wall (δ/d=7.5) boundary layer injection.

	J=1.2	J=2.7	J=5.2
x/d=5	0.89	0.87	0.84
x/d=10	0.79	0.89	0.92
x/d=20	0.88	0.84	0.82

Table 4.5 True Mixed Fraction for entire end view. Wedge (δ/d~0.7) boundary layer injection.

	J=1.2	J=2.7	J=5.2
x/d=5	0.92	0.90	0.90
x/d=10	0.88	0.94	0.91
x/d=20	0.89	0.92	0.90

Table 4.6 Plume area determined from end view plane (d^2). Wall (δ/d=7.5) boundary layer injection.

	J=1.2	J=2.7	J=5.2
x/d=5	36.47	59.01	81.95
x/d=10	56.32	94.05	128.06
x/d=20	56.61	98.31	171.72

Table 4.7 Plume area (d^2) determined from end view plane. Wedge (δ/d~0.7) boundary layer injection.

	J=1.2	J=2.7	J=5.2
x/d=5	18.17	29.16	39.48
x/d=10	26.45	45.6	68.3
x/d=20	35.61	52.28	89.58

Chapter 5 Conclusions

5.1 Conclusions

Three jets of different momentum flux ratios were injected into two different size boundary layers. The jets were imaged from two orthogonal views to investigate correlations between the two views in terms of mixing. The side view plane provided information about the jet trajectory and how the jet mixed in the streamwise and transverse direction. The results in Fig. 4.2 suggested that the higher the jet momentum flux ratio of the jet, the better the jet centerline fit the power law. A comparison with Fig. 4.3 showed that for a particular *J* value, the thicker boundary layer fits the jet trajectory profile better than the thin boundary layer. The plots that showed the jet spread indicated that the jets together grow linearly for up to at least four jet diameters downstream of the injection point before they all grow nonlinearly with a slope less than one. In terms of the near field, the jets injected into the thick boundary layer have steeper spread slopes than the jets injected into the thin boundary layer. In the wall injection boundary layer, the *J*=5.2 jet spread the farthest into the crossflow, reaching almost 11.5 jet diameters in the transverse direction at 15 jet diameters downstream. In addition, the jets continued to grow in the transverse direction although the centerline trajectory of the jets stopped growing. This trend can be seen for all jets in both the wall and wedge injection boundary layers. In terms of pixel intensity decay, the jets injected into the wedge boundary layer decay to lower values than for the thick boundary layer in the near field. However in the far field, the jets in the thick boundary layer collapse to smaller pixel intensity values than for the wedge. In the thin boundary layer, the jets are able to interact with high speed

flow easier than for the thick boundary layer. In the far field wall boundary layer, the jets are able to work more with the turbulent fluctuations and long streamwise vortical structures that the thin boundary layer does not have. The log-log pixel intensity results conducted in the experiments were similar to what Smith (1996) recorded in his experiments with *d*- length scaling for various *J* value jets. In addition, the results in Fig. 4.14 showed that the delay in the branch points will occur earlier for the wedge injection cases than for the wall injections.

The end view plane provided an additional outlook in the lateral direction. Overall, the jets appear to be more symmetric when injected into the thin boundary layer than in the thick boundary layer. With the exception of the J=2.7 jet (Fig. 3.25), J=5.2 (Fig. 3.28) at x/d =5, and J=1.2 jet at x/d =20 (Fig. 3.24), the averaged end view images of the jet in the thin boundary layer are quite symmetric.

The pfd's provided insight for both side and end view imaging planes. Paths at z/d=0 were made for the jets from the windward side of the jet to the orifice plane. As the paths made their way through the core of the jet, the PDF's marched toward the centerline concentration value. After the paths passed through the centerline of the jet, the PDF's begin to march toward lower concentration values again. The trend of marching PDF's from low concentration values to high values and back to low values could be clearly seen in the x/d=5 PDF's for all J values in the end and side-view planes except in the side-view plane of the J=1.2. Overall, the PDF's calculated in the end-view plane provided better trends than the side-view for x/d=20.

The probability of finding unmixed fluid at the windward side of the jet was greater than finding unmixed fluid toward the center or near the orifice plane. Along the PDF paths, the true and mixed mean profiles came together, more so for the end-view profiles than for the side-view profiles. The true mixed fraction values near the windward side of the jets were smaller when calculated in the side-view plane when compared to calculated values in the end-view plane. For all cases except the J=5.2 (Fig. 4.73) and J=2.7 (Fig. 4.75) at x/d=10 it was quite clear that the jet injected into the thinner boundary layer mixed faster at its windward edge than in the thick boundary layer. This made sense because the jet interacted with greater shearing speeds at the windward side in the small boundary layer case than in the thick turbulent boundary layer. Although the wedge boundary layer exposed the top of the jet to higher shearing velocities, the thick boundary layer contained vortical structures that the jet was able to interact with near the wall. For the tested J values and stream wise stations, the jets injected into the wall boundary layer had higher mean values near the wall than the jets injected into the wedge boundary layer. The thick boundary layer was very turbulent and was able to move and mix jet fluid around near the wall easier than the thin boundary layer was able to move fluid.

The mean profiles at different z/d locations showed that jets injected into the wedge boundary layer were more symmetrical than jets injected into the wall boundary layer. This agreed well with the qualitative conclusions in section 3.1.2. Visually from inspection, the rate at which each true mixed fraction went to unity was quite the same. There are instances where the slopes for the non-zero z/d planes were shallower than the

z/d=0 profile. The profiles showed that toward the center of the jet, the jets mix better than the sides of the jet.

Overall the results for the total mixed fluid concentration values were greater for the jets injected into the thick boundary layer than for the thin boundary layer. For all cases, the total mixed fluid concentration values in Tables 4.2 and 4.3 are greater than 0.5. The average concentration across the paths seems to lean closer to the centerline jet fluid concentration value as opposed to the unmixed fluid concentration value.

The true mixed fraction results for the entire end-view plane of the jets were tabulated in Table 4.4 and Table 4.5. The values in both tables showed that jets were all well mixed. As stream wise distance increased downstream, the jet remained consistently mixed around the same values. The jet plume area was tabulated in Table 4.6 and Table 4.7. The jet plume area increased as the *J*-value and stream wise distance increased. The results showed that the jet plume area was greater in the thick boundary layer than for the thin boundary layer.

5.2 Future work

Future work could include taking images from the top or bottom of the jet. The images could provide information about the development of the horseshoe vortices that develop around the jet and how they affect mixing. Different injection angles could be examined and recorded in the end-view plane. In addition, changing the injector nozzle from being circular to another shape (rectangle or ellipse) could change the shape of the CVP and could provide insight from the end view plane. One could record multiple jets

in series and record how they mix from the end-view plane. The experimental work in this report could be compared and conducted to computational work.

References

Broadwell, J. E. and R. E. Breidenthal, “Structure and mixing of a transverse jet in incompressible flow” J. Fluid Mech. (1984). vol. 148, pp. 405–412.

Costa, M., Melo, M., Sousa, J.M., and Levy,Y., "Spray Characteristics of Angled Liquid Injection into Subsonic Crossflows", AIAA Journal, Vol. 44, No. 3 (2006), pp. 646-653.

Farokhi, S., “Aircraft Propulsion” John Wiley & Sons Inc, (2009). pp. 698.

Ferri, A.,“Mixing-controlled supersonic combustion”, Annual Review of Fluid Mechanics, (1973), vol. 5, pp. 301.

Fox, F.W., Pritchard, P.J., and McDonald, A.T., “Introduction to Fluid Mechanics” John Wiley & Sons Inc, seventh edition. (2009). pp. 406.

Freund, J.B., Moin, P., and Lele, S. K., “Compressibility effects in a turbulent annular mixing layer. Part 2. Mixing of a passive scalar” J. Fluid Mech. (2000), vol. 421, pp. 269-292.

Fric, T.F., and Roshko, A., “Vortical structure in the wake of a transverse jet,” J. Fluid Mech. (1994), vol.279, pp. 1-47.

Fuller,R.P., Nejad,.A.S., and Schetz, J.A. “Fuel vortex Interactions for Enhanced Mixing in Supersonic Flow” AIAA 96-2661, 1996.

Gamba, M., Mungal, M.G., Hanson, R.K., “OH PLIF imaging of reaction zone in combusting transverse jets in supersonic crossflow,” 16th Int. Symp. on Applications of Laser Technology to Fluid Mechanics, Lisbon Portugal July, 2012, pp. 9.

Gruber, M.R., Nejad, A.S., and Dutton, J.C., “Circular and Elliptical Transverse Injection into a Supersonic Crossflow-The Role of Large-Scale Structures” AIAA 95-2150, 1995.

Higgins, K., and Schmidt, S., “Simulation of a sonic jet injected into a supersonic cross-flow” 16th Australasian Fluid Mechanics Conference, 2007.

Island, T., “Quantitative Scalar Measurements and Mixing Enhancement in Compressible Shear Layers” 1995, Report NO. TSD-104.

Kawai, S., and Lele, S. K., “Mechanisms of jet mixing in a supersonic crossflow: a study of large-eddy simulation,” *Annual Research Briefs,* 2007, pp. 353-358.

Keffer, J. F. and W. D. Baines “The round turbulent jet in a cross wind”, J. Fluid Mech. (1963). vol. 15, pp. 481–496.

Koochesfahani, M.M., and Dimotakis, P.E., “Mixing and chemical reactions in a turbulent liquid mixing layer”, J. Fluid Mech. (1986), vol. 170, pp. 90-92.

Osthuizen, P.H., and Carscallen, W.E., "Compressible Fluid Flow", McGraw-Hill Inc. (1997). pp. 62-200.

Recker, E., Bosschaerts, W., Wagemakers, R., Hendrick, P., Funke, H., and Borner, S., "Experimental study of a round jet in cross flow at low momentum ratio", 15th Int. Symp. on Applications of laser technology to Fluid Mechanics, Lisbon Portugal July, 2010, pp. 9.

Santiago, J. C., "An experimental study of the velocity field of a transverse jet injected into a supersonic crossflow," Ph.D. thesis, University of Illinois, Urbana-Champaign, (1995).

Sau, A., Sheu, T. W. H., Tsai, S. F., Hwang, R. R., and Chiang, T. P., "Structural development of vortical flows around a square jet in cross-flow," Proceedings of the Royal Society of London Series A-Mathematical Physical and Engineering Sciences, Vol. 460, No. 2051, 2004, pp. 3340.

Shao, Y., Zhou, J., Zhang, S., and Lai, L., "Experimental Investigation of Supersonic Mixing of HYLTE Nozzle for DF Chemical Laser," Journal of Physics: Conference series 276 (2011).

Smith, S.H. "The Scalar Concentration Field of the Axisymmetric Jet in Crossflow" (1996), HTGL Report No. T-328 pp.45-60.

Smith, S.H. and Mungal, M.G. "Mixing, structure and scaling of the jet in crossflow", J. Fluid Mech. (1998), vol. 357, pp. 83-122.

Su, L.K., and Mungal, M. G., "Mixing in crossflowing jets: Turbulence quantities," AIAA 2005-0305, 2005.

Sukumaran, S., "Numerical study on mixture formation characteristics in a direct-injection hydrogen engine",Iowa State University, Mechanical Engineering, Graduate Thesis and dissertation. (2010). Paper 11277.

Sun, M.B., Zhang, S.P., Zhao, Y.H., Zhao, Y.X., and Liang, J.H., "Experimental investigation on transverse jet penetration into a supersonic turbulent crossflow," Science China Technological Sciences. (2013), vol. 56, pp. 1989-1998.

Teoh, W. H., "Fundamental Solubility Study Of Polycyclic Aromatic Hydrocarbons In Subcritical Water And Ethanol Mixtures", University of New South Wales, Chemical Sciences & Engineering, PhD Thesis, (2012), pp. 78.

Terzis, A., Kazakos, C., Kalfas, A.I., Zachos, P.K., and Ott, P., "Swirl Jets in Crossflow at Low Velocity Ratios" Journal of Mechanics and Automation (2012), pp. 256-266.

Zhang, L., and Yang, V., "Flow dynamics and mixing of a sonic jet into supersonic crossflow," AIAA 2012-0478, pp. 1.